TRANSPORTATION RESEARCH
RECORD

No. 1505

Pavement Design, Management, and Performance

Pavement Monitoring and Evaluation Issues

A peer-reviewed publication of the Transportation Research Board

TRANSPORTATION RESEARCH BOARD
NATIONAL RESEARCH COUNCIL

NATIONAL ACADEMY PRESS
WASHINGTON, D.C. 1995

Transportation Research Record 1505
ISSN 0361-1981
ISBN 0-309-06166-0
Price: $30.00

Subscriber Category
IIB pavement design, management, and performance

Printed in the United States of America

Sponsorship of Transportation Research Record 1505

GROUP 2—DESIGN AND CONSTRUCTION OF TRANSPORTATION FACILITIES
Chairman: Michael G. Katona, U.S. Air Force Armstrong Laboratory

Pavement Management Section
Chairman: Albert J. Bush III, U.S. Army Corps of Engineers Waterways Experiment Station

Committee on Pavement Monitoring, Evaluation, and Data Storage
Chairman: John P. Zaniewski, Arizona State University
Secretary: Richard B. Rogers, Texas Department of Transportation
A. T. Bergan, Billy G. Connor, Brian E. Cox, Jerome F. Daleiden, Gary E. Elkins, Wade L. Gramling, Jerry J. Hajek, Scott A. Kutz, Kenneth J. Law, Hosin Lee, W. N. Lofroos, Louay N. Mohammad, Robert L. Mullen, Edwin C. Novak, Jr., Linda M. Pierce, Dennis G. Richardson, Ivan F. Scazziga, Mohamed Y. Shahin, Roger E. Smith, Elson B. Spangler

Committee on Rigid Pavement Design
Chairman: Gary Wayne Sharpe, Kentucky Transportation Cabinet
Don R. Alexander, Mark W. Bintlzer, Brian T. Bock, Larry J. Buttler, Lawrence W. Cole, Judith B. Corley-Lay, Kathleen T. Hall, John E. Hunt, Anastasios M. Ioannides, Walter P. Kilareski, Starr D. Kohn, Roger M. Larson, Jo A. Lary, Brian R. McWaters, Theodore L. Neff, William Albert Nokes, Mauricio R. Poblete, Robert J. Risser, Jr., Wayne J. Seiler, Mark B. Snyder, Shiraz D. Tayabji, Mang Tia, John P. Zaniewski, Dan G. Zollinger

Transportation Research Board Staff
Robert E. Spicher, Director, Technical Activities
D. W. Dearasaugh, Engineer of Design
Nancy A. Ackerman, Director, Reports and Editorial Services

Sponsorship is indicated by a footnote at the end of each paper. The organizational units, officers, and members are as of December 31, 1994.

Transportation Research Record 1505

Contents

Foreword

Fifteen peer-reviewed papers appear in this volume. The first eleven papers were presented at two sessions sponsored by the TRB Committee on Pavement Monitoring, Evaluation, and Data Storage during the 1995 Annual Meeting. The final two papers, sponsored by the TRB Committee on Rigid Pavement Design, were also presented at the 1995 Annual Meeting.

Nazarian et al. describe the seismic pavement analyzer that uses wave propagation measurements to discern conditions associated with pavement deterioration such as voids or delaminated areas. Tomita et al. report the development of a sink hole detection device in Japan to detect subsurface cavities faster and more accurately. Mesher et al. discuss a technology used with ground penetrating radar to quantify more accurately multiple pavement layer thicknesses. Acosta et al. describe algorithms used for identification and classification of common pavement distress types on video images. Chou et al. analyze video images using fuzzy logic and moment invariants to classify types of cracks in pavements. Devore et al. describe an automated method for profilograph trace reduction into a profile index and an identification of bump locations for grinding. Al-Omari and Darter study relationships between present serviceability rating, International Roughness Index, and various pavement distress type, and make recommendations of data required for predicting rehabilitation needs. de Solminihac and Hudson describe the analysis to determine mean values and variability of the serviceability index for newly constructed pavements, pavements at the end of their service life, and rehabilitated pavements. Lee and Darter use robust and nonparametric regression models to study the effect of various steel placement methods on the performance of CRCP in Illinois. Elfino et al. describe a mechanistic model using falling weight deflectometer data to evaluate asphalt concrete pavements and provide in situ characterization of pavement layers. Wang and Elliott meld typical data base information on a pavement, such as type, thickness, construction and rehabilitation history, and so forth, with video images of the pavement to produce a multimedia-based highway information system suitable for use on any personal computer or workstation. Okamoto and Tayabji report on the instrumentation of a prestressed concrete pavement in Pennsylvania and summarize the data collected. Daleiden and Killingsworth describe a computerized system using electronic clipboard technology to store and summarize pavement distress data automatically.

Kuo et al. discuss the development of a three-dimensional model to analyze support under concrete pavements based on the ABAQUS general-purpose finite element software. Hall et al. present a philosophy and procedure for the selection of the modulus of subgrade support for concrete pavement design.

Use of Seismic Pavement Analyzer in Pavement Evaluation

SOHEIL NAZARIAN, MARK BAKER, AND KEVIN CRAIN

The Seismic Pavement Analyzer (SPA, patent pending) is an instrument designed and constructed to monitor conditions associated with pavement deterioration. It measures such conditions as voids or loss of support under a rigid pavement, moisture infiltration in asphalt concrete pavement, and delamination of overlays. The SPA detects these types of pavement conditions by estimating Young's and shear moduli in the pavement, base, and subgrade from the following wave propagation measurements: (a) impact echo, (b) impulse response, (c) spectral-analysis-of-surface-waves, (d) ultrasonic-surface-wave-velocity, and (e) ultrasonic-body-wave-velocity. The SPA records the pavement response produced by high- and low-frequency pneumatic hammers on five accelerometers and three geophones. A computer controls data acquisition, instrument control, and interpretation; measurements and interpretations are reported in both screen and data base formats. This paper briefly describes the device and summarizes the usefulness of the equipment in pavement evaluation. The results from several field tests are also discussed. The tests conducted so far have produced very promising results. The device is simple to use, and results have been reliable and repeatable.

In recent years, the focus of pavement engineering has shifted from design and construction of new highways to preventive maintenance and rehabilitation of the existing highways. A highway maintenance program is usually based on a visual condition survey and, to a lesser extent, on appropriate in situ tests. By the time symptoms of deterioration are visible, major rehabilitation or reconstruction is often required. If the onset of deterioration can be measured accurately in the early stages, the problem can often be resolved or stabilized through preventive maintenance.

A relatively inexpensive and precise device for project-level measurements has been developed. This device, the Seismic Pavement Analyzer (SPA, patent pending), can be of help in detecting these types of problems.

OVERVIEW OF SEISMIC PAVEMENT ANALYZER

To diagnose a pavement, mechanical properties of each of the pavement system layers should be determined. The SPA lowers transducers and sources to the pavement and digitally records surface deformations induced by a large pneumatic hammer that generates low-frequency vibrations, and a small pneumatic hammer that generates high-frequency vibrations (see Figure 1).

This transducer frame is mounted on a trailer that can be towed behind a vehicle and is similar in size and concept to a Falling Weight Deflectometer (FWD). The SPA differs from the FWD in that more and higher frequency transducers are used, and more sophisticated interpretation techniques are applied. The SPA is controlled by an operator at a computer connected to the trailer by a cable. The computer may be run from the cab of the truck towing the SPA or from various locations around the SPA.

All measurements are spot measurements; that is, the device has to be towed and situated at a specific point before measurements can be made. A complete testing cycle at one point takes less than 1 min. A complete testing cycle includes situating at the site, lowering the sources and receivers, making measurements, and withdrawing the equipment. During this 1 min, most of the data reduction is also executed.

The SPA collects two levels of data. The first level is raw data. These are the waveforms generated by hammer impacts and collected by the transducers. The second level is processed data. These are pavement layer properties derived from the raw data through theoretical models.

DESCRIPTION OF MEASUREMENT TECHNOLOGIES

Impulse-Response (IR) Method

Two parameters are obtained with the IR method—the shear modulus of subgrade and the damping ratio of the system. These two parameters characterize the existence of several distress precursors. In general, the modulus of subgrade can be used to delineate between good and poor support. The damping ratio can distinguish between the loss of support or weak support. The two parameters are extracted from the flexibility spectrum measured in the field. An extensive theoretical and field study (*1*) shows that except for thin layers (less than 75 mm) and soft paving layers (i.e., flexible pavements), the modulus obtained by the IR method is a good representation of the shear modulus of subgrade. In other cases, the properties of the pavement layers (AC and base) affect the outcome in such a manner that the modulus obtained from the IR test should be considered an overall modulus.

The IR tests use the low-frequency source and geophone G1 (see Figure 1). The pavement is impacted to couple stress wave energy in the surface layer. At the interface of the surface layer and the base layer, a portion of this energy is transmitted to the bottom layers, and the remainder is reflected back into the surface layer. The load and displacement time histories are simultaneously recorded and are transformed to the frequency domain using a Fast-Fourier Transform algorithm. The ratio of the displacement and load (termed flexibility) at each frequency is then determined.

A typical flexibility spectrum is shown in Figure 2(*a*). The response is as expected, except for frequencies below approximately 50 Hz. The erratic nature of the signal at low frequencies is probably because of the movement of the trailer. This problem has been solved in the new design.

The Center for Geotechnical and Highway Materials Research, The University of Texas at El Paso, El Paso, Tex. 79968.

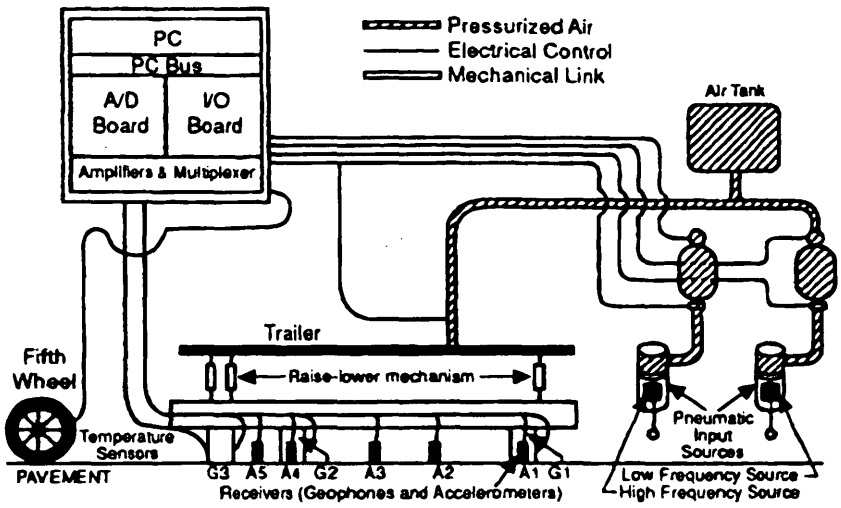

FIGURE 1 Schematic of seismic pavement analyzer.

The coherence function associated with this record is shown in Figure 2(*b*). The coherence values are close to unity except at low frequencies. A coherence value of unity corresponds to a highly coherent signal between the load cell and receiver. In other words, there was no incoherent background noise in the signals.

To determine the modal parameters (static flexibility and damping ratio), a curve is fitted to the flexibility spectrum according to an elaborate curve-fitting algorithm that uses the coherence function as a weighing function. A typical fitted curve is shown in Figure 2(*a*). The agreement between the measured and the fitted data is good. However, once again, because of a lack of quality data at low frequencies, the fit is not adequate in this region.

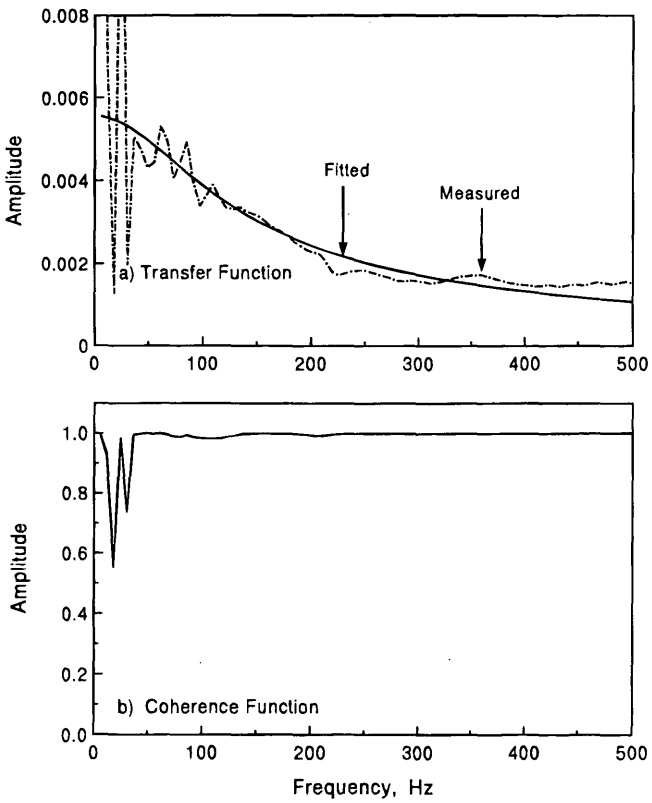

FIGURE 2 Typical spectral functions used in IR test.

The shear modulus of subgrade, G, is calculated from:

$$G = (1 - \nu) / [2L A_o I_s S_z] \quad (1)$$

where

ν = Poisson's ratio of subgrade;
L = length of slab; and
A_o = static flexibility of slab (flexibility at $f = 0$).

The shape factor, S_z, has been developed by Dobry and Gazetas (*2*). The value of S_z is equal to 0.80 for a long flexible pavement.

I_s is a parameter that considers the effect of an increase in flexibility near the edges and corners of a slab. Parameter I_s is a function of the length and width of the slab, as well as the coordinates of the impact point relative to one corner. Depending on the size of the slab and the point of impact, the value of I_s can be as high as 6.

The damping ratio, which typically varies between 0 to 100 percent, is an indicator of the degree of the slab's resistance to movement. A slab that is in contact with the subgrade or contains a water-saturated void demonstrates a highly damped behavior and has a damping ratio of greater than 70 percent. A slab containing an edge void would demonstrate a damping ratio in the order of 10 to 40 percent. A loss of support located in the middle of the slab will have a damping ratio of 30 to 60 percent.

Spectral-Analysis-of-Surface-Waves (SASW) Method

The SASW method is a seismic method that can determine shear modulus profiles of pavement sections nondestructively.

The key point in the SASW method is the measurement of the dispersive nature of surface waves. A complete investigation of a site with the SASW method consists of collecting data, determining the experimental dispersion curve, and determining the stiffness profile (inversion process).

The set-up used for the SASW tests is depicted in Figure 1. All accelerometers and geophones are active. The transfer function and coherence function between pairs of receivers are determined during the data collection.

A computer algorithm utilizes the phase information of the transfer function and the coherence functions from several receiver spacings to determine a representative dispersion curve in an automated fashion (*3*). The dispersion curves obtained from all receiver spacings from a site is shown in Figure 3(*a*). A curve is fitted to this data to obtain the "fitted-measured dispersion curve." This idealized curve is representative of the raw data.

The last step is to determine the elastic modulus of different layers, given the dispersion curve. A recently developed automated inversion process (*4*) determines the stiffness profile of the pavement section. This fitted curve is used in the inversion process. The modulus profile at the example site is shown in Figure 3(*b*). To ensure that the inversion process is successful, the fitted-measured dispersion curve is compared with the theoretical dispersion curve (obtained from the Young's modulus profile shown in Figure 3(*b*)). This comparison is depicted in Figure 3(*a*). The theoretical (labeled "from inverted model" in the figure) and experimental data (labeled "L1-norm fitted" in the figure) compare favorably.

Ultrasonic-Surface-Wave Method

The ultrasonic-surface-wave method is an offshoot of the SASW method. The major distinction between these two methods is that in the ultrasonic-surface-wave method the properties of the top paving layer can be easily and directly determined without a complex inversion algorithm. To implement the method, the high-frequency source and accelerometers A2 and A3 (see Figure 1) are utilized.

Up to a wavelength approximately equal to the thickness of the uppermost layer, the velocity of propagation is independent of wavelength. Therefore, if one simply generates high-frequency (short-wavelength) waves, and if one assumes that the properties of the uppermost layer are uniform, the shear modulus of the top layer, G, can be determined from

$$G = \rho\,[(1.13 - 0.16\nu)\,(m/360D)]^2 \qquad (2)$$

Parameter m (degree/Hz) is the least-squares fit slope of the phase of the transfer function in the high-frequency range.

A typical phase spectrum is shown in Figure 4(*a*). The phase oscillates on a radius between π and $-\pi$ radians (180 and -180 degrees). This is the standard method of presenting phase data, because the detailed variation in the data can be observed in a small space.

The coherence function associated with this record is shown in Figure 4(*b*). The coherence is almost equal to 1, up to a frequency of 35 or 40 kHz. Above the frequency of 35 kHz, the data are of low quality and are not usable.

The frequency of 35 kHz for this experiment corresponds to a wavelength of less than 38 mm. Shorter wavelengths can be investigated using Accelerometer 1 and Accelerometer 2 (which are spaced 75 mm apart). One physical limitation is the aggregate size. Wavelengths shorter than the maximum aggregate size probably do not follow the laws of wave propagation in solid medium.

The shear modulus of the top layer was obtained using a complex-valued curve-fitting process with the coherence as the weighing function (*3*). The results are shown in Figure 4(*a*). The actual and fitted curves compare quite favorably up to a frequency of 30 kHz. In the next step, the phase is "unwrapped;" that is, the appropriate number of cycles is added to each phase. The unwrapped phase for the "wrapped" phase shown in Figure 4(*a*) is shown in Figure 4(*c*). The slope of the line, which is basically constant with frequency, is used in Equation 2.

Ultrasonic-Compression-Wave-Velocity Measurement

Once the compression wave velocity of a material is known, its Young's modulus can be readily determined. The same set-up used to perform the SASW tests can be used to measure compression wave velocity of the upper layer of pavement.

The body wave energy present in a seismic record generated using the set-up shown in Figure 1 is small, and for all practical purposes it does not contaminate the SASW results. However, compression waves travel faster than any other type of seismic wave, and are detected first on seismic records.

Typical travel times, expanded to demonstrate the arrival of the compression waves, are shown in Figure 5. The arrows in each

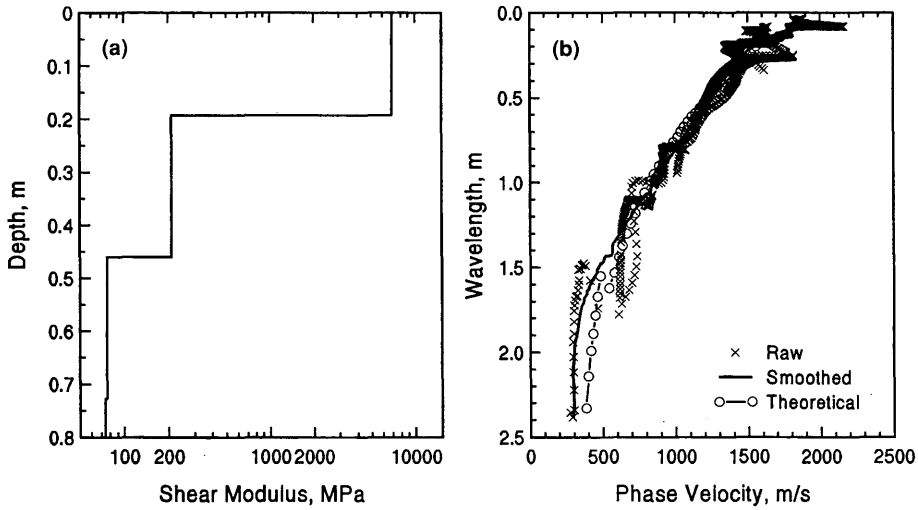

FIGURE 3 Typical results from SASW tests.

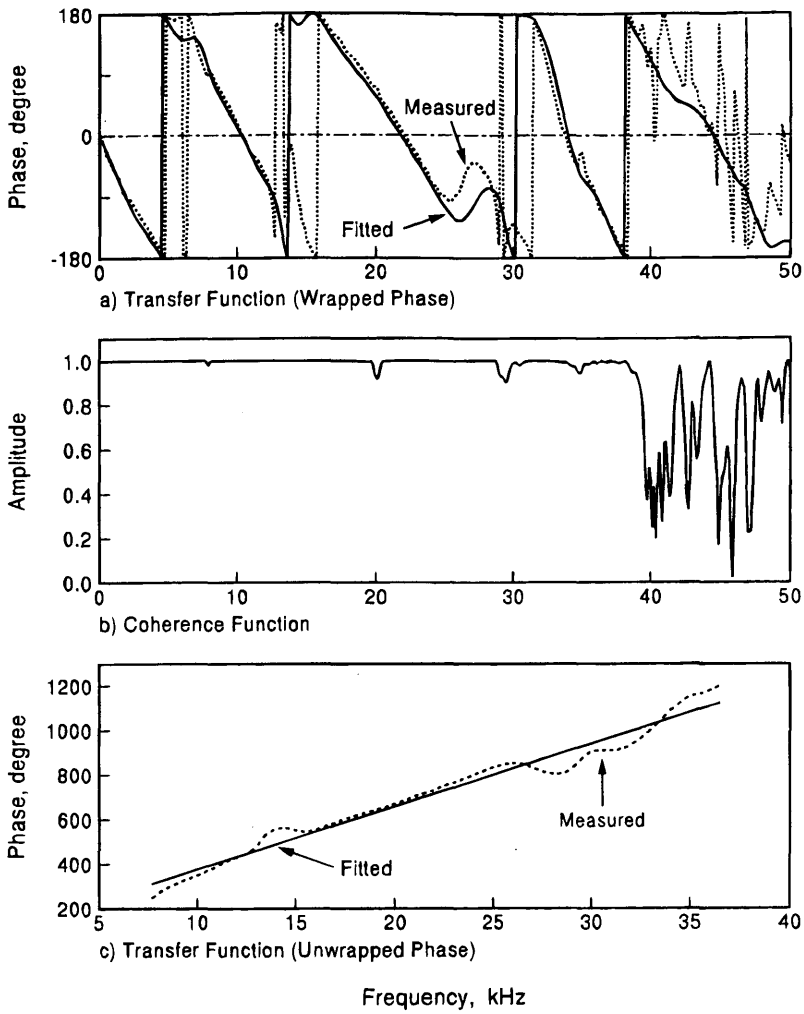

FIGURE 4 Typical spectral functions used in ultrasonic-surface-wave test.

record correspond to the arrival of these waves. Typically, Accelerometers 3 and 4 record the arrival of energy most consistently. The determination of the arrival of compression waves from Accelerometers 1 and 3 are typically not possible because of the closeness of the sensors to the source.

An automated technique for determining the arrival of compression waves has been developed. Times of first arrival of compression waves are measured by triggering on an amplitude range within a time window (*5*).

Impact-Echo Method

The impact-echo method can effectively locate defects, voids, cracks, and zones of deterioration within concrete.

The high-frequency source and accelerometer A1 are used, and possibly A2 as well (see Figure 1). Once the compression wave velocity of concrete, V_p, is known, the depth-to-reflector, T, can be determined from

$$T = V_p / 2f \quad (3)$$

where f is the resonant (return) frequency obtained by transforming the deformation record into the frequency domain.

A typical frequency-response spectrum for a site is shown in Figure 6(*a*). The major peak (at about 10 kHz) corresponds to the thickness of the layer and is called the return (resonant) frequency, which is input in Equation 3.

The coherence function is shown in Figure 6(*b*). In general, the data collected with the device have no incoherent noise, except at several isolated frequencies.

CASE STUDIES

Two case studies are incorporated here for demonstration purposes. Numerous other ones can be found in Nazarian et al. (*1*).

Case 1: Rigid Pavement

A jointed concrete pavement section was tested to determine the existence of voids and loss of support in the pavement. The pave-

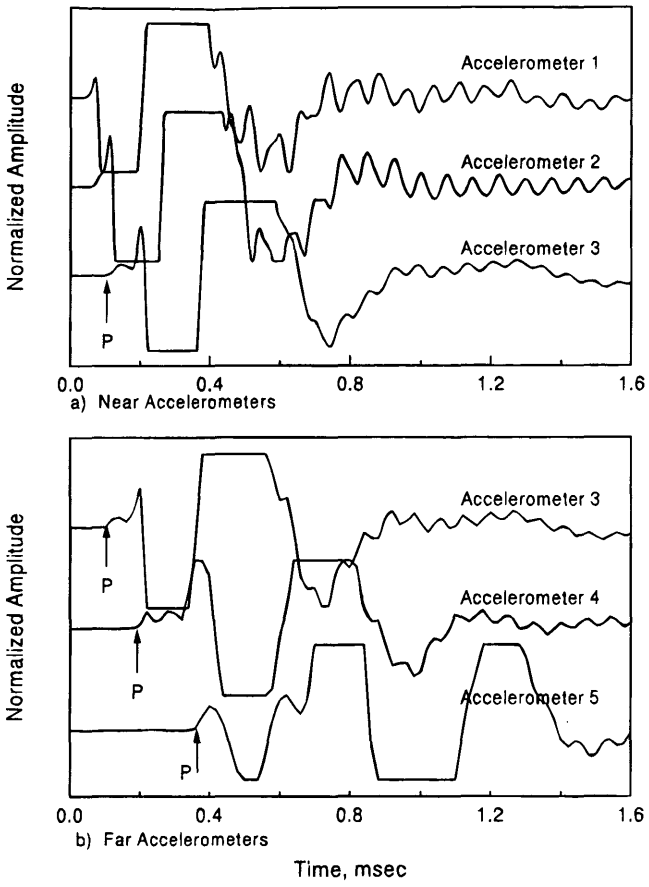

FIGURE 5 Typical amplified signals used in ultrasonic-body-wave test.

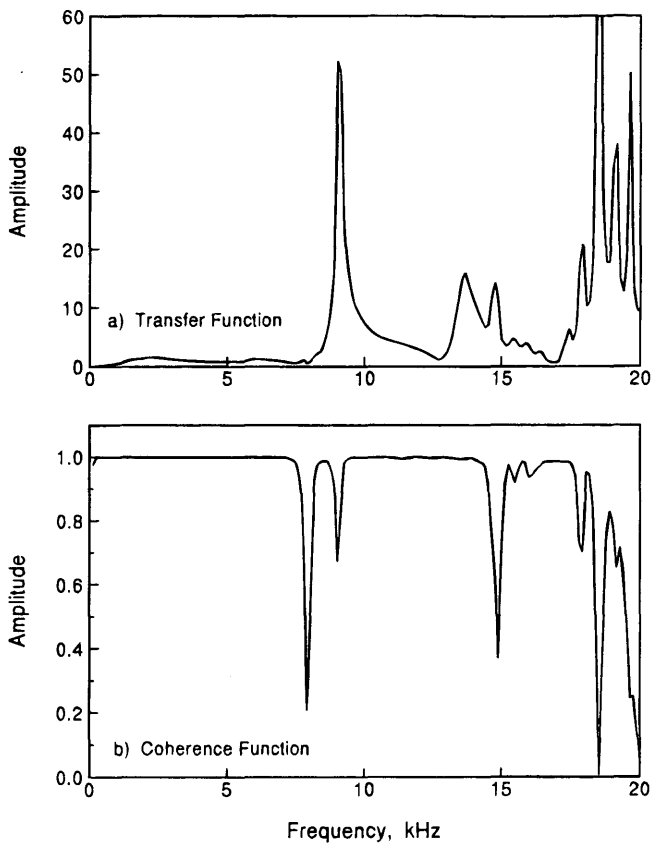

FIGURE 6 Typical spectral functions used in impact-echo test.

ment section at the site consisted of 225 mm jointed-concrete pavement over a cement-treated base.

The Portland cement concrete (PCC) slabs were 9 m long and 3.6 m wide. Twelve slabs (13 joints numbered 1 through 13) were tested. Three points were tested at each slab. The three points were located at 15 cm east and west of each joint and in the middle of each slab.

The IR test was used to detect voids and loss of support. The resulting moduli of subgrade and damping ratios are shown in Figure 7. The mean subgrade modulus is about 175 MPa. This indicates an above-average subgrade material. This section is in good condition, which is to be expected because the section was recently rehabilitated.

The data presented here indicate the need to inspect and maintain the approach side of each joint for possible voids, especially for Joints 2, 3, 5, 6, and 9. The two slabs between Joints 11 and 13 are in very bad condition and should be repaired. These recommendations are consistent with the condition of the pavement.

Most of the damping ratios shown in Figure 7(*b*) are above the critical damping ratio, indicating either water saturation of voids or good contact at the interface of the concrete and base layer. As indicated before, the water-saturated voids and intact locations are both highly damped; however, the intact points exhibit substantially higher moduli of subgrade.

To verify these results, five epoxy core holes were installed at the section, as marked in Figure 7. Points 2, 4, and 5 were selected as areas where voids were suspected. These three core points validated the SPA prediction that they were water-saturated voids (low modulus of subgrade, high damping ratio). Upon coring, the holes filled with water almost instantaneously. The other two cores were selected as intact concrete. Points 1 and 3 proved to be on relatively dry and intact subgrade.

The values of Young's and shear moduli of the slab are shown in Figure 8(*a*). Only the properties from the middle of the slab are shown here. Some variation in the results can be attributed to the variability in the material properties and also to some variability in data interpretation. In most cases, the material properties vary because both methods measure consistently lower or higher for the same points. In the middle of Slab 3, similar values for the shear and Young's moduli are reported; the reason for this discrepancy is the existence of a crack between the source and the accelerometer used to measure the compression wave velocity.

In general, the average Young's and shear moduli are 33 GPa and 15 GPa, respectively. These values represent average-quality concrete. From the average shear and Young's moduli, the average Poisson's ratio is about 0.14. This is an acceptable value for Poisson's ratio of concrete.

The measurements of the thickness of the PCC are shown in Figure 8(*b*). At the two core holes, the actual thicknesses of concrete is about 230 mm. The two points on Slabs 11 and 12 that exhibit smaller thickness are in the area where the concrete requires repair. The reason for the thinness of Slab 8 is not known.

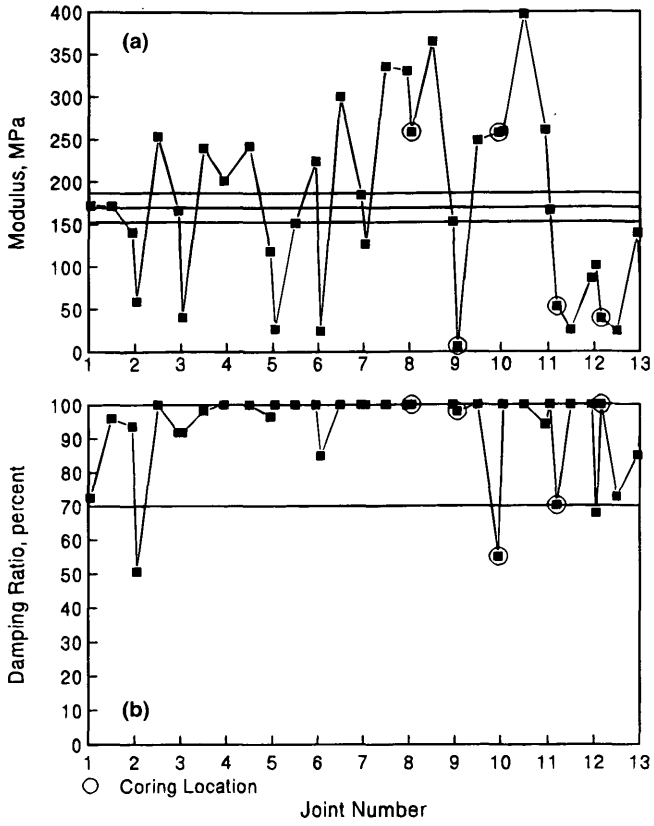

FIGURE 7 Variation in parameters measured with IR method at the rigid pavement site.

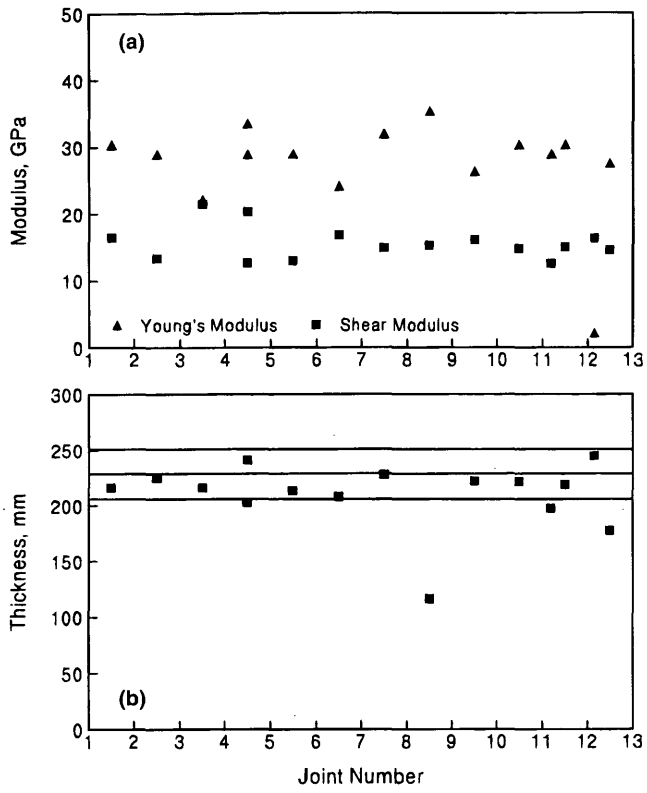

FIGURE 8 Variations in moduli and thickness of PCC at the rigid pavement site.

This case study demonstrates that the SPA is capable of evaluating rigid pavements for the existence of voids and loss of support in both dry and saturated conditions. At the five points where ground truth is available, the predictions were accurate.

Case 2: Flexible Pavement

The typical pavement cross section of this site consisted of 210 mm of AC over 250 mm of granular base over a corrodible sandy subgrade. A 1300-m section of the highway was selected and tested at 30-m intervals. The FWD device was used 3 weeks after the SPA tests were completed. These tests determine the softening of the subgrade as a result of the penetration of moisture.

The deflections for a nominal load of 40 kN are shown in Figure 9. A large variation in the deflection basins can be observed, possibly indicating the variability in the overall stiffness of the section. The variations in the deflections also may result from variations in the thickness or stiffness of the layers.

The modulus values obtained at the site from BISDEF are not included because back-calculation was not successful. At all points, the modulus of the AC was back-calculated as the upper prescribed range of 17.5 GPa, and the base modulus was always equal to 35 MPa (the lower range assigned to the material for the back-calculation). This may be partly the result of the dynamic interaction between the bedrock and the FWD. A large portion of the site was in a cut section.

The IR test was used to determine the effects of moisture variation in the base and subgrade. The IR test was utilized to determine the overall variation in stiffness, and the SASW method was employed for more thorough analysis.

The measurements of the modulus of the subgrade soil are shown in Figure 10. The pavement in the range of −50 m to −80 m corresponded to a saturated base and subgrade. The rest of the section seemed to be in reasonably good condition. However, the data indicate some potential problems in the 200-m to 350-m section. The level of water in a ditch on the side of the road was rather high in this area.

The results from the SASW tests are summarized in Table 1. These tests were carried out at some of the core locations; therefore, they do not correspond to test results described above. The moduli of the AC layer are relatively constant. The base moduli are similar, except for the two points tested at −84 m and −54 m. The base material at the −84 m location was saturated, and water was seeping to the pavement surface. The point tested at −54 m was also wet. The subgrade moduli are rather high for points 360 m and 900 m, and are representative of most of the pavement section. The test point at 270 m corresponds to the area that the IR tests diagnosed as soft. At this point, the subgrade is quite soft, whereas the AC and base layers are in good condition.

The water contents (also recorded in Table 1) were obtained in the field with a pan-dry oven. As indicated, the base at −84 m has the highest water content and also the lowest modulus. The two points located at 360 m and −54 m exhibit similar water content;

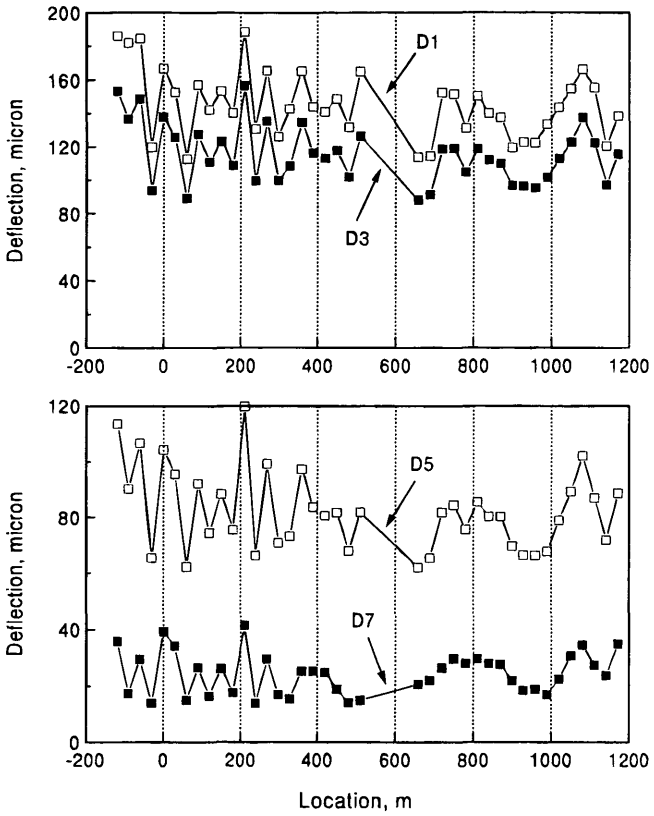

FIGURE 9 Variation in deflection basins at the flexible pavement site.

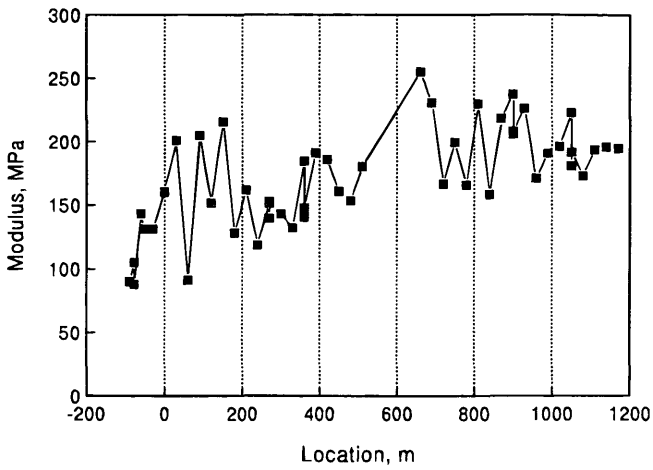

FIGURE 10 Variation in modulus of subgrade soil from IR tests at the flexible pavement site.

however, the moduli of these two points are significantly higher than that of point −84 m. Point 360 m, with base moisture similar to point −84 m, is significantly stiffer than point −84 m. Both independent tests (IR and SASW) concur that point −84 m is not as stiff as point −54 m or point 360 m. Based on engineering intuition, the pavement structure at point −84 m should therefore be softer than the other points. Points −84 m and −54 m are located in a rock cut, whereas point 360 m was almost in a fill section. Therefore, the dynamic interaction would affect the deflections from FWD, and the SPA results could not be verified.

Establishing a relationship between the modulus and water content, without considering other factors such as the type of the base and subgrade materials, optimum water content for the base and subgrade, and the period of time that the material is exposed to the moisture, may not be appropriate.

The values of the shear modulus of the asphalt concrete layer are shown in Figure 11(*a*). The pavement in locations around 600 m was not tested because there was a bridge. Moduli are clustered at two levels. Between locations 0 m and 600 m, the moduli are higher than the rest of the section, because of the temperature sensitivity of the AC layer. The 600-m section (between 0 m and 600 m) was tested in the early morning when the pavement was cold (ambient temperature of −2°C), and the other sections were tested later, when the sun had been out, raising ambient temperature to 22°C.

The values of Young's modulus as determined from the ultrasonic-body-wave tests are shown in Figure 11(*b*). The same clustering of moduli can be seen in the results of this test as well;

TABLE 1 Shear Modulus Profiles Obtained at the Flexible Pavement Site

Location, m	Shear Modulus, MPa			Water Content, percent		FWD Deflection*, micron	
	AC	Base	Subgrade	Base	Subgrade	D1	D7
-84	7530	78	45	6.2	14.4	179**	17
-54	6433	127	89	5.7	--	182**	29
270	6944	210	77	4.0	11.8	160	29
360	8486	214	150	6.0	14.1	160	25
900	7960	205	136	4.1	15.7	112	21

* Deflections, which are reported for a nominal load of 40 KN, should be considered with caution, since a stiff layer existed under the pavement at variable depths.

** FWD tests were not carried out at this location. The closest point tested is reported.

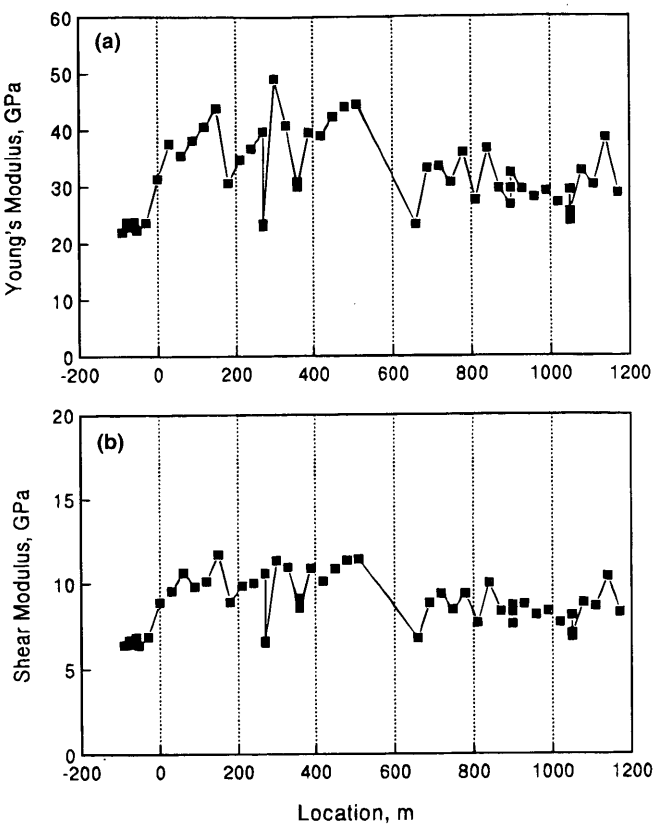

FIGURE 11 Variations in moduli of AC at the flexible pavement site.

the two independent testing methodologies yield relatively similar results. From the shear and Young's moduli, Poisson's ratio is in the range of 0.29 to 0.35, which is quite reasonable. In general, this case study clearly shows the potential, accuracy, and the robustness of the SPA.

CONCLUSIONS

Based on the information presented, it can be concluded that the new SPA nondestructive testing device is useful for pavement evaluation, and that the SPA can easily, accurately, and repeatably collect information about the condition of pavements.

ACKNOWLEDGMENTS

This work was funded by the Strategic Highway Research Program under Project H-104B. The financial and technical assistance of that organization is appreciated.

In addition, the support and financial backing of the Texas Department of Transportation should be mentioned. Without the trust and support of that organization, this project could not have been completed.

REFERENCES

1. Nazarian, S., R. D. Baker, and K. Crain. *Development and Testing of a Seismic Pavement Analyzer.* Research Report SHRP-H-375. Strategic Highway Research Program, TRB, National Research Council, Washington, DC, 1993.
2. Dobry, R., and G. Gazetas. Dynamic Response of Arbitrary Shaped Foundations. *Journal of Geotechnical Engineering*, Vol. 112, No. 2, 1986, pp. 109–135.
3. Nazarian, S., and M. Desai. Automated Surface Wave Testing: Field Testing. *Journal of Geotechnical Engineering*, Vol. 119, No. GT7, 1993, pp. 1094–1112.
4. Yuan, D., and S. Nazarian. Automated Surface Wave Testing: Inversion Technique. *Journal of Geotechnical Engineering*, Vol. 119, No. GT7, 1993, pp. 1112–1126.
5. Willis, M. E., and M. N. Toksoz. Automatic P and S Velocity Determination from Full Wave Form Digital Acoustic Logs. *Geophysics*, Vol. 48, No. 12, 1983, pp. 1631–1644.

Publication of this paper sponsored by Committee on Pavement Monitoring, Evaluation, and Data Storage.

Nature and Detection of Void-Induced Pavement Failures

H. TOMITA, H. TADA, T. NANBU, K. CHOU, T. NAKAMURA, AND T. MCGREGOR

Pavement failures caused by substructure cavities, or voids, have recently become a widespread problem in Japanese roads. Several cities in Japan have reported these problems. To ensure the safe flow of traffic and to avoid pavement failure-induced traffic accidents, the detection of sinkholes became a top priority. Acting on this situation, the Ministry of Construction developed a sinkhole detection vehicle that makes it possible to detect subsurface cavities with higher speed and precision. The Ministry of Construction formed a coordinating agency to oversee the implementation of this technology. This agency made actual site surveys and analyzed the results to ascertain the mechanical properties of subsurface cavities. With this knowledge, in 1992 an effective sinkhole detection method was developed. The method utilizes ground penetrating radar and a bore hole camera as field data acquisition tools. The detection method relies on using the analysis tools to provide an increasingly detailed look at the pavement substructure: from a general survey to a specific survey. Through many void identifications during daily operations in the field, we have arrived at an understanding of the nature of subsurface voids. This understanding has allowed pavement maintenance and construction engineers to catch voids before they evolve to dangerous pavement failures.

A growing number of accidents have been reported in recent years on the highways and roads of Japan that have been caused by sinkholes. As a result of this situation, it became necessary to develop a way to detect sinkholes that was quick, accurate, reliable, and nondestructive to the pavement. The Ministry of Construction accepted this challenge and in 1990 developed the first practical sinkhole detection method in the world. The method relies on a primary survey with vehicle-mounted, low-frequency ground penetrating radar (GPR), a secondary survey using hand-operated GPR, and a final confirmation with a bore hole camera (BHC).

DEVELOPMENT OF A SINKHOLE DETECTION VEHICLE

Previous sinkhole detection surveys were performed using portable GPR devices or infrared devices. From a careful study of the results of these surveys, it was determined that these methods were not satisfactory because they were not accurate enough and the speed of the survey was too slow. Therefore, before development, the Ministry of Construction constructed a test field in which sample voids, pipes, and other subsurface anomalies were buried. Various methods of detection (not immediately relevant to this discussion) were used in this controlled environment to determine which method was the most effective at subsurface detection. The public dissatisfaction over the many sinkholes in Japan caused this situation to be pursued on an emergency basis. The analysis tools were mounted in a convenient vehicle as shown in Figure 1.

H. Tomita, Road Management Technology Center and Geo Search Company Ltd., 15-12, Nishikamata 8-Chome Ohta-ku, Tokyo 144, Japan. H. Tada, Road Management Technology Center, 9-9 Nihonbashi, Hisamatsu-Cho, Chuo-ku, Tokyo 103, Japan. T. Nanbu, Ministry of Construction, Road Bureau, 2-1-3 Kasumigaseki, Chiyoda-ku, Toyko, Japan. K. Chou, Kanto Engineering Laboratory, Ministry of Construction, 7-1 Hatsutomitobichi, Matsudo City, Chiba Pref., Japan. T. Nakamura, Pavement Division, Public Works Institute, Ministry of Construction, 1-Asahi, Oaza, Tsukuba City, Ibaragi Pref., Japan. T. McGregor, Geo Search America, 4611 Turf Valley Drive, Houston, Tex. 77084.

FEATURES OF THE SINKHOLE DETECTION VEHICLE

Penetration Depth

The low frequency penetrates to approximately 1.2 to 1.5 m. This figure will vary based on the electromagnetic conductivity of the soil composition. This target depth specification was chosen based on investigation of the records of the depths of actual sinkholes. The evolution of a sinkhole is shown in Figure 2; loose sands migrate upward from their point of origin (see also Figure 10) to the pavement subsurface.

Width of Inspection

The inspection path covered during one pass is greater than 2 m. The GPR antennas have a field width of 1 m each and two antennas were installed in a parallel mounting configuration on the vehicle. Using this method, it became possible to inspect almost all of a lane on a single pass with minimum obstruction to normal vehicular traffic. The mounting style and position of the antennas is shown in Figure 3.

Speed of Inspection

The vehicle can perform the survey function at over 20 km/hr. The previously used GPR inspection methods cannot proceed at over 2 to 4 km/hr, but the developed vehicle has a hydraulic lifter, which makes possible running and turning the GPR antenna without repeated antenna to ground contact. One data acquisition period is now over 10 times faster than previously used GPR methods, and it is possible to survey at over 20 km/hr.

It should be noted that the problem of dispersed radio frequency isolation was addressed by the installation of electromagnetic wave damping skirts around the perimeter of the antennas to form a barrier between the antenna, the pavement surface, and the damping skirt.

FIGURE 1 Sinkhole detection vehicle.

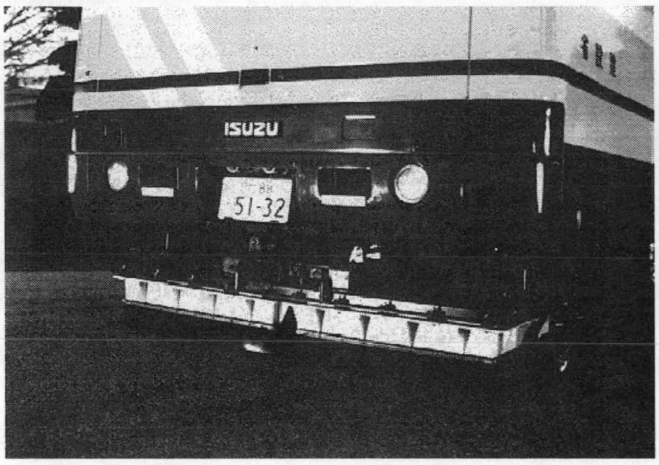

FIGURE 3 Mounting of the dual antennas at the rear of the vehicle.

Void Detection Capability

In the previously mentioned field work, 212 possible voids were identified with the method and 191 voids were confirmed by cutting and filling. This produces a nominal success rate of about 91%. The overriding concern with this void detection method is to avoid costly cut-and-fill operations. The importance of this method becomes apparent in the secondary survey when the marginal void targets can be determined to be void or nonvoid areas. The system can distinguish voids from other buried objects. This process was proven in test fields, and also in actual site surveys in which noise problems caused by poorly matched circuit components and tip deflection were finally eliminated, suitable frequencies of GPR wave were chosen, and the typical signal pattern of the void was determined. Video cameras are mounted at the front and left and right of the vehicle as shown in Figure 4. Their recorded data are synchronized with the GPR data to provide distance measurement. This technique ensures that the void location will be found in the proper road position. This system is called a positioning system (*1*).

BORE HOLE CAMERA

The BHC system is shown in Figure 5. It consists of four parts, the video probe, the counter roller insertion device, the microprocessor-based control unit, and the diamond-tipped core boring equipment.

SINKHOLE DETECTION METHOD

After the road to be surveyed has been determined, the following steps of the primary and secondary surveys should be followed. This method is shown in flowchart form in Figure 6.

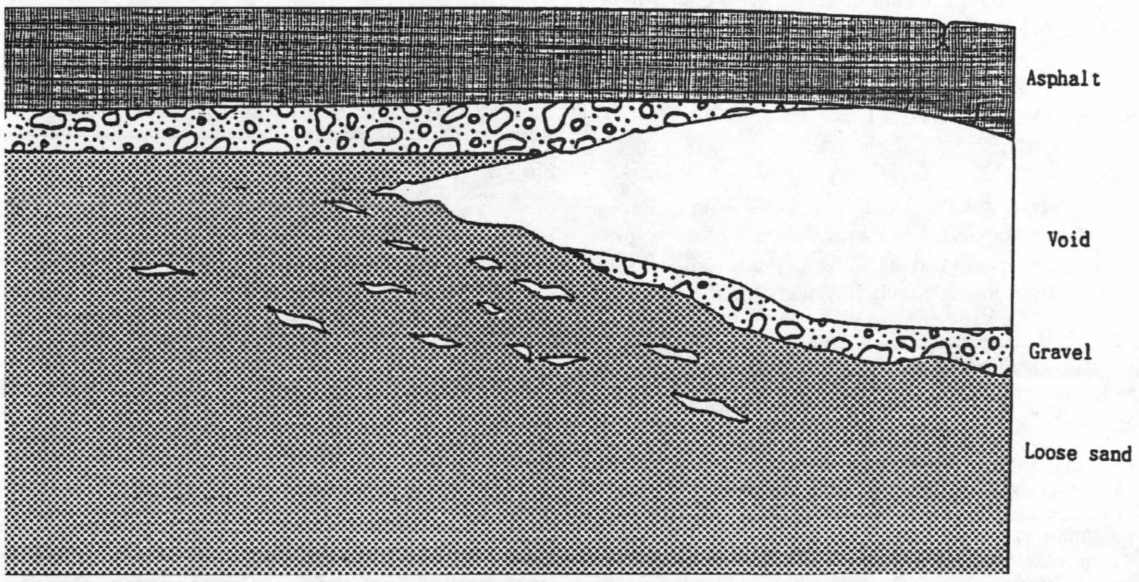

FIGURE 2 A typical subsurface void in the actual and formative states.

FIGURE 4 Positioning system orientation showing location and field of view of cameras.

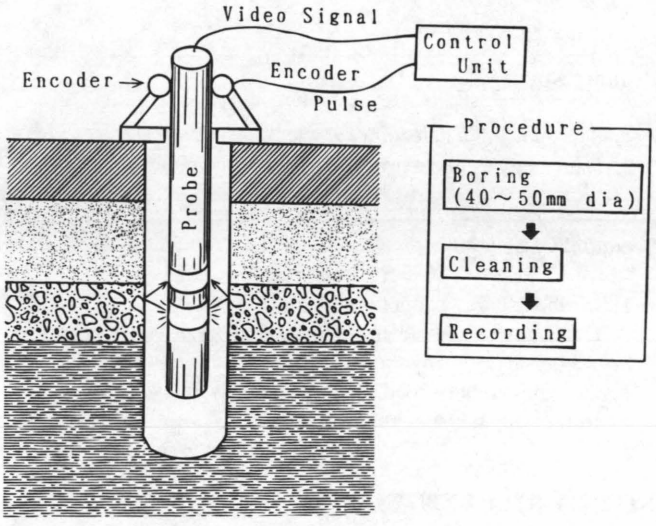

FIGURE 5 Drawing of BHC probe during data acquisition process.

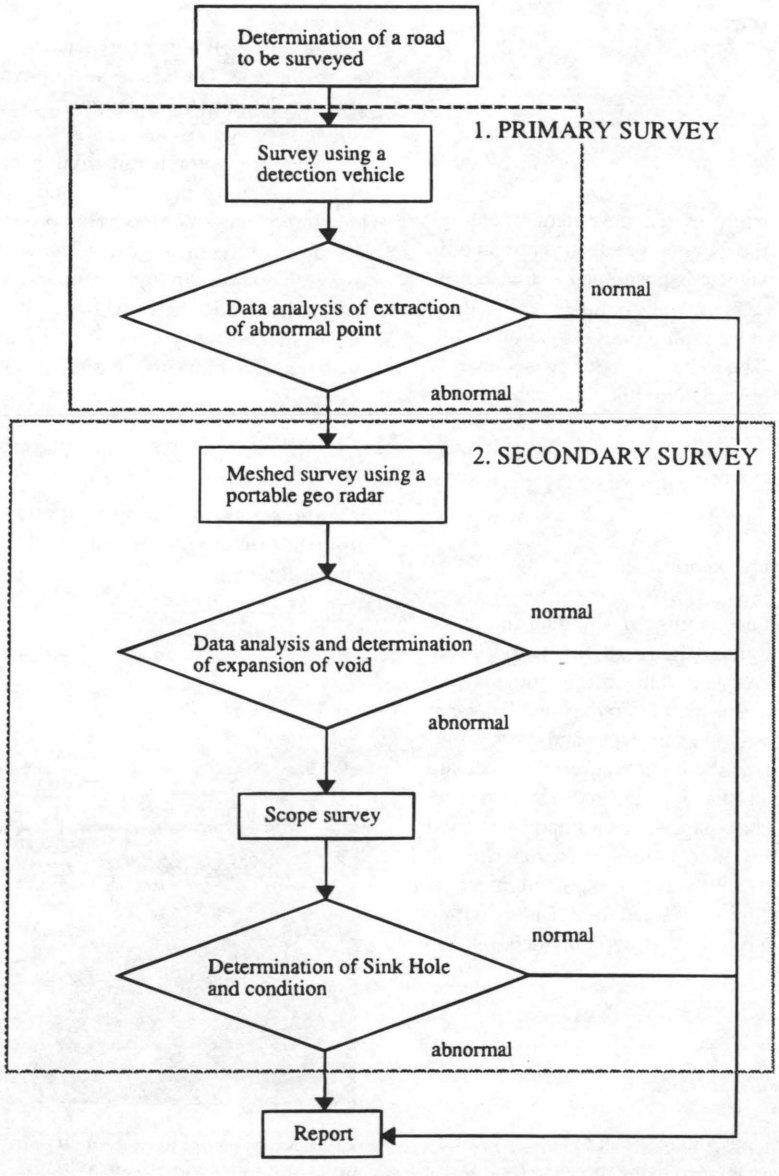

FIGURE 6 Flowchart of detection method.

Primary Survey

1. Survey using a detection vehicle.
2. Data analysis and extraction of abnormal point.

Secondary Survey

1. Meshed survey using portable radar gear.
2. Data analysis and determination of cavity dimensions.
3. Scope survey using the BHC system.
4. Determination of road subsurface cavity and condition.
5. Report to pavement engineer.

STEP-BY-STEP EXPLANATION OF METHOD

Determination of a Road To Be Surveyed

The determination of the road to be surveyed is made by the road authority. The selection criteria is ordinarily based on visually detected pavement distress or surface anomaly.

Primary Survey

Survey Using a Detection Vehicle

In the first look at the substructure of the pavement, the low-frequency radar vehicle detects the location of substructure anomalies such as voids. The survey vehicle is positioned at the start of the target lane segment, the GPR equipment is initiated, verbal cues are inserted onto the eight-track tape, and the investigation of the pavement substructure begins. The vehicle gradually achieves a speed of 20 km/hr and moves forward along the designated route. As the completion of the lane segment is achieved, the machinery is placed on standby mode, the vehicle is turned around and positioned to survey the opposite lane, and the procedure is repeated (*2*).

Data Analysis and Extraction of Anomalies

After the field survey has been accomplished, the data that have been acquired are turned over to the office staff for the post-data acquisition analysis. The storage media delivered to the analysis crew are the roll of chart paper on which the radar data has been recorded (a sample of a GPR trace on chart paper and its relationship to the position of the vehicle is shown in Figure 7), the backup 8-track magnetic tape that contains the radar and audio information, and the 8-mm videotape. The chart paper is examined by trained readers for examples of anomalies. If no anomalies are determined, the report is made and delivered to the pavement engineer. If abnormal points are determined by the trained data readers within the target pavement, the secondary survey is implemented.

Secondary Survey

Meshed Survey Using Portable Radar Gear

The field crew returns to the site previously subjected to the primary survey. Subsurface anomalies are located using the video and linear

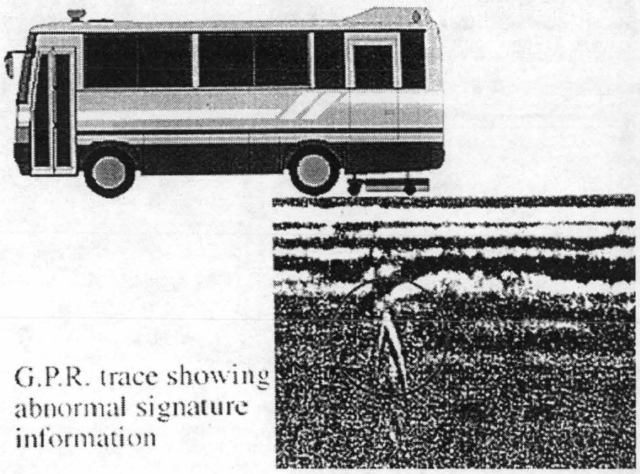

FIGURE 7 Detection vehicle with GPR trace juxtaposed showing orientation of data acquisition sequence.

feet data, as well as the verbal cues and radar data from the 8-track magnetic tape. On arrival at the investigation site, the field crew uses special portable radar gear developed for the purpose of void detection to determine the exact parameters of the subsurface anomaly. The portable radar unit is passed over the target area and as the borders of the void are located, spray paint determines the location of these borders. This process is shown in Figure 8. The operators of the radar gear in the vehicle (the comfortable interior of which is shown in Figure 9) transmit to the radar transducer operators when and where the anomaly border has been detected by means of a two-way radio. In a short time, the subsurface void has been mapped with surface-applied spray paint.

Data Analysis and Determination of Cavity Dimensions

This process is similar to the previously noted data analysis step from the primary survey, but special care is taken to determine void dimensions.

FIGURE 8 Void area on a city street isolated by portable GPR units and marked with spray paint.

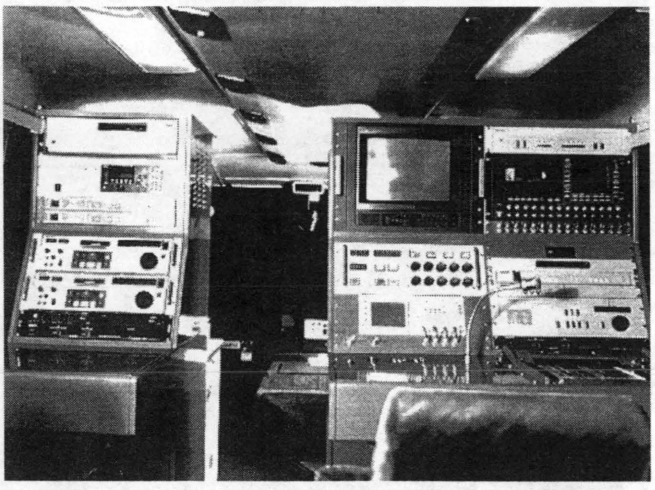

FIGURE 9 Interior of vehicle showing operator controls and data acquisition monitoring equipment.

Scope Survey

The common method for confirming the presence of a void is to cut and fill, but this method destroys the in situ condition of the possible void and does not allow the pavement engineer to know the true nature of the void. To perform the scope survey, a 40-mm hole is bored. After the bore hole has been drilled, the hole is cleaned with water and then vacuumed to remove any mud left over from the boring process. After the bore hole has been cleaned, the counter roller is positioned over the hole. The probe is then lowered into the hole. When the video portion of the probe descends just below the surface of the hole, the camera controller is activated and then the speed regulated descent of the probe begins. As the probe travels down the bore hole, the high resolution video equipment shows exactly the layer thickness, material composition, and void location, as shown in Figure 10. After data acquisition, the probe and the counter roller are removed. The hole is then repaired with a fast-cure concrete. The length of activity is about 45 to 55 min as opposed to 4 to 5 hr for cut-and-fill methods, which saves labor hours and driver inconvenience (*3*).

Determination of Road Subsurface Cavity and Condition

In this secondary survey, the planar expansion of the cavity is determined through the previously noted mesh survey investigation. Mesh survey and horizontal information is confirmed by the previously noted scope survey method.

Report to Pavement Engineer

Previous methods of reporting included excess amounts of data that posed a problem to the pavement engineer because they were difficult to read and interpret. The new reporting system that is currently being employed consists of the following components:

- Raw data. The actual field data are turned over to the pavement engineer, which includes the video and the magnetic tape record. These data are labeled with appropriate dates and lane identification.
- Printed report. Only those areas of the surveyed portion that include actual voids or suspected voids are included in the written report, which is designed to be easily read by the pavement engineer.
- Data base report. The same data are also prepared for easy data input into the pavement engineer's pavement management data base. More emphasis at this stage is placed on preparing the data for integration into the larger network.
- Summary report. The data are additionally compiled into an annual reporting format that allows the pavement engineer to see the long-term trend of void location, frequency, and size. This information allows the pavement engineer guidance to plan future surveys.

ACTUAL FIELD INSPECTION RESULTS USING THE DEVELOPED TECHNOLOGY

From November of 1990 to December 20, 1993, the total lane length surveyed by this method was 1,635 km. This survey detected a total of 212 possible sinkholes and, on investigation, 191 confirmed sinkholes were located in the pavement substructure, which had not yet migrated to the surface to cause a visible pavement failure. The remaining 21 areas that were identified as possible void areas contained buried wood, concrete blocks, or crushed concrete, which produce a GPR signal similar to a GPR void signal. All target areas were cut open and the existence of the voids or wood or concrete was confirmed.

Void Detection

1. Size of void. This detection system has enabled investigators to detect the development of underground voids. Figure 11 presents the size (expansion, thickness, volume) of detected voids and indicates the conclusion that 60% of the voids detected were less than 3 m^2 in area and less than 50 cm in thickness. The largest detected void was more than 9 m^2 and 2.8 m thick (approximately 25 m^3).
2. Location depth (the position of the top of the void and characteristics of pavement structure). A large percentage of the detected voids were located in a position with the depth of the top of the void less than 70 cm from the pavement surface and were positioned in or directly below the upper layer of the road bed. Additionally, the bottom of most pavements affected by voids showed sagging.
3. Rate of occurrence. The roads tested were those that had a history of detected voids in the past or that showed a possibility of developing a void condition. In this sample, which does not apply to all of the national and prefectural roads, voids were detected at least every 1.3 road kilometers (every 7.7 lane km) in the metropolitan area.
4. Causes. As soon as a void was detected, a repair was made. In about 30% of these cases, it was possible to determine the cause immediately, such as a broken rainwater conduit, a sewer pipe, or an empty pipe no longer in use. Based on void detection surveys conducted so far in the metropolitan area, where there is much underground pipe and construction, it is suspected that these underground objects and their method of installation are directly related to the development and existence of voids as shown in Figure 12. Corrosion of sewers by sulfur gas gradually causes sewer line failure, which can initiate a migrating void pocket, and large structures such as subway tunnels produce constant vibration, which contributes to the initiation of void pockets. Further, as a void migrates

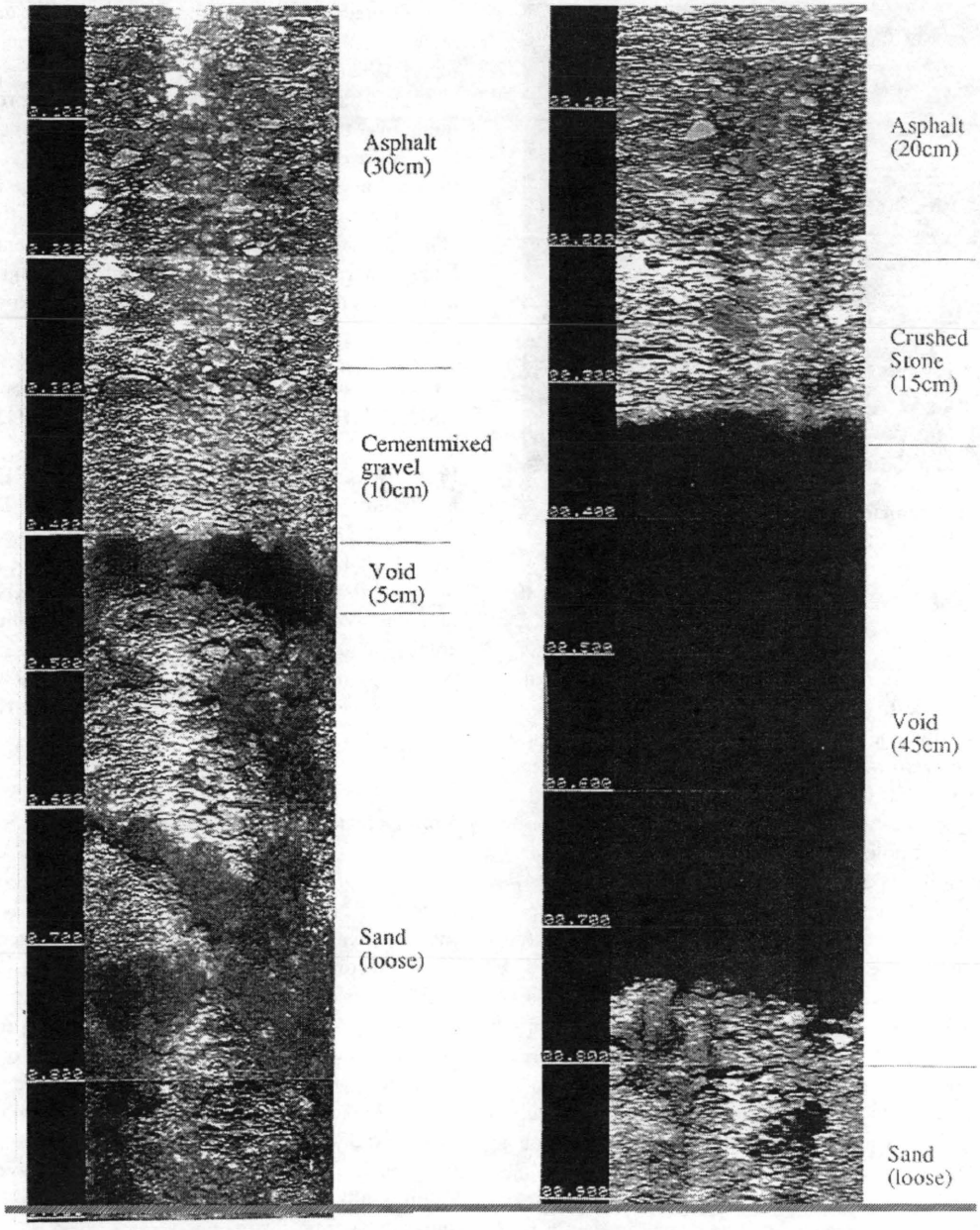

FIGURE 10 Sample of BHC records showing material composition and substructure configuration.

upward through the complex lattice-work of subsurface utilities infrastructure, the support of these conduits is undermined, thereby contributing to their possible failure.

Survey Result from Road Offices in Tokyo Ward

Tokyo consists of 23 ward offices. The annual number of sinkholes is collected by direct contact with area-responsible pavement officials. As a result, the average number of sinkholes is 100 holes per ward office per annum. This makes the total amount of pavement failures caused by voids per year over 2,000 in the Tokyo area. The identification of 212 possible voids and subsequent confirmation of 191 voids before the pavement failure stage represents 191 possible transit accidents avoided. With the continued application of the system, it is hoped that the ratio of actual pavement failures caused by voids, and voids detected before pavement failure, will shift in favor of prior detection.

Investigation of Mechanism of Sinkholes

From the experience gained in site survey result analysis, the following mechanical nature of sinkholes are thought to exist. The migration of the loose sand begins around a buried object forming an air pocket. From the time of void formation, the migration of the

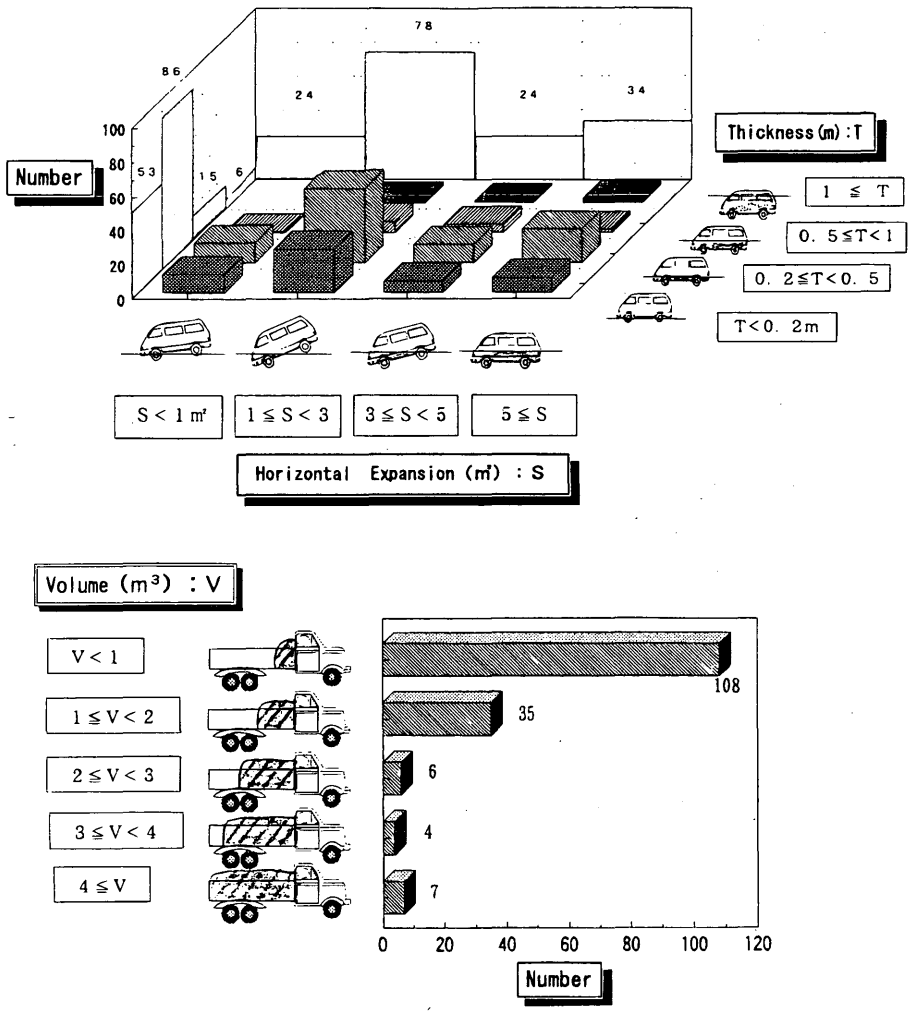

FIGURE 11 Condition of void development.

air pocket moves upward as the ceiling of the pocket falls to the floor of the pocket, thereby leaving fresh ceiling exposed. This process repeats itself until the resisting subsurface of the pavement is encountered. In a cold pavement condition, the load-bearing stress of the pavement may be sufficient for the vehicle support surface to continue to perform normally and not fail, but in hot weather, the heat of the sun causes the asphalt to become soft and the load-bearing stress capability of the pavement is lowered. The pavement then becomes subject to the lack of support caused by the migrated void and pavement failures that have been latent in cold weather reach the critical point of the failure curve as the weather—and hence the asphalt—becomes warmer, as shown in Figures 2 and 13.

Test Field Data

To confirm the above theory of void migration, ice was buried between gravel and a sand phase in a test field. Soon after soil-compacted burial, the ice melted and created an artificial void in the layer between the sand below and the crushed gravel above. The artificial void was monitored over a 2-year period, and the artificial void migrated upward to the pavement substructure as predicted. By this means, the process of void movement was confirmed. This movement through migration process was confirmed by periodic monitoring using GPR and the BHC site surveys.

CONCLUSION

The Developed System

The combination of the three equipment systems, the void detection vehicle, low-frequency GPR, and the BHC, make it possible to realize an effective void detection method, increase the safety level, and keep the traffic flow smooth. BHC survey results, investigation of sinkhole accident records, and test field investigation are clarifying the mechanical nature and process of void occurrence and subsurface pavement failure.

Future Improvement

The Ministry of Construction has contracted for extensive void surveys using the new vehicle over a 5-year period. During this period, all national roads in the Tokyo area will be surveyed. This will provide the pavement engineers with a broad overview of the road sit-

Condition of Void

Size of Void
(L 3.3 m x W 3.2 m x H 2.3 m)

Cause:
The cause of the void is not clear, but numerous underground constructions were noted such as subway lines, water pipes, electrical conduits, sewer pipes, etc.

Condition of Void

Size of Void
(L 3.0 m x W 3.0 m x H 1.0 m)

Cause:
It appears that a broken link of underground sewer pipe causes a leak of sewer water which erodes the soil.

Condition of Void

Size of Void
(L 2.5 m x W 3.0 m x H 0.5 m)

Cause:
The connector of a rainwater drainage pipe broke causing the soil to be eroded by rainwater runoff.

FIGURE 12 Photographs showing excavation of detected voids.

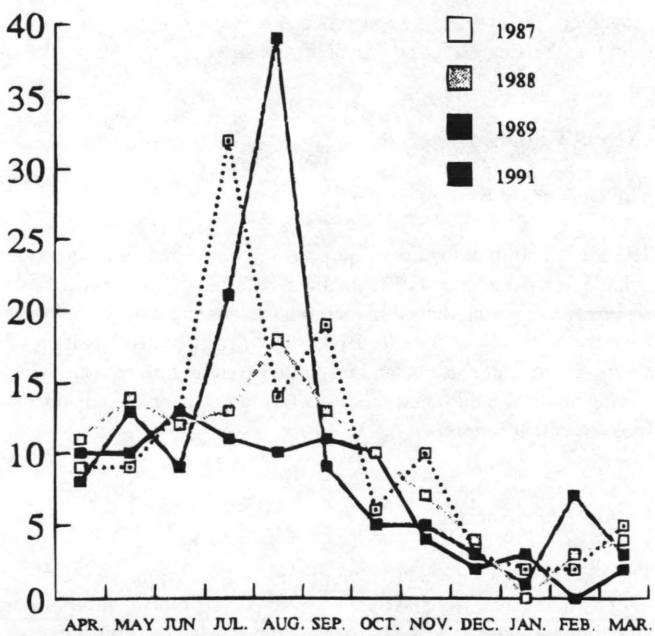

FIGURE 13 Annual distribution of sinkhole accidents reported in a typical Tokyo ward office.

uation, void frequency, and it will allow the determination of areas that are chronic problem areas. These trouble spots will be investigated with more frequency in an attempt to determine and solve the structural problems that cause repeated void formation. Ongoing investigations about what kind of repair material and method will be most effective for the repair of sinkholes are being conducted by the Ministry of Construction together with Public Works Research Institute. There is a feeling of confidence that these measures will cause an overall increase in road safety and driver comfort in Japan.

REFERENCES

1. Koike, K., M. Gotoh, and T. Maeda. *Development of a Sink Hole Detection Vehicle* (in Japanese). Special Report 927, 19th Japan Road Conference, Oct. 1991, pp. 1124–1125.
2. Sasaki, T., and T. Maeda. *Sink Hole Detection Method* (in Japanese). Special Report 704, 19th Japan Road Conference, Oct. 1991, pp. 236–238.
3. Gotoh, M., and I. Tanemura. Sink Hole Detection Method (in Japanese). *Hosoo*, Vol. 26, No. 11, 1991, pp. 28–31.

Publication of this paper sponsored by Committee on Pavement Monitoring, Evaluation, and Data Storage.

Evaluation of New Ground-Penetrating Radar Technology To Quantify Pavement Structures

D. E. MESHER, C. B. DAWLEY, J. L. DAVIS, AND J. R. ROSSITER

Pavement engineers routinely utilize mechanistic-based models for pavement rehabilitation design and for assessing the remaining service life of existing pavement structures. Dynamic and rolling load equipment is used to measure pavement response to those applied loads. The analytical models that utilize such data are dependent on the availability of accurate pavement layer thickness values at the load application points. Ground-penetrating radar (GPR) technology has been used to quantify pavement structures, but the technique has not provided sufficient accuracy or reliability to gain general acceptance. GPR accuracies have generally improved when core data are made available for system calibration; however, the number of cores required to maintain acceptable accuracies effectively defeats the purpose of nondestructive measurements. A new GPR technology, known as Road Radar, takes a different approach to the thickness measurements of multiple pavement layers in pavement structures. This technology uses multiple antennas that provide accurate non-intrusive thickness measurements of multiple layers from 50 mm to greater than 2 000 mm without benefit of any destructive calibration procedure, such as drilled cores. The Road Radar technology, designed into the Road Radar System and proven through extensive field trials and data-acquisition programs, is described in this report. Comparative analysis is presented of pavement structure thickness measurements, using both Road Radar measurements without core calibrations and drilled core measurements. The results of these comparisons are reported for a number of individual projects, as well as statistical analysis performed on approximately 150 pieces of paired data "pooled" from a number of field test sites.

Pavement engineers are becoming increasingly dependent on alternative, versus historically used, technologies to manage their paved road inventories. Superior and more effective systems have been developed to evaluate structural characteristics of existing pavements and to assess remaining service life in existing structures through back-calculation procedures designed for that purpose. These systems typically measure pavement response to dynamically imposed loads. This type of technology is relatively mobile, cost-effective, and provides superior operator safety. Various computer models exist to provide system managers with information that is fundamental to project planning.

Computer models, such as those identified above, depend on reliable input data, including pavement structure thickness and elastic properties of constituent layers, to yield meaningful output information. Construction or "as-built" records, if they exist, are at best approximations and are frequently based on the original design instead of on layer thicknesses actually placed. Furthermore, pavement engineers recognize the limitations and expense of historically collected data from drilled core specimens.

Ground-penetrating radar (GPR) has long been known as a technology amenable to the determination of pavement layer thicknesses (*1–7*). However, past applications of this technology to pavement structure investigations have generally provided neither sufficient accuracy, requiring extensive layer thickness calibrations through drilled cores, nor reliability to achieve wide acceptance by pavement engineers and technologists. These limitations of existing GPR systems are discussed in detail elsewhere (*8,9*). Dawley and Mesher (*10*) have described the GPR enhancements that are embodied in the Road Radar System technology.

Existing GPR technology has been enhanced in the Road Radar System for the purpose of providing a non-intrusive technique for obtaining subsurface information on existing roadway pavement structures. The primary enhancements have been twofold. The first enhancement has been to render the radar unit essentially self-calibrating. This has been accomplished by innovations that enable both the signal travel time and velocity of the signal to be determined at every measurement point, thereby accounting for varying material properties within the structure. The second enhancement has been to develop computer software that permits rapid processing of vast quantities of collected data.

Within this paper a description is provided of some of the innovations that have been incorporated into Road Radar technology to produce the aforementioned enhancements. Furthermore, some of the field testing, which has been undertaken to verify the new technology, is described and some statistical data are provided to validate the system.

ROAD RADAR INNOVATIONS

Initial investigations that utilized general purpose GPR systems for quantifying multilayer pavement structures identified serious shortcomings of these systems as a quantitative engineering tool. Through these critical investigations, a detailed specification was generated to address the requirements of a comprehensive system that would provide accurate quantitative multilayer structure information. This process identified the need for a nondestructive radar system with the capability to resolve multiple pavement structure layers as thin as 50 mm to a total depth of greater than 2 m with quantifiable accuracy. Additionally, the design specification recognized the need for a comprehensive signal-processing environment to allow the automated interpretation of the vast volumes of data typically produced by radar surveys.

D. E. Mesher, EBA Engineering Consultants Ltd., 14535-118 Avenue, Edmonton, Alberta, T5L 2M7, Canada. C. B. Dawley, EBA Engineering Consultants Ltd., #255, 1715 Dickson Avenue, Kelowna, British Columbia, V1Y 9G6, Canada. J. L. Davis and J. R. Rossiter, Road Radar Ltd., 14535-118 Avenue, Edmonton, Alberta, T5L 2M7, Canada.

To this end, the Road Radar System discussed herein combines a novel hybrid multiple radar configuration with an extensive signal-processing software environment to provide an accurate, user-friendly environment for automated multilayer data interpretation. The following sections describe the unique aspects of both the system hardware and interpretation software.

Hardware

All GPR systems operate on the principle of the accurate measurement of the propagation times of electromagnetic energy radiated through and reflected from dielectric materials. As this energy propagates through a layered structure, a portion of the energy is reflected at each boundary of electrically dissimilar materials, and the remaining energy propagates into any subsequent layers.

A simplistic block diagram of a bistatic (separate transmitter and receiver antennas) GPR system is depicted in Figure 1. Given this physical configuration for the transmitter (T) and receiver (R), a pulse radiating from the transmitter at time t_0 and reflecting from a planar reflector at a distance d would produce a scaled replica pulse at the receiver (R) at some later time t_1. The relationship between the propagation time and propagated distance is given as:

$$p = \frac{1}{2} v(t_1 - t_0) = \frac{1}{2} vt \tag{1}$$

where

p = one way propagation distance;
t = propagation time ($t_1 - t_0$); and
v = radar pulse propagation velocity in the material.

It becomes apparent that Equation 1 is under-determined; for nondestructive scenarios using conventional GPR equipment, both the distance term and velocity are unknown. The traditional solutions to this dilemma required varying degrees of approximation. In purely nondestructive situations the velocity term was presumed consistent and was approximated based on empirical experience, producing typically inaccurate results. In order to increase the accuracy of such under-determined systems, cores are extracted at noted locations, velocities are determined at these locations, and a piecewise linear velocity assumption is applied to sections between cores. Depending on the number of cores extracted, such an approach may or may not produce acceptable results.

A second purely nondestructive technique for velocity approximation may be derived from the amplitude ratio of the incident and reflected energy at a dielectric interface. This reflection coefficient allows the determination of the layer velocity from the following relationships:

$$v = \frac{c}{\left[\frac{1+|\rho|}{1-|\rho|}\right]} \quad \text{and} \quad \rho = \frac{A_r}{A_i} \tag{2}$$

where

ρ = reflection coefficient;
A_r = reflected signal amplitude;
A_i = incident signal amplitude;
c = speed of light (constant); and
v = velocity of the material at the surface of the interface.

Although this technique is commonly used, the calculated velocity values are extremely sensitive to the following elements.

- Accurate signal amplitude measurements. GPR system amplitude measurements are susceptible to fluctuations arising from antenna displacement (spherical losses) and planar surface-interface roughness properties (scattering losses). It becomes evident from Equation 2 that slight amplitude perturbations manifest themselves as severe calculated velocity variations.
- Propagating errors for multiple layer velocity estimation. Subsequent layers in a multilayer structure rely on previous layer velocity determination. These cumulative errors render this technique for multiple layer velocity estimation inappropriate.

In the Road Radar System this velocity determination problem is addressed by employing a novel multiple antenna array configuration (Surface-Coupled Subsystem). This multipath solution provides a technique to accurately calculate the velocity at each radar measurement point. By using the radar antenna configuration depicted in Figure 2, multiple reflection path propagation times for each receiver are recorded simultaneously. As the antenna array configuration geometry is accurately known, the following deterministic system may be developed.

$$p_n = 2\sqrt{d^2 + \left[\frac{s_n}{2}\right]^2} \quad \text{and} \quad p_n = v\,t_n \tag{3}$$

where

p_n = propagation path length from transmitter to receiver$_n$;
t_n = propagation time (path n);
d = layer thickness;
s_n = transmitter-receiver$_n$ separation; and
v = layer velocity.

This allows the determination of the bulk material velocity and therefore the parameter of interest d, the layer thickness when (the number of antennas) $n \geq 2$.

The Surface-Coupled Subsystem is capable of resolving layers from 0.1 m to greater than 2 m. For the thin layer resolution, identified during the system design phase as being of paramount importance to pavement engineers, a second high resolution radar is added. The multilayer structure evaluation system combines a com-

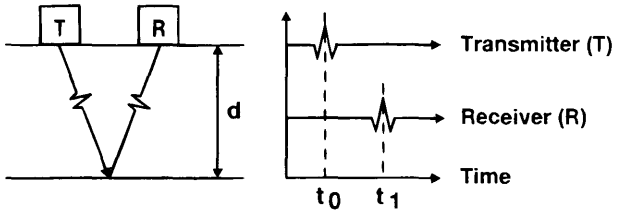

FIGURE 1 Simple bistatic radar antenna configuration and propagation path for a layer of thickness d. Time relationship between the transmitter and receiver for a radiated pulse.

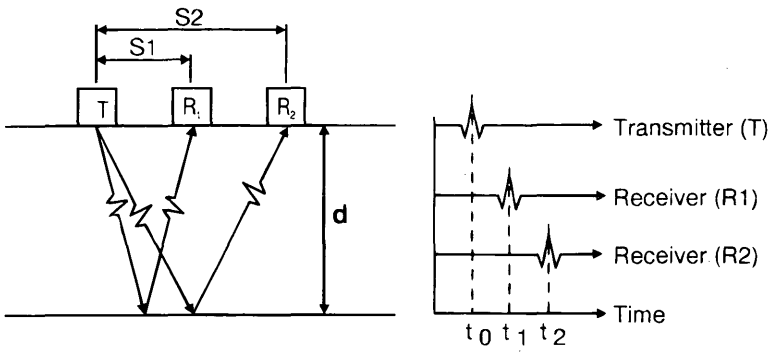

FIGURE 2 Bistatic radar antenna array configuration and multiple propagation paths for a layer of thickness *d*. Time relationship between the transmitter and multiple receivers for a radiated pulse.

plementary high resolution air launch horn-type antenna (Air-Launched Subsystem) with the velocity determining Surface-Coupled Subsystem. The Air-Launched Subsystem allows the resolution of structure layers thinner than 50 mm.

Software

A comprehensive radar signal-processing environment provides the means to effectively combine the large volumes of raw radar data from both radar subsystems and to allow automated interpretation to provide continuous multiple pavement layer thickness and velocity profiles. The data processing environment represents a synergism of many programming domains, effectively combining artificial intelligence, time domain digital signal processing, neural networks, and pattern recognition.

This graphical radar interpretation environment exploits a rule-based expert system paradigm to allow a technical individual with limited radar experience to successfully process typical road data. On simplistic planar layer road structures, the system can perform automatic interpretation of the radar data. On more typical variable construction surveys, the system interprets consistent sections and defers to the operator for guidance at the transition points typically representing construction joints or other discrete subsurface anomalies.

The output of the data interpretation operation includes graphical radar data profiles indicating a section of the data acquired during the survey. These profiles present the pavement engineer with the unique opportunity of being able to examine the road cross-section for more qualitative features. Such features include base course or subgrade constituent variations (granular material size variations) and anomalous area investigation. In conjunction with this qualitative data are the quantitative continuous thickness and velocity profiles for each layer in the road structure generated during interpretation. The usefulness of the thickness profiles is self-evident, but initial indications suggest that the velocity profiles are as important, and perhaps more so. It has been suggested that road material properties of interest to pavement engineers may have substantial empirical relationships with the material velocity. These properties include moisture content, compaction (related to density and air voids), and mixture constituent volumetric ratios. All data produced by the system are easily formatted for any pavement management system and can produce statistical analysis as well as tabular and graphical profiles. Typical road section outputs are presented in Figure 3.

SELECTED DATA COLLECTION PROJECTS

Methodology

Data collection programs have been conducted on numerous paved highways, with the cooperation of the highway agencies. Highway locations to be monitored were usually selected by highway agency personnel. Points at which structural data were to be acquired by conventional methodology (coring, auguring) were premarked on the pavement. The outer wheelpath of the travel lane was typically selected for that purpose, and for performing the continuous survey with the Road Radar. After completion of Road Radar data collection, the data were processed, and measured structural layer thickness values were presented to the highway agency personnel. Results from the coring or auguring activity were then used to compare with Road Radar results.

Accuracy and Variability of Measurements

In comparing data acquired by alternative acquisition and measurement techniques, it is essential to recognize the limitations that are applicable to each set of paired data.

With respect to the drilled core procedure for representing pavement layer thickness, reference is made to ASTM Designation D3549, "Standard Test Method for Thickness or Height of Compacted Bituminous Paving Mixture Specimens." Test specimens may be laboratory compacted or from compacted bituminous pavements. The ASTM standard states that no measurement precision data are presently available. It is recommended that none be established, since the documented variability in thickness of constructed layers is very large in relation to the expected measurement variability. The following tabulation exists in the ASTM standard, which is a summary of data from studies undertaken by user agencies (S.I. units, in millimeters, are included by the authors).

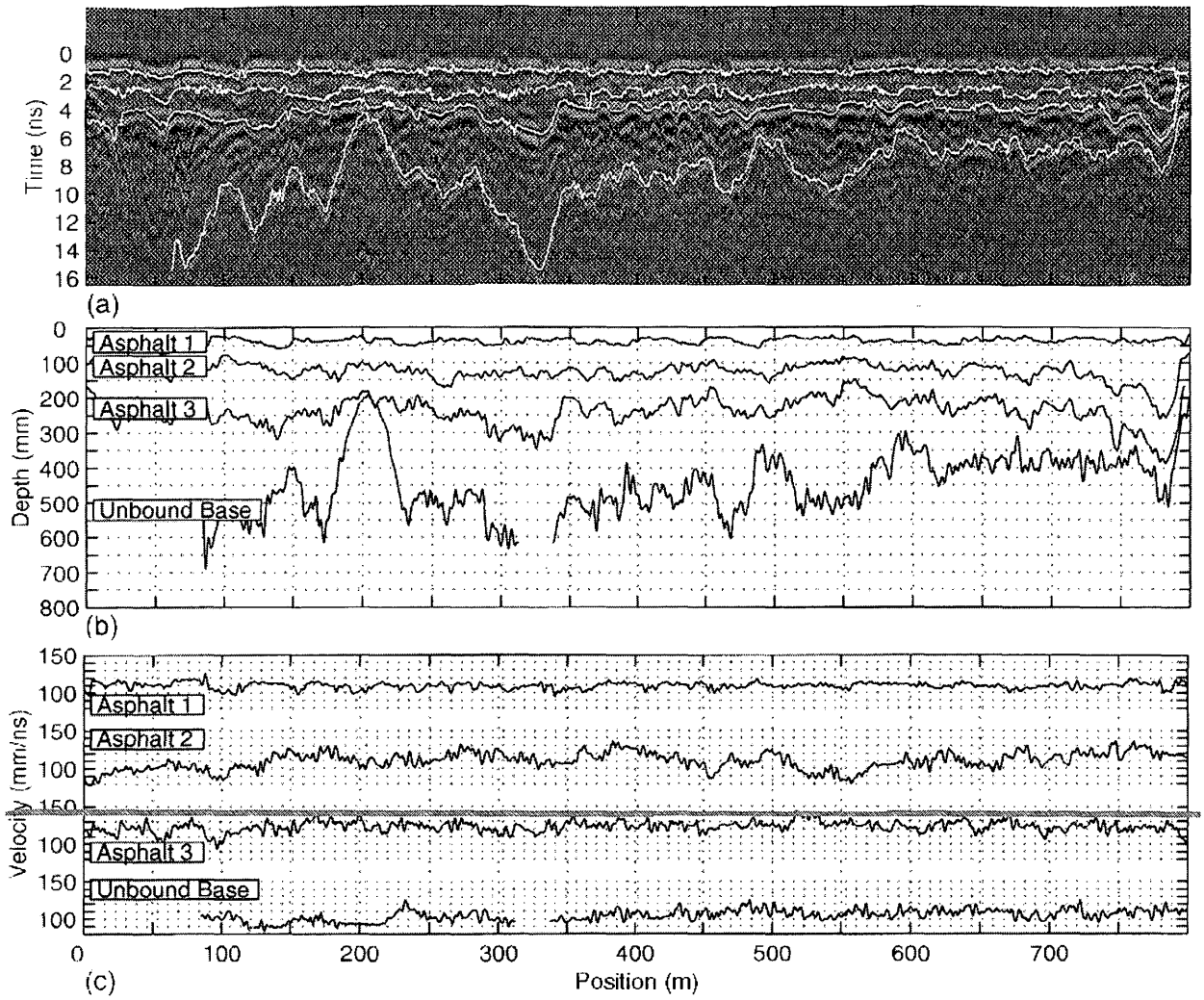

FIGURE 3 (a) Raw radar data with interpreted interface overlays. (b) Interpreted layer thickness profiles. (c) Interpreted layer velocity profiles.

Bituminous Pavement Thickness Variability

Thickness Range in. (mm)	*Standard Deviation in. (mm)*	*Coefficient of Variability (percent)*
1.0 to 1.9 (25.4 to 48.3)	0.21 (5.3)	14.7
2.0 to 2.9 (50.8 to 73.7)	0.29 (7.4)	13.0
3.0 to 3.9 (76.2 to 99.1)	0.37 (9.4)	11.3
4.0 to 4.9 (101.6 to 124.5)	0.53 (13.5)	12.5
6.0 (152.4)	0.75 (19.1)	12.5

In the absence of a precision statement in the ASTM standard, the above values of standard deviation (in millimeters) are used hereafter as a means of assessing how closely the alternative procedures (coring and Road Radar) represent existing pavements at each measurement point.

With respect to measuring thickness of in situ granular base layers using the auguring procedure, no relevant standard exists. However, it is commonly accepted that the field measurement procedure is difficult and imprecise.

The Road Radar operational specification for thickness accuracy is (a) wearing surface (pavement layer)—greater of ± 6 mm, or 5 percent, and (b) base course (second layer)—greater of ± 12 mm, or 10 percent.

For all paired data that were collected at every measurement point at each site, linear regression analysis has been undertaken to ascertain whether or not a statistically significant correlation exists. Commentary is provided hereafter with respect to calculated correlation coefficients (r) and their significance.

Site 1: Highway 21, Alberta, Canada

Highway 21 is a four-lane rural divided highway located in east-central Alberta. The pavement structure was known to be a two-layer system composed of deep strength asphalt concrete pavement constructed on a granular base layer. The section of highway pavement structure, which was identified for survey by personnel of

TABLE 1 Asphalt Concrete Pavement Thickness as Determined by Drilled Cores, and by Road Radar Measurements, Site 1—Highway 21, Alberta, Canada

Chainage (km)	Thickness From Cores (mm)		Thickness From ROAD RADAR™ (mm)				
	Recorded	$\pm 1\sigma$[a]	Closest[b]	Accuracy Limits[c]	Max[d]	Min[d]	Avg.[e]
20.130	155	136-174	154	149-165	199	147	157
20.221	148	129-167	156	152-168	170	151	160
20.324	150	131-169	155	146-162	160	148	154
20.469	181	162-200	186	185-205	204	186	195
20.566	140	121-159	144	141-155	151	144	148
20.666	181	162-200	185	173-191	187	178	182
20.767	210	191-229	210	198-218	210	205	208
20.867	188	169-207	200	186-206	200	192	196
20.957	164	145-183	165	161-177	174	165	169
$\bar{x}$	168.6		172.8				174.3
σ	21.6		21.8				20.4

[a]See ASTM D3549, Table 1.
[b]At measurement point closest to core location.
[c]ROAD RADAR™ specification of ±5%.
[d]Value limits within 1 m of core location.
[e]Average of all ROAD RADAR™ measurements within 1 m of core location.

Alberta Transportation and Utilities, comprised 1 km in the northbound lanes.

The outer wheelpath of the travel (outer) lane was chosen for an initial survey, and wherein both Road Radar and drilled core data were collected. Pavement thicknesses as determined by drilled cores and by Road Radar measurements are presented in Table 1. In Table 1, the asphalt concrete pavement thickness measured by the Road Radar is reported both as a single measured value at the point closest to the drilled core location, as well as the average of all radar measurements within a 1-m distance on either side of the core location (usually six pieces of data). For this site, nine pieces of paired test data were used for analysis by linear regression. Figure 4 consists of a plot of these paired data as well as linear regression statistics. The calculated value of $r = 0.99$ confirms that there is greater than a 99 percent probability that the paired data are associated (i.e., less than 1 percent level of significance).

A plot of core thickness variability versus Road Radar accuracy boundaries for the paired data is presented in Figure 5 and is based on limiting values indicated in Table 1. It is reasoned that if the probable pavement thickness represented by the accuracy statement for the Road Radar lies within an envelope representing the pavement thickness variability associated with the drilled core data, then the Road Radar data are at least as representative of the pavement structure as is the drilled core information. This hypothesis is confirmed as indicated in Figure 5.

Site 1 has afforded a unique opportunity to assess the Road Radar accuracy to measure thickness of the second (granular) layer, that is, a multilayer structure. Relevant data are presented in Table 2.

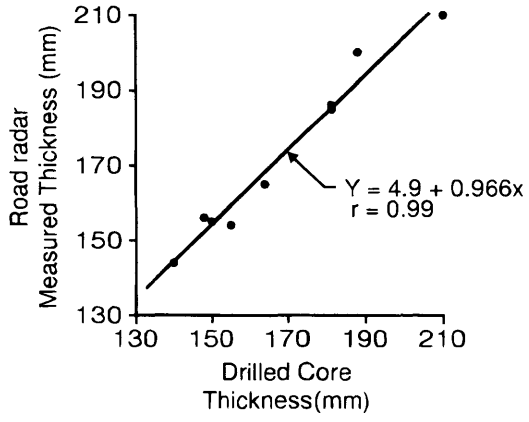

FIGURE 4 Asphalt concrete pavement thickness determined by drilled cores versus Road Radar measurements, Site 1-Highway 21, Alberta, Canada.

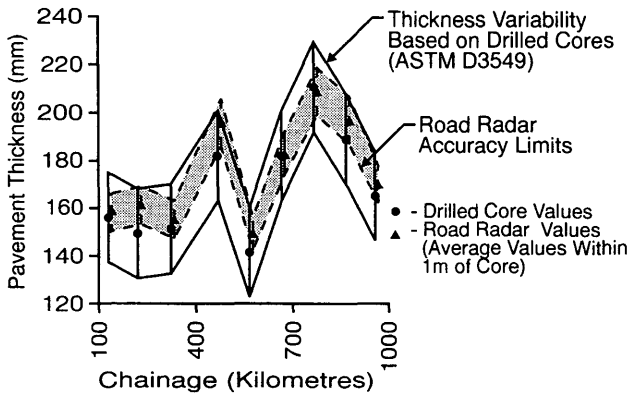

FIGURE 5 Asphalt concrete pavement thickness from drilled cores and Road Radar measurements, Site 1-Highway 21, Alberta, Canada.

TABLE 2 Granular Base Course Thickness as Determined by Augured Holes and by Road Radar Measurements, Site 1—Highway 21, Alberta, Canada

Chainage (km)	Thickness From Augured Holes (mm)	Thickness From ROAD RADAR™ (mm)	
		Closest[a]	Accuracy Limits[b]
20.130	345	335	302-368
20.221	372	299	269-329
20.324	380	354	319-389
20.469	339	318	286-350
20.566	250	236	202-260
20.666	279	303	273-333
20.767	270	272	245-299
20.867	302	253	228-278
20.957	316	263	237-289
$\bar{x}$	317	293	
σ	43	37	

[a]At measurement point closest to core location.
[b]ROAD RADAR™ specification of ±10%

Figure 6 is a plot of paired data as well as linear regression statistics. The r value of 0.76 indicates that there exists at least a 95 percent probability that the paired data are associated. Recognizing the sensitivity of the layer thickness values acquired by the auguring technique, it is considered that the Road Radar precision and accuracy is competent for measurement of multilayer structures.

Site 2: Interstate Highway 15 (I-15), Montana, USA

I-15 is a rural, four-lane freeway. The test site, selected by the Montana Department of Transportation (MDT), comprised a 1.6-km section of the travel (outer) lane in the southbound lanes. Data, which were collected over the most southerly 1.1 km, are presented in Table 3. Relevant data are plotted in Figure 7. In this case, analysis of the paired data has been undertaken in two separate ways. The purpose of this exercise was to identify the most appropriate statistic to use from the data base developed using the Road Radar.

The reasoning for this approach was that, since ASTM recognizes actual pavement construction variability, perhaps it may be valid to average several individual Road Radar statistics. Figure 7, left, is a plot of drilled core values and the single Road Radar value, whereas Figure 7, right, is a similar plot using the averaged Road Radar data. The recorded r values indicate that there exists a 99 percent probability that the paired data are associated, irrespective of the alternative Road Radar statistics used.

Figure 8 is a plot of core thickness variability (ASTM) versus Road Radar accuracy boundaries. As was the case for Site 1, it is demonstrated that Road Radar methodology provides information that is as reliable as the data acquired by coring methodology.

Granular base thickness values were obtained using the Road Radar. However, MDT staff were unable to acquire similar data using conventional auguring methodology.

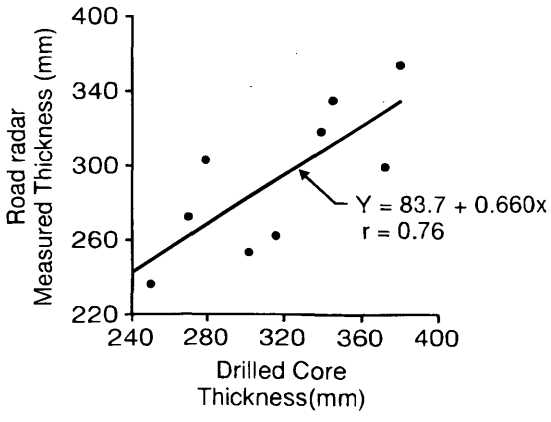

FIGURE 6 Granular base course thickness determined by drilled cores versus Road Radar measurements, Site 1-Highway 21, Alberta, Canada.

Site 3: Highway 20, Taivalkoski District, Finland

The Finnish National Road Authority organized an extensive data collection program on paved highways in Finland in the autumn of 1993. The Road Radar was used for data collection purposes.

A number of separate sites were surveyed on Highway 20, one of which is reported in Table 4. Road Radar measurement data include both the single measurement value at the point closest to the drilled core and averaged data from measurements taken within 1 m of the core location. These data are plotted in Figure 9, left and right, respectively. The recorded r values indicate that there exists at least a 95 percent probability that the paired data are associated, irrespective of the alternative Road Radar statistics used. However, in this case, use of the single radar value, measured at the core location, provides 99 percent probability of data association, whereas use of averaged radar data does not.

Data Base of Road Radar Versus Drilled Core Pavement Thicknesses

A total of 147 pieces of paired data (Road Radar versus drilled cores) representing asphalt pavement thicknesses have been utilized in a linear regression analysis. Figure 10 contains a plot of the paired data and a plot of the best fit line where:

TABLE 3 Asphalt Concrete Pavement Thickness as Determined by Drilled Cores and by Road Radar Measurements, Site 2—Interstate Highway 15, Montana, USA

Chainage (Ft)	Thickness From Cores (mm)		Thickness From ROAD RADAR™ (mm)				
	Recorded	$\pm 1\sigma$[a]	Closest[b]	Accuracy Limits[c]	Max[d]	Min[d]	Avg.[e]
13 + 24	165	146-184	150	143-159	158	146	151
19 + 83	134	115-153	136	125-139	137	126	132
26 + 43	137	118-156	137	131-145	142	134	138
32 + 34	149	130-168	153	144-160	173	132	152
39 + 62	159	140-178	148	134-148	148	134	141
46 + 23	207	188-226	199	188-208	200	193	198
52 + 80	149	130-168	142	134-148	144	139	141
$\bar{x}$	157.1	N/A	152.1	150.4			150.4
σ	22.8	N/A	21.6	20.5			20.5

[a]See ASTM D3549, Table 1.
[b]At measurement point closest to core location.
[c]ROAD RADAR™ specification of ±5% (of average).
[d]Value Limits recorded within 1 m of core locations.
[e]Average of all ROAD RADAR™ measurements within 1 m of core location.

$$Y = 1.027X - 5.623$$

where Y = GPR (Road Radar) measurement (mm) and X = drilled core measurement (mm).

The calculated correlation coefficient $r = 0.974$ indicates that there is a greater than 99 percent probability that the paired data are associated. The shaded area indicated in Figure 10 represents the uncertainty in the core thickness values in accordance with ASTM Designation D3549. It is noted that a vast majority of the data points lie within the uncertainty limits for the drilled core values.

DISCUSSION OF RESULTS

It has been previously stated that variability may be expected in the velocity of the signal travelling through a nonhomogeneous material. Construction materials cannot be assumed to be homogeneous by their very nature. Manufacturing, placing, and finishing activities all contribute to this reality. Even stringent quality assurance specifications recognize the potential existence of product variability.

The question is, just how important is it to have access to technology that is able to measure the actual signal velocity at each data collection point?

The actual signal velocities measured by the Road Radar unit, at the above three test sites, are presented in Table 5. A number of observations may be made from these tabulations.

- The mean signal velocity at each site is relatively consistent. This might infer that it is valid to assume signal velocity.
- The velocity values recorded at Site 1 are very uniform (V = 1.9 percent). This might support the contention that signal velocity can be responsibly estimated.
- Sites 2 and 3 yielded substantially larger ranges in values than Site 1, even though the mean signal velocity values were similar. At each site individual velocity values exceeded the mean value by at least 13.5 percent. An even greater concern is that 19 percent and 22 percent differences existed between the minimum and maximum measured velocity values at Sites 3 and 2, respectively.
- It is the practice with some other GPR systems, which are used to measure pavement layer thickness, to perform a site-specific cal-

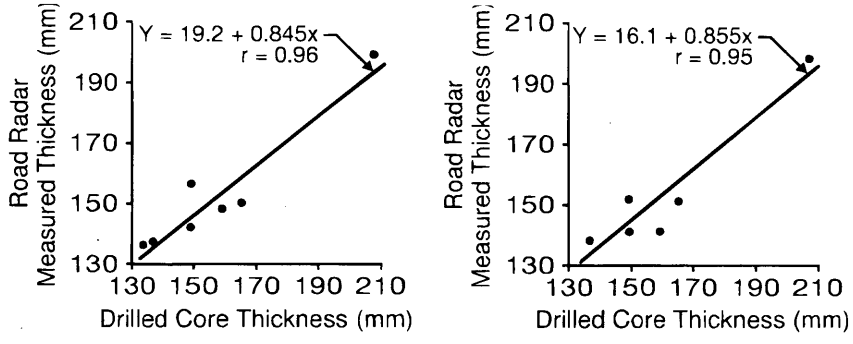

FIGURE 7 Asphalt concrete pavement thickness determined by drilled cores versus Road Radar measurements, Site 2-Highway 15, Montana, USA.

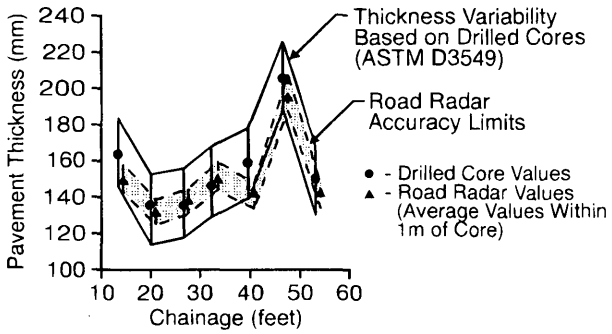

FIGURE 8 Asphalt concrete pavement thickness from drilled cores and Road Radar measurements, Site 2-Interstate 15, Montana, USA.

ibration using a single piece of drilled core data to provide the layer thickness information, and then to back-calculate the signal velocity. Significant errors can exist when this practice is followed.

Following is an illustration of how pavement layer thickness calculations are influenced by signal velocity.

Case: Interstate Highway 15, Montana

Assume the unit calibration is performed at core location chainage 32+24, at which point the signal propagation time was determined to be 2.01 ns (1E-9 sec). The measured core thickness at this point was 149 mm.

$$d = \frac{1}{2} vt \quad (4)$$

where:

d = layer thickness (mm);
v = signal velocity (mm/ns); and
t = propagation time (ns).

Given $t = 2.01$ ns and $d = 149$ mm, therefore $v = 148$ mm/ns.

At Station 46+23, the core thickness was determined to be 207 mm (Road Radar measured thickness was 199 mm), at which point the signal velocity was 121 mm/ns (with $t = 3.29$ ns).

However, if the velocity value was assumed to be 148 mm/ns, then the calculated pavement layer thickness would be 243.5 mm (an error of 17.6 percent).

GPR systems are recognized to be very precise in measuring signal travel time. The heterogeneous nature of the material, through which the signal is transmitted, has to be recognized with respect to the velocity of the signal during its elapsed propagation time. The fact that changes in signal velocity exist within a survey data set is a signal that a non-uniform condition exists, and that different sections of the pavement structure may perform differently because of this condition. Velocity variations within a pavement layer may result when pavement density is variable, or when moisture is present within the pavement layer (which may be expected when pavement density is substandard).

Similarly, moisture build-up in underlying granular base and subbase layers appears as an anomaly on the data outputs. These "indicators" can serve to alert pavement engineers of a condition that may require attention to mitigate the occurrence of premature structure distress.

TABLE 4 Asphalt Concrete Pavement Thickness as Determined by Drilled Cores and by Road Radar Measurements, Site 3—Highway 20, Taivalkoski District, Finland

Chainage (m)	Thickness From Cores (mm)		Thickness From ROAD RADAR™(mm)				
	Recorded	$\pm 1\sigma$[a]	Closest[b]	Accuracy Limits[c]	Max[d]	Min[d]	Avg.[e]
SITE 1							
20	50	45-55	51	45-57	55	48	52
40	50	45-55	49	43-55	51	46	49
60	47	42-52	49	43-55	50	47	49
90	45	40-50	46	40-52	50	45	47
140	42	37-47	39	33-45	43	38	39
180	45	40-50	42	36-48	42	39	40
210	55	50-60	52	46-58	55	48	52
260	50	45-55	48	42-54	49	44	48
280	52	47-57	49	43-55	49	36	47
300	53	48-58	49	43-55	51	39	48
$\bar{x}$	48.9		47.4				47.1
σ	3.9		3.8				4.2

[a]See ASTM D3549, Table 1.
[b]At measurement point closest to core location.
[c]ROAD RADAR™ specification of the greater of ±6 mm or ±5%.
[d]Value limits within 1 m of core location.
[e]Average of all ROAD RADAR™ measurements within 1 m of core location.

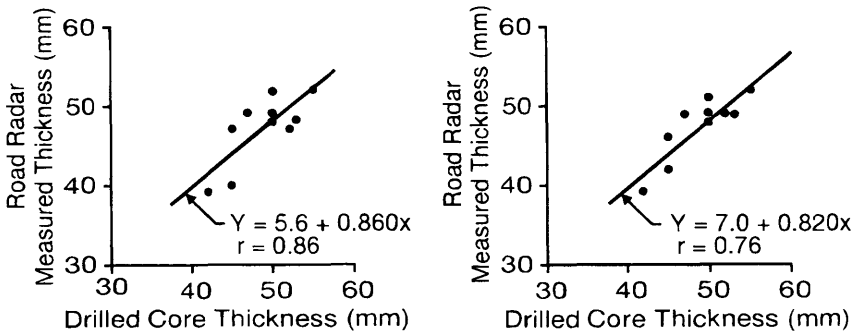

FIGURE 9 Asphalt concrete pavement thickness determined by drilled cores versus Road Radar measurements, Site 3-Highway 20, Taivalkoski, Finland.

CONCLUSIONS

This paper has described adaptations that have been made to conventional GPR technology for the purpose of developing a non-intrusive technique to measure layer thickness in composite pavement structures. In the past, scepticism on the part of potential users of the GPR technology has been primarily related to unsatisfactory reliability and accuracy as a result of the inability of earlier GPR systems to determine signal velocity at each data collection point. This deficiency has been overcome through innovations that are incorporated in the Road Radar.

Core and Road Radar data collected as described in this paper displayed excellent correlations in all cases. It is not realistic to expect such close associations as a routine. The mere task of ensuring that comparative sampling locations are exact requires technologists to be extremely careful—usually in the presence of heavy vehicular traffic volumes. Experienced pavement construction engineers recognize the real limitations that are associated with producing uniform pavement structures, both in profile and in cross-section.

GPR technology has been developed to provide a reliable, non-intrusive method for obtaining subsurface information on roadway pavement structures. The primary enhancements were threefold:

1. An effective self-calibrating capability that provides multi-layer pavement thickness measurements that are at least as accurate as standard coring and auguring methods, as determined from measurements made in Canada, the United States, and Finland, where construction methods and materials differ substantially.
2. Layers as thin as 50 mm were resolved using a 2.5 GHz centre-frequency radar.
3. A semi-automated interpretation software package can process and interpret pavement layer thicknesses on very large data sets, which allows greater reliability and reduced turn-around time. The system also provides a warning if it cannot interpret a response so that the operator can guide the process. Often this warning also indicates that there is a change in the pavement structure.

With these developments, GPR offers pavement engineers a quantitative, nondestructive method to determine pavement thickness on a continuous basis as accurately as core sampling. In addition, it potentially offers quantifiable information on the pavement properties such as material composition, density, and moisture content. These enhancements are expected to make GPR technology a practical operational measurement instrument for pavement engineers.

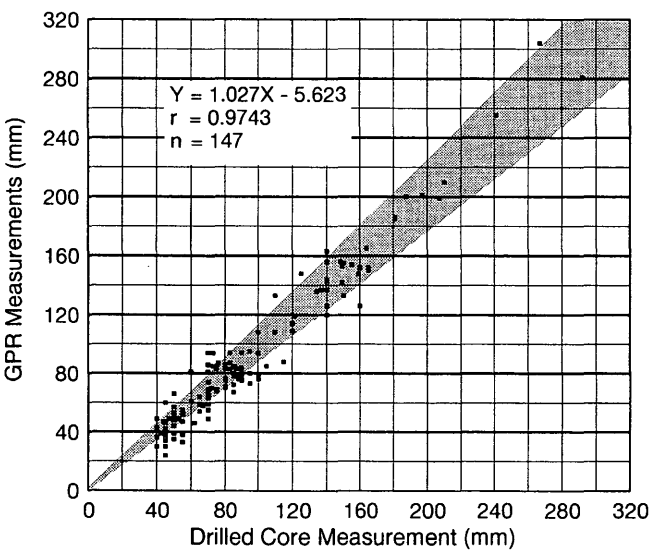

FIGURE 10 Comparison of 147 GPR measurements of asphalt pavement thickness to direct core measurements. The shaded area indicates uncertainty in core results according to ASTM standard D3549.

ACKNOWLEDGMENTS

The authors acknowledge the positive support received from representatives of transportation agencies in Canada, the United States, and Finland who are too numerous to mention, but whom we remember for their hospitality, encouragement, and enthusiasm.

The authors also acknowledge the financial support given by the Government of Canada's National Research Council, IRAP; the Western Economic Diversification programs; EBA Engineering Consultants Ltd., Edmonton, Alberta; and Canpolar Inc., Toronto, Ontario.

TABLE 5 Road Radar Signal Velocities at Various Test Sites

Site 1 - Highway 21, Alberta, Canada	
Chainage (km)	Velocity (mm/ns[a])
20.130	126
20.221	133
20.324	130
20.469	129
20.566	131
20.666	125
20.767	128
20.867	129
20.957	131
$\bar{x}$	129.1
σ	2.4
V(%)	1.9
Range	125-133

Site - 2 Interstate Highway 15, Montana, USA	
Chainage (ft)	Velocity (mm/ns)
13 + 24	128
19 + 83	130
26 + 43	131
32 + 34	148
39 + 62	124
46 + 23	121
52 + 80	128
$\bar{x}$	130.0
σ	8.0
V(%)	6.2
Range	121-148

Site 3 - Highway 20 Taivalkoski District, Finland	
Chainage (m)	Velocity (mm/ns)
20	120
40	127
60	127
90	134
140	127
180	143
210	120
260	120
280	120
300	120
$\bar{x}$	125.8
σ	7.3
V(%)	5.8
Range	120-143

[a]Velocity unit is millimetres per nanosecond (mm/ns).

REFERENCES

1. Maser, K. Highway Speed Radar for Pavement and Bridge Deck Evaluation. Presented at 4th International Conference on Ground Penetrating Radar, Rovaniemi, Finland, Geological Survey of Finland, Special Paper 16, June 8–13, 1992.
2. Maser, K. R., and T. Scullion. Automated Pavement Subsurface Profiling Using Radar: Case Studies of Four Experimental Field Sites. In *Transportation Research Record 1344*, TRB, National Research Council, Washington, D.C., 1992.
3. Maser, K. R., and A. Rawson. Network Bridge Deck Surveys Using High-Speed Radar: Case Studies of 44 Decks. In *Transportation Research Record 1347*, TRB, National Research Council, Washington, D.C., 1992.
4. Roddis, W. M. K., K. Maser, and A. J. Gisi. Radar Pavement Thickness Evaluations for Varying Base Conditions. In *Transportation Research Record 1355*, TRB, National Research Council, Washington, D.C., 1992.
5. Lau, C. L., T. Scullion, and P. Chan. Modelling of Ground-Penetrating Radar Wave Propagation in Pavement Systems. In *Transportation Research Record 1355*, TRB, National Research Council, Washington, D.C., 1992.
6. Lau, C. L., T. Scullion, and P. Chan. Using Ground Penetrating Radar Technology for Pavement Evaluations in Texas, USA. Presented at 4th International Conference on Ground Penetrating Radar, Rovaniemi, Finland, Geological Survey of Finland, Special Paper 16, June 8–13, 1992.
7. Smith, S., and T. Scullion. *Development of Ground-Penetrating Radar Equipment for Detecting Pavement Condition for Preventive Maintenance*. Strategic Highway Research Program Report SHRP-H-672, Washington, D.C., 1993.
8. Parry, N. S., and J. L. Davis. GPR Systems for Roads and Bridges. Presented at 4th International Conference on Ground Penetrating Radar, Rovaniemi, Finland, Geological Survey of Finland, Special Paper 16, June 8–13, 1992.
9. Davis, J. L., J. R. Rossiter, D. E. Mesher, and C. B. Dawley. Quantitative Measurement of Pavement Structures Using Radar. Presented at 5th International Conference on Ground Penetrating Radar, Kitchener, Ontario, Canada, 1994.
10. Dawley, C. B., and D. E. Mesher. Characterization of Multi-Layer Pavement Structures Using a New GPR Technology. Presented at International Road Federation Conference, Calgary, Alberta, Canada, 1994.

Publication of this paper sponsored by Committee on Pavement Monitoring, Evaluation, and Data Storage.

Algorithms for Pavement Distress Classification by Video Image Analysis

J. ADOLFO ACOSTA, J. LUDWIG FIGUEROA, AND ROBERT L. MULLEN

A fundamental component of computer-based video image analysis for pavement distress evaluation is identification of the type of distress from geometric and textural properties of an area of interest identified during image analysis. This study describes the algorithms used to identify and classify the most common pavement distress types once a possible distress region is identified on an image. The classification is accomplished in three steps. First, geometric and textural features are calculated for a region of interest. Next, the features of that region are used to determine whether any other regions in an image are actually part of the same pavement distress. Finally, the extracted image features are used with a decision tree to identify the specific pavement distress type, its severity, and its extent. The features and decision trees have been tested on several thousand pavement images and the system that contains the decision tree has been used successfully by the Ohio Department of Transportation since May 1994.

Computer-based image analysis has become a major topic of research due to its broad application in almost all sciences, including pavement engineering. Identification and quantification of distress that can be measured by width, length, area, and in some cases by depth is made possible by automatic analysis of images captured by a computer from video or film recordings. Analysis of images to obtain a pavement rating based on the amount of distress is being developed at several universities and private companies.

Acosta (*1*) and Figueroa et al. (*2*) investigated different techniques for the automatic segmentation of concrete, asphalt concrete, and composite pavement images; thresholding of gray-level pictures using one- and two-dimensional entropy; and innovative techniques for the identification of cracks in textured media. In addition, they developed and evaluated another method, the vertical region segmentation (VRS), and they performed a preliminary cluster classification using several geometrical and statistical features computed for each cluster and extracted from the background. The reliability and accuracy of the methods employed in automatic segmentation and the distress classification were assessed.

A fundamental component of computer-based video image analysis for pavement distress evaluation is the identification of the type of distress from geometric and textural properties of the area of interest, which was identified during image analysis. This study describes the algorithms used in the identification and classification of the most common pavement distress types once a possible distress region is identified on an image. The classification is accomplished in three steps. First, geometric and textural features are calculated for a region of interest. Next, the features of a region are used to determine whether any other regions of an image are actually part of the same pavement distress. Finally, the extracted image features are used with a decision tree to identify the specific pavement distress type. In the following section a brief review of image processing is given first. Following this review, the definition of 19 features that were found to be required for identification of pavement distress types are defined. The procedure for making connections between neighboring clusters and the decision tree for determining the type, severity, and extent of pavement distress are presented.

J. A. Acosta, Resource International, Inc., Westerville, Ohio 43081. J. L. Figueroa and R. L. Mullen, Department of Civil Engineering, Case Western Reserve University, Cleveland, Ohio 44106.

IMAGE PROCESSING OVERVIEW

Computer-based image analysis was originally developed as a powerful tool in the medical sciences (*3,4*). Since then, its use has been extended to a variety of disciplines, as shown by several texts on digital image processing (*5,6*).

The general concept behind the image-processing approach of this study can be illustrated by explaining the five steps needed for image analysis: image digitization, image filtering or segmentation, clustering, feature extraction, and cluster classification.

The image digitization is accomplished through an image capturing board residing in the computer. The analog signal from a videotape player is transformed into a two-dimensional array of pixel elements in which each element has a value proportional to its brightness. The range of values of the array (the gray-level) typically varies from 0 (black) to 255 (white).

The image filtering is done by adaptive techniques using convolution, histogram, and primal sketch methods (*7–10*). It consists of separating the pixels belonging to the foreground (objects of interest) from those of the background.

The VRS method developed by Acosta (*1*) and Acosta et al. (*11,12*) is a statistical approach to image segmentation that is applied to pavement images, based on thresholds calculated by regression analysis. This method divides the image in narrow longitudinal (vertical) regions; each region is analyzed separately to minimize problems caused by a nonhomogeneous background or nonuniform illumination. The gray-level histogram is obtained to extract the gray-level average and the gray-level standard deviation (SD), taking into account only the gray levels with significant occurrences in the frequency distribution. Three zones are delimited: background, connective (possible), and foreground. The zones are distinguished based on two thresholds, s and t, obtained by regression analysis (Figure 1):

Q_1: True-foreground zone
Q_2: Possible-foreground zone
Q_3: True-background zone

An extension of this method was developed by Acosta (*13*) and Acosta et al. (*14*) that improves the detection of longitudinal cracks by also applying horizontal region segmentation (HRS). The

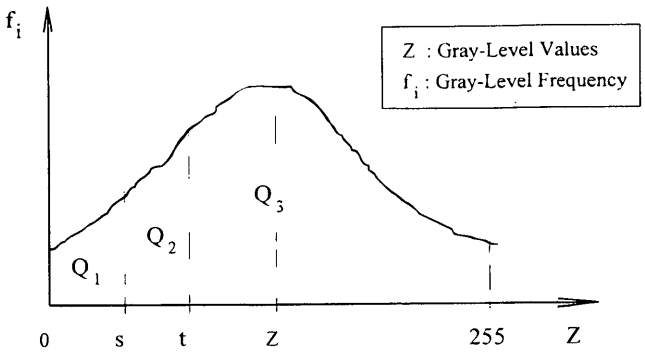

FIGURE 1 VRS zones.

improved method consists of tracing horizontal regions across the vertical regions described above, and analyzing each region separately, similar to the analysis of the vertical regions. Thresholds s^H and t^H are obtained and the pixels in the region are assigned to zones Q_1^H, Q_2^H, or Q_3^H, depending on their gray-level value, as follows:

Q_1^H: True-foreground zone from HRS
Q_2^H: Possible-foreground zone from HRS
Q_3^H: True-background zone from HRS

Pixels are pre-identified as background, Q_b and foreground, Q_f. They are designated as pre-identified because in the clustering procedure, clusters having a total number of pixels (both true-foreground and possible-foreground) less than a minimum value p and those with a number of possible-foreground pixels less than a minimum value q are automatically eliminated from further consideration. The improvement essentially consists of applying region segmentation in both directions, when needed, or combining both the VRS and the HRS methods into vertical and horizontal region segmentation VHRS. Adjacent areas of interest that were highlighted by filtering are clustered to and from objects.

Once an object in the image is found, geometric and statistical properties related to shape and gray level are calculated (feature extraction). From the information extracted, using appropriate guidelines, the object can be classified (cluster classification) as pavement distress, pavement feature, or unknown object (litter, debris, etc.). Pavement is then rated by applying the dimensional guidelines specified by the rating procedure.

This paper specifically addresses the rules necessary for cluster classification applied to pavement distress analysis, using properties obtained during feature extraction. Detailed discussions of other aspects required in image processing for pavement distress and condition evaluation can be found in Acosta (*13*) and Acosta et al. (*14*).

FEATURE EXTRACTION

Feature extraction reduces a region on an image to a limited number of geometric or textural properties. Certain features are selected that provide the capability of distinguishing between the different classes of pavement distress types. More than 50 preliminary features were chosen and extracted from a representative sample of images. The output values were analyzed and the features that best characterized the types of distress were adopted as the final features to be used in the pavement distress analysis.

A digitized image after contrast enhancement can be defined by:

$$I^* = \{f^*(x, y) \mid (0 \le x \le M) \wedge (0 \le y \le N)\} \quad (1)$$

$$Z_{min} \le f^*(x, y) \le Z_{max} \quad (2)$$

$$f^*(x, y) = \frac{f(x, y) - \rho_{min}}{\rho_{max} - \rho_{min}} \times (Z_{max} - Z_{min}) \quad (3)$$

where:

$f^*(x, y)$ = gray level value (after transformation) of pixel at (x,y) coordinates;
M, N = number of rows and columns in image;
ρ_{min}, ρ_{max} = maximum and minimum gray level values in image; and
Z_{min} = 0 and Z_{max} = 255 (minimum and maximum values in gray scale).

For a situation in which b_{ij} is the characteristic function of the cluster O_k such that:

$$b_{ij} \begin{cases} = 1 \text{ if } f^*(i,j) \in Q_f \wedge f^*(i, j) \in O_k \\ = 0 \text{ if otherwise} \end{cases} \quad (4)$$

Where Q_f is defined as follows:

$$Q_f = \{f(x, y) = z \mid z \in (Q_3 \cup Q_3^H)\} \quad (5)$$

The following geometric features are defined:

- Cluster area: number of pixels forming the cluster.

$$A = \sum_i \sum_j b_{ij} \quad (6)$$

- Aspect ratio: ratio between sides of a bounding box enclosing the cluster (Figure 2).

$$SF = \frac{\Delta_y}{\Delta_x}$$

where $\Delta_y = y_{max} - y_{min}$ and $\Delta_x = x_{max} - x_{min}$ (7)

- Angle of principal moments of inertia: angle of principal moment of inertia with respect to the horizontal, obtained from the following equations.

$$\tan 2\Theta = \frac{2I_{\bar{x}\bar{y}}}{I_{\bar{y}} - I_{\bar{x}}} \quad (8)$$

where

$$I_{\bar{x}} = I_x - \frac{P_x^2}{A}$$

$$I_{\bar{y}} = I_y - \frac{P_y^2}{A} \quad (9)$$

$$I_{\bar{x}\bar{y}} = I_{xy} - \frac{P_x P_y}{A} \quad (10)$$

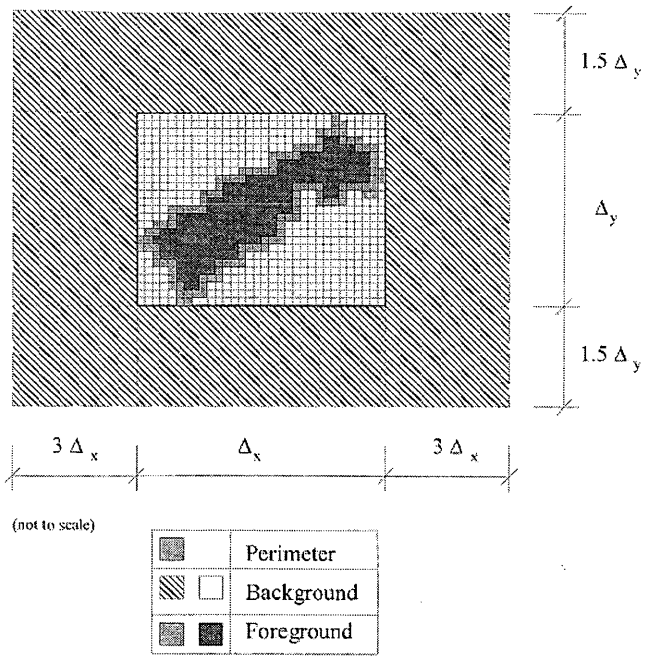

FIGURE 2 Foreground, perimeter, and background areas.

are the second moments of inertia (for both axes) and the product moment of inertia, respectively.

$$P_x = \sum_i \sum_j y \cdot b_{ij} \qquad P_y = \sum_i \sum_j x \cdot b_{ij} \tag{11}$$

are the first moments of area about the image coordinate axes, and

$$I_x = \sum_i \sum_j y^2 \cdot b_{ij}$$

$$I_y = \sum_i \sum_j x^2 \cdot b_{ij} \tag{12}$$

$$I_{xy} = \sum_i \sum_j xy \cdot b_{ij} \tag{13}$$

are the moments of inertia and the product moment of inertia, respectively.

- Coordinates of the center of gravity:

$$x_{cg} = \frac{P_x}{A}$$

$$y_{cg} = \frac{P_y}{A} \tag{14}$$

- Inertia ratio is calculated (*15*) as follows:

$$IR = \frac{I_{\max}}{I_{\min}} \tag{15}$$

where

$$I_{\max}, I_{\min} = \frac{I_{\bar{x}} + I_{\bar{y}}}{2} \pm \sqrt{(I_{\bar{x}} - I_{\bar{y}})^2 + 4\,(I_{\bar{x}\,\bar{y}})^2} \tag{16}$$

are the principal moments of inertia.

- Density: the ratio between the cluster's number of pixels and the area of the box enclosing the cluster.

$$D = \frac{A}{\Delta_y \times \Delta_x} \tag{17}$$

- Ratio between the number of possible-foreground and true-foreground pixels:

$$MTPR = \frac{\sum f_i \in (Q_2 \cup Q_2^H)}{\sum f_i \in Q_f} \tag{18}$$

- Cluster length along the angle Θ, L: obtained by scanning the cluster in the Θ direction.
- Average width:

$$W = \frac{A}{L} \tag{19}$$

- Ratio between length and width:

$$LWR = \frac{L}{W} \tag{20}$$

- Gray-level average:

$$\mu = \frac{\sum_i \sum_j f_{ij}}{A} \tag{21}$$

- Gray-level standard deviation:

$$\sigma_z = \frac{\sum (\mu_i - \mu)^2}{A} \tag{22}$$

- Perimeter, P, and perimeter area, A_p: calculated by scanning the cluster and adding up the number of pixels from its perimeter (Figure 2).
- Perimeter gray-level average: average of gray-level values of perimeter pixels f_{ij}^p

$$\mu_p = \frac{\sum_i \sum_j f_{ij}^b}{A_p} \tag{23}$$

- Background gray-level average: an area around the cluster was set as shown in Figure 2, and the gray-level values corresponding to pixels residing in this area were averaged.

$$\mu_b = \frac{\sum_i \sum_j f_{ij}^b}{A_b} \tag{24}$$

- Perimeter foreground ratio: ratio between the perimeter area and the foreground area, as follows.

$$PFR = \rho = \frac{A_p}{A} \tag{25}$$

- Squareness constant, K_s: calculated from above expression, for a rectangle as follows.

$$\rho = \frac{2(W + L)}{W \times L} \tag{26}$$

then

$$K_s = \frac{\rho WL}{W + L} = 2 \tag{27}$$

- Roundness constant, K_r: from Equation 25, for a circle, if D is the diameter:

$$\rho = \frac{\pi D}{\pi D^2} = \frac{4}{D} \tag{28}$$

then

$$K_r = \rho D = \rho L = 4 \tag{29}$$

- Square perimeter factor: obtained as the ratio between the cluster perimeter and the perimeter of a rectangle.

$$SPF = \frac{P}{2L + 2W} \quad \begin{cases} \text{Rectangle} \cong 1 \\ \text{Circle} \cong 0.79 \end{cases} \tag{30}$$

- Background-foreground gray-level ratio: ratio between the average gray-level of background pixels (Figure 2) and the cluster pixels.

$$BFGLR = \frac{\mu_b}{\mu_f} \tag{31}$$

The previously defined 19 features (Equations 4–31) were found to be sufficient to identify and quantify the severity and extent of all pavement distress types considered.

CLUSTER CONNECTION AND CLASSIFICATION

Prior to the final classification of a selected region on an image, a neighbor cluster connection was implemented to facilitate the identification of cracks during classification. The cluster is scanned along its perimeter to find adjacent clusters. In the event a neighboring cluster is detected, some properties (extracted features) are compared. If they satisfy the conditions imposed, they are merged to form a single cluster. The procedure continues until all clusters are scanned and compared with their neighbors.

For a case in which cluster k is being scanned and cluster l is found as a neighbor,

if $(\Theta_k \approx \Theta_l \approx \Theta_{kl}) \wedge (LWR_k \approx LWR_l)$ then clusters k and l are merged

where:

Θ_k, Θ_l = Angle of principal moment of inertia
Θ_{kl} = Average between angles Θ_k and Θ_l
LWR_k, LWR_l = Ratio between cluster length and cluster width

Following the cluster (neighbor) connection, the features described above are calculated for the new clusters so that they can be classified as one of the distress types included in the pavement condition rating (PCR) manual (*16*) or discarded from further analysis if they are nondistress.

The classification is performed in five main stages: depth-related cluster classification, cluster preliminary identification, cluster identification, cluster preclassification, and final classification. A description of the stages is given in the following sections, taking into account the distresses found in flexible, composite, and jointed portland cement concrete pavements.

Depth-Related Cluster Identification (Figure 3)

Flexible and Composite Pavements

The transverse depth is checked every 18 ft to verify the existence of rutting. Rutting is considered when it is greater than 0.1 in. The existence of corrugations is detected if five consecutive longitudinal readings indicating unevenness of pavement surface in the longitudinal profile greater than 0.1 in. are obtained. The readings are considered 18 ft apart.

Jointed Pavements

The existence of faulting is detected if a longitudinal unevenness greater than 0.1 in. is obtained. The readings are considered 18 ft apart.

Both transverse and longitudinal depth readings are obtained from ultrasonic devices that measure for rutting, corrugation, and faulting. These readings are directly encoded on the videotape using a gray-level scale for easy decoding during the analysis of individual frames, as described by Acosta (*13*) and Acosta et al. (*14*). Similarly, the longitudinal length is also continuously encoded on tape from readings obtained with a distance measuring instrument. The transverse length remains constant because the camera height and focus remain constant.

Cluster Preliminary Identification (Figure 4)

Six parameters that are helpful in the preliminary identification of the cluster, regardless of the type of pavement, are obtained based on the features extracted from the cluster.

- Longitudinal unevenness:
  - Significant — Longitudinal reading > 0.2 in.
  - Not significant — Otherwise
- Location (Figure 5):
  - In road edge zone
  - In wheel track zone
  - In corner break zone on left side of lane or on right side of lane
- Shape factor:
  - Longitudinal shape factor (SF) — $SF > 2$
  - Transverse shape factor — $SF < 0.5$
  - Normal shape factor — Otherwise
- Squareness:
  - Semisquare — $K_s < 3$ and $K_r < 10$
  - Not semisquare — Otherwise
- Size:
  - Small — $A < 30$ in.^{2}
  - Medium — $A > 30$ in.^{2} and $A < 60$ in.^{2}
  - Large — Otherwise
- Darkness with respect to background:
  - Dark — $BFGLR < 2$.
  - Not dark — Otherwise

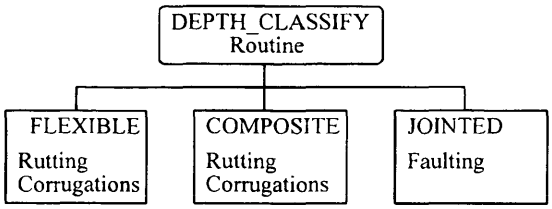

FIGURE 3 Depth-related cluster identification.

Cluster Identification

The cluster is identified based on the preliminary identification and additional features extracted from the object. Figure 6 shows the hierarchical top-down rule-based identification performed on the cluster.

Cluster Preclassification

In this stage, the cluster is preclassified as one of the distress types, considering the type of pavement being analyzed. Figures 7, 8, and 9 present the cluster preclassification for flexible, composite, and jointed pavements, respectively.

Cluster Final Classification

The distress types preclassified and marked by an asterisk (*) in Figures 8 and 9 are further analyzed in this stage, either to identify new distress types or to validate their classification. These figures show that only clusters in composite and jointed pavements need to be processed. Figures 10 and 11 present the steps followed in the cluster final classification for these two types of pavements, respectively. Figure 12 shows the scanned areas close to cracks in the final classification stage to verify the presence of joints and crack-related distress referenced in Figures 10 and 11.

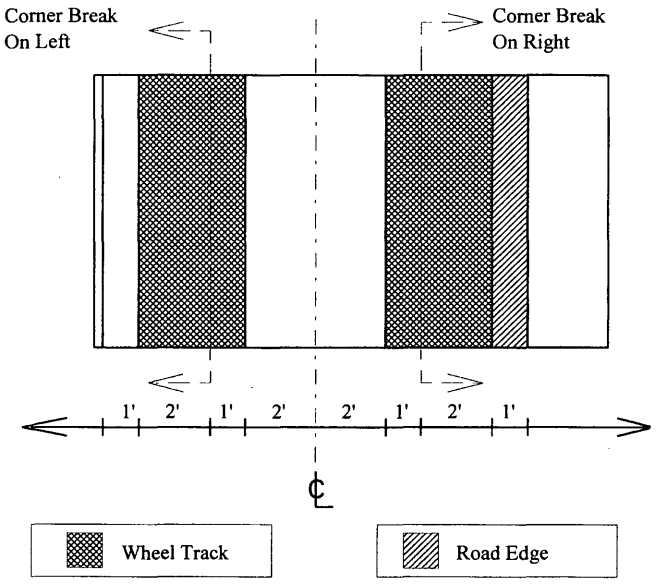

FIGURE 5 Roadway zones.

Calculation of Severity and Extent Parameters

Once the cluster is classified, its quantification in terms of severity and extent has to be determined. Guidelines included in the PCR rating procedure (*16*) were followed in the implementation. The analysis program outputs a file containing the information needed to calculate the PCR value. This information corresponds to parameters such as average crack width, percentage of occurrence in section length, percentage of occurrence in section area, crack spacing, and so forth.

Different factors affect the estimation of the parameters needed for the distress quantification. Acosta (*13*) mentioned that the segmentation does not necessarily completely highlight the area

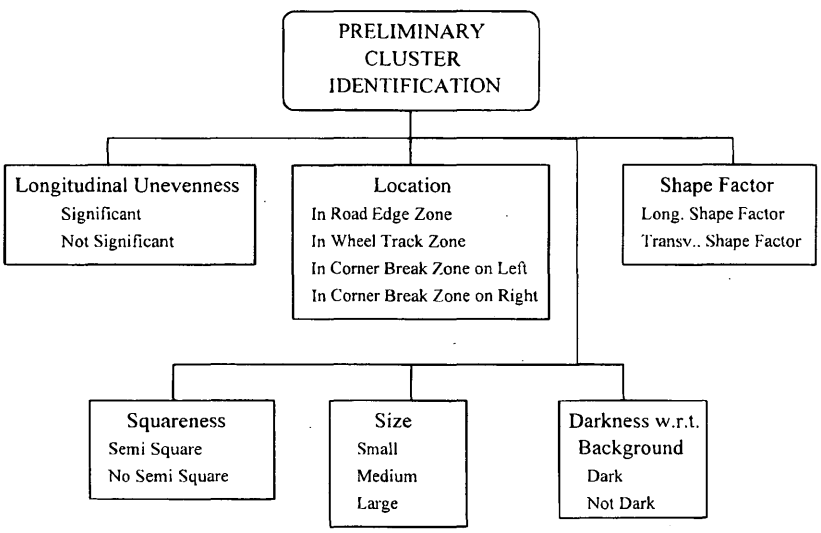

FIGURE 4 Preliminary cluster identification.

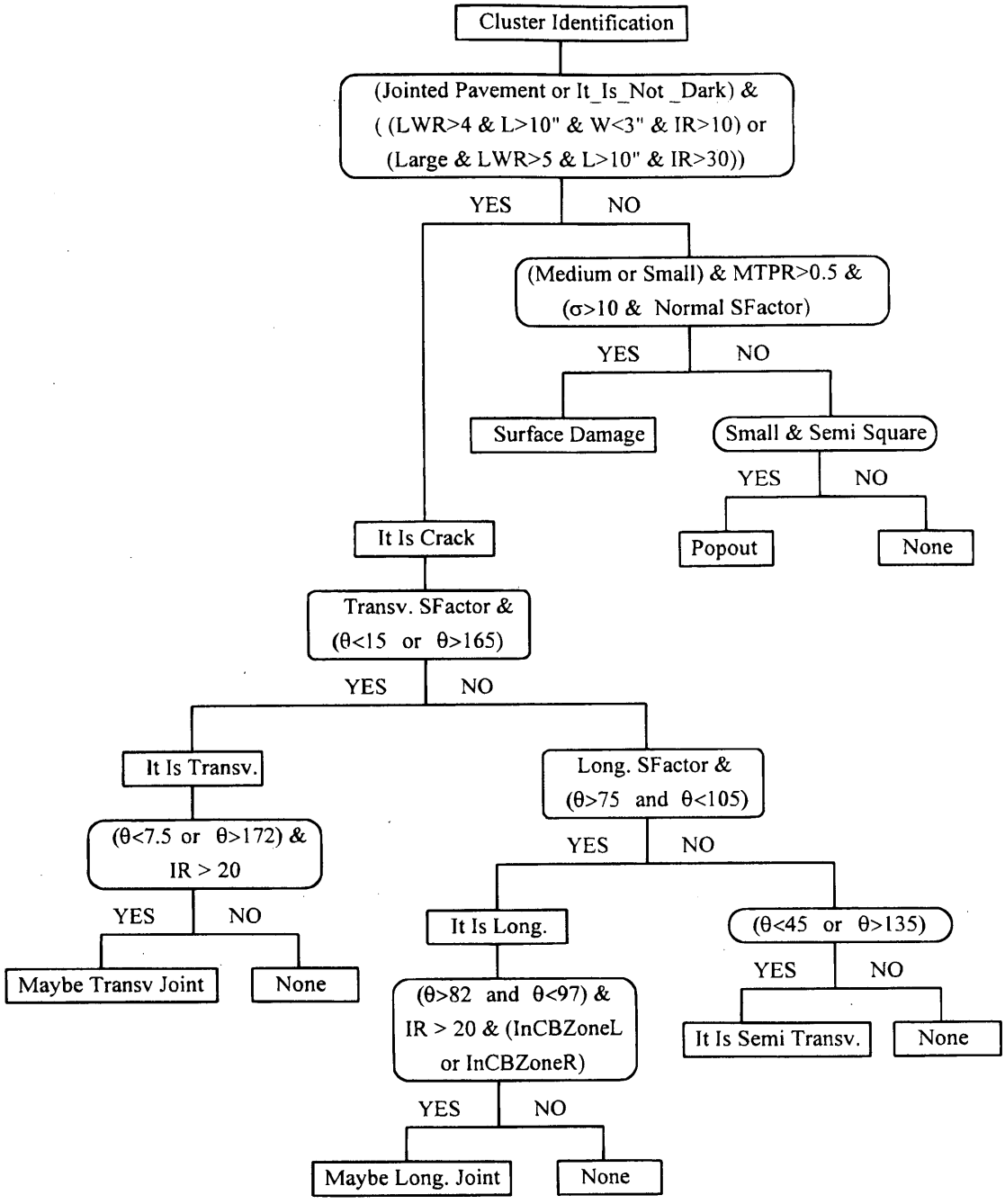

FIGURE 6 Cluster identification.

affected by the distress, and furthermore, it is necessary to estimate parameters spatially related. Consequently, there are two kinds of quantification parameters: local (e.g., crack width, crack length, etc.) and spatial (e.g., occurrence of single or multiple cracking, area affected by distress, etc.).

The estimation of local parameters is straightforward, whereas the estimation of spatial parameters requires additional work. Two data structures were implemented: distress information (*Distress-Info*) and distress region information (*Distress-Region-Info*) for the estimation of the severity and extent parameters. The image is subdivided into 18 in. × 18 in. regions, and each region is scanned to update the variables contained in the data structures that are to be used in the estimation of the spatial parameters.

The data structure variables are presented in the following tables.

Distress-Info

Acum. Cluster Area: summation of physical cluster area.
Acum. Length: summation of physical cluster length.
Acum. Area Affected: summation of area affected by distress.
Acum. Section Length Affected: summation of section length affected by distress.

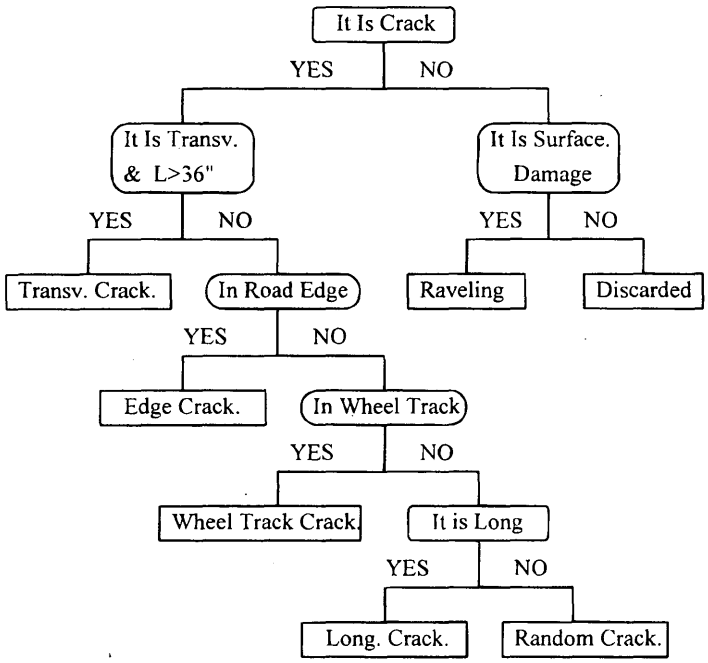

FIGURE 7 Cluster preclassification for flexible pavements.

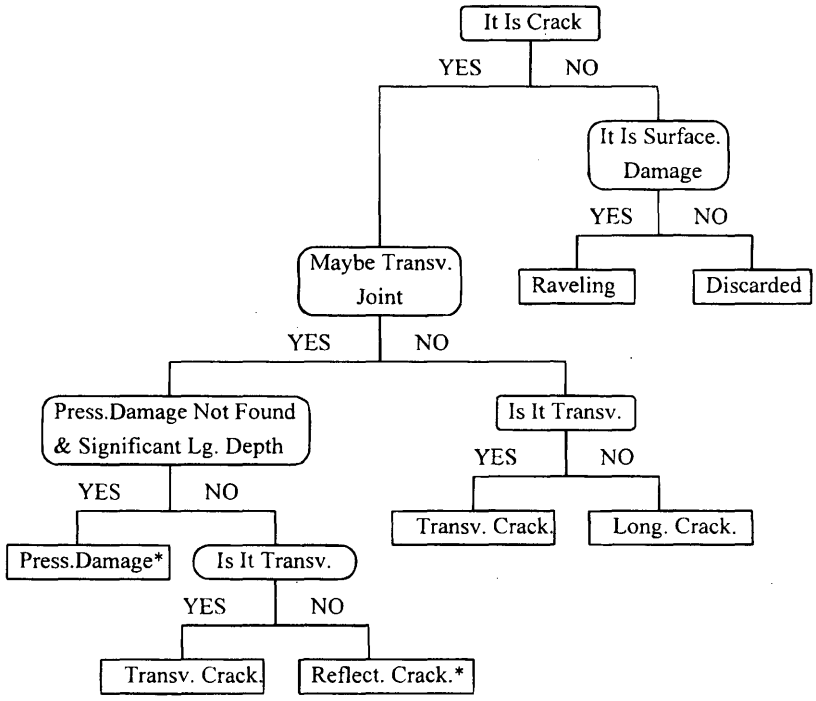

* Distress is further analyzed in the Final-Classification Stage.

FIGURE 8 Cluster preclassification for composite pavements.

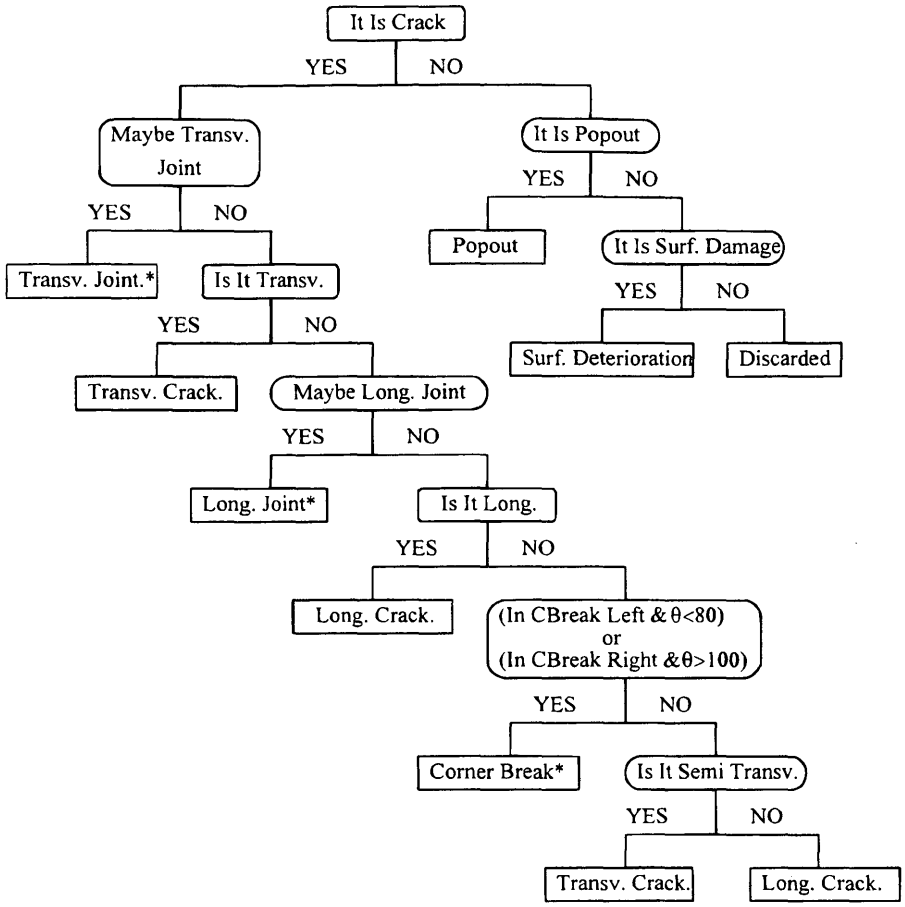

* Distress is further analyzed in the Final-Classification Stage.

FIGURE 9 Cluster preclassification for jointed pavements.

Acum. Depth: summation of depth reading (where applicable).

Acum. Gray-Level Std. Deviation: summation of standard deviations of gray-level values in clusters.

Acum. Number of Distresses: number of distresses identified in the section analyzed.

Acum. No. of Distress Region: summation of number of distresses in the region.

Number of Regions With Distress: summation of number of regions presenting the distress type.

Distress-Region-Info

Tot. No. of Pixels: total number of pixels belonging to the distress type.

No. of Distress Region: number of clusters classified under the distress type that is present in the region.

Note that for each distress type there are separate data structures, which contain the information mentioned above.

In summary, the procedure to estimate the parameters needed for the distress quantification follows three stages: local distress quantification, region distress quantification, and reporting of results for the analyzed section.

Local Distress Quantification

After the cluster is classified, the following variables are updated: Acum. Cluster Area, Acum. Length, Acum. Number of Distresses, Acum. Gray-Level Std. Deviation, and Acum. Depth (for depth-related distresses).

Region Distress Quantification

The following steps are performed in this stage:

- Count number of distress of each type in region,
- Update number of regions with distress for each type,
- Obtain area in the region in which each distress type occurs,
- Update the following equations:

$$\text{AcumAreaAffected} = \text{RegionArea} \times \frac{\text{DistressArea}_i}{\sum_i \text{DistressArea}} \quad (32)$$

$$\text{AcumLengthAffected} = \text{Region Length} \times \frac{\text{DistressLength}_i}{\sum_i \text{DistressLength}} \quad (33)$$

(1) Verify existence of Reflection Cracking

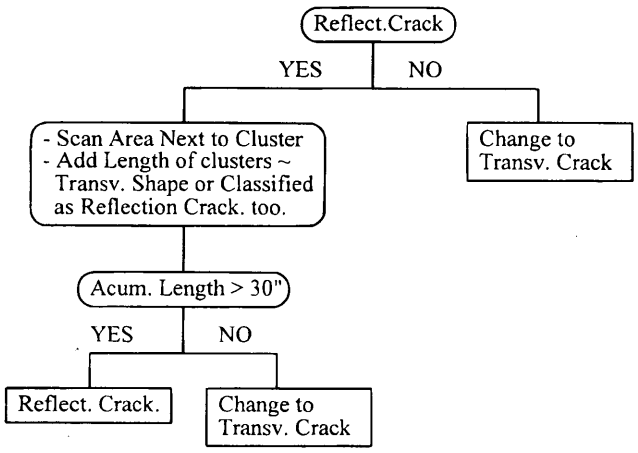

(2) Verify existence of Pressure Damage/Upheaval or Shattered Slab

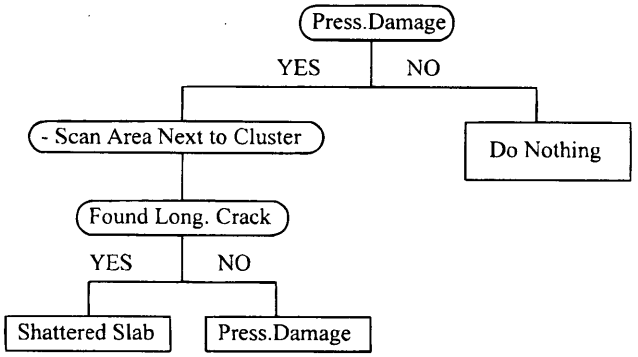

FIGURE 10 Cluster final classification for composite pavements.

This operation is performed only once, for regions within the same transverse location of the image.

Report of Results for Analyzed Section

The parameters needed for distress quantification in terms of severity and extent are obtained based on the values stored in the data structure: *Distress-Info.* They are summarized in the following equations.

- Average number of distresses per region:

$$\text{AveNDisPerReg} = \frac{\text{AcumNDisReg}}{\text{NRegWithDis}} \tag{34}$$

Useful in determining single or multiple cracking:

if (AveNDisPerReg $\leq$ 1), single otherwise, multiple.

- Average crack width:

$$\text{AveCrackWidth} = \frac{\text{AcumDisArea}}{\text{AcumLength}} \tag{35}$$

- Average distress length:

$$\text{AveDisLength} = \frac{\text{AcumLength}}{\text{AcumNDistress}} \tag{36}$$

- Average distress area:

$$\text{AveDisArea} = \frac{\text{AcumArea}}{\text{AcumNDistress}} \tag{37}$$

- Average gray-level SD:

$$\text{AveStdDeviation} = \frac{\text{AcumStdDev}}{\text{AcumNDistress}} \tag{38}$$

Useful in determining texture:

if AveStdDeviation $>$ 65 surface severely rough.
if 65 $<$ AveStdDeviation $>$ 25 open texture, medium roughness.
if AveStdDeviation $<$ 25 very little coarse aggregate.

- Percentage of occurrences per section area:

$$\text{PerOccSecArea} = \frac{\text{AcumAreaAffected}}{\text{SecArea}} \tag{39}$$

(1) Verify existence of Transverse Joints

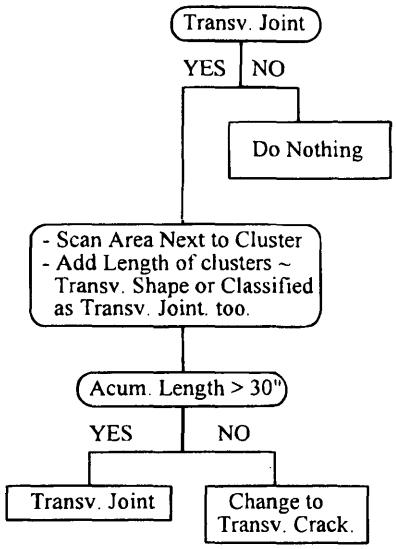

(2) Verify existence of Long. Joints

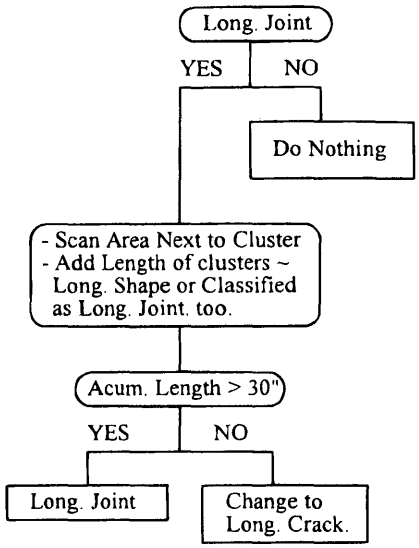

(3) Verify existence of Corner Breaks

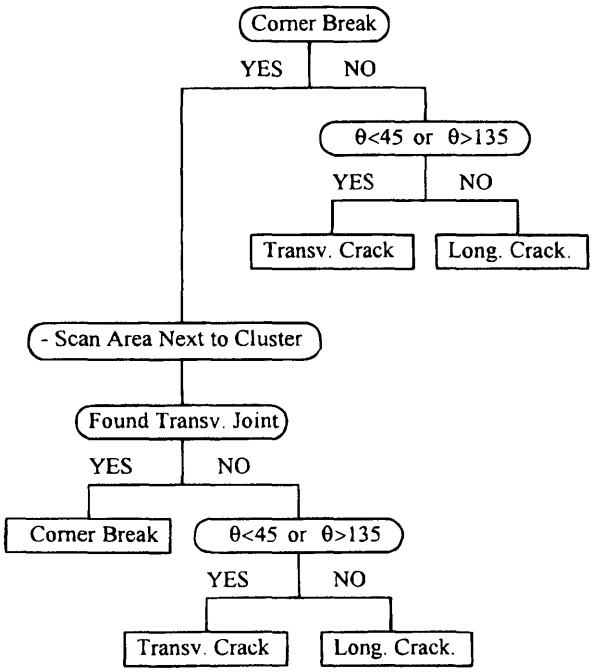

(4) Verify existence of Joint Spalling and Pressure Damage

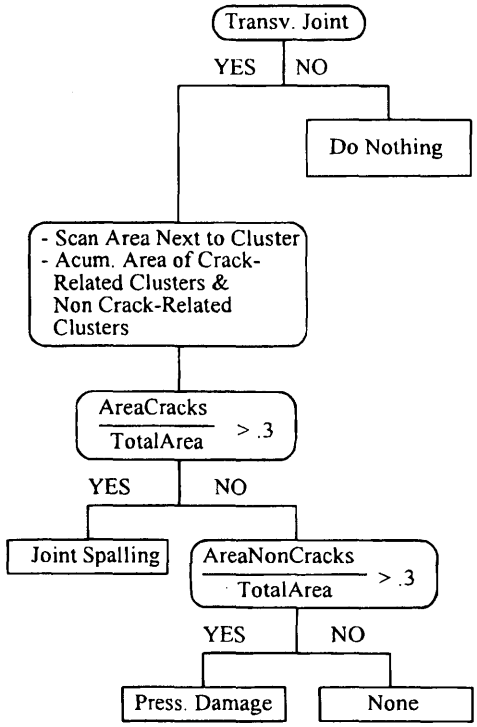

FIGURE 11 Cluster final classification for jointed pavements.

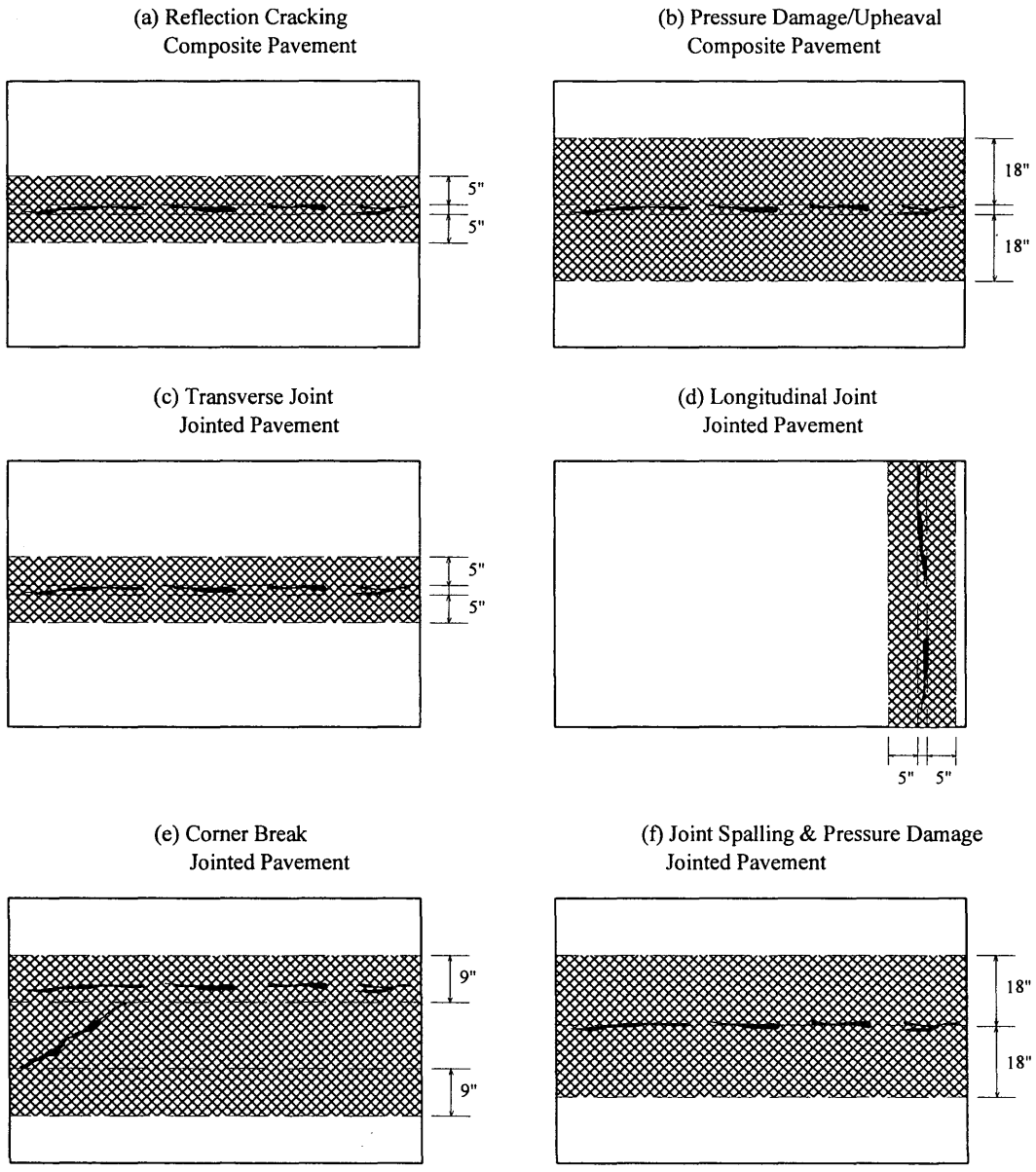

FIGURE 12 Scanned areas in final classification stage.

where SecArea = area of the section analyzed

- Percentage of occurrences per section length:

$$\text{PerOccSecLength} = \frac{\text{AcumSecLengthAffected}}{\text{SecLength}} \tag{40}$$

where SecLength = length of the section analyzed; or, in jointed pavements (where applicable):

$$\text{PerOccSecLength} = \frac{\text{AcumNDistress}}{\text{NSlabs}} \tag{41}$$

where NSlabs = number of slabs in the section analyzed.

- Average distress spacing:

$$\text{AveDisSpacing} = \frac{\text{SecLength}}{\text{AcumNDistress}} \tag{42}$$

- Average distress depth (for depth-related distresses):

$$\text{AveDisDepth} = \frac{\text{AcumDepth}}{\text{AcumNDistress}} \tag{43}$$

- Number of distress types per mile (where applicable in jointed pavements):

$$\text{AveDisDepth} = \frac{\text{AcumNDistress}}{\text{SecLength [miles]}} \tag{44}$$

TABLE 1 Comparison Between Manual and Automated PCR Values

Section	1	2	3	4
Length (meters)	5520	3685	4343	1931
Number of images	14,844	9,910	11,680	5,193
Data acquisition time. (min.)	4.12	2.75	3.24	1.44
Data processing time (min.)	41	27	32	14
Manual survey PCR	68.26	71.66	74.22	71.66
Automated survey PCR	65.10	72.20	75.30	71.70
% Difference of automated system with respect to manual values	-4.6%	0.8%	1.5%	0.06%

RESULTS

The distress classification system described herein was used to determine the PCR (*16*) for four pavement sections that were also rated by the Ohio Department of Transportation (ODOT). A summary of the manual and automated PCR is presented in Table 1. The images were collected using a vehicle, described by El Sanhouri (*13*), traveling at 80 km/hr (50 mi/hr). The collected video images were processed from videotape using a SUN Sparc-2 computer. As implemented, processing takes approximately 10 times as long as acquisition. The difference between manual and automated PCR is less than 5 percent in all test sections.

SUMMARY

Several methods have been proposed to identify regions of distress using image-processing techniques. The required region properties and a decision tree for reducing selected regions of an image to conventional type, severity, and extent of pavement distress have been presented in this study. The features and decision trees have been tested on several thousand pavement images. The system of which the decision tree is part has been used successfully by ODOT since May 1994.

ACKNOWLEDGMENTS

This paper is based on research sponsored by ODOT under Grant OD-6606. The authors gratefully acknowledge the assistance of William F. Edwards, Kenneth Corns, and the engineers from the Research and Development Division at ODOT.

REFERENCES

1. Acosta, J. A. *Implementation of the Video Image Processing Technique for Evaluating Pavement Surface Distress.* M. S. thesis. Department of Civil Engineering, Case Western Reserve University, Cleveland, Ohio, 1991.
2. Figueroa, J. L., R. L. Mullen, and J. A. Acosta. A Low Cost Pavement Distress Survey and Analysis System. *Second International Symposium on Road Surface Characteristics,* Technische Universität Berlin Fachgebiet Straβenbau, 1992, pp. 528–541.
3. Chow, C. K., S. K. Hilal, and K. E. Neibuhr. X-Ray Image Subtraction by Digital Means. *IBM Journal of Research and Development,* Vol. 7, 1973, pp. 206–218.
4. Inoue, S. Video Image Processing Greatly Enhances Contrast, Quality and Speed in Polarization Based Microscopy. *Journal of Cell Biology,* Vol. 89, 1981, pp. 346–356.
5. Hung, T. S. *Picture Processing and Digital Filtering.* Springer-Verlag, Berlin, 1979.
6. Pratt, W. K. *Digital Image Processing.* John Wiley & Sons, Inc., New York, N.Y., 1978.
7. Kasturi, R., and J. F. Walkup. Nonlinear Image Restoration. *Digital Image Processing,* SPIE, Vol. 528, 1985, pp. 43–60.
8. Victor, T. T. Adaptive Filter Techniques for Digital Image Enhancement. *Digital Image Processing,* SPIE, Vol. 528, 1985, pp. 29–42.
9. Hummel, R. Image Enhancement by Histogram Transformation. *Computer Vision, Graphics, and Image Processing,* Vol. 6, 1977, pp. 184–185.
10. Pitas, I., and A. N. Venetsanopoulos. Nonlinear Order Statistic Filters for Image Filtering and Edge Detection. *Signal Processing,* Vol. 10, 1986, pp. 395–413.
11. Acosta, J. A., J. L. Figueroa, and R. L. Mullen. Low-Cost Video Image Processing System for Evaluating Pavement Surface Distress. In *Transportation Research Record 1348,* TRB, National Research Council, Washington, D.C., 1992, pp. 63–72.
12. Acosta, J. A., J. L. Figueroa, and R. L. Mullen. *Feasibility Study to Implement the Video Image Processing Technique for Evaluating Pavement Surface Distress in the State of Ohio.* Final Report No. FHWA/OH-91/010. Ohio Department of Transportation, January 10, 1992.
13. Acosta, J. A. *Pavement Surface Distress Evaluation Using Video Image Analysis.* Ph.D. dissertation. Department of Civil Engineering, Case Western Reserve University, Cleveland, Ohio, 1994.
14. Acosta, J. A., J. L. Figueroa, and R. L. Mullen. *Implementation of the Video Image Processing Technique for Evaluating Pavement Surface Distress in the State of Ohio.* Final Report No. FHWA/OH-94/005. Ohio Department of Transportation, May 1994.
15. El Sanhouri, I. M. *Computer-Based Segmentation and Interpretation of Pavement Surface Distress Images.* M.S. thesis. Massachusetts Institute of Technology, Cambridge, 1990.
16. Majidzadeh, K., and M. S. Luther. *Development and Implementation of a System for Evaluation and Maintenance and Repair Needs and Priorities.* Vol. 2. Report No. FHWA/OH-80/003. Resource International, Inc.; Ohio Department of Transportation, 1980.

Publication of this paper sponsored by Committee on Pavement Monitoring, Evaluation, and Data Storage.

Pavement Distress Evaluation Using Fuzzy Logic and Moment Invariants

JACHING CHOU, WENDE A. O'NEILL, AND HENGDA CHENG

A novel approach of applying the theory of fuzzy sets and moment invariants to analyze pavement images is proposed in this paper. By applying the theory of fuzzy sets and calculating moment invariants from different types of distress, features are obtained. Then, a back-propagation neural network is used to classify these features. The crack density is used to obtain extent information. This approach is illustrated using randomly selected samples from NCHRP Project 1-27 video images of real cracks. Based on these samples, the feasibility of using the theory of fuzzy sets and moment invariants to classify different types of crack is proven. High accuracy of classification is also obtained.

Pavement distress surveys are one of the key components in a pavement management system (PMS). Currently, most states use manual surveys to obtain measurements of pavement distress. Manual surveys are inconsistent, costly, tedious, labor intensive, and subjective. Several researchers have investigated the use of image processing and pattern recognition techniques to achieve automated pavement distress ratings.

LITERATURE REVIEW

Previous Work in Pavement Image Processing

Baker et al. (*1*) discussed the use of image processing in pavement analysis for the Idaho Transportation Department. Caroff et al. (*2*) developed and validated the use of digital image processing in pavement distress to extract, recognize, and quantify longitudinal cracks, transverse cracks, and alligator cracks. Fukuhara et al. (*3*) introduced a Komatsu system for pavement condition surveys. Mohajeri and Manning (*4*) discussed the ARIA pavement distress image processing system. Li, Chan, and Lytton (*5*) proposed an approach to detect thin (width $<$ 1/4 inch) cracks. Ritchie, Kaseko, and Bavarian (*6*) applied neural networks to determine (recognition, high level processing) the type, severity, and extent of distress from video images in real time. Acosta, Figueroa, and Mullen (*7*) developed image processing procedures with several system components, such as image digitizing and deblurring, image segmentation and clustering, feature extraction and cluster classification, and a pavement condition rating routine. Koutsopoulos and Downey (*8*) adopted a primitive-based classification approach to classify distress type. Chua and Xu (*9*) proposed a prototype system that consists of an ordinary 8-mm camcorder, an inexpensive image-digitizing board, and an algorithm running on an IBM 486-compatible personal computer to detect pavement distress.

Departments of Civil and Environmental Engineering and Computer Science, Utah State University, Logan, Utah 84322.

In general, previous studies show that the following steps are required in pavement image processing: (*a*) image acquisition, (*b*) image enhancement, (*c*) image segmentation, and (*d*) image classification. The following sections will discuss algorithms used in research applications of using video image processing.

Moment Invariants and the Theory of Fuzzy Set in Image Analysis

Pal and King (*10*) said, "The theory of fuzzy sets provides a suitable algorithm in analyzing complex systems and decision processes when the pattern indeterminacy is due to inherent variability and/or vagueness (fuzziness) rather than randomness." There are several reasons that images are fuzzy: (*a*) images are generally ambiguous when represented by pixels because of the varied levels of brightness (0 to 255) and the lack of crisp boundaries between edges and nonhomogeneous regions; (*b*) information is lost in the transformation from a three-dimensional image to a two-dimensional image; and (*c*) ambiguity and vagueness in interpreting results from low level image processing. So the use of fuzzy set theory may be more suitable than ordinal set theory for an image-processing problem.

Pal (*11*) introduced an index of fuzziness and entropy as a quality index of enhanced images. In Pal and Ghosh's work (*12*), fuzzy geometry is used in image analysis. Pal and Rosenfeld (*13*) proposed image enhancement and thresholding by optimizing the compactness of fuzziness. Linear index of fuzziness, quadratic index of fuzziness, entropy, and index of nonfuzziness are also introduced. Pal, King, and Hashim (*14*) used fuzzy sets to describe images and to extract primitives. Keller and Carpenter (*15*) used fuzzy set theory to segment images. Zhao, Li, and Cheng (*16*) applied a fuzzy logic approach to image enhancement. Huntsberger, Jacobs, and Cannon (*17*) have developed an iterative fuzzy clustering technique based on a fuzzy c-means algorithm for image segmentation.

Moments and functions of moments have been applied as pattern features in several applications to recognize objects. Hu (*18*) introduced moment invariants based on algebraic invariants. Noll (*19*) discussed some general properties of Zernike polynomials, such as their Fourier transforms, integral representations, and derivatives. Reddi (*20*) introduced radial and angular moments, which are more general in moment functions compared with Hu's moment invariants. Teague (*21*) introduced Zernike moments based on the theory of orthogonal polynomials and Legendre moments based on Legendre polynomials. In Teague's research (*22*), moments with arbitrarily high orders were developed. In 1984 (*23*) and 1985 (*24*), Abu-Mostafa and Psaltis introduced complex moments as a simple and straightforward way to derive moment invariants. Maitra (*25*) found that moments are not contrast invariant between two images.

Hsia (*26*) discussed moment variations due to numerical integration and interpolation in digital images.

Previous efforts show that moment invariants and the theory of fuzzy sets have been successfully applied to image processing and analysis for a variety of applications. These applications include recognition of hand-printed characters, aircraft identification, interpretation of ship photos, recognition of vehicle images, and others. Preliminary results from Chou's work (*27,28*) show that: (*a*) fuzzy image-processing techniques can provide a better approach to process pavement images; and (*b*) by the properties of moment invariants under change of size (scale), change of position (translation), change of orientation (rotation), and reflection, cracks' features can be extracted, and cracks can be correctly classified.

This paper focuses on models and algorithms for automated asphalt pavement image processing. Algorithms of image preprocessing, image enhancement, image segmentation, distress feature extraction and classification, and obtaining extent information are presented.

METHODOLOGY

Pavement Image Acquisition and Digitization

Sample images for this work were provided by the NCHRP, Project 1-27. Images were digitized using a Panasonic S-VHS AG-7500 editing machine controlled by a DIAQUEST board in an IBM compatible personal computer and a TARGA+ image-digitizing board. The image size for each frame is 482 × 512 pixels, and the gray scale is from 0 to 255.

Pavement Image Preprocessing

Because of the nonuniform illumination, some images' right and left portions are darker than their central area. Figure 1 shows this situation in a nondistress image. In this case, a nonlinear equation is used to adjust the image histogram. This equation is

$$f(x,y) = f(x,y) + \begin{cases} p_1 \times \sqrt{x_b - x_i} & 0 \le x_i \le x_b \\ 0 & x_b < x_i \le x_e \\ p_2 \times \sqrt{x_i - x_e} & x_e < x_i \le 255 \end{cases} \quad (1)$$

where

x_i = current x-position,
x_e = position where the right dark area begins,
x_b = position where the left dark area ends, and
p_1, p_2 = parameters.

The values of x_e and x_b are derived from 45 sample images. The values of p_1 and p_2 are calibrated from 45 sample images by manually examining images. In practical situations, these parameters can be calibrated from field images and used for the remaining pavement images because the lighting condition is under control. This step is only required when images are darker along the edges.

Pavement Image Rotation

To generate enough image samples and test moment invariants under rotation for pavement distress images, a rotating technique is used. This technique is referred to as a geometric transformation. In this transformation the relationship between a source image and a rotated image is

$$\begin{bmatrix} x_{new} \\ y_{new} \end{bmatrix} = \begin{bmatrix} \cos\theta & \sin\theta \\ -\sin\theta & \cos\theta \end{bmatrix} \times \begin{bmatrix} x_{old} \\ y_{old} \end{bmatrix} \quad (2)$$

According to Lindley (*29*), to guarantee one-to-one mapping of source to rotated pixels, reverse mapping is used. Interpolation is used to calculate the coordinates for the pixels whose locations are fractional during the rotating process. Bi-linear interpolation is used here.

The relationship between $f(x,y)$ and the four surrounding points is described in Figure 2 as follows.

$$\begin{aligned} j &= \text{INT}[x] & \alpha &= x - y \\ k &= \text{INT}[y] & \beta &= y - k \end{aligned} \quad (3)$$

where INT[] is an integer function.

In Y-direction,

$$\begin{aligned} A &= (1 - \beta) * f(j, k) + \beta * f(j, k + 1) \\ B &= (1 - \beta) * f(l, k) + \beta * f(j + 1, k + 1) \end{aligned} \quad (4)$$

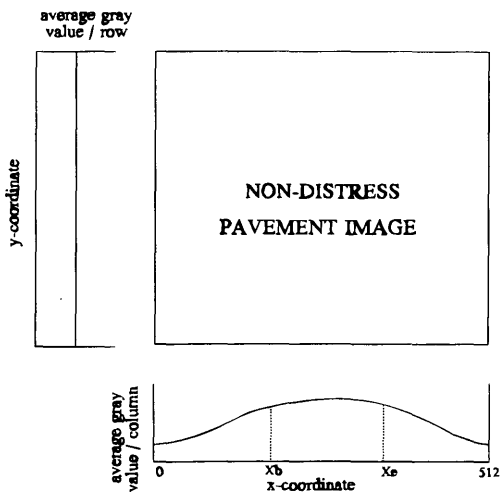

FIGURE 1 Nonuniform illumination in a nondistress pavement image.

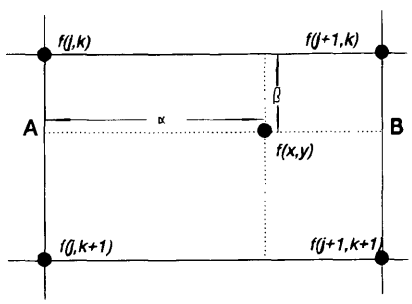

FIGURE 2 Bilinear interpolation in image rotation.

In X-direction,

$$f(x,y) = \alpha * \beta + (1 - \alpha) * A \tag{5}$$

Finally,

$$f(x,y) = (1 - \alpha)(1 - \beta) * f(j, k) + \alpha(1 - \beta) f(j+ 1, k) + \beta (1 - \alpha) * f(j, k + 1) + \alpha\beta f(j + 1, k + 1) \tag{6}$$

when $\alpha = \beta = 0, f(x, y) = f(j, k)$.

Pavement Image Enhancement

Zhao et al. (*16*) used a fuzzy algorithm to enhance images. In this research, a Z-function is used instead of S-function because the S-function is typically used for bright objects, and pavement cracks are dark. First, a function complementary to the S-function [i.e., (1-S)-function] is used. The Z-function is defined as

$$Z(x,a,b,c) = \mu_x(x) = \begin{cases} 1 & x < a \\ 1 - \dfrac{(x-a)^2}{(b-a)(c-a)} & a \le x < b \\ \dfrac{(x-c)^2}{(c-b)(c-a)} & b \le x < c \\ 0 & x \ge c \end{cases} \tag{7}$$

where

a and c = parameters determining the fuzzy region and associated with the histogram of the gray scale of the image,
$b = (a + c)/2$, and
$\times$ = pixel value.

Second, an averaging filter is used to remove noise, thus smoothing the image. And the output is $v(m,n)$. The definition of $v(m,n)$ is

$$v(m,n) = \text{average } [\mu_x(m - k, n - l), (k,l) \in W)] \tag{8}$$

where W is the averaging filter window, and its size is 3×3. Third, a transformation function (T) is used to enhance the image in the fuzzy domain. The transformation function is

$$\mu'_x(x_{mn}) = T[\, v(m,n)]$$

$$= \begin{cases} 2 \times [v(m,n)]^2 & 0.0 \le v(m,n) < 0.5, \\ 1 - 2 \times (1 - v[m,n)]^2 & 0.5 \le v(m,n) < 1.0 \end{cases} \tag{9}$$

Finally, fuzzy membership values are converted to gray-level values.

Pavement Image Thresholding

A fuzzy thresholding technique based on the principle of maximum fuzzy entropy is used. The degree of ambiguity of an image can be measured by the entropy of a fuzzy set. A threshold is obtained by maximizing the fuzzy entropy of an image. The fuzzy entropy is defined as

$$H(x_i) = \frac{-1}{M\,N\,(\ln 2)} \sum_{x=L_{\min}}^{L_{\max}} \{\mu_x(x_i) \ln[\mu_x(x_i)] + [1 - \mu_x(x_i)] \ln[1 - \mu_x(x_i)]\} \times h(x_i) \tag{10}$$

where $h(x)$ is the histogram. After thresholding, a binary image is obtained.

Pavement Image Feature Extraction

There are seven types of distress that are considered in this research. These distresses are longitudinal cracks, transverse cracks, combined longitudinal and transverse cracks, right and left diagonal cracks, alligator (fatigue) cracks, and nondistress. Let $f(m,n)$ be the function of distress in a segmented image R containing M by N pixels and first order moments of the centroid of the shape,

$$M_{p,q} = \sum_m \sum_n m^p n^q f(m,n)$$

$$\overline{m} = \frac{M_{1,0}}{M_{0,0}} = \frac{1}{M * N} \sum \sum m f(m,n)$$

$$\overline{n} = \frac{M_{0,1}}{M_{0,0}} = \frac{1}{M * N} \sum \sum n f(m,n) \tag{11}$$

where $f(m,n) = 1$ for binary images. The moment-based features include the following.

Hu Moments

Hu's approach was proposed in 1962 (*18*). The seven moments up to three orders are

$$\begin{aligned}
HM_1 &= \eta_{2,0} + \eta_{0,2} \\
HM_2 &= (\eta_{2,0} + \eta_{0,2})^2 + 4\eta_{1,1}^2 \\
HM_3 &= (\eta_{3,0} + 3\eta_{1,2})^2 + (3\eta_{2,1} - \eta_{1,2})^2 \\
HM_4 &= (\eta_{3,0} + \eta_{1,2})^2 + (\eta_{2,1} + \eta_{0,3})^2 \\
HM_5 &= (\eta_{3,0} - 3\eta_{1,2})(\eta_{3,0} + \eta_{1,2})[(\eta_{3,0} + \eta_{1,2})^2 - 3(\eta_{2,1} + \eta_{0,3})^2] \\
&\quad + (3\eta_{2,1} - \eta_{0,3})(\eta_{2,1} + \eta_{0,3})[3(\eta_{3,0} + \eta_{1,2})^2 - (\eta_{2,1} + \eta_{0,3})^2] \\
HM_6 &= (\eta_{2,0} - \eta_{0,2})[(\eta_{3,0} + \eta_{1,2})^2 - (\eta_{2,1} - \eta_{0,3})^2] \\
&\quad + 4\eta_{1,1}(\eta_{3,0} + \eta_{1,2}) + (\eta_{2,1} + \eta_{0,3}) \\
HM_7 &= (3\eta_{2,1} - \eta_{3,0})(\eta_{3,0} + \eta_{1,2})[(\eta_{3,0} + \eta_{1,2})^2 \\
&\quad - 3(\eta_{2,1} + \eta_{0,3})^2] + (3\eta_{1,2} \\
&\quad - \eta_{3,0})(\eta_{2,1} + \eta_{0,3})[3(\eta_{3,0} + \eta_{1,2})^2 - (\eta_{2,1} + \eta_{0,3})^2]
\end{aligned} \tag{12}$$

where $n_{p,q} = \sum_m \sum_n (m - \overline{m})^p (n - \overline{n})^q f(m,n)$

Bamieh Moments

The Bamieh moment (*30*) can be expressed by using central moments as shown

$$\begin{aligned}
BM_1 &= \eta_{02}\eta_{20} - \eta_{11}^2 \\
BM_2 &= (\eta_{03}\eta_{30} - \eta_{21}\eta_{12})^2 - 4(\eta_{03}\eta_{12} - \eta_{21}^2)(\eta_{21}\eta_{30} - \eta_{12}^2) \\
BM_3 &= \eta_{40}\eta_{04} - 4\eta_{31}\eta_{13} + 3\eta_{22}^2 \\
BM_4 &= \eta_{40}\eta_{22}\eta_{04} - 2\eta_{31}\eta_{22}\eta_{13} - \eta_{40}\eta_{13}^2 - \eta_{04}\eta_{31}^2 - \eta_{22}^3
\end{aligned} \tag{13}$$

Zernike (Teague) Moments

The Zernike moments (*21*) expressed in terms of usual moments are:

$$ZM_1 = \frac{3}{\pi}\,[2 \times (\eta_{20} + \eta_{02}) - 1]$$

$$ZM_2 = \frac{9}{\pi^2}\,[(\eta_{20} - \eta_{02})^2 + 4(\eta_{11})^2]$$

$$ZM_3 = \frac{16}{\pi^2}\,[(\eta_{03} - 3\eta_{21})^2 + (\eta_{30} - 3\eta_{12})^2]$$

$$ZM_4 = \frac{144}{\pi^2}\,[(\eta_{03} + \eta_{21})^2 + (\eta_{30} + \eta_{12})^2]$$

$$ZM_5 = \frac{13824}{\pi^4}\,[(\eta_{03} - 3\eta_{21})(\eta_{03} + \eta_{21}) \times [(\eta_{03} + \eta_{21})^2 - 3(\eta_{30} + \eta_{12})^2] - (\eta_{30} - 3\eta_{12})(\eta_{30} + \eta_{12}) \times [(\eta_{30} + \eta_{12})^2 - 3(\eta_{03} + \eta_{21})^2]\}$$

$$ZM_6 = \frac{864}{\pi^3}\,\{(\eta_{02} - \eta_{20})[(\eta_{30} + \eta_{12})^2 - [(\eta_{30} + \eta_{21})^2] + 4\eta_{11}(\eta_{03} + \eta_{21}) \times (\eta_{30} + \eta_{12})\} \quad (14)$$

Pavement Image Classification

A backpropagation neural network is used to classify the type of distress based on Hu's seven moment invariants (HM), Zernike's six moment invariants (ZM), and Bamieh's four moment invariants (BM). There are 18 nodes: 4 for BM, 7 for HM, 6 for ZM, and 1 for bias in the input layer, 17 nodes in the hidden layer, and 7 nodes in the output layer to represent seven different types of cracks.

Extent of Pavement Distress

Crack density (D_P) is used as an index of extent in this paper. Originally, the crack density is defined as

$$D_P(\text{crack density}) = \frac{P_M}{P_N} \quad (15)$$

where P_M is the number of distress pixels, and P_N is the total number of image pixels. For example, if the number of distress pixels is 20,000, and the number of total image pixels is 246,784 (482 × 512), then the crack density is 8.1 percent (20,000/246,784 · 100 percent).

Simply using the number of pixels to calculate the crack density causes errors. For example, in a longitudinal crack with broken line segments some pixels are missing in the crack density calculation, and the calculated crack density will be smaller than the actual one. In this paper a modified crack density is used. By assuming that there are B_N numbers of total image blocks in an image and B_M numbers of image blocks containing distress, the crack density (D_B) is defined as

$$D_B(\text{crack density}) = \frac{B_M}{B_N} \quad (16)$$

The modified crack density can prevent problems associated with missing pixels due to image processing.

Image blocks are generated by partitioning a binary pavement image into certain regions. The mean and the variance of the pixel values within each image block are used to determine the existence of distress in that block. For example, if the size of image and image block is 482 × 512 and 48 × 48, respectively, then there are 121 blocks in an image. The crack density is 9.1 percent (11/121 · 100 percent) if there are 11 blocks containing distress.

The relationship between the crack density and a density rating (extent) is shown on Table 1. From this table, an image with crack density between 41 and 80 percent will receive an integer rating of 5 (Table 1).

To reasonably interpret extent of pavement distress using the crack density, the crack density of alligator cracks are treated differently from the other types of distress. With the same crack density value alligator cracks should have a higher extent rating. Alligator cracks are "area" (two-dimensions) types of cracks, and longitudinal and transverse cracks are linear.

There are two ways to handle this problem. Different criteria may be used to select distress image blocks. Otherwise, different density rating tables may be used for alligator cracks but the same criteria in deciding distress image blocks. In this paper, the former approach is used.

RESULTS

Pavement Image Preprocessing

This step is only required when images are darker in the edges. The values of x_e and x_b are derived from 45 sample images. The values of p_1 and p_2 are calibrated from 45 sample images by "trial and error." The results are: p_1 is 2.0, p_2 is 4.0, x_e is 430, and x_b is 100.

Pavement Image Enhancement and Thresholding

Originally 18 combinations of transverse and longitudinal crack images, 14 longitudinal crack images, 13 alligator crack images, 7 transverse crack images, and 7 nondistress images were used. Left and right diagonal cracks were generated by rotating longitudinal and transverse cracks with 45 degrees and 135 degrees, respectively. These original images were rotated by 0.5, 1.0, 1.5, 2.0, 358.0, 358.5, 359.0, and 359.5 degrees to generate more test samples.

Because of nonuniform illumination and background noise in NCHRP images, different a, b, and c values in the Z-membership function are related to the histogram of the images and can be determined by experimentation. In thresholding, the maximum entropy

TABLE 1 The Density Rating

Rate	Density range
0	less than 1%
1	1% to 5%
2	6% to 10%
3	11% to 20%
4	21% to 40%
5	41% to 80%
6	81% to 100%

approach is used to determine threshold values for adaptively thresholding subimages. Two subimages of 256 × 256 and two subimages of 226 × 256 are processed.

Pavement Image Feature Extraction

Moment features based on Bamieh's, Hu's, and Zernike's moments were calculated. Moment values were computed in the format of logarithms with base 10, and then they were normalized and input to the neural network. Figures 3–7 show the result of image processing for longitudinal cracks, transverse cracks, combined longitudinal and transverse cracks, alligator cracks, and nondistress, respectively.

Pavement Image Classification

A backpropagation neural network was used to classify different types of cracks. Figure 8 shows the structure of this neural network.

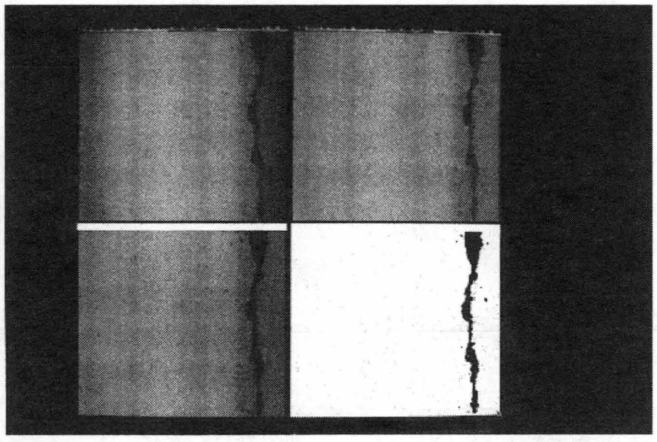

FIGURE 3 Results of longitudinal cracks after image processing (*top left*: original image; *top right*: preprocessed image; *bottom left*: enhanced image; *bottom right*: binary image).

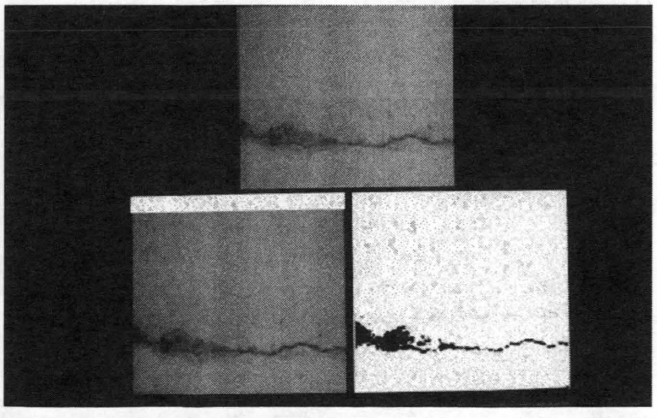

FIGURE 4 Results of transverse cracks after image processing (This image does not require preprocessing) (*top*: original image; *bottom left*: enhanced image; *bottom right*: binary image).

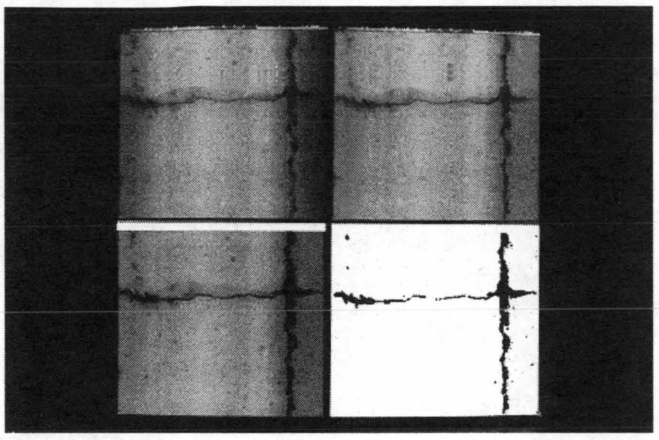

FIGURE 5 Results of combined longitudinal and transverse cracks after image processing (*top left*: original image; *top right*: preprocessed image; *bottom left*: enhanced image; *bottom right*: binary image).

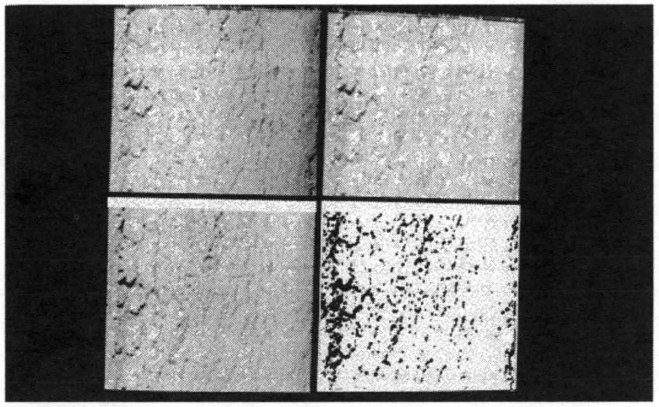

FIGURE 6 Results of alligator after image processing (*top left*: original image; *top right*: preprocessed image; *bottom left*: enhanced image; *bottom right*: binary image).

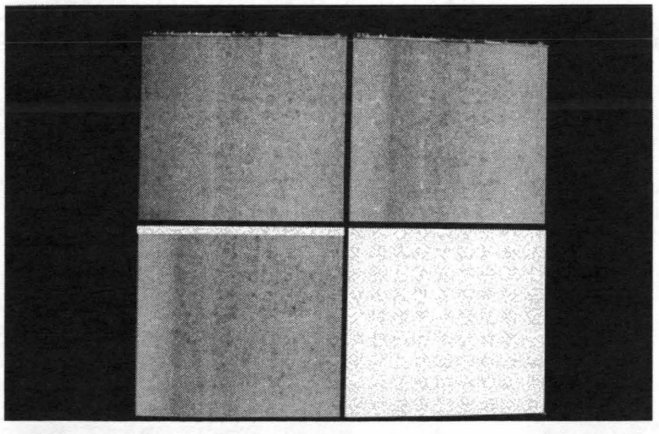

FIGURE 7 Results of nondistress after image processing (*top left*: original image; *top right*: preprocessed image; *bottom left*: enhanced image; *bottom right*: binary image).

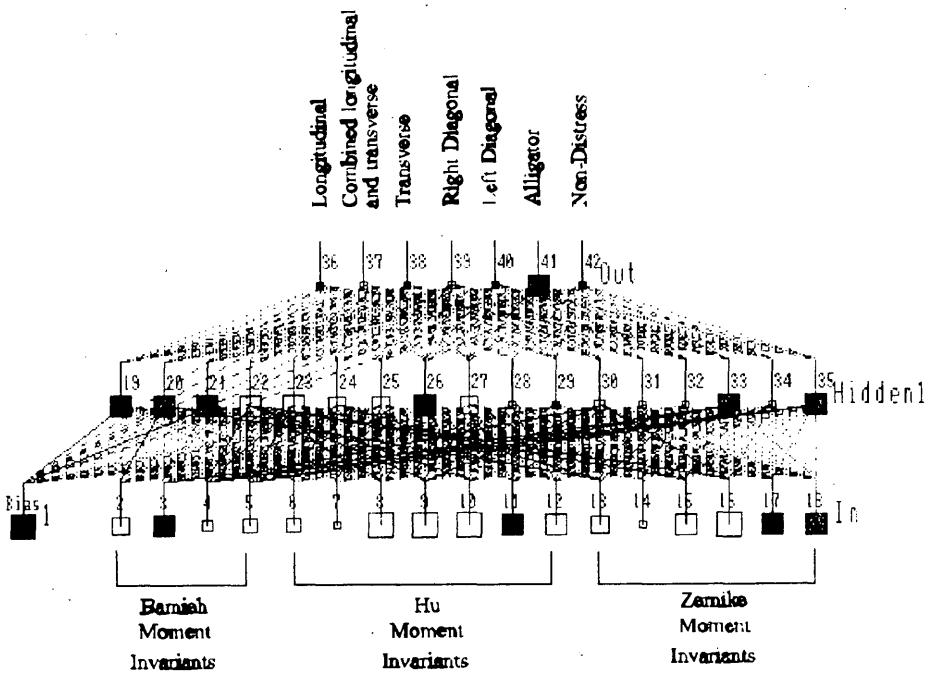

FIGURE 8 The structure of a backpropagation neural network (this figure is generated from NeuralWork's NeuralWare software simulator).

TABLE 2 Comparison of Classification Accuracy

	Chua	Lee	Ritchie	Acosta	Mohajeri	Koutsopoulos	This Research
Transverse	100%	50%[a]	93%	——	——	100%	100%
Longitudinal	100%	100%	96%	——	——	100%	100%
Diagonal	93%	——	——	——	——	——	100%
Alligator	80%	67%	——	——	——	73%	100%
Block	67%	——	——	——	——	33%	——
Combined of longitudinal and transverse	——	——[b]	——	——	——	——	100%
Non-Distress	75%	——	99%	——	——	——	100%
Combined distress	——	——	60%	——	——	——	——
Overall	——	——	——	90%	95%	——	100.00%

[a] Two transverse cracks in an image were considered as transverse cracks here.
[b] These were combinations of longitudinal and transverse cracks. Since there was no template for this type in this paper, it will not be counted here.

TABLE 3 Computation Time Required in Each Step for the Same Image

Procedures	Time required
Image preprocessing	1.5 sec
Image enhancement	9.8 sec
Image segmentation	6.2 sec
Moment calculation	7.8 sec
Neural network classifier	< 1 sec
Total time required	35.3 sec

A total of 126 longitudinal cracks (Class 1), 162 combined longitudinal and transverse cracks (Class 2), 78 transverse cracks (Class 3), 126 right diagonal cracks (Class 4), 126 left diagonal cracks (Class 5), 117 alligator cracks (Class 6), and 42 nondistress (Class 7) were generated. During the learning process, 108 Class 1 samples, 135 Class 2 samples, 68 Class 3 samples, 108 Class 4 samples, 108 Class 5 samples, 99 Class 6 samples, and 36 Class 7 samples were used. The remaining samples were used as the test data. The competition approach (win-and-take) was applied, which means the largest output value in the seven neural output nodes determines the type of distress. For example, a sample is classified as an alligator crack if Node 6 has the largest value.

Table 2 shows the classification result. Every type of distress is classified correctly for these test images used in this research. In terms of computational efforts, Table 3 shows the average computation time required for each step for a single image. This algorithm was implemented using the C language in IBM RS-6000 machine.

Extent of Pavement Distress

The mean and the variance of the pixels within each image block are used to determine the extent of distress in an image block. The size of the image block used in this experiment was 48 × 48 pixels. In alligator cracks distress is evaluated if the mean is smaller than 245 and the variance is greater than 0. For other types of distress, distress extent is evaluated if the mean is smaller than 245 and the variance is greater than 1 (Table 2). Values of the mean (245) and the variance (0 and 1) are found by "trial and error" in this experiment. Table 4 shows results of the density rating. From Table 3, an alligator crack image with a crack density of 65 percent (Image 1)

TABLE 4 The Result of Severity Rating

Image #	Longitudinal		Combined of longitudinal and transverse		Transverse		Alligator	
	Density (%)	Extent Rating	Density (%)	Extent Rating	Density (%)	Extent Rating	Density (%)	Extent Rating
1	11	3	25	4	12	3	65	5
2	17	3	21	4	22	4	39	4
3	11	3	21	4	26	4	31	4
4	12	4	22	4	22	4	40	4
5	14	3	17	3	22	4	86	6
6	12	3	26	4	25	4	74	5
7	12	3	20	3	17	3	69	5
8	8	2	21	4	26	4	69	5
9	9	2	17	3			52	5
10	10	2	18	3			89	6
11	8	2	17	3			71	5
12	7	2	17	3			41	5
13	7	2	21	4			64	5
14	9	2	28	4				
15			23	4				
16			24	4				
17			19	3				
18			20	3				

will have an extent rating of 5, and a combined longitudinal and transverse crack with a crack density of 17 percent (Image 2) will have an extent rating of 3.

CONCLUSIONS

A fuzzy enhancement algorithm, moment invariant features, and neural networks were used to classify pavement cracks (alligator cracks, longitudinal cracks, transverse cracks, combinations of longitudinal and transverse cracks, diagonal cracks, and nondistress). Moment invariants are shown to be feasible for pavement crack classification. Although the shape of pavement crack is irregular and fuzzy, which results in the loss of invariant properties, moment invariants still perform well. The extracted features are input to the neural network, and the classification accuracy is quite satisfactory. Using different criteria in the crack density to determine severity between alligator and other types of cracks provides more reasonable results.

REFERENCES

1. Baker, J., B. Dahlstrom, K. Longenecker, and T. Buu. Video Image Distress Analysis Technique for Idaho Transportation Department Pavement Management System. *Transportation Research Record 1117*, TRB, National Research Council, Washington, D.C., 1987, pp. 159–163.
2. Caroff, G., P. Joubert, F. Prudhomme, and G. Soussain. Classification of Pavement Distress by Image Processing. *Proc., First International Conference on Applications of Advanced Technologies in Transportation Engineering*, ASCE, San Diego, Calif., 1989, pp. 46–51.
3. Fukuhara, T., K. Terada, M. Nagao, A. Kasahara, and S. Ichihashi. Automatic Pavement-Distress-Survey System. *Journal of Transportation Engineering*, ASCE Vol. 116, No. 3, 1990, pp. 280–286.
4. Mohajeri, M. H., and Patrick J. Manning, ARIA: An Operating System of Pavement Distress Diagnosis by Image Processing. *Transportation Research Record 1311*, TRB, National Research Council, Washington, D.C., 1991, pp. 120–130.
5. Li, L., P. Chan, and R. L. Lytton. Detection of Thin Cracks on Noisy Pavement Images. *Transportation Research Record 1311*, TRB, National Research Council, Washington, D.C., 1991, pp. 131–135.
6. Ritchie, S. G., M. Kaseko, and B. Bavarian. Development of an Intelligent System for Automated Pavement Evaluation. *Transportation Research Record 1311*, National Research Council, Washington, D.C., 1991, pp. 120–130.
7. Acosta, J. J. Adolfo, L. Figueroa, and R. L. Mullen. Low-Cost Video Image Processing System for Evaluating Pavement Surface Distress. *Transportation Research Record 1348*, TRB, National Research Council, Washington, D.C., 1992, pp. 63–72.
8. Koutsopoulos, H. N., and A. B. Downey. Primitive-Based Classification of Pavement Cracking Images. *Journal of Transportation Engineering*, ASCE, Vol. 119, No. 3, pp. 402–418, 1993.
9. Chua, K.-M., and L. Xu. Simple Procedure for Identifying Pavement Distress from Video Images. *Journal of Transportation Engineering*, ASCE, Vol. 120, No. 3, pp. 412–431.
10. Pal, S. K., and R. A. King. Image Enhancement Using Smoothing with Fuzzy Sets. *IEEE Transactions on Systems, Man, and Cybernetics*, Vol. 11, No. 7, 1981, pp. 494–501.
11. Pal, S. K. A Note on the Quantitative Measure of Image Enhancement Through Fuzziness. *IEEE Transactions on Pattern Analysis and Machine Intelligence*, Vol. 4, No. 2, 1982, pp. 204–208.
12. Pal, S. K., and A. Ghosh. Fuzzy Geometry in Image Analysis. *Fuzzy Sets and Systems*, Vol. 48, 1992, pp. 23–40.
13. Pal, S. K., and A. Rosenfeld. Image Enhancement and Thresholding by Optimization of Fuzzy Compactness. *Pattern Recognition Letter*, Vol. 7, 1988, pp. 77–86.
14. Pal, S. K., R. A. King, and A. A. Hashim. Image Description and Primitive Extraction Using Fuzzy Sets. *IEEE Transactions on Systems, Man, and Cybernetics*, Vol. 13, No. 1, 1983, pp. 94–100.
15. Keller, J. M., and C. L. Carpenter. Image Segmentation in the Presence of Uncertainty. *International Journal of Intelligent Systems*, Vol. 5, 1990, pp. 193–208.
16. Zhao, Z., X. Li, and H.D. Cheng. An Effective Fuzzy Logic Approach to Image Enhancement. *SPIE Visual Communication and Image Processing*, Vol. 2094, 1993, pp. 244–251.
17. Huntsberger, T. L., C. L. Jacobs, and R. L. Cannon. Iterative Fuzzy Image Segmentation. *Pattern Recognition*, Vol. 18, No. 2, 1985, pp. 131–138.
18. Hu, M.-K. Visual Pattern Recognition by Moment Invariants. *IRE Transactions on Information Theory*, Vol. 8, 1962, pp. 179–187.
19. Noll, R. J. Zernike Polynomials and Atmospheric Turbulence. *Optical Society American Journal*, Vol. 66, No. 3, 1976, pp. 207–211.
20. Reddi, S. S. Radial and Angular Moment Invariants for Image Identification. *IEEE Transactions on Pattern Analysis and Machine Intelligence*, Vol. 3, No. 2, 1981, pp. 240–242.
21. Teague, M. R. Image Analysis via the General Theory of Moments. *Optical Society American Journal*, Vol. 70, No. 8, 1980a, pp. 920–930.
22. Teague, M. R. Optical Calculation of Irradiance Moments. *Applied Optics*, Vol. 19, No. 8, 1980b, pp. 1353–1356.
23. Abu-Mostafa, Y. S., and D. Psaltis. Recognitive Aspective of Moment Invariants. *IEEE Transactions on Pattern Recognition and Machine Intelligence*, Vol. 6, No. 6, 1984, pp. 698–706.
24. Abu-Mostafa, Y. S., and D. Psaltis. Image Normalization by Complex Moments. *IEEE Transactions on Pattern Recognition and Machine Intelligence*, Vol. 7, No. 1, 1985, pp. 46–55.
25. Maitra, S. Moment Invariants. *Proceedings of the IEEE*, Vol. 67, No. 4, 1979, pp. 697–699.
26. Hsia, T. C. A Note on Invariant Moments in Image Processing. *IEEE Transactions on System, Man, and Cybernetics*, Vol. 11, No. 12, 1981, pp. 831–834.
27. Chou, J., W. A. O'Neill, and H. D. Cheng. Evaluation of Pavement Distress Image Using Artificial Neural Networks. accepted by *27th International Symposium on Advance Transportation Applications*, Oct. 31–Nov. 4, 1994a, Aachen, Germany.
28. Chou, JaChing, W. A. O'Neill, and H. D. Cheng. Pavement Distress Classification Using Neural Networks. Presented at *IEEE International Conference on Systems, Man, and Cybernetics*, San Antonio, Tex., 1994.
29. Lindley, C. A., *Practical Image Processing in C*. John Wiley & Sons, Inc., New York, 1991.
30. Belkasim, S. O., M. Shridhar, and M. Ahmadi. Pattern Recognition with Moment Invariants: A Comparative Study and New Results. *Pattern Recognition*, Vol. 24, No. 12, 1991, pp. 1117–1138.

Publication of this report sponsored by Committee on Pavement Monitoring, Evaluation, and Data Storage.

Automated System for Pavement Profile Analysis from Profilograph Traces

JOHN DEVORE, MUSTAQUE HOSSAIN, AND WILLIAM H. PARCELLS, JR.

An automated method, KSCAN, for reduction of the profilograms produced by the mechanical profilograph into a profile index (PRI) and for identification of bump locations for grinding has been developed. The algorithm followed was the Kansas Test Method KT-46I: Determination of Pavement Profile with the 7.62 m (25-ft) Profilograph. The profilograph trace is scanned to digitize its tracing. An image enhancement program is used to prepare the image for analysis, and then a line is identified, tracked, and digitized. A linear regression analysis is performed to establish the location of the "floating" centerline (corresponding to a "null" or "zero" blanking band) along this line. The PIs are calculated based on deviation of the line from the floating centerline, and bumps are located based on any specified deviation from a 25.4 mm (1-in.) reference moving baseline. Options are available to incorporate blanking band widths of any value into the PRI calculations. Comparison of the results of profile reduction using the manual methods, automated profilographs, and KSCAN showed that KSCAN results should easily satisfy the KT-46I requirement that the results of comparison between manual trace reduction by the Kansas Department of Transportation and automated trace reduction should not differ by more than 32 mm/km (2 in./mi) on a segment by segment basis (0.16 km or 0.1 mi). Extensive tests indicated that the PRI computed by the KSCAN for a given segment generally varied less than ±3 percent from scan to scan, and five or more successive segments showed totals that rarely differed by more than ±1 percent. The process has been implemented on a personal computer, and an assembled system consisting of the software, the special scanning hardware, an IBM-compatible 486 computer, and a printer costs under $7,500.

Pavement smoothness/roughness can be described by the magnitude of profile irregularities and their distribution over the measurement interval. The road surface smoothness on newly constructed pavement is a major concern for the highway industry. This "smoothness" or "riding comfort" is a measure of the quality of the newly constructed pavements because it affects the road users directly. According to Hudson (*1*), the purposes for smoothness measurement are:

1. To maintain construction quality control,
2. To locate abnormal changes in the highway, such as drainage, subsurface problems, or extreme construction deficiencies,
3. To establish a statewide basis for allocation of road maintenance resources, and
4. To evaluate pavement serviceability performance life histories for evaluation of alternate designs.

Since its introduction in 1940, the profilograph has successfully been used to date for the measurements of pavement profile for the construction control of concrete pavements. It was later extended for as-constructed smoothness control of bituminous pavements. The profilograph is a multi-wheeled, rolling straightedge and is propelled by hand. It measures the vertical deviations from a moving, fixed-length reference plane. The result of this test is usually a graphical record, a profilogram or profilograph trace, which indicates the smoothness of a newly paved surface. The scale of the profilogram is usually 1:300 horizontally (longitudinally) and 1:1 vertically. The profilogram is interpreted by an operator/interpreter using a blanking band and a bump template. The blanking band, a plastic scale 43.18 mm (1.70 in.) wide and 536.4 mm (21.12 in.) long, represents a pavement length of 161 m (528 feet) or 0.161 km (1/10 mi). An opaque band of 5.08 mm (0.2 in.) width extends throughout the entire length of the plastic scale near the center. On either side of this band are scribed lines 2.54 mm (0.1 in.) apart, parallel to the opaque band. These lines serve as a convenient scale to measure deviations of the profile trace or "scallops" above and below the blanking band. The bump template is a plastic template having a marked length 25.4 mm (1 in.) long on one face and a slot (or edge) parallel to the marked length. A distance equal to the maximum bump specified, normally 10.16 mm (0.40 in.), separates the two reference lines. The 25.4-mm (1.0-in.) line corresponds to a distance of 7.62 m (25 ft) on the longitudinal scale of the profilogram. The bump template and the blanking band are used for identifying locations of bumps and total deviation from "true" surface in inches/mile, the profile index (PRI), respectively.

Three uniquely different designs for the profilograph are available; California-style, Ames, and Rainhart. Currently, profilographs are manufactured by three companies: (*a*) Ames Profilograph of Ames, Iowa, (*b*) International Pipe Machinery Corporation (McCracken Division) of Sioux City, Iowa, and (*c*) Cox and Sons of Colfax, California. The latter two also manufacture automated or "computerized" profilographs. The outlining procedure used by the manual operator during the profile trace reduction process is accomplished within the computer program by the use of "filters." The blanking band is simulated using offsets from the best-fit centerline, and "deviations" are computed. These devices have become very popular despite higher initial prices (2).

PROBLEM STATEMENT

The road surface smoothness on newly constructed pavement is a major concern for the highway industry. This smoothness or riding comfort indicates the quality of newly constructed pavements because it affects the road users directly. There is a growing interest in attaining smoother pavement surfaces. Results from a 1992 NCHRP study show that of the 22 states reporting, 91 percent used smoothness criteria on new pavement construction (2).

J. Devore and M. Hossain, Department of Electrical and Computer Engineering and Civil Engineering, Kansas State University, Manhattan, Kans. 66506. W. H. Parcells, Jr., Kansas Department of Transportation, Bureau of Materials and Research, Materials and Research Center, 2300 Van Buren, Topeka, Kans. 66611-1195.

The Kansas Department of Transportation (KDOT) uses a 7.62-m (25-ft) California-type profilograph for determining the smoothness of both concrete and bituminous pavements. Within KDOT, the applicable procedure for identifying locations of bumps and total deviation from true surface in millimeters/kilometer (inches/mile), the PRI, is Kansas Test Method KT-46I: Determination of Pavement Profile with the 7.62-m (25-ft) Profilograph (*3*). Currently this procedure requires the use of a 0 (0.254 mm/0.01 in. for the computerized profilograph) banking band width (or "null" blanking band). With the null blanking band, a reference line placed approximately at the center of the trace is used as a datum for finding deviations from it. This process is very labor intensive and time consuming. The results also vary among operator/interpreters. The relatively high incentives now possible with many of the smoothness specifications place an ever-increasing burden not only on the measurement process but also on the data-reduction process. Variability in test results and interpretation of test results can significantly affect contractor payments (*2*).

According to the 1992 NCHRP study (*2*), the top 10 problems regarding smoothness measurement and interpretation of test results faced by the states are:

1. Comparing profilograph results with other roughness measuring devices,
2. Trace reduction repeatability,
3. Effect of surface type (e.g., short wavelengths on PRI),
4. Interpretation of profilograph traces,
5. Production rate of testing,
6. Equipment repeatability,
7. Operator training,
8. Comparing profilograph results with present serviceability index,
9. Identifying grinding locations, and
10. Ease of operation.

Significant differences between PRI obtained from manual interpretation of profilograph traces and those obtained by profilographs that use on-board computers for interpretation have been observed recently. A 1990 study by the Arizona Department of Transportation has shown that 67 percent of the total operator profilogram interpretation variability was due to the difference between the operators and the repeated trace reductions. There was more variability between the average values among operators than there was variability between the two readings of a single operator (*4*). A Pennsylvania Transportation Institute study in 1989 reported that the variations among operators in profilogram reductions were the same size as the total variations of multiple runs with one person interpreting the data (*5*). It is well established that the major cause of variability in mechanical profilograph test results is the manual interpretation of results.

Since 1987 the Central Federal Lands Highway Division in Denver, Colorado has extensively studied the acceptance of newly constructed bituminous pavements using California-type profilograph measurements (*6*). The study concludes that, when used in conjunction with statistical evaluation procedures, the test method is suitable for acceptance purposes and that computerized trace reduction is superior to manual reduction.

From this discussion, it is clear that there is need for an automated system for interpretation of profilograms. Bonus clauses are associated with pavement smoothness, so it is important that a more rational methodology of interpretation of profilograms be developed.

OBJECTIVE

The major objective of this study was to automate the profilograph trace reduction process. The algorithm was that described in Kansas Test Method KT-46I: Determination of Pavement Profile with the 7.62-m (25-ft) Profilograph. This objective was accomplished by selecting the hardware and developing the software necessary for computation of the PRI and by identification of locations of bumps for grinding.

CURRENT KDOT SMOOTHNESS SPECIFICATIONS

Based on the results of the study of profilographs on both concrete (PCC) and bituminous (AC) pavements from 1985 to 1991, a new set of special provisions was incorporated for construction projects in 1992. The PCC pavements will have the Special Provision 90P-111-R1. This requires use of the null blanking band (or 0.254 mm or 0.01 in. for computerized profilographs) for profilograph trace reduction and establishes the limits on calculated PRI as shown in Table 1. Special Provision 90P-39-R4, incorporated for AC pavement projects, also requires the use of "null" or "zero" blanking band for mechanical profilographs or 0.254-mm (0.01-in.) blanking band for computerized profilographs. The schedule for adjusted payments at various levels of roughness is shown in Table 2. This requirement is applicable to all projects with multiple paver passes, including cold milling with overlay or cold recycle with an overlay. The working depth in those cases may be less than 101.6 mm (4 in.). However, pay adjustment does not apply if the plan thickness is less than 101.6 mm (4 in.) on the existing surfaces (*7*). The implementation of these special provisions resulted in the critical need for fast reduction of profilograph traces for KDOT. This is more important for AC pavements, for which the contractor needs to know within 24 hours whether or not corrective action needs to be taken. The agency also needs to verify the results quickly. It will be difficult for the contractor crew for trace reduction to keep up with the pace of paving, especially for AC, without interrupting the construction. This leads to the need for an automated trace reduction procedure so that the results can be obtained very quickly. The results also are expected to be more reproducible.

DEVELOPMENT OF THE AUTOMATED METHOD FOR PROFILE REDUCTION

Approach

An automated method, KSCAN, for reduction of profilogram into PRI and for identifying locations of bumps for grinding following the algorithm in Kansas Test Method KT-46I: Determination of Pavement Profile with the 7.62-m (25-ft) Profilograph was developed in this study. The approach for automating these tasks began with an image-processing step to convert the strip-chart traces into one-dimensional signals. The profilograph trace was scanned to digitize its tracing. An image enhancement program was used to prepare the image for analysis. After enhancement, a line was tracked using a noncausal moving-average filter to reduce the problem to a single dimension. This simulates the process in which a human operator usually draws a line to outline the trace. A linear regression analysis was used to establish the location of the floating centerline (corresponding to the null blanking band). The PRIs were

TABLE 1 Schedule for Adjusted Payment for PCC Pavements (Special Provision 90P-111-R1)

Profile Index millimeter per kilometer per 0.16 kilometer section (> 72 km/h speed limit)	Profile Index millimeter per kilometer per 0.16 kilometer section (72 km/h or less speed limit & ramps)	Price Adjustment Percent of Contract unit bid price
175 or less	238 or less	108
176 to 238	239 to 397	104
239 to 476	398 to 715	100
477 to 794	716 to 1032	100 (Grind back)
795 or more	1033 or more	95 (Grind back or remove and replace)

Note : 1 in = 25.4 mm, 1 mile = 1.6 km

calculated based on deviations from the floating centerline, and bumps were located based on the specified deviation from a 25.4-mm (1-in.) reference moving baseline. Options are also available to incorporate blanking bands of any value (0 to 10.6 mm or 0 to 0.4 in. or higher) into the calculations.

Hardware

The digitizer for this project was a hand-operated 101.6-mm (4-in.) wide 400-dpi gray scale scanner. Two different hand scanners, ScanMan Model 32 and Matador Plus, were evaluated. Both scanners worked satisfactorily with the supplied software on an IBM-compatible 486 PC for short distances, but the supplied software was not flexible enough for the length of scans required. A software development kit for the ScanMan scanner provided the support needed to write the customized scanning programs (in "C") that can scan unlimited lengths of a trace. Therefore, the ScanMan model 32 hand scanner was selected for the digitizing device. The scanner interfaces to a 486 IBM-compatible PC compatible computer through a board that fits in an Instrument Society of America expansion slot. The scanner is operated in a 200-dpi mode for KSCAN.

Filter Selection

Several filters were tested for preprocessing of the profilograph traces once they had been digitized by the hand-held scanner and extracted using the software developed for that purpose. The filtering was necessary because of the noisy nature of the traces due to vibrations in the profilograph during the recording process (e.g., due to debris).

It is to be noted that a degree of filtering occurs in the mechanical system that provides the trace on paper from movement of the

TABLE 2 Schedule for Adjusted Payment for AC Pavements (Special Provision 90P-39-R4)

Profile Index (mm per km)	Contract Price Adjustment* (Dollars)
110 or less	+ 152.00
111 to 158	+ 76.00
159 to 473	0.00
474 to 631	0.00 (correct back to 473 mm/km or less)
632 to more	-203.00 (correct back to 473 mm/km or less)

* applies to each 0.16 lane-km segment

Note : 1 in = 25.4 mm, 1 mile = 1.6 km

pickup wheel. Also high-speed chatter in the system results in a thicker line rather than distinguishable back and forth movement of the pen. Thus, it does not follow that filtering of a scanned trace should be identical to filtering used in computerized profilographs that obtain unfiltered data from the pickup wheel.

In fact the stated purpose of filtering the data on those systems is to try to duplicate the effect of a person drawing a single line through mechanically produced profilograph trace. Therefore, in this project, we attempted to duplicate that same effect, rather than just filtering this scanned data the same way the computerized units filter raw data. A variety of filtering algorithms were tried, and KDOT personnel picked the one that worked the best. The judging was performed by looking at plots of the various filtered signals overlaid on the original traces using a light table. To our knowledge similar tests of comparing raw data with the filtered output have never been attempted for the automated units.

A variety of Butterworth and Chebyshev low-pass filters with various number of poles and cut-off frequencies were included in the tests, but all were judged inferior to a simple two-sided moving average filter. Also, moving-average filters of various widths were tested. A noncausal, moving-average filter, with a window of 1.91 mm (0.075 in.) (0.57 m or 22.5 in. of pavement) was judged to be the best and was incorporated as the default into the automated trace reduction process. A least-square error analysis was done to fit a straight line to the data points on the 1/10-mi segment. Plot drivers were created for both Epson and Toshiba printers to reproduce the scanned traces along with the best-fit straight line through the data.

Trace Reduction Procedure

The trace information was captured using a hand scanner. Early in the project, the scanner was pulled along the segment with the aid of a straightedge. Later a computer-controlled paper transport unit was developed to automate that process. KDOT now uses these units, which can process unlimited length traces without operator interventions.

During the scanning process the image being scanned will scroll by on the computer monitor. The scanning process is the most important part of the user's interaction with the program. A section to be scanned is marked by drawing a 25.4-mm (1-in.) (or longer) line across the two ends of the section. The length of the section that is marked can be a normal segment or a short segment or can encompass many segments. The scanner itself measures the distance covered so that correct PRI values are calculated for any length. If multiple segments exist between the two marks, the system automatically measures each segment (0.16 km or 0.1 mi) and calculates a PRI value for each segment as well as the entire section. The standard length of a segment is easily changed in a configuration file.

The marking of a section is much the same as marking the individual segment during manual reduction, except that the vertical position of the rule and each segment need not be marked. It is important that the lines marking the end of the segment be perpendicular to the length of the profilogram. This is necessary because the scanner "sees" only a 0.127-mm (1/200-in.) wide strip of the paper at a time, and this strip is perpendicular to the edges of the paper. The program "recognizes" an end mark when a 25.4-mm (1-in.) high (or longer) dark region of that strip is centered (or nearly centered) about the position of the line it has been tracking. If the mark is misaligned by several degrees from the scanner head, the scanner may never see the entire mark during a single strip of the image.

The scanning process takes about 22 sec/0.16-km (0.1-mi) segment. Once the trace of a set of segments has been scanned, the user is given the option of repeatedly analyzing it under a variety of options. Any given analysis may be plotted on a printer so that an annotated record of the analysis is produced. All scanned information is written to a disk file so that it can be read in later for further analysis. Figure 1 illustrates the original and scanned traces of a certain pavement section.

Specifying Reduction Parameters

Several of the reduction parameters are specified interactively during the time that the program is running and the scanning is done. These parameters are the ones that the user may wish to change from one value to another during the processing of a single section of the trace. One such parameter is the blanking band size. For example, the user may wish to reduce a segment under both a 0- and 5.1-mm (0.2-in.) blanking band. Other reduction parameters are constant within one execution of the program and are contained in a special configuration file. These are read by the program when it is first started and are used for all segments processed until the program is terminated. Examples of this type of parameter are the length of a normal length segment and the resolution of scallop height measurements.

RESULTS AND DISCUSSIONS

Comparison with Existing Methods

Nine different traces with average PRI values between 24 mm/km (1.5 in/mi) and 142 mm/km (9.0 in/mi) as determined by the Cox and Sons automated profilograph from a set of 19 0.16-km (0.1-mi) segments of AC were selected for this study. These traces, supplied by Jerry L. Budwig, Division Administrator of the Central Federal Lands Highways Division (CFLHD) in Denver, Colorado, represent the 19 sublots used in profilograph trace reduction study conducted by CFLHD (*6*). In that study, the 19 sublots (Project A) were subdivided to create two additional projects; that is, the nine smoothest sublots formed one of the additional projects (Project B), and the 10 roughest formed the other (Project C). In this study, the smoothest sublots (Project B) were chosen because the range of PRI values of these traces was found to be representative of the smoothness values achieved by the contractors on AC in Kansas. Also, the PRIs of these traces represent the values that are usually harder to reproduce consistently by manual method.

The selected traces were reduced by KSCAN and compared with the results obtained by CFLHD. The CFLHD results were from 14 experienced operators as well as from the programs used in the computerized profilographs (McCracken and Cox and Sons). Table 3 tabulates the results of the comparison for these segments.

In Table 3, the PRI values in the second column were found by averaging the results produced by the Cox and Sons and McCracken automated profilographs. Columns 3 and 5 are the KSCAN results at two standard resolutions. These are 1.27 mm (0.05 in.) and 0.25 mm (0.01 in.), respectively. Columns 4 and 6 show the difference between the KSCAN values and the values for automated profilographs in Column 2. The corresponding values in Row 9 are for the

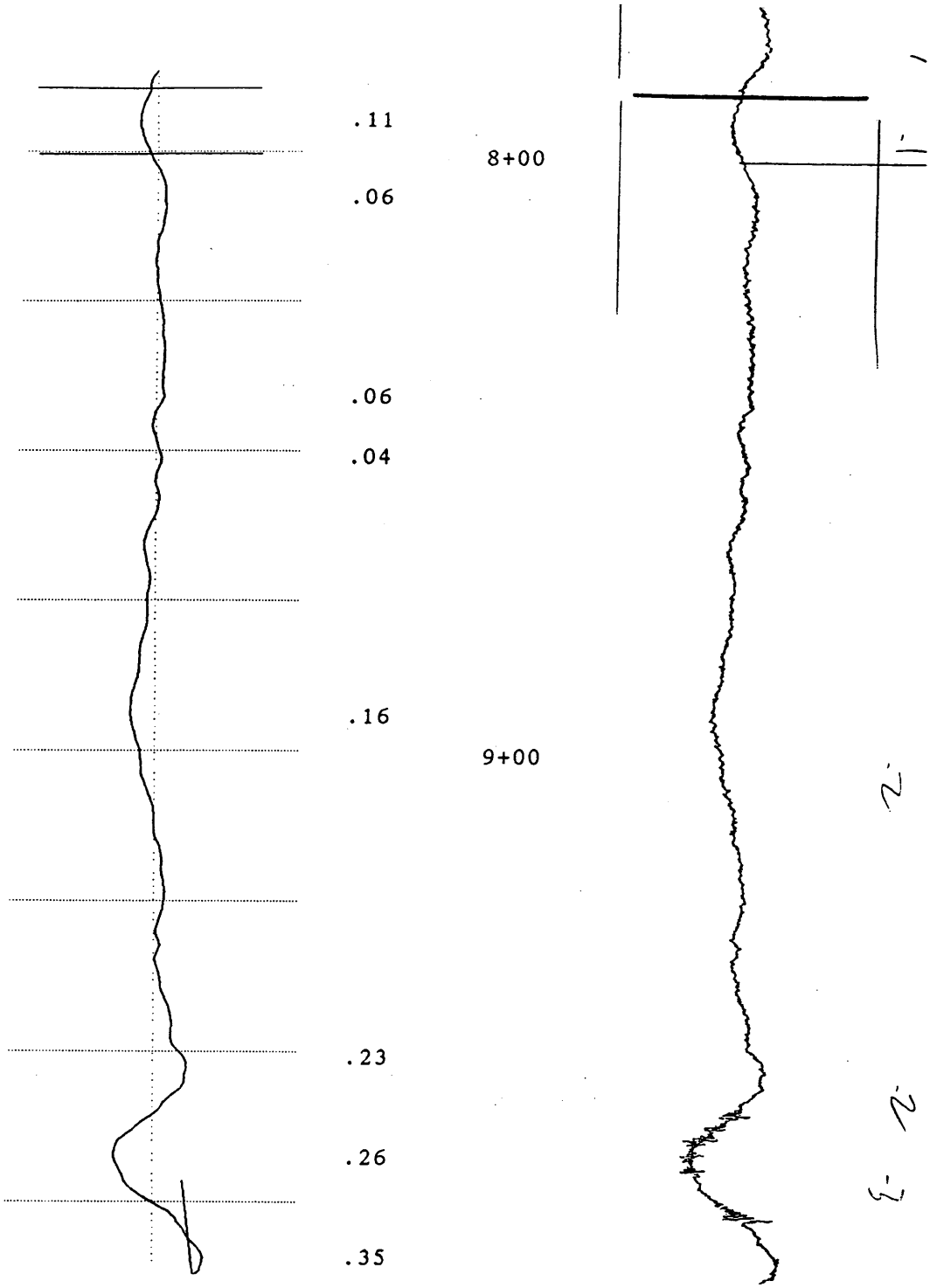

FIGURE 1 Original and scanned traces of a pavement section.

entire nine segments considered together. Row 11 gives PRI differences found by averaging the magnitudes of the segment-by-segment differences. This tends to better reflect the average variation than Row 10, which gives the overall difference. The last row shows the magnitude of the worst-case difference in the nine segments. All of these differences are quite small. However, these results indicate that the KSCAN results show better agreement with the automated profilograph results when the calculations are rounded to 0.254 mm (0.01 in.) instead of 1.27 mm (0.05 in.). A smaller resolution (rounding to the larger value) simply introduces random noise in the trace reduction or PRI computation process, which has no effect on very large sections but has increasing impact as the length decreases. KSCAN PRI values with higher resolution (rounding to a smaller value) are used in the later analysis.

TABLE 3 Comparison of Different Methods of Trace Reduction (KSCAN Resolution = 1.27 mm or 0.05 in.)

Segment No. / CFLHD Segment No.	PRI (mm/km)				
	Automated Profilo-graphs*	KSCAN (Resolution =1.27 mm)	Difference	KSCAN (Resolution =0.254 mm)	Difference
1/1	24	16	-8	22	-2
2/3	83	63	-20	82	-1
3/4	122	110	-12	115	-7
4/10	110	103	-7	101	-9
5/12	71	71	0	66	-5
6/13	87	87	0	98	+11
7/17	142	142	0	140	-2
8/18	114	110	-4	106	-8
9/19	79	79	0	76	-3
Set	93	87	-6	90	-3
Avg. of Abs. Diff.			6		4
Max. of Abs. Diff.			20		11

* Average of Cox & Sons and McCracken results
Note : 1 in/mile = 15.78 mm/km

Table 4 compares manual trace reduction with automated reduction of traces, and Figure 2 illustrates the average PRI for the entire section computed by different methods and KSCAN with different resolutions. Column 2 of Table 4 gives the average value of the PRI found by the 14 experienced operators cited in the CFLHD study. The next two columns give information about the considerable variations between the reducers. Columns 5 and 7 show corresponding computer generated values, and 6 and 8 show the respective differences between the values in those columns and the average of the manual reductions. Again, as in Table 3, the last three rows show information about the complete set of nine segments. This table shows very good agreements between the computer reductions and the average manual reductions. The PRI values for the automated profilographs and the KSCAN, in no case, vary more than 17 mm/km (1.08 in/mi) and 12 mm/km (0.76 in/mi), respectively. The values in the last two rows are important relative to the KT-46I test method cited earlier. KT-46I requires that for a given test track, the automated PRI values and manual PRI values vary by no more than 32 mm/km (2 in/mi). Both sets of automated results in Table 4 satisfy this requirement. The worst-case values were 53 percent (Segment 4 for automated) and 38 percent (Segment 7 for KSCAN) of the allowable deviations. The entire-set difference of 3 mm/km (0.02 in/mi) for KSCAN shown for the entire 1.45-km (0.9-mi) section is virtually 0. The sum of all the scallops found in this section differed by less than 4.5 mm (0.2 in.) when comparing the experienced operator average with

TABLE 4 Comparison of Different Methods of Trace Reduction (KSCAN Resolution = .254 mm or 0.01 in.)

Segment No.	PRI (mm/km)						
	Expert Operators			Automated Profilographs*		KSCAN (Resolution = 0.254 mm)	
	Avg.	Std. Dev.	Range	Avg.	Diff.	Value	Diff.
1	33	15	16-71	24	-9	22	-11
2	85	18	55-118	83	-2	82	-3
3	110	13	95-150	122	12	115	5
4	93	13	71-118	110	17	101	8
5	70	9	55-87	71	1	66	-4
6	88	30	55-142	87	-1	98	10
7	128	19	95-166	142	14	140	12
8	107	21	63-142	114	7	106	-1
9	68	15	47-95	79	11	76	8
Set	87			93	6	90	3
Avg. of Abs. Diff.					8		7
Max. of Abs. Diff.					17		12

* Cox & Sons and McCracken automated profilographs
Note: 1 in/mile = 15.78 mm/km

KSCAN. This is less than the amount a manual operator rounds each scallop!

Repeatability of Scanning Process (5.08-mm or 0.2-in blanking band)

Table 5 shows the results from the two different runs of trace reduction using a 5.08-mm (0.2-in.) blanking band on the nine 0.16-km (0.1-mi) segments used earlier. The results show little or no difference in the PRI values from the two runs. More extensive tests indicated that the PRI computed by the KSCAN for a given segment generally varied less than ±3 percent from scan to scan, and five or more successive segments showed totals that rarely differed by more than ±1 percent.

Effect of Filtering on the Computation of PRI

Table 6 shows the effect of filtering on the PRI computation of the nine segments. The difference varies from 0.0 mm/km (in./mi) or 0 percent to 15.78 mm/km (1.0 in./mi) or 10.6 percent for these segments. A shorter than normal filter (KSCAN Filter 5, which averages only five consecutive points instead of the normal 15) was used to reduce the trace. This resulted in less smoothing of the scanned data and thus higher PRI

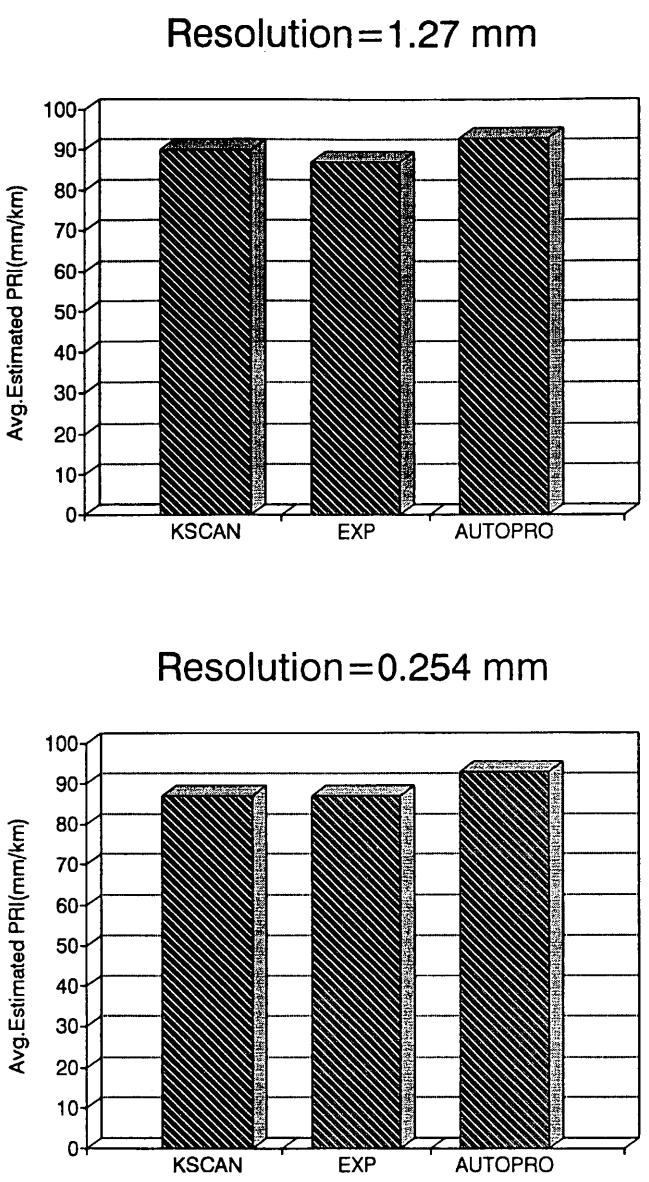

FIGURE 2 Computed PRI values by different methods and KSCAN (with different resolutions).

values. However, KSCAN is normally configured to use a longer (15) filter.

Determination of Location of Bumps

The methodology followed in locating bumps is similar to that of the Cox and Son's automated profilograph (*8*). According to KT-46I, a 10.2-mm (0.4-in.) bump template needs to be used for locating bumps. KSCAN uses a mathematical scheme to locate the bumps with a moving 7.6-m (25-ft) (25.4 mm or 1-in. on the digitized trace) baseline. Normally the template is set at 7.6 m (25 ft) (25.4 mm or 1 in.) in length and 10.2 mm (0.40 in.) in height. The equation for a line between each data point and the data for a point 7.6 m (25 ft) away is calculated. The data point that is the furthest above the line in that 7.6-m (25-ft) length is found. This is repeated for each data point in the segment being processed. Each maximum of this set of values that is greater than the specified grind height (10.16 mm or 0.4 in. in Kansas) represents a must grind location.

It should be noted that this procedure of bump location by KSCAN varies from the manual reduction process as suggested by KT-46I. The manual reduction process uses a fixed length plastic template, so it will measure the correct distance when the 25.4-mm (1-in.) line is horizontal. However, when steep lines are used to match the bump, the angle of the template combined with the highly exaggerated vertical scale causes the plastic template to measure less than the desired running length and less than the desired height. The KSCAN procedure uses the 25.4-mm (1-in.) horizontal distance and 10.16-mm (0.4-in.) vertical height regardless of the slope of the trace. This may sometimes result in the detection of bumps that could go undetected in the manual method.

CONCLUSIONS

An automated method (KSCAN) for reduction of the profilogram produced by the mechanical profilograph into a PRI and for identification of bump locations for grinding has been developed. The algorithm followed was the Kansas Test Method KT-46I: Determination of Pavement Profile with the 7.62-m (25-ft) Profilograph. The profilograph trace was scanned to digitize its tracing. An image enhancement program was used to prepare the image for analysis, and then a line was identified and digitized. A linear regression analysis was performed to establish the location of the floating centerline (corresponding to a null or 0 blanking band) along this line. The PRI were calculated based on deviation of the trace line from the floating centerline, and bumps were located based on the specified deviation from a 25.4-mm (1-in.) reference moving baseline. Parameters such as blanking band width and bump template height can be varied by the operator to conform to the existing specifications.

Comparison of the results of profile reduction for nine, smooth, 0.16-km (0.1-mi) segments using the manual methods, automated profilographs, and KSCAN showed that KSCAN results easily satisfy the KT-46I requirement and that the results of comparison between manual trace reduction by the KDOT and automatic trace reduction should not differ by more than 32 mm/km (2 in./mi). It appeared that KSCAN results showed better agreement with the automated profilograph results when the calculations were rounded to 0.25 mm (0.01 in.) instead of 1.27 mm (0.05 in.). Extensive tests indicated that the PRI computed by the KSCAN for a given segment generally varied less than ± 3 percent from scan to scan, and five or more successive segments showed totals that rarely differed by more than ± 1 percent. The process has been implemented on a personal computer, and an assembled system consisting of the software, the special scanning hardware, an IBM-compatible 486 computer, and a printer costs under $7,500.

ACKNOWLEDGMENTS

This project was funded under the Kansas Transportation Research and New Development (K-TRAN) program by KDOT. The authors are grateful to KDOT for this support. Thanks are due to Lon Ingram, P.E., Chief of Bureau of Materials and Research, and Richard McReynolds, P.E., Engineer of Research, for their continued interest and support for smoothness research in Kansas. The following graduate students of the EECE Department at KSU contributed to the development of computer code for KSCAN: M.

TABLE 5 Repeatability of Scanning Process (5.08 mm or 0.2 in Blanking Band)

Segment No.	Avg. Estimated PRI (mm/km)			
	Run 1	Run 2	Diff.	Diff. (%)
1	22.09	22.09	0.0	0.00
2	82.03	82.03	0.00	0.00
3	115.16	113.59	-1.57	-1.39
4	100.96	100.96	0.00	0.00
5	66.26	66.26	0.00	0.00
6	97.81	97.81	0.00	0.00
7	140.41	140.41	0.00	0.00
8	105.70	104.12	-1.58	-1.52
9	75.73	75.73	0.00	0.00

Note: 1 in/mile = 15.78 mm/km

TABLE 6 Effect of Filtering on the Computation of PRI

Segment No.	Avg. Estimated PRI (mm/km)			
	Filter 1	Filter 2*	Diff.	Diff. (%)
1	22.09	22.09	0.0	0.00
2	82.04	91.50	9.46	10.34
3	115.16	123.05	7.89	6.41
4	100.97	108.85	7.88	7.25
5	66.26	74.17	7.91	10.64
6	97.81	107.27	9.46	8.82
7	140.41	156.18	15.77	10.10
8	105.69	112.01	6.32	5.63
9	75.73	75.73	0.00	0.00

*shorter filter

Note: 1 in/mile = 15.78 mm/km

Ediger, B. Ensminger, J. Herrmann, T. Peglow, and R. Zhou. Their enthusiastic support for KSCAN is acknowledged.

REFERENCES

1. Hudson, W. R. Road Roughness: Its Elements and Measurement. In *Transportation Research Record 836*, TRB, National Research Council, Washington D.C., 1981, pp. 1–7.
2. Scofield, L.A. *Final Report, NCHRP Project 20-7, Task 53, Profilograph Limitations, Correlation, and Calibration Criteria for Effective Performance Based Specifications*. TRB, National Research Council, Washington D.C., 1992.
3. Parcells, Jr., W. H. *Control of Pavement Trueness in Kansas*. Interim Report, Kansas Department of Transportation, Topeka, Kans., January 1992.
4. Scofield, L. A., S. Kalevela, M. Anderson, and M. Hossain. *A Half Century with the California Profilograph*. Report FHWA-AZ-SP9102. Arizona Department of Transportation, Phoenix, Ariz., February 1992.
5. Kulakowski, B. T. and J. W. Wambold. *Development of Procedures for the Calibration of Profilographs*. Report FHWA-RD-89-110. The Pennsylvania Transportation Institute, University Park, Pa., August 1989.
6. Budwig, J. L. Bituminous Pavement Smoothness: A Statistically Based Approach to Accept Utilizing the California Type Profilograph, California Test Method 526 and Computerized Profilogram Reduction. Presented at the 73rd Annual Meeting of the Transportation Research Board, Washington, D.C., January 1994.
7. Parcells, Jr., W. H. *Control of Pavement Trueness in Kansas*. Interim Report. Kansas Department of Transportation, Topeka, Kans., May 1992.
8. *User's Manual for the CS 8200 Profilograph*. Cox & Sons, Inc., Colfax, Calif., 1992.

Publication of this report sponsored by Committee on Pavement Monitoring, Evaluation, and Data Storage.

Effect of Pavement Deterioration Types on IRI and Rehabilitation

BASHAR AL-OMARI AND MICHAEL I. DARTER

A study of the relationships between present serviceability rating (PSR), international roughness index (IRI), and selected pavement distress types was conducted. A predictive model was developed between PSR and the IRI. Relationships between IRI and selected asphalt pavement and jointed concrete pavement distress types were developed. Some of the distress types have stronger effects on IRI than do others, and the severity of these distresses is also very important. The relationship of IRI to critical levels of rehabilitation was evaluated. It was found that as distress amounts increase in number and in severity, the IRI increases also. It is believed that in addition to IRI, visible distress is an important aspect to proper selection of timing and type of rehabilitation techniques. It is recommended that the Highway Performance Monitoring System utilize both the IRI and selected pavement distress types as trigger values for more consistent and realistic results in predicting future rehabilitation needs on the nation's highways.

The second phase of a research study conducted to develop relationships between the international roughness index (IRI) and pavement condition is documented in this paper. The first phase of this research concentrated on the development of a relationship between IRI and the present serviceability rating (PSR) for pavement types included in the Highway Performance Monitoring System (HPMS) database. A predictive model for PSR as a function of profile IRI was developed for flexible, rigid, and composite (asphalt over concrete) pavements. The results of the first phase have been documented (*1*).

The second phase of this research concentrated on the relationships between IRI and various pavement distress types. In this second phase, data from the Long-Term Pavement Performance (LTPP) database, including IRI and pavement distresses, were analyzed to determine the relationships of key distress types to IRI and critical levels for rehabilitation. These results will be very useful in the HPMS analytical process to achieve improved and consistent estimates of the current conditions and the future highway pavement rehabilitation needs in the United States.

Currently, the states are required to report both IRI and PSR to FHWA. The PSR ranges from 0 (very poor) to 5 (very good). The levels of PSR are defined according to HPMS, which include descriptions of ride quality, physical distress such as cracking, and rehabilitation needs. The PSR is determined by the states, on the basis of this general definition but also by other methods. The PSR concept is important since it is built into the HPMS analytical software and is a vital part of the procedures used to estimate long-term pavement rehabilitation needs. The PSR is also well known in the highway community as an indicator of pavement condition. Visual distress also is a widely used indicator of pavement condition and is strongly related to rehabilitation needs. Not much is currently known about the IRI on the nation's highways, especially critical levels at which pavements should be rehabilitated. If correlations can be made between the objectively measured IRI (an index of pavement profile) and the PSR and visual distress, the IRI could become a more reliable indicator of pavement condition and rehabilitation needs.

Department of Civil Engineering, 1208 Newmark Civil Engineering Lab, 205 North Mathews Avenue, University of Illinois at Urbana-Champaign, Urbana, Ill. 61801.

CORRELATION OF IRI AND PSR

In the first phase of this research the primary objective was to develop a predictive model for PSR as a function of profile IRI that was applicable to flexible, rigid, and composite (asphalt over concrete) pavements. Relationships between IRI and PSR were analyzed for data from the states of Louisiana, Michigan, New Jersey, New Mexico, and Ohio. These data were obtained from the NCHRP Project 1-23 database, with some additional data obtained from Indiana. Data for all six states were entered into a Statistical Analysis System data set, and the following nonlinear model was found to best fit the boundary conditions and the actual data:

$$PSR = 5 * e^{(-a*IRI)} \quad (1)$$

Regression analysis was conducted for all possible sets of data considering different states and pavement types. No significant difference was found between the models for different states and pavement types. Therefore, the following model was recommended for all pavement types:

$$PSR = 5 * e^{(-0.0026*IRI)} \quad (2)$$

where IRI is in units of cm/km, or

$$PSR = 5 * e^{(-0.0041*IRI)} \quad (3)$$

where IRI is in units of in./mile.

Figure 1 shows the plot of the recommended model with all the data (*3*).

CORRELATION OF IRI AND DISTRESS—ASPHALT-SURFACED PAVEMENTS

Two approaches were followed to analyze the effect of asphalt concrete (AC) pavement distresses on IRI and/or PSR. The first approach used profile and distress data from the available test sections in the Strategic Highway Research Program's Long-Term Pavement Performance (SHRP LTPP) database. The second approach used "manufactured profiles" developed mathematically

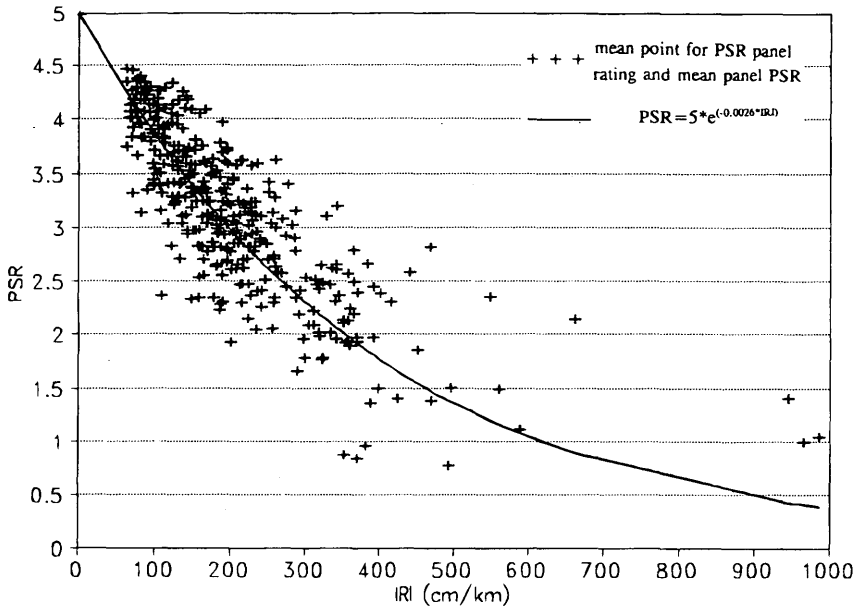

FIGURE 1 PSR versus IRI data and model recommended for all pavement types (*3*).

to incorporate different additional distresses to examine how these distresses affect the values of IRI and PSR. Computation of the IRI for various profiles was accomplished using a computer program named PROFILE, prepared by using standard procedures described by Sayers et al. (*1*).

After summarizing and testing all the available LTPP data, it was found that rutting was the only distress for which a sufficient number of test sections showing distress were available, from which reasonable results were obtained. Very few sections contained fatigue cracking, for example. Rutting was therefore the only distress analyzed on the basis of LTPP data.

Rutting, transverse cracking, potholes, depressions, and combined distresses were analyzed using manufactured profiles. Fatigue cracking was not considered directly in the analysis because there were no distinctive profile characteristics available, and its effect on the pavement profile is already considered as an associated distress with rutting. When fatigue cracking occurs, rutting normally develops also. The effect of each distress on IRI was analyzed first. Then the effect of combined distresses on IRI was determined.

Rutting

Correlation Based on LTPP Data

No significant correlation was found between the IRI and either the average rut depth (RD) or the RD standard deviation when individual pavement sections were considered.

However, when the data were grouped for ranges of IRI and RD means and standard deviations were averaged over these ranges, it was found that the midpoints of IRI for those ranges correlate with both mean RD and RD standard deviation, with R^2 values of 0.93 and 0.94, respectively. The following linear equation was obtained by regression for IRI as a function of RD:

$$IRI = 57.56 * RD - 334.28 \quad (4)$$

where IRI is in units of cm/km and RD is in units of mm. This equation gives an IRI of about 250 (PSR = 2.6) if rutting is 10 mm (0.4 in.).

The following linear equation was obtained for IRI as a function of RD standard deviation:

$$IRI = 136.19 * SD - 116.36 \quad (5)$$

where IRI is in units of cm/km and SD is in units of mm.

A correlation also was found between average RD and RD standard deviation with an R^2 of 0.80.

Correlation Based on Manufactured Profile Analysis

The LTPP data were reviewed to find sections with no distresses other than rutting. There were a few sections that satisfied this criterion, and three of these were used in the profile analysis with a range of IRI from low to high. The three sections had the following IRI, estimated PSR, mean RDs and standard deviation of RD along the section.

Estimated		*Mean*	*Rut_Depth*
PSR	*IRI*	*Rut Depth*	*Standard Deviation*
4.54	37.5 cm/km	6.46 mm	0.0445 mm
3.37	151.0	8.43	0.0773
2.35	289.9	10.48	0.1175

The PSR values were estimated from Equation 2. Therefore, three sections that contain only rutting with known IRI, mean RD, and RD standard deviation were obtained.

The section having a PSR value of 4.54 (IRI = 37.5 cm/km) and no other distresses is in excellent condition. The profile of this section was used in the remaining flexible pavement analyses to determine the effect of each of the other distresses on the IRI value. This profile will be referred to as the "smooth" profile.

Transverse Cracking (Thermal or Reflection)

To examine the effect of transverse cracking on the value of IRI, the "smooth" profile section was utilized. A typical deteriorated transverse crack with a width of 50 mm (2 in.) and a maximum depth of 25 mm (1 in.) was added to this smooth profile. The effect of transverse cracking on IRI was determined by adding deteriorated transverse cracks to the profile and computing the IRI using the PROFILE software, as shown in Table 1.

It was found that the IRI value increases nearly linearly as the number of cracks in the 50-m (164-ft) section increases.

The specific shape of the transverse crack will have a major effect on IRI. The crack dimensions used in this analysis are typical of cracks that have settled, which would generally be rated as high severity. These results show that high severity transverse cracks have a significant effect on IRI.

Potholes

The effect of potholes on the IRI and the corresponding PSR was determined by adding potholes to the "smooth" profile over a range of frequencies (0, 1, 2, 3, and 4 potholes per 50 m). Each pothole had a diameter of 400 mm (15.75 in.) and a depth of 25 mm (1 in.). The IRI and calculated PSR values are shown in Table 1.

It was found that as the number of potholes in the section increases, the IRI increases in an approximate linear relationship. The specific dimensions of the pothole will have a major effect on IRI. The dimensions used in this analysis are typical of potholes that would be rated high severity. Potholes have a very strong effect on IRI.

Depressions and Swells

The effect of depressions and/or swells on the IRI and the corresponding PSR was determined by adding a number of depressions to the "smooth" profile. The depressions have a depth of 25 mm (1 in.) and a length of 2 m (6.56 ft). After adding the depressions and/or swells to the section, the new IRI and PSR values were calculated as shown in Table 1.

Note that depressions have exactly the same effect as swells since IRI measures the absolute difference between the elevations of the consecutive points. This measurement is not affected by the direction of upward or downward movement. A swell and a depression of the same shape and dimensions will have the same value of IRI.

It was found that as the number of depressions per given length increases, the IRI increases with an approximate linear relationship. The specific shape of the depression and/or swell will have a major effect on IRI. The depression dimensions used in this analysis are typical of depressions that would be rated high severity. These depressions and/or swells have a large effect on IRI.

Combination of Distresses

Most pavements contain more than one distress. Thus, it is desirable to be able to determine the effect of combined distresses on IRI and PSR values. To find the effect of combined distresses on IRI and PSR, the three sections that contain different amounts of rutting with known IRI and PSR values were used. After combining the distresses in different combinations, their corresponding IRI and PSR values were calculated. A set of 81 sections was obtained as shown in Table 2.

Regression analysis was applied to the data to find a model representing the relation between PSR and the combined distresses. Two models were obtained, one considering the mean RD and the other considering the RD standard deviation.

The model that includes mean RD is as follows:

$$PSR = 4.95 - 0.685\,D - 0.334\,P - 0.051\,C - 0.211\,RD \quad (6)$$

where

D = high severity depressions (number per 50 m);
P = high severity potholes (number per 50 m);

TABLE 1 Calculated PSR and IRI Values for Sections with Individual Distresses

Distress	Number per 50 m	IRI (cm/km)	PSR
Transverse Cracking	0	37.5	4.54
	1	52.0	4.37
	2	64.0	4.23
	3	78.3	4.08
	7	129.5	3.57
	15	205.2	2.93
Potholes	0	37.5	4.54
	1	117.7	3.68
	2	191.6	3.04
	3	273.1	2.46
	4	339.3	2.07
Depressions and Swells	0	37.5	4.54
	1	174.9	3.17
	2	335.4	2.09
	3	468.9	1.48

TABLE 2 PSR Values for Sections with Combined Distresses

D	P	C	RD=6.46 SD=4.45	RD=8.43 SD=7.73	RD=10.84 SD=11.75
0	0	0	4.54*	3.37*	2.35*
		3	4.08	3.18	2.23
		7	3.57	2.99	2.11
0	1	0	3.68	2.78	2.13
		3	3.30	2.58	1.95
		7	2.90	2.43	1.85
0	2	0	3.04	2.47	1.83
		3	2.73	2.33	1.72
		7	2.37	2.11	1.60
1	0	0	3.17	2.33	1.82
		3	2.76	2.16	1.67
		7	2.43	2.04	1.58
1	1	0	2.54	1.92	1.56
		3	2.28	1.78	1.43
		7	2.02	1.68	1.35
1	2	0	2.09	1.71	1.36
		3	1.89	1.60	1.28
		7	1.65	1.46	1.19
2	0	0	2.09	1.78	1.21
		3	1.87	1.60	1.11
		7	1.66	1.49	1.06
2	1	0	1.71	1.46	1.10
		3	1.52	1.30	0.98
		7	1.35	1.22	0.94
2	2	0	1.41	1.26	0.94
		3	1.26	1.13	0.86
		7	1.10	1.02	0.81

Where: D = depressions per 50 m
P = potholes per 50 m
C = transverse cracks per 50 m
RD = average rut depth, mm
SD = standard deviation of rut depth, x 100 mm
R^2 = 0.92 & SEE = 0.226 (standard error of the estimate of PSR)

C = high severity transverse cracks (number per 50 m);
RD = average RD (mm);
R^2 = 0.92; and
SEE = 0.226 (standard error of the estimate of PSR).

The model that includes the standard deviation of RD is as follows:

$$PSR = 4.151 - 0.685\,D - 0.334\,P - 0.051\,C - 0.127\,SD \quad (7)$$

where

D = depressions (number per 50 m);
P = potholes (number per 50 m);
C = transverse cracks (number per 50 m); and
SD = RD standard deviation (× 100 mm).

PSR can be predicted for a pavement section if the depressions, potholes, transverse cracking, and average RD (or RD standard deviation) are known and no other distresses exist. As mentioned before, the models assume generally high severity levels for the distresses. Similar models could be developed for IRI.

CORRELATION OF IRI AND DISTRESS—CONCRETE-SURFACED PAVEMENTS

A similar analysis was conducted to determine the effect of several distresses on IRI and PSR of jointed concrete-surfaced pavements. The distresses considered include joint faulting, transverse cracking, and joint spalling. The effects of depressions and/or swells and potholes would be the same on concrete pavements as on asphalt pavements. Joint faulting was analyzed based on both LTPP data and manufactured profiles, while the other distresses were analyzed using manufactured profiles, since the LTPP sections did not have sufficient quantities of the other distresses.

Joint Faulting

Correlation Based on LTPP Data

The following linear equation was developed for IRI as a function of faulting ($R^2 = 0.5$):

$$IRI = 147.1 + 27.94 * F \quad (8)$$

where IRI is in units of cm/km and average section faulting F is in units of mm.

However, it is known that those sections have distresses other than faulting, which means that no pure relationship can be found between IRI and faulting.

Correlation Based on Manufactured Profile Analysis

A slab length of 5 m (16.4 ft) was used to find the effect of faulting on IRI and PSR. The depth of the faulting "y" was assumed as a constant value at all slab joints to represent the average faulting in the assumed section. The IRI value for the section was calculated for different values of average faulting. The calculated IRI and its corresponding PSR value are as shown in Table 3.

The following linear relationship between IRI and mean joint faulting was developed for a joint spacing of 5 m (16.4 ft).

$$IRI = 35.816 * F \quad (9)$$

Where IRI is in units of cm/km and faulting F is in units of mm.

Comparison of Manufactured Profile Analysis with the LTPP Analysis

The manufactured profile analysis provides a relationship between IRI and mean joint faulting, and the LTPP data provide another relationship. The relationship determined from the manufactured profile is considered to accurately show the effect of joint faulting as the only distress type, while in the LTPP data, joint faulting was not the only existing distress type. By comparing the two relationships, the effect of other profile deviations on IRI may be determined. At each value of mean joint faulting the non-joint faulting share of the IRI can be determined by taking the difference between the two values. This difference decreases as the mean joint faulting value increases. This indicates that as the mean value of joint faulting increases, its effect becomes increasingly larger than the other profile deviations on the calculated value of IRI.

Transverse Cracking

It is impossible, in practice, to find a section of roadway with an IRI of 0 (PSR = 5.0). A new pavement usually has a PSR value of approximately 4.5. Therefore, for this analysis a manufactured profile was produced with a mean joint faulting of 1 mm (0.04 in.), which was found previously to produce an IRI value of 4.06 cm/km and a corresponding PSR value of 4.5. This profile is referred to as the "smooth" profile. Transverse cracking was added to this profile to find its effect on IRI and PSR values. Each transverse crack was assumed to be spalled, with a width of 50 mm (2 in.) and an average depth of 25 mm (1 in.). The transverse crack was placed in the center of the slabs. In addition, each transverse crack was faulted 2.5 mm (0.1 in.), which is typical of high severity cracks. The calculated IRI and PSR values for different percentages of slabs with transverse cracks are shown in Table 4. Joint spacing was assumed to be 5 m (16.4 ft).

It was found that as the percentage of transverse cracking increases, IRI increases with an approximate linear relationship. The specific dimension of the transverse crack will have a major effect on IRI. The crack dimensions and faulting used in this analysis are typical of cracks that would have a medium to high rating of severity.

TABLE 3 Calculated IRI and Corresponding PSR Values

Mean faulting, y (mm)	IRI (cm/km)	PSR
1	35.8	4.50
2	71.6	4.15
4	143.3	3.45
6	214.9	2.86
8	286.5	2.37
10	358.2	1.97

Joint spacing = 5 m (16.4 ft), 1 in = 25.4 mm

TABLE 4 Calculated PSR and IRI Values for Sections with Individual Distresses

Distress Type	(% Slabs/Joints)	IRI (cm/km)	PSR
Transverse cracking	0	40.6	4.50
	20	80.0	4.06
	50	134.5	3.52
Joint Spalling	0	40.6	4.50
	20	75.8	4.11
	50	128.5	3.58

Joint Spalling

The analysis of the effect of joint spalling was conducted using the "smooth" profile, and IRI and PSR values calculated for different percentages of joints spalled. The spalling width across the joint was 100 mm (4 in.) and its depth was 37.5 mm (1.48 in.). The calculated IRI and PSR values are shown in Table 4. The joint spacing used was 5 m (16.4 ft).

It was found that IRI increases approximately linearly as the percentage of joints spalled increases. The specific dimensions of the joint spalling will have a major effect on IRI. The dimensions used in this analysis are typical of spalled joints that would be rated as having high severity.

Combination of Distresses

After determining the effect of each distress on both IRI and PSR values, the effect of combined distresses was determined. The PSR value was calculated for different combinations of distresses, as shown in Table 5.

Regression analysis was performed to find a relationship between PSR and the combined distresses, and the following equation was obtained for a joint spacing of 5 m (16.4 ft):

$$PSR = 4.115 - 0.01083\ S - 0.00949\ TC - 0.22667\ F \quad (10)$$

where

S = high severity joint spalling (percent of joints);
TC = high severity transverse cracking (percent of slabs cracked);
F = average joint faulting (mm); and
$R^2 = 0.91$
SEE = 0.183.

The PSR can be predicted for a pavement section if the joint spalling, transverse cracking, and average joint faulting are known and no other distresses exist. A similar equation could be developed for IRI.

SELECTING CRITICAL LEVELS OF IRI FOR REHABILITATION

As a pavement ages and is loaded by traffic, distresses such as rutting, faulting, and cracking develop that often adversely affect the longitudinal profile so that the IRI increases and the PSR decreases. Some of the relationships between IRI and distresses were explored in this study and it was found that, all other things being equal, several distress types at their high severity levels have a significant effect on IRI. It is important to point out, however, that at lower severity levels and for a variety of other distresses (e.g., raveling, "D" cracking), the longitudinal profile (and thus IRI) may not be affected very much until a large amount of pavement deterioration has occurred. In other words, a pavement could be relatively smooth and still have a significant amount of distress. If the pavement was not rehabilitated until it became relatively rough (high IRI), the resulting rehabilitation cost might be very large. The amount and quality of maintenance applied to keep distresses at low levels of severity are also a major factor.

The key point to be made is that although the longitudinal profile (as measured by the IRI) may be a good indicator of the highway user ratings (as indicated by the PSR), it may not be a good indicator of when the pavement should be rehabilitated from a structural viewpoint to develop a cost-effective rehabilitation program for pavements relying only on the longitudinal profile (IRI). Visible distress is another important aspect in proper selection of rehabilitation type and timing.

The HPMS analytical software currently uses minimum PSR trigger values for rehabilitation and reconstruction. The trigger values vary depending on pavement functional class and urban or rural location. It is desired to use the IRI and other pavement condition indicators as trigger values for more consistent and realistic results. This is an excellent goal for HPMS to strive to achieve, but there remains a lot of additional research work needed to accomplish it. For example, if rutting were added as a distress in the HPMS database to improve the rehabilitation selection procedure, there would need to be a methodology for predicting rutting into the future so that trigger values could be set for rehabilitation, as trigger values are currently specified for PSR.

With this broader background in mind, this section addresses the potential problem of using only IRI as a trigger value for resurfacing and reconstruction work for different functional classes, pavement types, and urban or rural locations. Both the highway user and the structural integrity of the pavement must be considered. It is well known that some distresses (and severity levels) significantly influence IRI, but there are other important distresses that, at least at lower levels of severity, do not have much effect on longitudinal profile and, thus, IRI. For these types of distresses, to wait until the IRI is at a high trigger value would be to wait too long past the time when the distresses can be repaired cost-effectively. Complete high-cost reconstruction may be required at this point. In the following section some results obtained herein are presented to illustrate these results.

Highway User IRI Trigger Levels

The conventional way of selecting rehabilitation trigger values for PSR is to determine the level at which approximately 50 percent of highway users decide that a pavement ride is unacceptable for a given functional class of highway and pavement type. The upper values in Table 6 are the mean PSR ratings from several studies at which 50 percent of the panel in the study indicated yes or no as an answer to the question: Is the pavement acceptable? As can be seen from the table, there is a difference between the PSR value at which 50 percent of the panel indicated "yes" and the PSR at which 50 percent of the panel indicated "no." This is because some panel raters made no decision about the acceptability of some pavement sections. Also, the PSR trigger values were taken from the best fit of the data or the fraction of the panel stating "yes" or "no" versus PSR. The lower values in Table 6 are the corresponding calculated IRI values, which were calculated from PSR values using Equation 2.

Additional information was obtained in the second phase of NCHRP Project 1-23, in which the following equation was obtained showing that the mean panel rating is a predictor of the public's subjective perception of whether a pavement surface needs repair (*6*):

$$NR = 131.7 - 33.9\ RN \quad (11)$$

where NR is percentage of drivers who believe a pavement requires repair, and RN is the riding number, an approximation to the mean panel rating (PSR). By substituting Equation 2 in Equation 11 the following equation is obtained:

TABLE 5 PSR Values for Jointed Concrete Pavement Sections with Combined Distress [Joint Spacing 5 m (16.4 ft)]

Spalling (% Joints)	Transverse Cracking (% Slabs)	Fault=0mm	Fault=2.5mm	Fault=5mm
0	0	4.50	3.45	2.65
	20	4.06	3.38	2.62
	50	3.52	3.27	2.55
20	0	4.11	3.30	2.59
	20	3.69	3.14	2.51
	50	3.19	2.96	2.42
50	0	3.58	3.07	2.48
	20	3.22	2.85	2.38
	50	2.75	2.56	2.22

$$NR = 131.7 - 169.5\, e^{(-0.0026*IRI)} \quad (12)$$

where IRI is in units of cm/km and NR is as defined before.

This equation results in a *RN* (or approximate PSR) = 2.4 and IRI = 2.81 for the 50th percentile of highway users. Considering all of this information collectively shows that about 50 percent of the highway users believe a pavement is unacceptable when PSR values and corresponding IRI values are at the following levels:

Highway Class	*PSR*	*IRI*	
		cm/km	*in./mile*
Secondary	2.0	352	223
Primary	2.5	267	169
Interstate	3.0+	196+	124

PHYSICAL DETERIORATION OF PAVEMENT IRI TRIGGERS VALUES

Given the above highway user criteria for triggering rehabilitation, what is the consequence of these levels on pavement deterioration and rehabilitation costs? The following data show how the PSR and IRI change for asphalt-surfaced pavements as the amounts of individual distresses change independently. For example, 40 potholes per kilometer would result in an IRI of only 196 and a PSR of 3.0, whereas it requires 24 depressions or swells per kilometer for the same IRI and PSR.

PSR	*IRI*	*Rutting*	*Transverse cracks*	*Potholes*	*Depressions and swells*
2.0	352	11.9	533	84	43
2.5	267	10.5	408	58	32
3.0	196	9.2	283	40	24
3.5	137	8.2	160	26	14

These results show that individual distresses do not reduce the PSR lower than 2.5 to 3.0 (IRI greater than 196 to 267) until a large amount of deterioration is present. For primary and Interstate highways, RDs in excess of about 10 mm (0.4 in.) would generally be considered maximal for preventing hydroplaning, and rehabilitation should be performed, which occurs at a PSR = 2.5 and IRI = 267. There are no such criteria for the other types of distress. However, for PSR less than 2.5 for primary highways and less than 3.0 for Interstate highways, the levels of these distress severity types

TABLE 6 PSR and Estimated IRI (cm/km) at Which 50 Percent of Panel Indicated Yes or No for Acceptability

Data Source	Secondary and Primary Classes Combined				Pavement Types Combined			
	Rigid		Flexible		Secondary		Primary	
	Yes	No	Yes	No	Yes	No	Yes	No
AASHO Road Test (2)	2.9	2.5	2.9	2.5	-	-	-	-
	210	267	210	267	-	-	-	-
Purdue University (4)	2.2	1.5	2.2	1.7	2.0	1.5	2.4	-
	316	463	316	415	352	463	282	-
Nakamura (4)	-	-	-	-	2.0	1.5	2.5	2.0
	-	-	-	-	352	463	267	352
Texas DOT (5)	-	-	-	-	1.9	-	3.4*	-
	-	-	-	-	372	-	148	-

**Interstate highway*

appear to be quite excessive. For example, 40 potholes per kilometer is equivalent to an average pothole spacing of 25 m (83 ft).

The other important aspect to note is the relative increase in distress types as the PSR and IRI change from level to level. For example, a PSR decrease from 3.5 to 3.0 corresponds to an increase of 14 potholes per kilometer, whereas a drop in PSR from 3.0 to 2.5 corresponds to 18 additional potholes per kilometer, and 2.5 to 2.0 corresponds to 26 additional potholes per kilometer. This large increase in deterioration would cause a significant increase in maintenance and rehabilitation costs.

Of course, there are many different combinations of these distress types that could also lead to the various levels of PSR and IRI. Equations 6 and 7 may be used to show how a combination of distress types can result in different levels of PSR (and IRI). The following table shows how the PSR and IRI change for jointed concrete pavements as the levels of individual distress change. For example, 89 percent joints spalled would reduce IRI to 196 and PSR to 3.0. It requires 5.5 mm (0.217 in.) mean faulting for the same IRI and PSR.

PSR	*IRI*	*Faulting*	*Transverse cracks*	*Joint spalling*
2.0	352	9.8	100	100
2.5	267	7.5	100	100
3.0	196	5.5	82	89
3.5	137	4.0	50	55

where IRI is in units of cm/km.

These results show that a high level of faulting, cracking, or spalling is required to reduce individually the PSR to below 3.0. As these distresses increase, rehabilitation costs also increase. For example, when the PSRs drop from 3.0 to 2.5, the mean faulting increases from 5.5 to 7.5 mm (0.217 to 0.295 in.), which would increase diamond-grinding costs. Of course, there are many different combinations of these distress types that could also lead to the various levels of PSR and IRI. Equation 10 may be used to show how a combination of distress types can result in different levels of PSR (and IRI).

These results show that for PSR levels typically recommended for triggering rehabilitation based upon the 50th percentile of highway users, a substantial amount of pavement deterioration may be present. These levels may not be the most cost-effective points at which to perform rehabilitation.

The current HPMS PSR trigger values for selection of resurfacing are shown in Table 5 along with the corresponding IRI values (*7*). Also shown in Table 5 are comments on the level of physical deterioration that is expected to exist and whether or not repair at this level appears to be cost-effective.

As can be seen from Table 7, several of the levels of PSR are believed to be too low for cost-effective resurfacing of AC pavements. However, detailed cost studies are needed to actually demonstrate that these levels are too low. As a general guide, a minimum PSR of 3.0 (IRI = 196 cm/km) is recommended for principal arterials and above. A minimum PSR of 2.5 (IRI = 267 cm/km) or greater is recommended for all other classes. If IRI is to be used as a trigger for resurfacing, then it should be set at a reasonably high level to avoid extreme deterioration. Further research into the most appropriate levels based on economic analysis is needed. The relationships provided in this study among PSR, IRI, and visible distresses provide some useful results to assist in that analysis.

CONCLUSIONS

A study of the relationships among PSR, IRI, and selected pavement distress types was conducted. A predictive model was developed between PSR and the IRI in the first phase of this work, as reported by Al-Omari and Darter (*3*). The second phase of the study concentrated on the relationships between IRI and selected asphalt pavement and jointed concrete pavement distress types. For asphalt pavements, correlations were identified between IRI and mean RD, RD standard deviation, potholes, transverse cracks, and depressions and/or swells. For concrete pavements, correlations were determined between IRI and joint faulting, transverse cracking, and joint spalling (depressions and/or swells would be the same as with asphalt pavements). Some of these distress types have stronger effects on IRI than others, and the severity level of these distresses is also very important. Large quantities of some of these distress types could develop without reducing the PSR (or increasing the IRI) below conventional levels for resurfacing, especially if exten-

TABLE 7 HPMS Analytical Process Recommended PSR trigger values (with Estimated IRI) and Comments on Level Pavement Deterioration for Resurfacing

	Functional System	PSR	IRI (cm/km)	Physical Deterioration
	Interstate	3.0	196	Reasonable
R	Principal Arterials (ADT > 6000)	3.0	196	Reasonable
U	Principal Arterials (ADT < 6000)	2.8	223	Reasonable
R	Minor Arterials (All ADT)	2.4	282	Excessive
A	Major Collectors (ADT > =400)	2.0	352	Reasonable
L	Major Collectors (ADT < 400)	1.8	393	Excessive
	Minor Collectors (ADT > =400)	2.0	352	Excessive
	Minor Collectors (ADT < 400)	1.8	393	Excessive
U	Interstate	3.2	172	Reasonable
R	Other Freeways, Expressways	3.0	196	Reasonable
B	Other Principal Arterials	2.8	223	Reasonable
A	Minor Arterials	2.4	282	Excessive
N	Collectors	2.0	352	Excessive

sive maintenance was applied that maintained distresses at lower severity levels.

The relationship of IRI to critical levels of rehabilitation was evaluated. As distress quantities increase in number and severity, the IRI increases also. However, a pavement could be relatively smooth and still have a significant amount of distress. If the pavement was not rehabilitated until it became relatively rough (low PSR or high IRI), the resulting rehabilitation cost might be very high.

Although the longitudinal profile (as measured by the IRI) may be a good indicator of highway-user acceptance of the pavement (as indicated by the proportion of a panel of users), it may not be a good indicator of when the pavement should be rehabilitated from a structural viewpoint or from a rehabilitation cost standpoint. Thus, it is not believed possible to develop a cost-effective rehabilitation program for pavements by relying only on the longitudinal profile (or IRI). Visible distress is another important aspect in proper selection of rehabilitation type and timing.

It is recommended that HPMS utilizes both the IRI and selected pavement distress types as trigger values for more consistent and realistic results in predicting rehabilitation needs. Several of the trigger levels of PSR currently recommended in HPMS for resurfacing are believed to be too low for cost-effective resurfacing of AC pavements. Relationships provided in this study among PSR, IRI, and visible distresses provide some useful results to assist in further detailed analysis of this subject.

ACKNOWLEDGMENTS

This research was conducted for the Illinois Department of Transportation in cooperation with the Federal Highway Administration by the Department of Civil Engineering, University of Illinois. Appreciation is expressed to Carla Berroyer of the Illinois Department of Transportation for assistance with the study and to Robert Rozycki of the Federal Highway Administration, who served as the COTR for the contract.

REFERENCES

1. Al-Omari B. and M. I. Darter. Relationships Between IRI and PSR. In *Transportation Research Record 1435*, TRB, National Research Council, Washington, DC, 1994.
2. Carey, W. N. and P. E. Irick. The Pavement Serviceability Performance Concept. *Highway Research Bulletin*, No. 250, 1960.
3. Sayers, M. W., T. D. Gillespie, and W. D. O. Paterson. *Guidelines for Conducting and Calibrating Road Roughness Measurements.* World Bank Technical Paper No. 46, The World Bank, Washington, DC, 1986.
4. Yoder, E. J. and R. T. Milhous. *NCHRP Report 7: Comparison of Different Methods of Measuring Pavement Condition Interim Report.* HRB, National Research Council, Washington, DC, 1964.
5. Roberts, F. L. and W. R. Hudson. *Pavement Serviceability Equations Using the Surface Dynamics Profilometer.* Research Report 73-2, University of Texas at Austin, 1970.
6. Janoff, M. S. *NCHRP Report 308: Pavement Roughness and Rideability Field Evaluation.* TRB, National Research Council, Washington, DC, 1988.
7. *Highway Performance Monitoring System—Analytical Process.* Vol. 2, Version 2.1, Technical Manual. FWHA, U.S. Department of Transportation, Dec. 1987.

Publication of this paper sponsored by Committee on Pavement Monitoring, Evaluation, and Data Storage.

Measurement of Serviceability Indices for New, Overlay, and Terminal Pavements in Texas

HERNÁN E. DE SOLMINIHAC AND W.R. HUDSON

Serviceability Index (SI) relates to the riding comfort that a section of pavement provides to highway users and is a required input parameter for several design methods. Accurate pavement design requires good estimates of the SI value at key points in the pavement's life: (*a*) immediately after construction of a new pavement, (*b*) just before rehabilitation, and (*c*) just after rehabilitation. The analysis used to find the mean values and the variability of the SI for pavements in Texas during each stage is described.

The measurement of pavement serviceability has increased in importance since the development of the concept at the AASHO Road Test, because it defined performance and it relates directly to the road user and vehicle operating costs.

Serviceability index (SI) relates to the riding comfort that a section of pavement provides to highway users and is a required input parameter for several design methods. The AASHTO design method for both flexible and rigid pavements uses a formula to predict SI loss as a function of traffic, structural, and environmental variables (*1*).

In Texas, SI is an important input for the Flexible Pavement Design System (FPS) (*2*) and the Rigid Pavement Design System (RPS) (*3*). In these two methods, the initial serviceability index (pi), the terminal or minimum serviceability level (pt), and the serviceability index after overlaying (po) are used to predict pavement life and performance.

The initial serviceability index is related to different factors; some of them are: quality of construction procedures, specifications, and equipment. If the assumed initial serviceability is not achieved during the construction, the design life will be less than predicted. Better estimates of pavement performance can be achieved by more accurate initial serviceability estimates.

The terminal serviceability index is a value set by the design engineer and depends on when rehabilitation activity needs to be specified. The serviceability index which is achieved after an overlay is related to the serviceability before the overlay, the thickness of the overlay, and the quality of the rehabilitation technique. If the assumed serviceability index after the overlay is not achieved, the actual performance life of the pavement could be lower than predicted.

Accurate pavement design requires good estimates of the SI for at least three stages (see Figure 1): (*a*) SI immediately after a new construction or new pavement, (*b*) SI of worn out pavement or just before rehabilitation, and (*c*) SI restored in the pavement or just after rehabilitation. Therefore, the main objective of the project was to measure the present SI of both rigid and flexible pavements to determine: (*a*) mean values and variability of initial serviceability index immediately after construction, (*b*) mean values and variability of serviceability index before scheduled rehabilitation projects, (*c*) mean values and variability of the serviceability index of the pavements resulting after rehabilitation, and (*d*) mean values and variability of SI of pavements just after reconstruction.

This study followed a combination of the systems method recommended by Haas, Hudson and Zaniewski (*4*) and the design of experiment concept recommended by Anderson and McLean (*5*). The main steps of this approach are:

Step 1. Problem recognition exists—This step resulted in the proposal for this research.

Step 2. Problem formulation—In the research proposal, the problem was formulated and the objectives were presented.

Step 3. Experiment design—An experiment was designed to collect and to analyze efficiently all the information required for this study. The main aspects considered are: (*a*) factors and levels to be used in the experiment, (*b*) variables to be measured, (*c*) definition of the inference space for the problem, (*d*) amount of replication to be used, and (*e*) random selection of the experimental units.

Step 4. Data collection—The success of scientific research depends on the validity of all data obtained; therefore special care was given to this particular aspect of the study.

Step 5. Data analysis—The analysis of the data depends on the experiment design. Basically, there were three stages during the analysis: (*a*) check that all the assumptions required for the statistical analysis were met, (*b*) analysis of the main factors, and (*c*) analysis of the of the secondary factors.

Step 6. Conclusions and recommendations—Once the analysis of the data has been completed, the conclusions are formalized and the recommendations for implementation are reported.

This paper includes a summary of references about past serviceability indices, a description about the design of experiment used on the study, a discussion of the results, findings, conclusions, and recommendations.

PAST SERVICEABILITY INDICES

Average SI values, based on the AASHO Road test experience for new pavements is 4.2 and for new rigid pavements is 4.5. On the other hand, AASHTO recommends a terminal SI of 2.5 for major highways and 2.0 for highways with lesser traffic volumes (*1*).

A survey in fall and winter of 1961 sponsored by the Bureau of Public Roads (BPR) (*6*) found the average SI values indicated in Table 1.

H. E. de Solminihac, Pontifica Universidad Católica de Chile, Casilla 306-Correo 22, Santiago, Chile. W.R. Hudson, Dewitt C. Greer Centennial Professor of Civil Engineering, The University of Texas at Austin, Suite 6.10 ECJ Hall, Austin, Tex 78712.

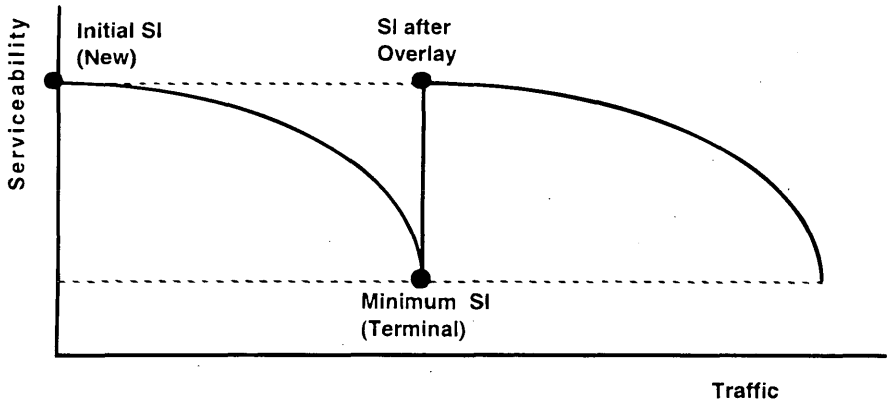

FIGURE 1 Points of interest on pavement performance curve.

A study done by the Center for Transportation Research (CTR) at The University of Texas at Austin shows that the average Texas resident deems the quality of ride acceptable for pavements sections on an interstate highway is 3.06 and the corresponding value for pavements sections on a secondary highway is 2.20 (*7*).

For the design of flexible pavements, the state of Texas recommends the following serviceability for different categories of use in FPS (*2*):

(a) Initial Serviceability Index (pi): "This input depends on the materials used and construction practices. Initial serviceability indices have a statewide average of about 4.2. Surface treatments may be near 3.8 and a very smooth asphalt concrete pavements (ACP) or continuous reinforce concrete pavements (CRCP) might be as high as 4.8" (*2*).

(b) Minimum Serviceability Index (pt): "It is recommended that a minimum serviceability index of 3.0 be used on highways with "Legal Posted Speeds" in excess of 72 km/hr) (45 mph) and 2.5 for those posted 72 km/hr (45) mph or less. If signal spacing, stop signs, dips, etc. prevent drivers from operating faster than 32 km/hr (20 mph) the minimum serviceability index may be relaxed to 2.0" (*2*).

(c) po: "In general, the serviceability index after an overlay should be about the same as that of initial construction. In this design system it must be specified by the engineer" (*2*).

DESIGN OF EXPERIMENT

The main objective of a design of experiment is to determine the effect of various factors (independent variables) on some characteristic of a variable of interest (dependent variable). The factorial approach is efficient and results in a considerable savings of time and resources, when compared to the alternative procedure of conducting separate experiments where each of these deals with a single factor. Moreover, in a factorial experiment, the effects of each factor are examined for every combination of all other factors (interaction) included in the experiment.

TABLE 1 Average Terminal SI Based on BPR Survey

Highway Surveyed	Terminal SI values Based on BPR Survey	
	Rigid	Flexible
Major	2.2	2.1
Lesser	--	1.8

The main objective of this analysis is to estimate the SI (dependent variable) of the Texas highways at different time intervals. The inference space, defined as the space where the results of the study may be applied, is the highway system in Texas. This concept is important and it is necessary to keep it in mind when applying the results or the conclusions of the study.

According to Anderson and McLean (*5*), the experimental or elemental unit is the type of experimental material used to receive the application of various treatments and is of the desired inference space. For this study, any road is an experimental unit.

There are many independent variables that could be studied for example: environmental condition, construction procedure, structural design, surface materials, traffic, and many others. After statistical, timing, and economical considerations, a three-factor experiment was developed. Three main factors were selected: (*a*) environmental-geographical regions, (*b*) type of pavement, and (*c*) category of use. These are fixed factors because the levels of interest were selected by the experimenter.

The first factor, "environmental/geographical regions," has four levels. This factor was developed from the six climatic regions in the United States, which are differentiated on the basis of moisture availability and freeze-thaw activity (Figure 2) (*8*). This study shows that Texas is divided into four areas according to this national classification. To keep a uniform system, it was decided to use this division for this study. Therefore, the levels on this factor are the four climatic zones present in Texas: (*a*) Climatic Zone I, which is wet but does not freeze; (*b*) Climatic Zone II, which is wet but has freeze-thaw cycling; (*c*) Climatic Zone IV, which is dry but does not freeze; and (*d*) Climatic Zone V, which is dry but has freeze-thaw cycling.

The second factor, "type of pavement," has two levels and it was considered from the two most representative pavement types: rigid pavements and flexible pavements.

The third factor, "category of use," has four levels. These four levels are: (*a*) serviceability immediately after construction (new pavements), (*b*) serviceability before scheduled overlay projects (terminal pavements), (*c*) serviceability immediately after rehabilitation (resurfaced pavements), and (*d*) serviceability after reconstruction (reconstructed pavements).

Finally, with these three main factors, it is possible to build a factorial design matrix that we will use for the analysis. This matrix is presented in Figure 3.

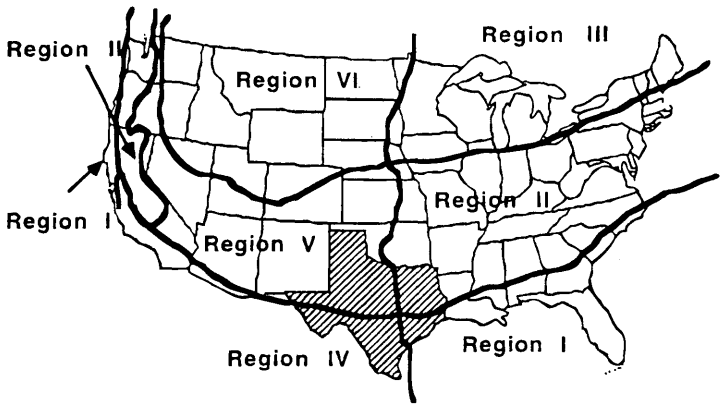

REGION	CHARACTERISTICS
I	Wet and no freeze
II	Wet and freeze-thaw cycling
III	Wet, hard freeze and spring thaw
IV	Dry and no freeze
V	Dry and freeze-thaw cycling
VI	Dry, hard freeze and spring thaw

FIGURE 2 Six climatic regions in United States (*8*).

Two other variables were selected as secondary fixed factors: highway classification (*H*), and surface type (*S*). Highway classification has two levels: primary highways and secondary highways. Surface type has different levels for each pavement type. Rigid pavements have continuous and jointed surfaces. On the other hand, flexible pavements have asphalt concrete and surface treatment.

The selection method adopted in this study was a screening process that used the monthly list of bids and construction reports from the Texas Department of Transportation (TxDOT).

To determine the pavement type of each section, there are two basic sources of information needed. First, the tabulation of bids, which normally shows the type of work to be be done; second, the report of the Pavement Evaluation System in Texas (PES), which indicates the type and pavement condition existing before the work was completed.

If the profile was obtained before the rehabilitation work, the pavement is in "terminal" condition. On the other hand, if the profile was obtained after the overlay, the pavement is in the "resurfaced" category.

Climatic Zones		Region I		Region II		Region IV		Region V	
Pavement Types		Rigid	Flexible	Rigid	Flexible	Rigid	Flexible	Rigid	Flexible
Category of Use	New								
	Reconst.								
	Resurfaced								
	Terminal								

FIGURE 3 Factorial design matrix.

RESULTS

Data Processing

Ideally, the analysis should include all the factors of interest to the researcher in one single model; but when this condition is not possible, the data may be divided using more than one model.

The procedure followed during the analysis is summarized in Figure 4. The first step was to verify if the data met the assumptions required for the analysis. The second step in this analysis was to run an analysis of variance (ANOVA) with a complete model, using SAS (*9,10*); including the dependent variable (SI), and all independent factors of interest: region (*R*), pavement type (*P*), category of use (*C*), highway classification (*H*), and surface type (*S*). The results of this analysis were unsatisfactory. Some of the sum square (*SS*) were undefined, mainly, because there was not enough data to run this complete model.

The third step of the analysis considered only the main factors of interest, that is, *R* and *C*. After obtaining the results of that model, some of the factors that were nonsignificant at a predetermined level could be discarded. The fourth step was to run a separate ANOVA for rigid and flexible pavements. In both cases, the model included factors *C, H,* and *S*.

The fifth step, a multiple comparison test among the significant factors found in the previous steps, enabled the final conclusions over the factors of interest. The next step of this analysis involved interpreting the results, but this step will be discussed in the following section.

Finally, the variability of the SI was studied. To achieve this new task an ANOVA was run using as the dependent variable the coefficient of variation and as the independent variables the climatic region, the pavement type, and the category of use.

There were 145 sections around the state of Texas selected and profiled for this study. Of these, 36 are on rigid pavements and 109 are on flexible pavements. The information collected for all sections is presented in two parts. The first part contains a general description and location of the sections. The second part mainly includes the roughness information.

A summary of the data collected is presented in Figure 5. Each cell of that figure contains the sample size, the average SI value, and

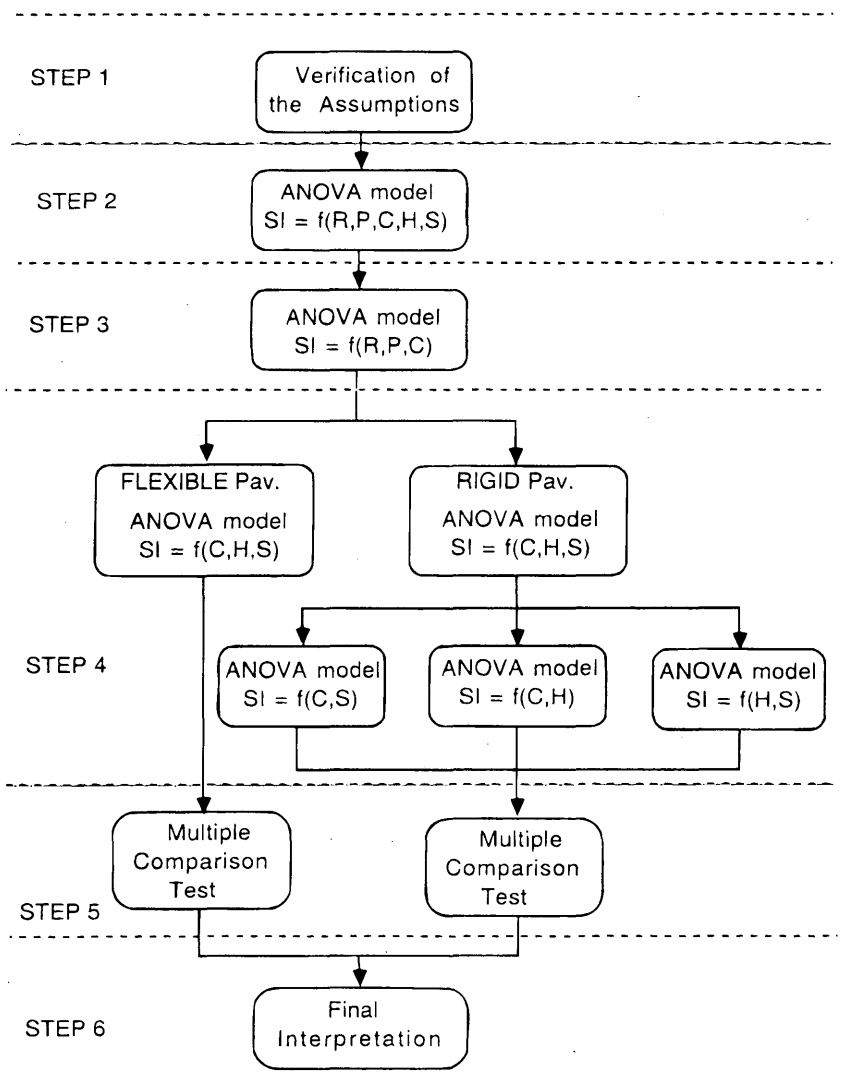

FIGURE 4 Summary of steps used in analysis.

Climatic Zones		Region I		Region II		Region IV		Region V	
Pavement Types		Rigid	Flexible	Rigid	Flexible	Rigid	Flexible	Rigid	Flexible
Category of Use	New	5 3.71 0.62	- - -	4 3.67 0.28	3 3.47 1.14	1 4.04 - - -	1 3.84 - - -	3 3.94 0.08	4 3.64 0.58
	Reconst.	- - -	- - -	- - -	- - -	- - -	1 3.73 - - -	- - -	1 4.13 - - -
	Resurfaced	2 4.02 0.45	7 4.06 0.15	6 3.71 0.41	4 3.52 0.21	1 4.16 - - -	14 3.95 0.20	2 4.15 0.10	18 3.81 0.59
	Terminal	4 3.25 0.34	12 2.85 0.72	4 3.67 0.12	13 3.01 0.65	2 3.26 0.89	17 3.24 0.55	2 4.12 0.04	14 3.07 0.77

FIGURE 5 Summary of results.

the standard deviation for all the studied sections located in that specific condition.

From that figure it is possible to conclude that the second category of use, "reconstruction," does not contain sufficient sections to allow a good statistical analysis. Therefore, this category was not considered for further analysis.

Data Analysis

Before performing the ANOVA, we must check the fundamental assumptions that are required in the analysis. The four traditional assumptions are: (*a*) variable of interest (*y*) is a random variable, (*b*) variances are homogeneous, (*c*) model used for the analysis is additive, and (*d*) response variable (*y*) is normally and independently distributed (*11*).

The analysis of the main factors (*R, P,* and *C*) was performed using the Generalized Linear Model (GLM) procedure available in SAS (*9,10*). The GLM procedure is used in data from an unbalanced design, such as the one in this study. The ANOVA variance model can be written as a linear model, in the form of an equation that predicts the response variable (SI) as a linear function of the design variables (*R, P,* and *C*) and their interactions (*R*P, P*C,* and *R*P*C*). In other words:

$$SI_{ijkl} = \mu + Ri + Pj + R*Pij + Ck + R*Cik + P*Cjk + R*P*Cijk + e(ijk)l$$

where:

SI_{ijkl} = serviceability index of section located on region *"i,"* for pavement type *"j"*, and category of use *"k";*
μ = overall mean;
Ri = effect of region *"i";*
Pj = effect of pavement type *"i";*
$R*Pij$ = effect of interaction of region *"i"* with pavement type *"j";*
Ck = effect of category of use *"k";*
$R*Cik$ = effect of interaction of pavement type *"j"* with category of use *"k";*
$P*Cjk$ = effect of interaction of pavement type *"j"* with category of use *"k";*
$R*P*Cijk$ = effect of interaction of region *"i"* pavement type *"j,"* and category of use *"k";* and
$e(ijk)l$ = random error of *"lth"* section in region *"i,"* with pavement type *"j,"* and in category of use *"k."* Where *"e"* is Normally and Independently Distributed with zero mean and variance s2, NID (0,s2).

The factors included in this analysis, besides the main factors (*P* and *C*), are the highway classification (*H*) and the surface type (*S*).

This part of the analysis will consider separately the flexible pavements from the rigid pavements. The main reason for that decision is that the two levels of surface types selected in this study for flexible pavements are completely different from the ones for rigid pavements (*12*).

Analysis of the Results

The previous section reported the statistical analysis of the data collected during the study. This section focuses on the physical interpretation of the results obtained.

Step 3 of the analysis concluded that climatic region does not have any influence in the variation of the SI around Texas (*12*). This conclusion confirms the initial assumption that the climatic zone does not appear to affect the quality of new or overlaid pavements, or how the engineers decide when to overlay a pavement. However, the climatic regions were included in the analysis mainly to provide a broader inference space for the results.

All cells in the factorial were filled except the one corresponding to a new flexible pavement located in Region I and under the category of use "reconstruction." Therefore, the conclusions obtained herein are good inferences for pavement conditions in Texas.

This section presents a discussion of the results obtained for flexible pavements, followed by the interpretation of the results for rigid pavements, then, a discussion of the variability of the serviceability index within section. Finally, a comparison among the SI values found in this research and the SI values reported in previous studies is presented.

Flexible Pavements

The analysis shows that the following pairs of average SI are statistically different (*12*): (*a*) Terminal SI of flexible pavements located on principal highways is higher than terminal SI of flexible pavements located on secondary highways, (*b*) SI of new flexible pavements located on principal highways is higher than terminal SI of flexible pavements located on principal highways, (*c*) SI of resurfaced pavements located on principal highways is higher than the terminal SI of pavements located on principal highways, and (*d*) SI of resurfaced pavements located on secondary roads is higher than the terminal SI of pavements located on secondary roads.

Furthermore, we may infer that the following pairs of average SI are statistically equivalent (*12*): (*a*) SI of new flexible pavements located on principal highways and SI of new flexible pavements located on secondary highways, (*b*) SI of resurfaced flexible pavements located on principal highways and SI of resurfaced flexible pavements located on secondary highways, (*c*) SI of new flexible pavements located on principal highways and SI of resurfaced flexible pavements located on principal highways, (*d*) SI of new flexible pavements located on secondary highways and SI of resurfaced flexible pavements located on secondary highways, and (*e*) SI of new flexible pavements located on secondary highways and terminal SI of flexible pavements located on secondary highways.

On the other hand, the analysis also shows that the following pairs of average SI are statistically different: (*a*) SI of resurfaced flexible pavements with asphalt concrete is higher than SI of resurfaced flexible pavements with surface treatment, (*b*) SI of new asphalt concrete pavements is higher than terminal SI of asphalt concrete pavements, (*c*) SI of resurfaced flexible pavements with asphalt concrete is higher than terminal SI of asphalt concrete pavements.

Furthermore, the following pairs of average SI are statistically equivalent (*12*): (*a*) SI for new asphalt concrete pavements and SI for new surface treatment pavements, (*b*) terminal SI for asphalt concrete pavements and terminal SI for surface treatment pavements, (*c*) SI of new asphalt concrete pavements and SI of resurfaced pavements, (*d*) SI of new surface treatment pavements and SI of pavements resurfaced with surface treatment, (*e*) SI of new surface treatment pavements and terminal SI of surface treatment pavements, and (*f*) terminal SI of surface treatment pavements and SI of pavements resurfaced with surface treatment.

Therefore, the conclusions for flexible pavements are: (*a*) principal highways, in general, have a better average SI than secondary roads, and (*b*) surface treatment does not improve the SI of a road. The average SI values for flexible pavements found in the analysis are summarized in Table 2.

Rigid Pavements

The average SI values for rigid pavements are shown in Table 3. The SI values of new, resurfaced, and terminal pavements are similar to each other, mainly, because their terminal condition has a high serviceability index. This situation is caused by the characteristic of the performance curve of rigid pavements and the criteria used by the engineers to decide when a rigid pavement needs rehabilitation. The main conclusion for rigid pavements is that the three levels of category of use on rigid pavements appear to be statistically equivalent.

TABLE 2 Average SI Values for Flexible Pavements

a) Category of use and highway classification

Category of Use	Highway Classification	
	Primary	Secondary
	mean	mean
New	4.0	3.0
Resurfaced	3.9	3.5
Terminal	3.2	2.8

b) Category of use and surface type

Category of Use	Surface Type	
	Asphalt Concrete	Surface Treatment
	mean	mean
New	4.0	3.0
Resurfaced	4.0	2.9
Terminal	3.2	2.9

TABLE 3 Average SI Values for Rigid Pavements

a) Category of use

Category of Use	Average SI - value
New	3.8
Resurfaced	3.9
Terminal	3.5

b) Highway classification

Highway Classification	Average SI - value
Principal	3.8
Secondary	3.3

c) Surface type

Surface Type	Average SI - value
Jointed	3.7
Continous	3.7

Variation of the SI Within a Section

The variation within a section was studied using the coefficient of variation (CV) of the SI values obtained in that particular section. According to Figure 6, the following pairs are statistically different: (*a*) CV for terminal rigid pavements is smaller than CV for terminal flexible pavements, (*b*) CV of new flexible pavements is smaller than CV for terminal flexible pavements, and (*c*) CV of resurfaced flexible pavements is smaller than CV of terminal flexible pavements. All the other combinations presented in Figure 6 show no significant differences.

The conclusions for the variability of the SI within section are: (*a*) rigid pavements have low variability at all three categories of use (new, resurfaced, and terminal) than flexible pavements; (*b*) terminal flexible pavements show an important variation in serviceability index; and (*c*) both rigid and flexible pavements have a low variability in the categories "new" and "resurfaced."

Comparison of SI Values

This part of the section presents a comparison among the SI values obtained in this study and the SI values recommended in the literature.

SI of New Pavements Table 4 summarizes the new SI values recommended by AASHTO (*1*), the state of Texas (*2*), and this study. The last row of this table shows the difference in percentage between the SI obtained in this research and the SI previously recommended by the state of Texas.

This table shows that the SI assumed on the design of new pavements has, on the average, never been reached in the field. For flexible pavements, the difference between the average SI value found in this study and the SI recommended in the Texas design manual is only about 5 percent for asphalt concrete, but it increases to 21 percent for surface treatment. For rigid pavements, the difference between the average SI found in this study and the SI recommended in the manual is, in general, higher than for flexible pavements. Specially, for CRCP, the average SI found in this study is 20 percent lower than the SI recommended in the Texas design manual.

SI of Resurfaced Pavements Table 5 summarizes the SI values recommended by the state of Texas (*2*) and the SI values found in this research. The state of Texas does not have any special recommendation for resurfaced pavements. For resurfaced pavements, in general, the present rehabilitation techniques do not produce pavements with the SI assumed in the design models.

For flexible pavements, the difference between the SI value found in this research and the SI assumed on the design is not so critical for asphalt concrete pavements, but it is important for surface treatment, where this difference is on the average 24 percent. For rigid pavements with an asphalt concrete overlay, the difference is 19 percent.

SI of Terminal Pavements Table 6 presents a summary of the terminal SI recommended in previous studies and compares them

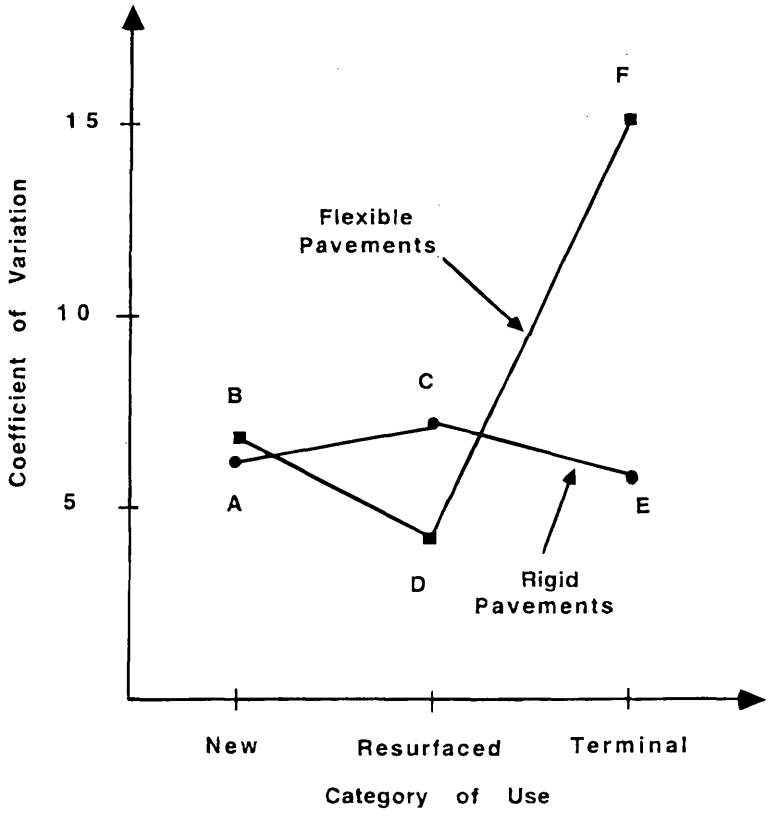

FIGURE 6 Pavement type and category of use—CV interaction.

TABLE 4 Comparison of New SI by Pavement Type

AGENCY	FLEXIBLE		RIGID	
	Asphalt Concrete	Surface Treatment	Jointed	Continuous
(1) AASHTO	4.2	- - -	4.5	- - -
(2) Texas (T)	4.2	3.8	4.5	4.8
(3) This Study (S)	4.0	3.0	3.8	3.8
Δ [S - T] (%)	-5%	-21%	-16%	-20%

TABLE 5 Comparison of Resurfaced SI by Pavement Type

AGENCY	FLEXIBLE		RIGID	
	Asphalt Concrete	Surface Treatment	Jointed	Continuous
(1) Texas (T)	4.2	3.8	4.5	4.8
(2) This Study (S)	4.0	2.9	3.9	3.9
Δ [S - T] (%)	-5%	-24%	-13%	-19%

TABLE 6 Comparison of Terminal SI by Pavement Type

AGENCY	FLEXIBLE		RIGID
	Primary	Secondary	Primary
(1) AASHTO	2.5	2.0	2.5
(2) BPR	2.1	1.8	2.2
(3) Project 354	3.1	2.2	3.1
(4) Texas (T)	3.0	2.5	3.0
(5) This Study (S)	3.2	2.8	3.5
Δ [S - T] (%)	+7%	+12%	+17%

with the SI obtained in this study. The previous terminal SI values shown in this table are recommended by: AASHTO (*1*), BPR (*6*), CTR—Project 354 (*7*), and the state of Texas (*2*).

This table shows that the Texas standards recommend higher terminal SI than the terminal SI recommended by the AASHTO. The terminal SI values found in this research are higher than the SI recommended by the State of Texas.

DISCUSSION, CONCLUSIONS, AND RECOMMENDATIONS

The main objective of this study was to obtain better estimates of the serviceability indices (SI) of the Texas highway system to be used in the Texas pavement management system. Three levels of SI were finally selected: new pavements, resurfaced pavements, and terminal pavements.

This section is divided in two sections. The first part summarizes the findings and the conclusions obtained during the study. The second part presents the recommendations derived from these findings.

The findings and conclusions are presented in four different categories: (*a*) general findings about the SI, (*b*) conclusions about flexible pavements, (*c*) conclusions about rigid pavements, and (*d*) conclusions about the variability of the SI.

General Findings

The findings of this research can be summarized as follows:

- SI for New Pavements: When the pavement is located on a principal highway, the initial SI is 4.0 for flexible pavements and 3.8 for rigid pavements. For secondary roads, the new SI is 3.0. The SI for new surface treatment is 3.0.

- SI after Resurfacing: When the pavement is located on a principal highway, the SI of resurfaced pavements is 4.0 for flexible pavements and 3.9 for rigid pavement resurfaced with asphalt concrete. For secondary roads, the SI is 3.5. When a surface treatment is used to resurface a pavement, the SI is 2.9.
- Minimum SI: When the pavement is located on a principal highway, the minimum SI of 3.2 was found for flexible pavements and 3.5 for rigid pavements. For secondary roads, the SI is 2.8. The terminal SI for surface treatment pavements is 2.9.
- Climatic regions do not affect the variability of the SI in Texas.
- The initial serviceability index (pi currently used by TxDOT) in its pavement design system is higher than the average SI observed in the field. This difference is 5 percent for asphalt concrete pavement and 20 percent for rigid pavements.
- The serviceability index after resurfacing (po used by the TxDOT) in its current pavement design system is higher than the average SI observed in the field. This difference is 5 percent for asphalt concrete pavements and 19 percent for rigid pavements.
- The minimum or terminal serviceability index pt currently used by TxDOT in its pavement design system is lower than the average SI observed in the field. This difference is 7 percent for asphalt concrete pavements and 17 percent for rigid pavements.

Conclusions

Flexible Pavements

The conclusions obtained in this research about the SI on flexible pavements can be summarized as follows:

- Surface treatment does not improve the SI of pavements.
- Principal highways, in general, have a better average SI than secondary roads.

Rigid Pavements

The conclusions obtained in this research about the SI on rigid pavements can be summarized as follows:

- There are no important differences in SI among the three levels of the category of use in rigid pavements (new, resurfaced, and terminal).
- The study shows no differences in SI between jointed pavements and continuous pavements.

Variability of the Serviceability Within a Section

The conclusions obtained in this research about the variability of the SI within section or project can be summarized as follows:

- Rigid pavements do not show an important SI variability in the three levels of the category of use analyzed.
- Flexible pavements show an important SI variability in terminal pavements.
- The SI variability of resurfaced flexible pavements is, in general, smaller than the SI variability of resurfaced rigid pavements.
- Both rigid and flexible new pavements have a low SI variability.

Recommendations

The following recommendations can be derived from the findings of this study:

- It is recommended that the SI values found in this study be implemented in all activities of the Texas pavement management system.
- It is not recommended to divide the state of Texas by climatic regions when analyzing serviceability.
- It is not recommended to use surface treatment to improve the SI of a pavement.
- The CV of the SI of a section could be used as a complementary tool to the decision making process when studying the alternative to rehabilitate flexible pavements.
- The CV of the SI of a section could be used as a complementary tool for the quality control of new pavements (rigid and flexible pavements).

REFERENCES

1. *AASHTO Interim Guide for Design of Pavement Structures 1972,* Chapter III Revised, AASHTO., 1981.
2. *Pavement Design System—Part I: Flexible Pavement Designer's Manual.* Highway Design Division, Texas Highway Department, 1972.
3. Kher, R. K., W. R. Hudson, and B. F. McCullough. *A System Analysis of Pavement Design and Research Implementation,* Research Report 123-5, Highway Design Division, Texas Highway Department, Texas Transportation Research—Texas A&M University, and Center for Highway Research, The University of Texas at Austin, January 1971.
4. Haas, R., W. R. Hudson, and J. Zaniewski. *Modern Pavement Management.* R. E. Kreiger Publishing Company, Malabar, Fla, 1994.
5. Anderson, V. L., and R. A. McLean. *Design of Experiments, A Realistic Approach.* Marcel Dekker, Inc., New York, 1974.
6. Bartelsmeyer, R. R., and E. A. Finney. *Use of AASHO Test Findings by The AASHO Committee on Highway Transport,* Special Report 73, Highway Research Board, 1962, pp. 415–438.
7. Nair, S. K., W. R. Hudson, and C. E. Lee. *Development of Realistic and Up-to-Date Pavement Serviceability Equations Using the New 690 D Surface Profilometer,* Research Report 354-1F, Preliminary Review Copy, Center for Transportation Research, The University of Texas at Austin, August 1985.
8. Lytton, R. L., and A. Garcia-Diaz. *Evaluation of AASHO Road Test Satellite and Environmental Studies,* Final Report, Research Foundation Project R. F. 4083, Texas Transportation Institute, Texas, September 1980.
9. SAS User's Guide: Basics. SAS Institute, Inc., Cary, N.C., 1985.
10. SAS User's Guide: Statistics. SAS Institute, Inc., Cary, N.C., 1985.
11. de Solminihac, H. *Serviceability Rating of the Texas Highway System for Pavement Management.* MS thesis, The University of Texas at Austin, 1986.
12. de Solminihac, H., W. R. Hudson, and E. Ricci. *Serviceability Ratings of the Texas Highway System for Pavement Management,* Research Report 400-1F. Center for Transportation Research, The University of Texas at Austin, 1986.

Publication of this paper sponsored by Committee on Pavement Monitoring, Evaluations, and Data Storage.

Development of Performance Prediction Models for Illinois Continuously Reinforced Concrete Pavements

YING-HAUR LEE AND MICHAEL I. DARTER

A new predictive modeling approach is presented and the approach for localized failures in Illinois continuously reinforced concrete pavements (CRCP) is demonstrated. Some data retrieval guidelines from the Illinois Pavement Feedback System data base is first presented. A preliminary data analysis was conducted to assist in data cleaning and assessing the variability of the data before the analysis was performed. Several modern regression techniques ("robust" and "nonparametric" regressions) were introduced in a proposed new predictive modeling approach. The proposed modeling approach was used to develop an improved model for localized failures in CRCP. The resulting model includes several variables such as cumulative ESALs, slab thickness, content and methods of the steel reinforcement, and base type for the prediction of CRCP failures. A sensitivity analysis was also performed to illustrate the effect of these variables on failures. Slab thickness and steel content are by far the most significant variables affecting failures. Crack spacing had no effect.

Continuously reinforced concrete pavements (CRC pavements or CRCP) have been extensively constructed throughout the 1960s and 1970s in Illinois. Approximately 60 percent of the Illinois Interstate highways (the third largest mileage in the nation) was originally constructed as CRC pavements. The main incentive for constructing CRC pavements was the elimination of contraction joints to minimize joint-related distresses. The structural integrity of the concrete slab is maintained by allowing the pavement to crack randomly while providing reinforcement to hold the cracks tightly. The major distress types that occurred in CRCP are localized failures (including punchouts and steel ruptures) and major spalling of transverse cracks.

The causes and factors relating to localized failures in CRC pavements have been a topic among many investigators in past years (*1–3*). Various algorithms and numerical models have been developed in an attempt to describe the behavior of a CRC pavement under contraction restraints. The main focus points of these algorithms and models are the prediction of crack spacing, crack width, concrete stress, and steel stress due to environmental changes and external wheel load. The cracking behavior due to the percentage of longitudinal steel reinforcement, concrete strength, aggregate type, and other environmental factors has also been analyzed in a work by Zollinger (*4*).

Most of the maintenance activities on CRC pavements are directly related to localized failures (i.e., punchouts and steel ruptures.) It is often necessary to estimate these distress quantities for preventive design and pavement rehabilitation planning. In an attempt to relate the total number of failures to traffic loading, slab thickness, percent steel reinforcement, and subbase types, the first known predictive model based on actual CRCP performance data was developed using the Illinois CRCP data base compiled during the research project IHR-901 (*2*).

As part of the project Implementation of Pavement Feedback System, a study of the effect of different placement methods of reinforcing steel (i.e., tubes versus chairs) on the performance of CRCP in Illinois was conducted (*5*).

Y.-H. Lee, Department of Civil Engineering, Tamkang University, E725, #151, Ying-Chuan Rd., Tarxsui, Taipei, Taiwan 25137, P.O.C. M. I. Darter, Department of Civil Engineering, University of Illinois, NCE L #12P, 205 N. Matthews Ave., Urbana, Ill. 61801.

DATA PREPARATION

The Illinois Pavement Feedback System (IPFS) data base (1977–1991), containing the most complete source of pavement-related information for Illinois Interstate highways, is the main source of data used for this study. It contains detailed information about original and rehabilitation construction contracts, pavement inventory data, materials, historical traffic data, distress survey, condition rating surveys, and maintenance and rehabilitation records. The IPFS data base is currently implemented in the Illinois Department of Transportation (IDOT) mainframe system (VM "I" system) using the NOMAD2 data base management program. Automatic summary reports of the pavement information may easily be generated. For the purpose of this study, it was decided, however, to download all the summary section information, traffic history, distress records, and rehabilitation history to a PC and store in several PC-SAS datasets for further analysis. The PC-SAS SUMMARY, TRANSPOSE, and TABULATE procedures (*6*) were used heavily to summarize the information of interest and to provide more reliable data for this study.

Design and Climatic Variables

The IPFS section summary data base includes codes for storing CRCP reinforcement data; however, few data on the type of steel reinforcement, diameter, spacing, and content are currently recorded in the data base. Fortunately, there exists some steel information, which was obtained from the IDOT district offices (*2*). This information was manually entered into the data base. In addition, IDOT's standard CRCP reinforcement designs (Standard 2225 and Standards 2225-1 to 2225-6) over the years were obtained for the rest of the CRC pavements for which no steel information was reported elsewhere. Generally speaking, the standard design of a given year was used to provide reinforcement data. The reinforcement type for these pavements was assumed to be deformed #5 and #6 bars for pavements constructed before and after 1981, respectively.

Different steel placement methods may affect the performance of CRCP pavements. Even though the IPFS data base includes a code for storing this information, very few data are recorded in the IPFS data base. Nevertheless, it is known that Illinois CRC pavements constructed before September 17, 1970, were mostly constructed using "chairs" with a few exceptions of "two-layer construction" for the steel placement. After this date pavements were constructed using "tubes" for placing reinforcement steels unless they were constructed in District 1, where chair placement was required. Therefore, this date was used as the cutoff point to determine whether the "chairs" or "tubes" placement method was used for a given CRC pavement.

Some additional construction data about drainage system, base type, and environmental data were also obtained. In addition, data on various subbase types, including granular, crushed stone, bituminous-aggregate mixture (BAM), and cement-aggregate mixture (CAM), were directly retrieved from the IPFS data base. Climatic data such as freezing index, average annual temperature, and average annual precipitation were also obtained.

Traffic Calculation and Estimation

Traffic maps for average daily traffic, heavy commercial traffic, and multiple unit traffic volumes are published approximately every four years by the IDOT Office of Planning and Programming. The yearly traffic history recorded in the IPFS data base was determined by interpolating between those four-year periods.

Because the IPFS data base contains traffic information only up to 1987, it is necessary to estimate the traffic growth rate for each pavement section. A NOMAD2 program was written to perform automatically a huge array of regression analyses assuming that the traffic was increasing yearly with constant compound growth rates. With the estimated average daily traffic and ESAL traffic growth rates, the latest 1987 traffic data were then used as a starting point to predict the traffic into the future.

Distress Quantities

The CRCP failures were recorded in various visible distress types, severities, amounts, and repairs in the distress data base. For example, a certain amount of medium-severity transverse cracking became high severity after a certain period of time; at the same time, some of the high-severity transverse cracking was corrected by full-depth repairs. To obtain a good single indicator of CRCP failures in each survey year, special efforts were conducted in deciding what distress types and severities should be included. After a considerable amount of effort and reexamination, the total number of CRCP failures (FAIL) per mile was defined as follows:

$$FAIL = 8.8\,PATCH + PUNCH + MHPOT + HTCRK \quad (1)$$

where

PATCH = all severities of permanent patches, percent area;
PUNCH = all severities of punchouts, #/mi;
HTCRK = high-severity transverse cracking, #/mi; and
MHPOT = medium- and high-severity of potholes and localized distresses, #/mi.

Because permanent patch deterioration was recorded in percent area of pavement surface, it was necessary to convert into number of patches per mile by assuming a $6 * 12$ ft^2 per patch. In addition, high-severity transverse cracking was included and treated as an indication of steel rupture. Medium-severity transverse cracking was not included here because there were good chances that different surveyors rated low severity and medium severity inconsistently.

In this study, if the pavement was surveyed but without the aforementioned distress types recorded in the data base, the total number of failures was assigned to zero for later analysis. On the other hand, those unsurveyed pavement sections were excluded from the consideration, for example, pavements located in Chicago area (District 1) where detailed surveys were not possible because of the heavy traffic conditions.

Additional Data from Old Vandalia Experimental Study

The longitudinal reinforcing steel content is known to have a very strong effect on the performance of CRCP pavements. Inadequate steel content often results in longer crack spacings, wider crack widths, and thus more punchout failures. To extend the range of analysis, several sections from the Vandalia CRCP experiment study (7) were also included in this study.

Eight sections of 7-in. and 8-in. experimental CRCP with 0.3, 0.5, 0.7, and 1.0 percent of longitudinal reinforcement constructed in 1947 to 1948 on US 40 west of Vandalia, Illinois, were studied over a 20-year service period (7). These pavements were placed directly on natural fine-grained soil and carried 4.27 million ESALs in 20 years. Many failures occurred in the 0.3 and 0.5 percent reinforcement sections in the 7-in. pavements.

Two major distress quantities, namely cracking (lin. ft/1000 ft^2) and patching (ft^2/1000 ft^2) were of particular interest (7) to quantify the equivalent total number of CRCP failures in these pavements. The reported cracking was defined as "cracks that are open or spalled at the surface to a width of 1/4in. or more for at least half the crack length, and sealed cracks" (7). Because most of them were still in a workable condition even after 20 years of service, only patching quantities were converted into total number of failures per mile for this study.

PRELIMINARY DATA ANALYSIS

Distress History and Additional Codes

A data cleaning process must be conducted before any regression analysis can be performed. With the help of graphical representation, failures were plotted against surveyed years for each section in the data base with additional information about route, direction, mileposts, D-cracking, slab thickness, and constructed year displayed. For example, a plot as shown in Figure 1 was used to examine the distress trends to eliminate possible data errors. The upper left-hand corner plot labeled '55-N-33.67-39.13-N-9"CRCP, conyr=75' indicated that a pavement located on I-55, northbound, mileposts 33.67 to 39.13, non–D-cracked, 9-in. CRCP, and constructed in 1975 was surveyed in 1985, 1987, and 1989 with approximate failures of 7, 6, and 15, respectively.

Each section was carefully examined. Two additional codes were assigned to each section to indicate the findings of the examination. The first code was used to indicate whether the total number of failures is reasonable according to the distress history. The second code supplements the first code to indicate which year of data to be

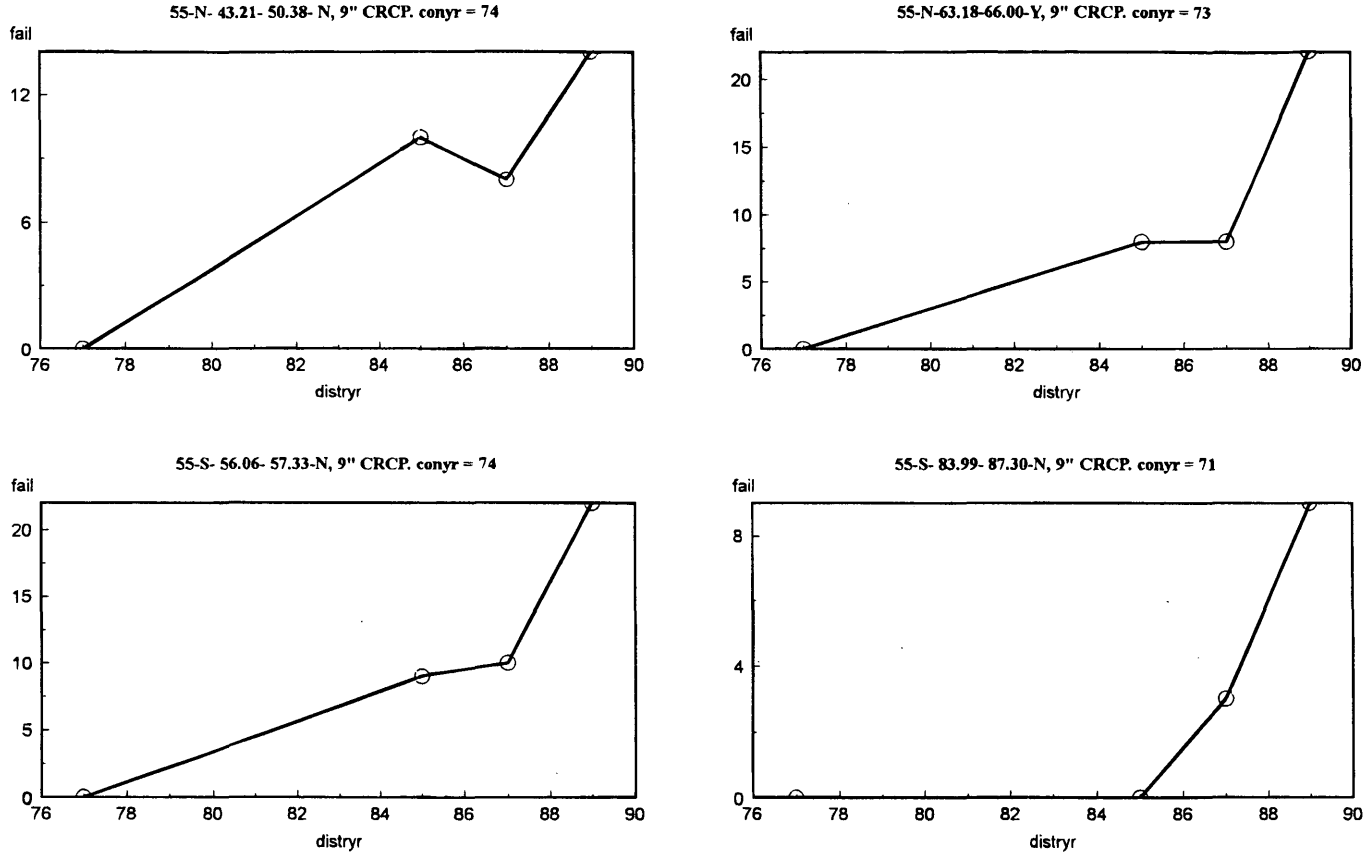

FIGURE 1 Sample plots of distress history along I-55.

deleted if necessary. Data correction was made in a way that could easily be traced back. A third code was also introduced to indicate the reliableness of the steel information. By doing so, different subsets of the final data base providing more reliable data might be analyzed for different purposes.

Final Data Base with Non–D-Cracked CRC Pavements

D-cracking is a serious problem in Illinois Interstate concrete pavements. The presence of this type of distress causes the pavement to deteriorate prematurely. The number of sections with and without D-cracking based on different slab thicknesses was summarized after deleting those sections having unrealistic distress history, a particular suspicious data point, or unreliable calculated crack spacings. The results showed that approximately 60 percent of 7-in. IPFS sections were D-cracked whereas 40 percent for 8-in. and 20 percent for 9-in. pavements were D-cracked. No 10-in. CRCP pavements were recorded as D-cracked pavements. After carefully cross-examining the data, excluding all D-cracked pavements, and deleting seven IPFS data points with extremely large numbers of failures (greater than 100 failures per mile) a data base with 586 data points was finally created for later analysis.

Correlation of Variables

A matrix plot containing the most important variables considered in this study are given in Figure 2. The variable correlations can be visually inspected through these plots. In addition, trimmed correlation matrixes showing the variable correlations after a certain portion of influential data points or possible outliers are eliminated were also obtained.

CRCP failures (indicated as "distr") were strongly correlated with age and cumulative ESAL (cesal) as expected even after 20 percent of data was trimmed. However, the correlations of slab thickness (pavthk), steel content (percent reinforcement, area of longitudinal reinforcement, and bonded area) to CRCP failures change dramatically. These are good indications of having influential data points in these variables, which should be used with extreme caution in later analysis.

The interrelationship between age and cumulative ESAL is also evident. The strong correlation between slab thickness and area of reinforcement almost guarantees the presence of one or the other in the later CRCP failure model development, but never both together to avoid strong collinearity in the model. This is also true for bonded area and percentage of reinforcement. Among these most important variables to CRCP failures, slab thickness, percent of reinforcement, and cumulative ESAL were chosen in the final CRCP failure model.

Factor Space and Limitations

The final data base was mainly constructed from the in-service pavements, which satisfies certain design guidelines. Thicker pavements were designed to carry heavy traffic loadings. A relatively constant percentage of longitudinal reinforcement was often used.

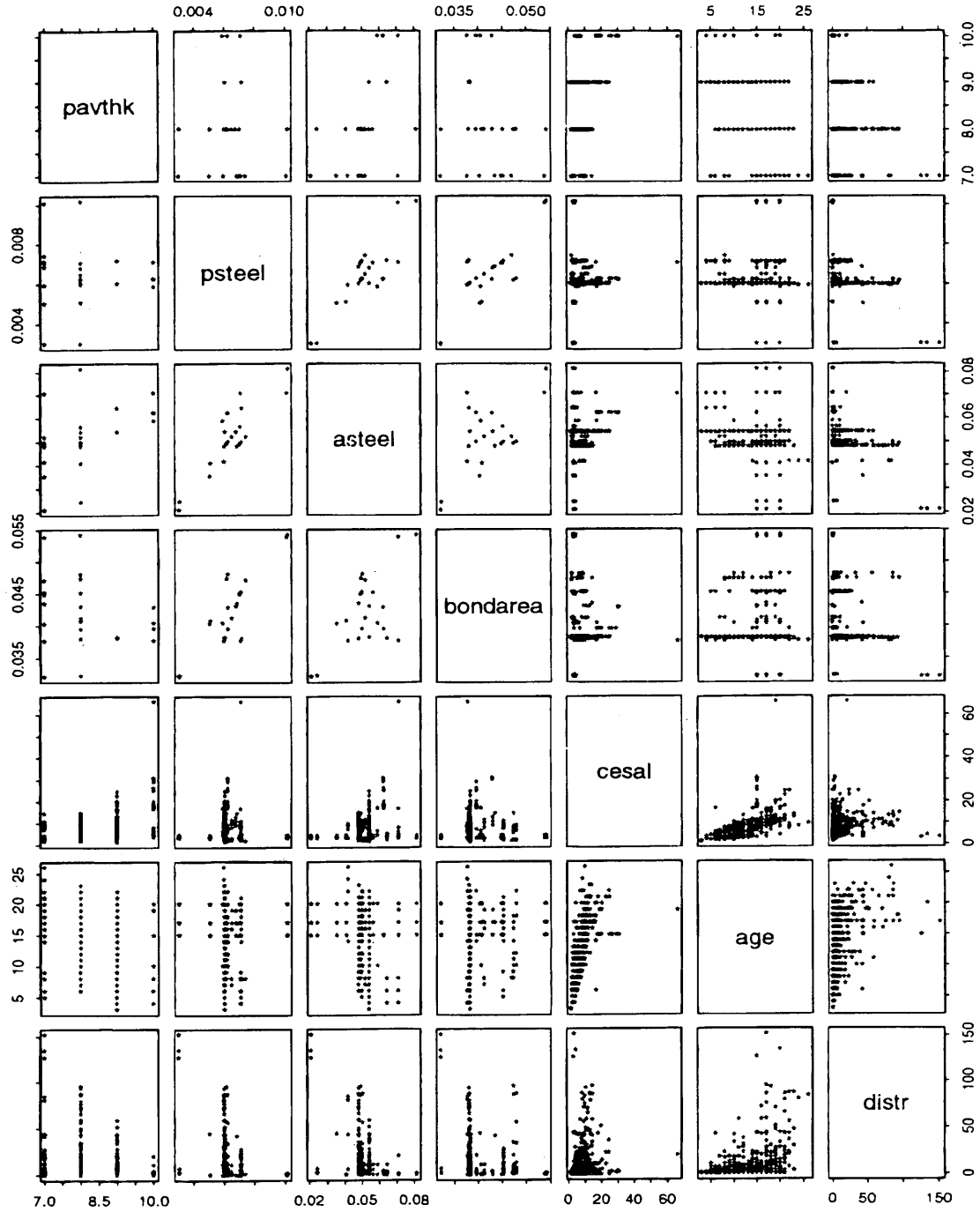

FIGURE 2 Matrix plot with most important variables to CRCP failures (distr = failures/mi).

For example, there was limited range of reinforcement content in the data except for the Vandalia experimental sections. Vandalia experimental sections provided some very low and very high steel contents for 7- and 8-in. pavements. However, there existed no such steel contents for 9- and 10-in. in-service pavements. Most of the final data base was 8- and 9-in. pavements, which had a fixed reinforcement content of approximately 0.60 to 0.62 percent.

In addition, the Vandalia experimental data were obtained under very low traffic (i.e., up to 4.3 million ESALs in 20 years). There existed no very low or very high steel contents under very high traffic loading conditions. Knowing that the deficiencies of the unbalanced factor space of the final data base exist, extreme care should be used during the modeling process as well as deriving conclusions beyond the range of data.

Variability of Data

Because most of the final data base was 8-and 9-in. pavements with constant reinforcement contents of approximately 0.60 to 0.62 per-

cent, a preliminary examination of the relationships among CRCP failures, age, and cumulative ESALs was performed. Under similar design conditions (BAM subbase, drainage system, and "tubes" reinforcement placement method), the performance of these two groups of 8- and 9-in. pavements showed high variation.

This high variation might be the result of some other hidden variables not considered in this study. However, it is also believed that the current practice of sampling only 10 percent of the entire project may be the major source of these variations. For example, three identical 1-mi pavement sections when surveyed in their first 0.1 mi and recorded to have 0, 1, and 2 failures might end up with 0, 5.3, and 10.5 failures per mile.

It is recommended that a full-length survey might be the best solution to minimize this high variability in the total number of failures counted. If this is not possible, a much higher portion of the project such as 20 to 30 percent should be surveyed instead so that the accuracy of the IPFS data base can be improved.

PROPOSED NEW PREDICTIVE MODELING APPROACH

The proper selection of regression techniques is one of the most important factors to the success of prediction modeling. Traditional "parametric" regression techniques such as linear and nonlinear regressions require imposing a parametric form on the functions and then obtaining the parameter estimates. With the multi-dimensional pavement engineering problems in mind, several unresolved deficiencies were frequently identified in the use of traditional stepwise regression and nonlinear regression. These include problems in the selection of correct functional form, large influence of potential outliers, violations of the embedded statistical assumptions, and failure to satisfy some engineering boundary conditions.

Because of the innovation of computers and the almost unlimited computing power, several ingenious iterative regression techniques in the area of "robust" and "nonparametric" regressions have been developed in the past 10 years and have gradually gained popularity. They are useful especially in situations in which large data contamination and little knowledge about the shape and the form of a function exist. For this study, particular attention is focused on the following advanced modern regression techniques (*8*):

1. Least median squared (LMS or "Robust") regression (*9,10*): a robust regression technique, extremely powerful in detecting outliers in either response variable or predictor variables;
2. Alternating conditional expectations (ACE or "Expectation") (*11*): a nonparametric regression technique, providing optional variable transformations to maximize the squared multiple correlation (R^2); and
3. Additivity and variance stabilization (AVAS or "Stabilization") (*12*): a nonparametric regression technique, transforming both sides of the additive model to achieve constant error variance assumption.

Without imposing an unjustified parametric assumption, nonparametric regression techniques strive to estimate the actual functional form that best fits the data through the use of scatter plot smoothers. They can be excellent supplements to traditional parametric regression techniques, especially in suggesting proper transformations of the response variable and the predictor variables to help uncover the underlying relationships and to satisfy some applicable boundary conditions.

A new statistical package named S-PLUS, which has been widely used by statisticians for data analysis, was selected because of the availability of these new regression techniques.

Multiple Linear Regression

Multiple linear regression is one of the most time-honored and widely used regression techniques for the study of linear relationships among a group of measurable variables. Suppose there exists a true model to describe the relationship between response variables (*y*s) and explanatory variables (or predictors, *x*s) (*13*):

$$y_i = x_i^T \beta + \epsilon_i \qquad i = 1, \ldots, n \tag{2}$$

where x_i^T is the ith row of the $(n \times p)$ matrix X of the column of 1s if including an intercept and the explanatory variables. The superscript T denoting the transpose of the column vector x_i is required because of the usual convention that all vectors are represented by column vectors. β is a $(p \times 1)$ vector of unknown regression coefficients and p and n are the number of parameter estimates in the model and the total number of observations, respectively.

The basic assumptions are usually that the random errors (ϵs) are mutually uncorrelated and normally distributed with zero mean and constant variance, and additive and independent of the expectation function. For any arbitrary β value of $\hat{\beta}$, the residuals $r_i(\hat{\beta})$ can be determined by the following expression:

$$r_i(\hat{\beta}) = y_i - x_i^T \hat{\beta} \qquad i = 1, \ldots, n \tag{3}$$

Based on those assumptions, multiple regression tries to find a set of parameters β such that the sum of the squared residuals given in Equation 4 is minimized, which is also best known as the least squares (LS) method.

$$RSS(\hat{\beta}) = \sum_{i=1}^{n} [r_i^2(\beta)] = r_1^2(\hat{\beta}) + r_2^2(\hat{\beta}) + \ldots + r_n^2(\hat{\beta}) \tag{4}$$

Nonlinear Regression

Practical real-world problems are often found to be nonlinear in nature. Because of its favorable feature of handling a complicated nonlinear model, nonlinear regression has been widely used as a modeling technique. However, nonlinear models are more difficult to specify and develop than linear regression models. "Some models are difficult to fit, and there is no guarantee that the procedure will be able to fit the model successfully" (*14*).

Suppose there exists a true model that best describes the relationship between response variables (*y*s) and explanatory variables (*x*s), (*14,15*):

$$y_i = F(\beta, x_i) + \epsilon_i \qquad i = 1, \ldots, n \tag{5}$$

where

$F(\beta, x_i)$ = nonlinear function based on the predictors,
β = $(p \times 1)$ vector of unknown regression coefficients to be estimated,
and n = total number of observations.

Similar to linear regressions, the disturbance (or error) term is usually assumed to be additive, mutually uncorrelated, and normally distributed with zero mean and constant variance. For any arbitrary β value of β, the residuals $r_i(\beta)$ are

$$r_i(\hat{\beta}) = y_i - F(\hat{\beta}, x_i) \qquad i = 1, \ldots, n \tag{6}$$

Unlike linear regressions whose parameters can be explicitly estimated by a closed-form expression, nonlinear regressions must use an iterative routine to find the best parameter estimates ($\hat{\beta}$) such that the sum of the squared residuals as given in Equation 4 is minimized.

LMS or "Robust" Regression

Recently, new robust statistical techniques have been developed to avoid the large influence of outliers. The results of these methods are still trustworthy even if a large amount of data is contaminated. They are extremely useful in identifying a group of potential outliers in a single attempt. Of many robust regression techniques, the least median of squares estimator introduced by Rousseeuw (*9*) and Rousseeuw and Leroy (*10*) is the most robust with respect to outliers in the dependent variable as well as outliers in the independent variables or predictors.

It is assumed that the true model and the residuals are the same as those given in Equations 1 and 2, respectively. The LMS estimator ($\hat{\beta}$) attempts to minimize the median instead of the sum of the squared residuals defined as follows:

$$RMS(\hat{\beta}) = \underset{i=1}{\overset{n}{\text{med}}} \{r_i^2(\hat{\beta})\} = \text{med}\,[r_1^2(\hat{\beta}), r_2^2(\hat{\beta}), \ldots, r_n^2(\hat{\beta})] \tag{7}$$

As Rousseeuw stated, LMS regression first tries to fit most of the data and then discover the potential outliers. The LMS method has a breakdown point of 50 percent, which is the largest possible value, whereas the LS method has a breakdown point of 0 percent. The breakdown point of a regression estimate is defined as the largest fraction of data that may be replaced by any arbitrary values without causing arbitrary parameter estimates. This means that the LMS estimates still continue to follow the trend of most of the data even when almost half is arbitrarily corrupted. Geometrically, it corresponds to finding the narrowest band that covers at least half of the observations such that potential outliers are discovered (*10*).

The advantages of LMS regression are obvious especially when analyzing field-collected pavement data that may contain as much as 10 to 20 percent contaminated data. "Robust" regression provides a more objective way to help identify some potential data and model problems. These problems include actual data errors, data from a different population, and the inadequacy of the regression model due to missing some important variables.

Thus, once these trouble data points are identified, more detailed investigations should be conducted to find out why and how they are different from the other tentative good ones. Some trouble data points may possibly be identified as errors and subsequently be corrected or excluded from the analysis. The possibility to include other explanatory variables or other model forms in the model should also be fully investigated to improve the fit including all the data points. It should be emphasized, however, that no data should be deleted without having justifiable reasons to do so. By conducting these analyses in an iterative manner, it is strongly believed that more reliable predictive models may be developed.

ACE or "Expectation" Algorithm

An algorithm to find the optimal transformations of the response variable and the predictor variables such that the R-square of a multiple regression is maximized was introduceful. Suppose that there exists a true additive model given as follows:

$$\theta(y) = \phi_1(x_1) + \phi_2(x_2) + \ldots + \phi_p(x_p) + \varepsilon \tag{8}$$

where

y = response variable,
$x_1, x_2, \ldots, x_p$ = predictor variables,
$\theta(y), \phi_1(x_1), \phi_2(x_2), \ldots, \phi_p(x_p)$ = unknown nonparametric transformation functions of each variable to be estimated, and
ε = random error.

The proposed algorithm uses a sophisticated supersmoother while it alternatively changes the conditional expectation functions to minimize the fraction of variance (e^2) not explained by regressing $\theta(y)$ on $\phi_1(x_1), \ldots, \phi_p(x_p)$. This algorithm is often called alternating conditional expectations algorithm. The e^2 given in the following expression is also called the goodness-of-fit measure (*8*).

$$e^2(\theta, \phi_1, \ldots, \phi_p) = \frac{E\left[\theta(y) - \sum_{i=1}^{p} \phi_i(x_i)\right]^2}{E\theta^2(y)} \tag{9}$$

This "nonparametric" algorithm will only give back data-dependent estimates of variable transformations that are not restricted to any particular functional form. However, the data analyst might be able to estimate particular parametric transformation for each variable by plotting the suggested transformed variables versus the original ones. The traditional Box-Cox transformation technique can be used for this purpose. If the suggested transformations are so desirable that a single family of power transformation is not adequate, polynomial regression, nonlinear regression, or any other curve fitting techniques can also be applied separately for the transformation of each variable. Thus, the R-square of the final additive model is optimally maximized.

The "Expectation" algorithm provides a fully automated routine to assist in selecting the optimal form of transformations for response and predictor variables. However, it should be used with caution, especially in the presence of outliers. Furthermore, because a smoothing technique often requires a certain number of degrees of freedom, the transformed vectors might be highly unstable if the number of observations is not large enough. The ACE algorithm may still produce strong looking transformations when there is little or no relationship between the predictors and the response variable. This problem may be detected by the resulting relatively small R^2. More detailed discussions of its applications and limitations are given elsewhere, (*8,11,16*).

AVAS or "Stabilization" Algorithm

In 1987, Tibshirani (*12*) successfully introduced the additivity and variance stabilization algorithm by applying the same alternatively backfitting techniques used in the Expectation algorithm. In contrast to the ACE algorithm that tries to maximize the squared multiple correlation (R^2), the Stabilization algorithm strives to achieve the

constant error variance assumption of regression and also improve the model fit.

Assuming that there exists an additive model of the same form given in Equation 8, the AVAS algorithm tries to achieve the following two goals simultaneously (*8*):

$$E[\theta(y) \mid x_1, x_2, \ldots, x_p] = \sum_{i=1}^{p} \phi_i(x)_i \quad (10)$$

$$\text{VAR}[\theta(y) \mid \sum_{i=1}^{p} \phi_i(x_i)] = \text{Constant} \quad (11)$$

where $E[z \mid w]$ and VAR$[z \mid w]$ stand for the conditional expectation function and the conditional variance function of z given w, respectively.

The AVAS transformation is more flexible than the traditional Box-Cox method and is often better suited to regression problems than the ACE algorithm (*8,12*). Because the objective functions that they attempt to optimize are different, the ACE and the AVAS transformations behave differently for different situations. It is too early to say which one is better. In general, some evidence shows that the AVAS algorithm is better behaved than the ACE algorithm when there is little or no relationship between the predictors and the response variable.

Proposed New Predictive Modeling Approach

For practical engineering problems, often little knowledge about the true functional form is available and the data collected are also confounded with substantial errors. So far there exists no regression algorithm that can perform outlier detections and variable transformations simultaneously to minimize these problems. To develop a more reliable predictive model for such complicated problems, it is proposed to incorporate the Robust regression, Expectation, and Stabilization algorithms into the modeling process.

The Robust regression is proposed because of its favorable feature of analyzing highly contaminated data by detecting outliers from dependent and independent variables. Through the iterative use of the combination of these outlier detection and nonparametric transformation techniques, it is believed that some potential outliers and proper functional forms may be identified. Subsequently, traditional regression techniques can be used more easily to develop the final predictive model.

The basic procedures and concepts behind the proposed modeling approach are briefly discussed. First, assume a plausible linear model relating the response variable to the explanatory variables. Then, apply Robust regression to delete some potential outliers based on the assumed model form. Subsequently, apply the Exception and Stabilization algorithms to find possible variable transformations that best fit the remaining data. The transformed vectors are then plotted against each original variable. In addition, a plot of the predicted versus the actual values and a plot of the residual versus the predicted values are also provided.

Through visual inspections, the reasonableness of the suggested transformations and the goodness of the fit can be easily accessed. Because the suggested transformations for each variable are displayed in two-dimensional plots, they can be properly formulated using traditional Box-Cox transformation, linear (or polynomial) regression, and nonlinear regression. These tasks are relatively easy, because they involve only one variable at a time.

Then, revise the assumed linear model using the suggested transformations and repeat the entire process until the detected outliers and the suggested transformations are acceptable. Finally, traditional linear regression is used to get the final regression statistics and diagnostics of the additive model using the transformed variables. Step-by-step procedures for the proposed new predictive modeling approach are summarized in Figure 3.

The potential outliers detected by Robust regression are temporarily excluded from the subsequent Expectation and Stabilization trials to minimize the influence of possible data errors. However, these data points should be added back to the original data base when analyzing the next trial linear model form. This is because the potential outliers detected by Robust regression may be affected by the assumed trial linear model form, but they may not be actually bad data points. The resulting transformations suggested by the Expectation and Stabilization algorithms may also be affected by excluding those data points. During each iteration, however, some erroneous data may be identified and subsequently eliminated form the analysis. These procedures can be routinely performed until an acceptable model is obtained.

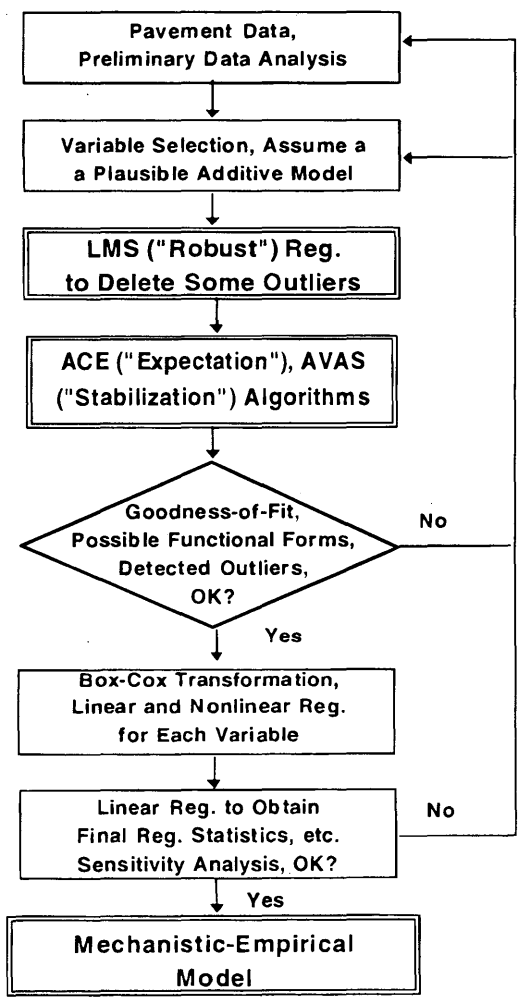

FIGURE 3 Proposed modeling procedures for outlier detection and selection of proper functional forms.

PROPOSED CRCP PERFORMANCE PREDICTION MODELS

As expected, developing a predictive model to adequately fit this type of data is not an easy task. Some preliminary trials using the traditional linear and nonlinear regression techniques have had difficulty in achieving a satisfactory model for the data.

The proposed new predictive modeling approach as described in the previous section was followed closely and used routinely to develop an improved model. This approach proved to have substantial improvement over the use of traditional regression techniques alone in an attempt to uncover the underlying relationships together with the consideration of the possible influence of outliers.

The results of many LMS regression trials indicate that a large portion of the zero failures in the data is questionable in spite of different model forms analyzed. Most of these zero failures were forced into the final data base because of some evidence showing that the given pavement section was surveyed but did not have any of these failures recorded in the original IPFS data base. By excluding these forced-in data points, a better model with more reasonable predictions could be developed, although very high variations were still present.

Several dozen predictive models using different model forms were developed with similar prediction accuracy. The final proposed model for predicting the number of CRCP failures on a per mile basis is given as follows:

$$\log_e(\text{FAIL}) = 6.8004 - 0.0334 * \text{PAVTHK}^2 - 6.5858 * \text{PSTEEL} + 1.2875 * \log_e(\text{CESAL}) - 1.1408 * \text{BAM} - 0.9367 * \text{CAM} - 0.8908 * \text{GRAN} - 0.1258 * \text{CHAIRS} \quad \text{statistics: } R_2 = 0.44, \text{SEE} = 1.06, N = 408 \tag{12}$$

where

FAIL = total number of failures in outer lane, #/mil;
THICK = CRCP slab thickness, in.;
PSTEEL = longitudinal reinforcement, percent;
CESAL = cumulative ESALs, millions;
BAM = 1 if subbase material is bituminous-aggregate mixture, 0 otherwise;
CAM = 1 if subbase material is cement-aggregate mixture, 0 otherwise;
GRAN = 1 if subbase material is granular, 0 otherwise; and
CHAIRS = 1 if chairs used for reinforcement placement, 0 if tubes used.

The regression summary outputs and the goodness-of-fit of the proposed model were presented elsewhere (*5*). Notice that a small number of 0.1 is added to the actual total failures ("distr") to avoid numerical difficulties. This model also satisfies the boundary condition of resulting zero failures when no traffic exists.

Some plots showing the sensitivity of the various factors in the proposed model are presented in Figures 4 and 5. Figure 4 shows the relationships among cumulative ESALs, slab thickness, reinforcement content, and total number of failures per mile (fit). Figure 5 shows the effects of reinforcement placements and different base types. The general trends of the effects appear to be reasonable. Note that the plots are extended a bit beyond the range of the actual data to show how the model performs. The reinforcement content of a given CRC pavement has a large effect on the occurrence of failures.

The proposed model also includes the type of reinforcement placement (CHAIRS). The use of chairs results in fewer total failures; however, the difference is not significant. Even though the analysis does not provide a lot of support for the placement method

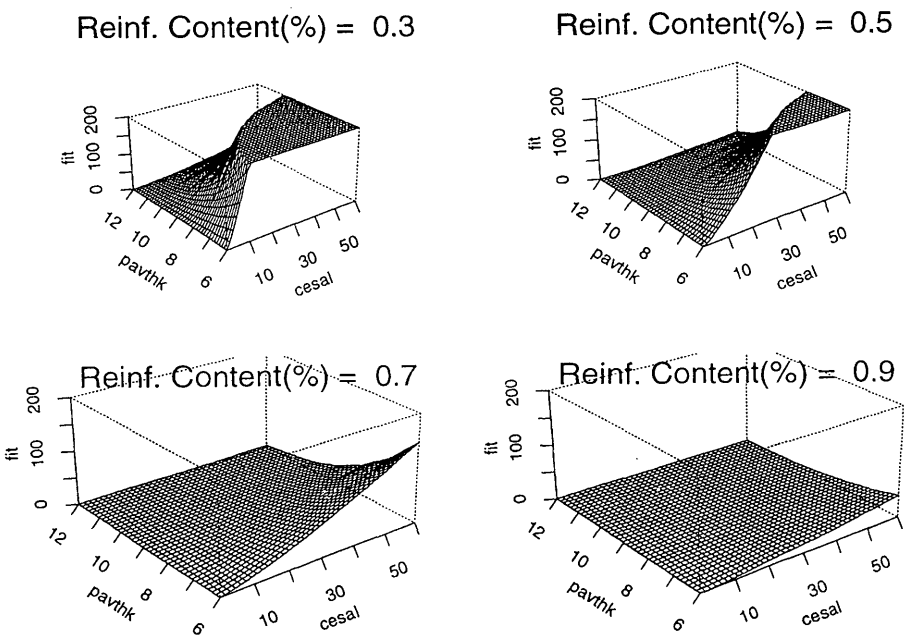

FIGURE 4 Three-dimensional sensitivity analysis for reinforcement contents (plot truncated at 200 failures/mi).

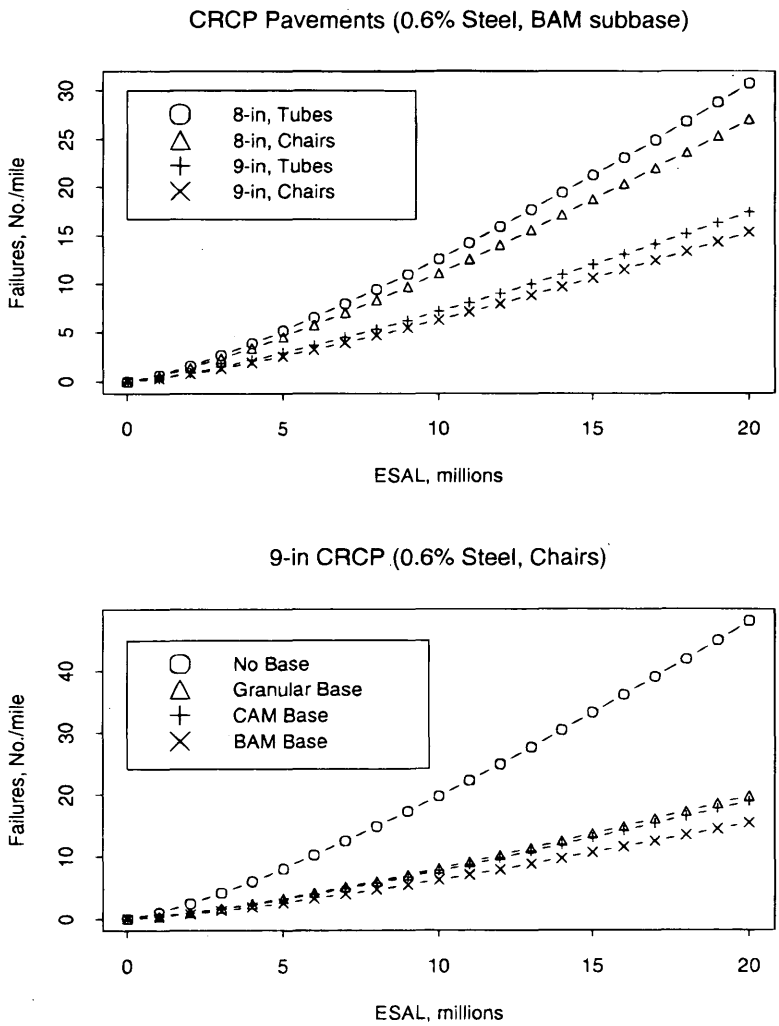

FIGURE 5 Two-dimensional sensitivity analysis; reinforcement placements and base types.

having a significant effect on the development of CRCP failures, this does not necessarily prove that this is the case. As previously discussed, the data base does not provide a clean separation of two identical groups of CRC pavements (i.e., one with tube placement and the other with chair placement). Many factors may be interacting with thickness, traffic loading, or other factors to cause the true effect of placement type to be hidden.

Some research performed in Illinois on I-70 has clearly shown that the depth of reinforcing steel greatly affects the crack width and thus the breakdown of cracks and development of CRCP failures. Thus, if the tube placement method results in a greater variation in depth of steel, there would likely be a greater chance for more failures. This may be the case even though the data did not clearly show this to be true.

The effects of different base materials were also investigated. A CRC pavement with BAM base has the best overall performance, which also agrees with previous findings (*17*). On the other hand, a conclusion different from the previous literature (*17*) is derived from this analysis that CAM base has about the same effect on the development of CRCP failures as granular base.

SUMMARY AND CONCLUSIONS

A study of the factors affecting the performance of CRCP was conducted using the in-service IPFS data base. Detailed guidelines for data preparation are provided. The entire performance records of bare CRC pavements in Illinois were retrieved. In addition, some of the old Vandalia experimental sections were included in this study because they provided additional ranges in steel content (0.3 to 1.0 percent). The data were cleaned carefully to remove sections that had D-cracking, questionable data (high failures), very short sections, and so forth because these would only increase the potential errors.

A preliminary data analysis was conducted to assist in data cleaning, assess the variability of the data, and understand the interrelationships between variables before actually performing the regression analysis. Very high variations of the data are evident, suggesting that the current practice of surveying 10 percent of the entire pavement network may be inadequate.

Several modern regression techniques (robust and nonparametric regressions) were introduced in a proposed new predictive modeling approach with detailed step-by-step guidelines. The proposed

modeling approach was routinely used to derive a more reliable predictive model. The resulting model includes several variables such as cumulative ESALs, slab thickness, content and methods of the steel reinforcement, and base type for the prediction of CRCP failures. A sensitivity analysis was also performed to illustrate the effect of various factors in the model, which also appeared to be reasonable.

ACKNOWLEDGMENTS

This research was originally sponsored by IDOT. The authors are grateful to David Wheat, David Lippert, and James Hall for their assistance. The support obtained from Tamkang University and the University of Illinois to finish this research work is also greatly acknowledged.

REFERENCES

1. Ma, J., and B. F. McCullough. *NCHRP Report 177-9: CRCP-2, An Improved Computer Program for the Analysis of Continuously Reinforced Concrete Pavements.* TRB, National Research Council, Washington, D.C., Aug. 1977.
2. LaCoursiere, S. A., M. I. Darter, and S. A. Smiley. *Performance of Continuously Reinforced Concrete Pavement in Illinois.* Illinois Cooperative Research Report 901-1, University of Illinois, Urbana, Dec. 1978.
3. Zollinger, D. G., and E. J. Barenberg. *Thickness Design Procedure for Continuously Reinforced Concrete Pavements.* Illinois Cooperative Highway Research Report IHR-518-3, University of Illinois, Urbana, May 1988.
4. Zollinger, D. G. *Investigation of Punchout Distress of Continuously Reinforced Concrete Pavement.* Ph.D. Thesis, University of Illinois, Urbana, 1989.
5. Lee, Y. H. *Development of Pavement Prediction Models.* Ph.D. Thesis, University of Illinois, Urbana, 1993.
6. *SAS User's Guide: Basics.* Ver. 5 Edition, SAS Institute, Inc, Cary, N.C; 1985.
7. Burke, J. E., and J. S. Dhamrait. A Twenty-Year Report on the Illinois Continuously Reinforced Pavement. On *Highway Research Record 239,* HRB, National Research Council, Washington D.C., Highway 1968, pp. 197–211.
8. *S-PLUS for Windows: User's Manual.* Vol. 1 and Vol. 2, Statistical Sciences, Inc, Seattle, Washington, March 1993.
9. Rousseeuw, P. J. Least Median of Squares Regression. *Journal of the American Statistical Association,* Vol. 79, 1984, pp. 871–880.
10. Rousseeuw, P. J., and A. M. Leroy. *Robust Regression and Outlier Detection.* Wiley Series in Probability and Mathematical Statistics, John Wiley & Sons, Inc., New York, 1987.
11. Breiman, L., and J. H. Friedman. Estimating Optimal Transformations For Multiple Regression And Correlation (With Discussion). *Journal of the American Statistical Association,* Vol. 80, 1985, pp. 580–619.
12. Tibshirani, R. Estimating Transformations for Regression via Additivity and Variance Stabilization. *Journal of the American Statistical Association,* Vol. 83, 1987, pp. 394–405.
13. Weisberg, S. *Applied Linear Regression.* Second Edition, Wiley Series in Probability and Mathematical Statistics, John Wiley & Sons, Inc., 1985.
14. *SAS User's Guide: Statistics.* Ver. 5 Edition, SAS Institute, Inc., Cary, N.C., 1985.
15. Bates, D. M., and D. G. Watts. *Nonlinear Regression Analysis and Its Applications.* Wiley Series in Probability and Mathematical Statistics, John Wiley & Sons, Inc., New York, 1988.
16. Buja, A. Remarks on Functional Canonical Variates, Alternating Least Squares Methods and ACE. *The Annals of Statistics,* Vol. 18, No. 3, 1990, pp. 1032–1069.
17. Heinrichs, K. W., M. J. Liu, M. I. Darter, S. H. Carpenter, and A. M. Ioannides. *Rigid Pavement Analysis and Design.* Federal Highway Administration Contract DTFH-61-85-C-00103, University of Illinois, Dec. 1988.

Publication of this paper sponsored by Committee on Pavement Monitoring Evaluation, and Data Storage.

Pavement Evaluation in Virginia: State of the Practice

MOHAMED K. ELFINO, BOUZID CHOUBANE, AND ROY D. MCQUEEN

The Virginia state-of-the-practice using the falling weight deflectometer for asphalt concrete pavement evaluation and in situ characterization of pavement layers and subgrade is described. The process is accomplished using the computer program PEDMOD (Pavement Evaluation Design Model) developed at the Virginia Department of Transportation. This mechanistic tool uses layered elastic concepts with the results from nondestructive testing to: (a) estimate the respective elastic moduli of pavement layers and subgrade, (b) evaluate the performance of various pavement systems, (c) provide rehabilitation options and (d) determine the life-cycle cost of rehabilitation alternatives. An example showing PEDMOD application is demonstrated. The procedures described herein are being routinely applied by VDOT personnel in their decision-making process for pavement rehabilitation at the project level.

The major problem that highway engineers face today is not how to design and construct new pavements but how to evaluate, maintain, and upgrade existing ones to meet today's demand of higher magnitudes of traffic loading and frequency.

Nondestructive Testing (NDT) methods have gained popularity in the past decade because of their ease of use and their ability to collect large amounts of data in a short time period. Basically, NDT methods for structural evaluation of pavements consist of performing nondestructive measurements on a pavement surface and relating these measurements to the in situ properties of the pavement system. The in situ pavement properties are then used to evaluate the structural adequacy of the pavement using the multilayered elastic theory.

The Dynatest 8000 Falling Weight Deflectometer (FWD) is currently used by the Virginia Department of Transportation (VDOT) to evaluate asphalt concrete pavement condition and performance. Data collected from the FWD are used, in conjunction with the Pavement Evaluation Design Model (PEDMOD) computer program, to evaluate the pavement structure and to better define its expected performance. This analysis has become an important part of the VDOT pavement management system, since it allows the following tasks to be performed:

1. Evaluation of design alternatives;
2. Determination of optimum time for rehabilitation; and
3. Development of rehabilitation priorities.

At the project level, FWD is used for the following purposes:

1. To separate the project length into relatively uniform analytical units. These are pavement sections exhibiting statistically homogeneous attributes (cross sections, subgrade support, construction histories, etc,) and performance. In other words, FWD is used to delineate unit boundaries when accurate historical data are not available.
2. To provide detailed analysis of the pavement structure for purposes such as the identification of localized base failure.
3. To determine the most appropriate rehabilitation design.

M. K. Elfino and B. Choubane, Virginia Department of Transportation, Materials Division, 1401 East Broad Street, Richmond, Va. 23219. R. D. McQueen, McQueen & Associates, Ltd., 3112 Fox Den Lane, Oakton, Va. 22124.

PAVEMENT EVALUATION DESIGN MODEL

PEDMOD Description

The computer program PEDMOD was developed by McQueen & Associates (*1*) to provide VDOT with an analytical tool for pavement evaluation and analysis. A modular concept was adopted to provide flexibility in updating the program as technology changes. These modules are shown in Figure 1 and include the following:

1. NDT data processing and reduction;
2. Evaluation of pavement performance;
3. Structural design of pavement;
4. Life-cycle cost analysis; and
5. Summary report.

NDT Data Processing and Reduction

A primary requirement for PEDMOD development was to enable VDOT to fully use field data collected with its FWD testing device. Because of the quantity of data collected by FWD to characterize pavement condition, PEDMOD is equipped to perform the following tasks:

1. To automatically input NDT field data to a spreadsheet program (data processing).
2. To reduce the NDT field data to yield the respective elastic moduli of pavement layers and subgrade (data reduction).

Data Processing

The function of the NDT Data Processing Module is to automatically transfer the field data file (XX. FWD) to a spreadsheet without manual keying. This feature alone saves the VDOT approximately 4 hours of keypunch time for every day's worth of acquired NDT field data and eliminates errors normally associated with manual keying. After the field data are input to the spreadsheet, the user can

1. Sort the data as a function of station, test number, deflection, etc.;
2. Process the data statistically; and

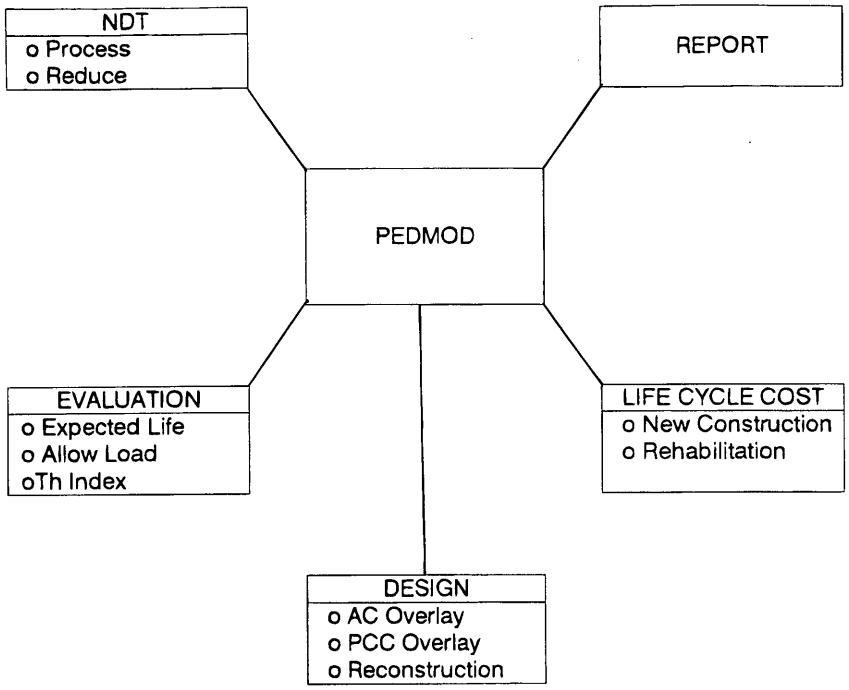

FIGURE 1 PEDMOD major components.

3. Graph the data to analyze trends and select a representative deflection basin.

Before the data are entered into the spreadsheet, preprocessing is done by averaging the three FWD "drops" per test point. The average load and average deflection sensor array (seven distinct averaged deflection measurements) are input to the spreadsheet for each test point along with test location information. The load and average deflections define the deflection basin for a particular test location. The spreadsheet also performs a composite stiffness computation at each test location to normalize minor load variations along a particular road profile. The composite stiffness (load/max deflection) values are then graphed as a function of stations to identify patterns of variability in pavement support for grouping of data for analysis. While grouping is subjective to a point, data should generally be grouped according to stiffness and pavement composition. A representative deflection basin(s) should then be chosen to characterize support conditions along the chosen length of road. While there are no firm rules for selecting a deflection basin, it is usually chosen to represent average or statistical conditions (mean plus or minus one standard deviation). This can either be the processed average or statistical basin or a particular basin in the group closest to the average or statistical basin. Comparing the average and statistically processed data to individual basins using the graph (XY) function is useful in basin selection. The spreadsheet and stiffness plot can be printed for further analysis and documentation as shown in Table 1 and Figure 2.

Data Reduction

Once a representative basin is chosen, that basin can be used in the NDT Data Reduction Module to estimate the elastic moduli of individual pavement layers and subgrade. This requires a knowledge of pavement type, thickness, and composition for each deflection basin (i.e., load and seven deflection sensor array).

To determine modulus values, the pavement structure is modeled as a layered system. PEDMOD uses WESDEF (*2*) as a subroutine for backcalculation.

WESDEF (*2*) determines a set of moduli values that provide the best fit between a measured deflection basin and a computed deflection basin. An example of WESDEF output is shown in Table 2.

VDOT is currently establishing a resilient modulus data base for all bound materials. This involves FWD testing of 54 (1.6 km or 1 mi) sections throughout the state and obtaining five asphalt concrete cores from each for indirect tension resilient modulus (diametrical) testing. Tests are run at 25°C (77°F) and at the average temperature established from the temperature profile in the asphalt concrete layers recorded during FWD testing. These resilient moduli can be used as initial (seed) values that would speed the backcalculations and provide confidence for the uniqueness of the solution obtained from WESDEF (*2*).

EVALUATION OF PAVEMENT PERFORMANCE

The purpose of the evaluation component is to gauge the expected performance of an existing pavement system. The evaluation relies heavily on the pavement strength inputs obtained from the NDT data reduction component output and projected traffic during the evaluation period. The evaluation methodology is based on a multilayered elastic model and limiting stress/strain criteria. The computer program BISAR (*3*) is incorporated into the evaluation component for calculation of stresses, strains, and displacements within the pavement structures.

The evaluation component is composed of the following primary modules.

TABLE 1 PEDMOD Data Processing Output

MP	F1(lbs)	D1(mil)	D2(mil)	D3(mil)	D4(mil)	D5(mil)	D6(mil)	D7(mil)	STIFF(lb/mil)
13.12	10475.00	7.47	4.70	4.46	3.68	2.78	2.01	1.50	1402
13.05	10491.00	9.58	6.77	6.09	5.10	4.02	3.02	2.35	1095
13	10464.00	10.30	6.89	6.34	5.39	4.27	3.26	2.51	1016
12.95	10499.00	9.32	5.20	4.88	4.14	3.29	2.52	1.97	1127
12.9	10504.00	8.52	5.69	5.51	4.61	3.39	2.62	2.06	1233
12.851	10459.00	8.99	5.35	4.96	4.26	3.39	2.61	2.01	1163
12.8	10467.00	9.15	6.74	6.28	5.37	4.31	3.35	2.68	1144
12.749	10461.00	10.27	6.38	6.06	5.06	4.01	3.05	2.39	1019
12.7	10544.00	7.39	4.77	4.22	3.40	2.52	1.79	1.33	1427
12.648	10405.00	9.32	5.66	5.13	4.31	3.40	2.56	1.99	1116
12.6	10429.00	8.86	7.45	6.85	5.83	4.61	3.55	2.80	1177
12.55	10288.00	7.73	5.02	4.61	3.93	3.08	2.33	1.81	1331
12.5	10408.00	6.97	4.05	3.83	3.15	2.42	1.79	1.43	1493
12.45	10400.00	7.73	4.89	4.81	3.62	2.58	1.80	1.38	1345
12.4	10443.00	9.87	6.06	5.59	4.57	3.34	2.22	1.54	1058
12.35	10493.00	6.70	4.48	4.03	3.24	2.45	1.76	1.35	1566
12.3	10427.00	8.61	6.31	5.66	4.69	3.58	2.59	1.94	1211
12.25	10429.00	9.16	5.36	4.95	4.08	3.15	2.32	1.77	1139
12.2	10453.00	8.21	4.88	4.57	3.78	2.92	2.18	1.69	1273
12.15	10456.00	6.33	5.94	5.24	4.19	3.12	2.28	1.70	1652
12.1	10424.00	11.99	5.64	5.42	4.53	3.54	2.62	1.99	869
12.05	10488.00	7.24	6.09	5.61	4.77	3.78	2.93	2.28	1449
12	10435.00	9.03	7.03	6.33	5.26	4.08	3.04	2.32	1156
11.949	10411.00	8.92	5.90	5.61	4.82	3.81	2.92	2.32	1167
11.9	10179.00	14.43	8.75	7.68	6.15	4.60	3.52	2.74	705
11.849	10363.00	9.31	5.85	5.31	4.53	3.55	2.74	2.13	1113
11.8	10427.00	10.84	7.20	6.52	5.54	4.29	3.28	2.52	962
11.75	10376.00	9.86	6.72	6.07	5.09	3.95	2.93	2.24	1052
AVERAGE	10432.07	9.00	5.92	5.45	4.54	3.51	2.63	2.03	1195.03
ST. DEV.	69.41	1.65	1.02	0.88	0.76	0.63	0.52	0.43	205.69
A.+(−S.D.	10501.49	10.65	6.94	6.33	5.30	4.14	3.15	2.45	989.34

1.00 inch = 25 mm
1.00 lbf = 4.45 N
1.00 lbf/mil = 0.175 N/m
1.00 mil = 0.025 mm

Pavement Expected Life

Nondestructive testing of pavement is used to estimate the expected life of an existing pavement and to determine the rehabilitation design thicknesses required to upgrade the pavement. Estimation of the expected life and the determination of the rehabilitation option require knowledge of the failure mechanisms that occur in pavements.

The failure of asphalt pavements is generally defined by cracking and rutting of the asphalt concrete layer along the wheel paths. Fatigue cracking from repeated loading is controlled by the magnitude of the tensile strain at the bottom of the asphalt layer, while rutting is governed principally by the vertical compressive strain at the top of the subgrade. Therefore, future performance and rehabilitation needs will be determined mainly by limiting the vertical compressive strain at the top of the subgrade and limiting the horizontal tensile strain at the bottom of the asphalt concrete layer. The limiting asphalt strain criterion is based on the need to keep the tensile strain at the bottom of the asphalt concrete layer low enough to prevent fatigue cracking. Cracking occurs when the imposed tensile strain exceeds the fatigue strain of the pavement material. Similarly, a limiting vertical subgrade strain criterion is used to limit the permanent deformation of the subgrade. By limiting the vertical strain on top of the subgrade, the deflection caused by the imposed loading can be kept in the elastic range of the soil, precluding permanent (plastic) deformation.

These limiting strain criteria relate allowable strain to the number of load repetitions. Consequently, asphalt pavement performance can be expressed as a function of allowable asphalt concrete layer and subgrade strains. In PEDMOD, the following limiting strain criteria were used for pavement design and evaluation purposes.

Asphalt Concrete Pavement Cracking

The horizontal tensile strain at the bottom of the asphalt concrete layer, a criterion developed by The Asphalt Institute (*4*) to control load-induced cracking, is used.

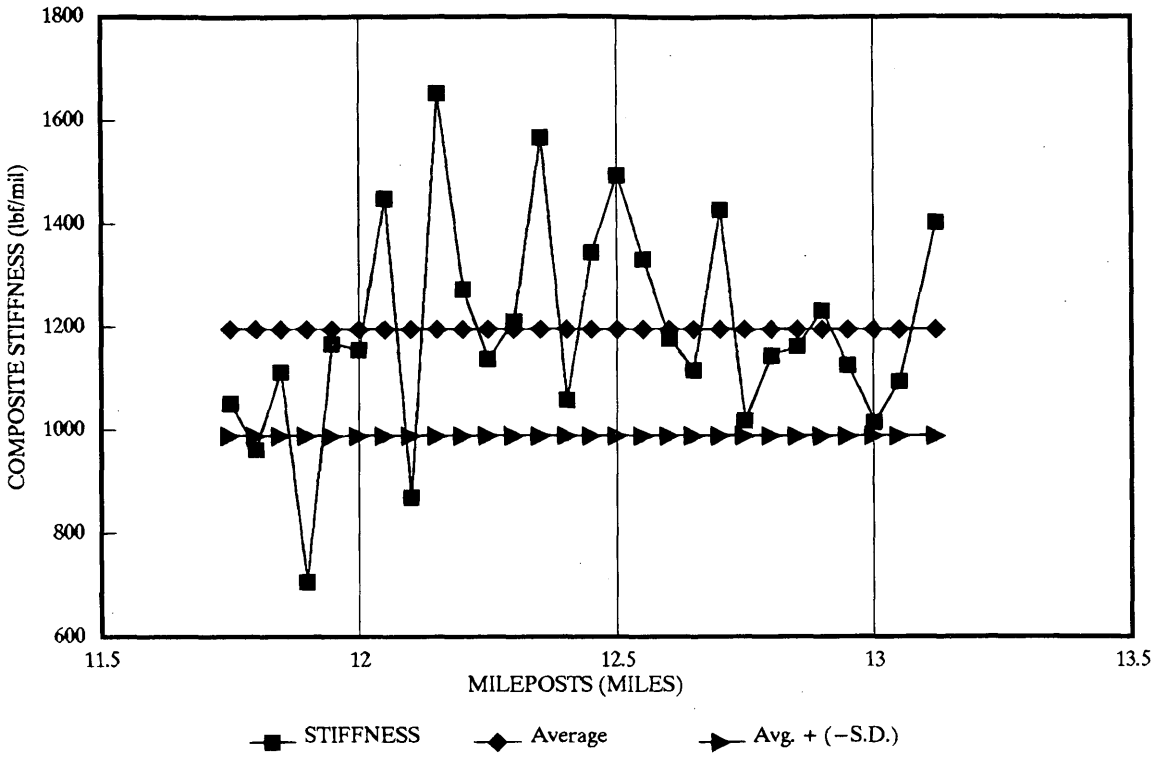

FIGURE 2 Stiffness versus stations.

The criterion is defined in the following equation:

$$N = f0 * [(10^{M}) * (f1 * e^{-f2}) * (E^{-f3})] \quad (1)$$

where

N = number of load repetitions,
$M = f4 * [V_b / (V_v + V_b) - f5]$,
e_t = limiting horizontal strain at the bottom of asphalt layer,
V_b = volume of asphalt,
V_v = volume of air voids,
E = elastic modulus of asphalt layer,
M = mix adjustment constant relating fatigue life to air voids, and
$f0$ to $f5$ = constants derived from laboratory testing.

Equation 1 is used in the design process to compute a limiting horizontal tensile strain and, in turn, the asphalt layer thickness for a given number of load repetitions. On the other hand, it can also be used to determine the allowable number of load repetitions for given horizontal tensile strains and, thus, to estimate the expected pavement life from an imposed axle load.

Pavement Rutting

The subgrade vertical strain criterion, also developed by The Asphalt Institute (*4*), is used to control rutting in the asphalt layer. The subgrade vertical strain criterion usually governs the design of asphalt pavements. It is given by the following equation:

$$N = d0 * (e_v^{-d1}) \quad (2)$$

where

N = number of load repetitions,
$d0 = 0.1365 * 10^{-8}$,
$d1 = 4.477$, and
e_v = limiting vertical strain.

Equation 2 is used in the design process to compute the thickness of pavement layers or overlay for a given number of load repetitions or to determine the allowable number of load repetitions from an imposed axle load.

The purpose of the expected-life module is to estimate the time remaining to a programmed rehabilitation project for an existing pavement. While the expected-life estimate addresses potential load-induced damage, it is used primarily to rank and program repairs and does not necessarily indicate the precise time to structural failure or pavement inoperability. The expected life is highly dependent on the accuracy of the traffic inputs (i.e., weight and number of vehicles). If the traffic input is in doubt, the user should run PEDMOD at several traffic levels to gauge the sensitivity of traffic in affecting the expected-life computation. The expected life is computed by dividing the total allowable number of load repetitions by the estimated yearly load repetitions. The allowable number of load repetitions is computed from Equation 1 or 2 with the imposed stress of strain computed by the BISAR subroutine from layer properties (i.e., elastic modulus, Poisson's ratio, and thickness) and 80 kN (18-kip) axle load application. Table 3 shows PEDMOD pavement expected life output using input data from the WESDEF example.

TABLE 2 WESDEF Output Summary

NUMBER OF ITERATIONS PERFORMED: 1

DEFLECTIONS COMPUTED FOR FINAL MODULUS VALUES

POSITION	SENSOR OFFSET IN.	MEASURED DEFLECTION MILS	COMPUTED DEFLECTION MILS	DIFFERENCE	% DIFF.
1	3.0	5.9	5.9	0.0	-0.4
2	12.0	4.5	4.5	0.0	-1.0
3	24.0	3.2	3.2	0.0	-1.2
4	36.0	2.3	2.3	0.0	2.0
5	48.0	1.6	1.6	0.0	1.9
6	60.0	1.1	1.1	0.0	-0.6
7	72.0	0.8	0.8	0.0	0.4
			ABSOLUTE SUM:	0.2	7.6
			ARITHMETIC SUM:		1.1
			AVERAGE:	0.0	1.1

FINAL MODULUS VALUES

LAYER NO.	MATERIAL TYPE	MODULUS PSI	POISSON'S RATIO	THICK. IN.	INTERFACE VALUE
1	AC	918692.	0.35	10.00	1.
2	BASE OR SUBBASE	35620.	0.35	6.00	1.
3	SUBGRADE	30625.	0.40	223.50	1.
4	RIGID BOUNDARY	1000000.	0.50	1.00	1.
5	RIGID BOUNDARY	1000000.	0.50	SEMI-INF	1.

ABSOLUTE SUM OF % DIFF. WITHIN TOLERANCE
CHANGE IN MODULUS VALUES NOT WITHIN TOLERANCE

1 inch = 25.4 mm
1 psi = 6.89 kPa

Effective Thickness Coefficient

The purpose of this module is to compute the layer coefficient, a_{im}, of existing pavement layers by using the layer elastic modulus, E_{im}, from the NDT data reduction component and standard VDOT layer coefficients, a_{is}, and elastic moduli, E_{is}. For asphalt pavements, the VDOT standard layer coefficients are shown in Table 4. The computational procedure for the flexible pavement effective thickness coefficient is referenced by Equation NN.13 of the 1986 *AASHTO Guide For Design of Pavement Structure,* Volume 2, *(5)* as

$$a_{im} = a_{is} * (E_{im}/E_{is})^{1/3} \quad (3)$$

TABLE 3 PEDMOD Pavement Expected Life Output Using Input Data From WESDEF/Expected Life Calculation—AC (Asphalt Content)

EXPECTED LIFE = 4.02 (YEARS)

NO. OF TOTAL ALLOWABLE 18-kip LOAD REPETITIONS = 1.0050E+07

18 KIP = 80 kN

TABLE 4 Thickness Equivalency Values for Materials Used in Interstate and Primary Road Pavements in Virginia

Location	Location Notation	Material	Material Notation	Thickness Equivalency Value
Surface	a_1	Asphalt Concrete	A.C.	1.0
Binder	a_1	Asphalt Concrete	A.C.	1.0
Base	a_2	Asphalt Concrete	A.C.	1.0
	a_2	[1]Cement treated aggregate material over untreated aggregate or soil cement or soil lime and under less than 4.5" thick A.C. material	C.T.A.	1.0
[2]Drainage Layer	a_3	Cement or Asphalt Stabilized open-graded material	D.L.	0.40
[3]Subbase(s)	a_4	[4]Select material Type I, II & III; and aggregate base Type II No. 21A	Sel. Mat.	0.20
	a_4	Soil cement or soil lime	S.C.	0.40
	a_4	Untreated aggregate material 21A or 21B	Agg.	0.35
	a_4	Cement treated aggregate material over untreated aggregate or soil cement or soil lime	C.T.A.	0.80
	a_4	Cement treated aggregate material directly over subgrade	C.T.A.	0.60
Full depth bituminous concrete shall have a thickness equivalency value of 0.95				

[1]All materials directly under less than 4.5 inches of total asphalt concrete material are considered as base.

[2]All drainage layers must be constructed on top of a filter/separator layer. The filter/separator layer may be either an untreated aggregate base material 21A or 21B primed with asphalt or a cement treated aggregate/soil material.

[3]A subbase may be more than one layer material.

[4]No structural strength shall be given to a select material used to replace unsuitable subgrade material

where

a_{im} = layer coefficient of material in place,
a_{is} = layer coefficient of VDOT standard material,
E_{im} = elastic modulus of material in place, and
E_{is} = elastic modulus of VDOT standard material.

The effective thickness index (equivalent to structural number in AASHTO) of the existing pavement, D_{eff}, is then computed as the summation of the layer coefficient (a_{im}) times the thickness (h_i) for each layer, or

$$D_{eff} = \Sigma\, a_{im} * h_i \quad (4)$$

For program implementation, the following standard elastic moduli for acceptable VDOT materials were used:

- Asphalt concrete (surface, binder, base), 3.8×10^6 kPa at 25°C (550,000 psi at 77°F).
- Aggregate base, 2.1×10^5 kPa (30,000 psi) (from AASHTO).
- Select subbase, 1×10^5 kPa (15,000 psi) (from AASHTO).
- Cement-treated aggregate, 4.3×10^6 kPa (600,000 psi).

For asphalt pavements this module also computes the adjusted asphalt modulus at 25°C (77°F) and 32°C (90°F) based on the AASHTO *(5)* temperature modulus relationship (Appendix L). The 25°C (77°F) asphalt modulus is used for the effective layer coefficient computation and the 32°C (90°F) value is used for design purposes. PEDMOD saves these values as default inputs to other modules.

Since the default VDOT standard elastic moduli used in PEDMOD are based on limited laboratory testing, users should exercise caution when interpreting effective thickness coefficient results. Until a validation study is implemented to verify the default values included in PEDMOD, the following guidelines are suggested:

1. Use experience to gauge the reasonableness of the results.
2. Perform sensitivity analyses with different default moduli to gauge the effect on the output.
3. Use a single asphalt layer to evaluate multiple asphalt layers consistent with NDT data reduction. Since only the asphalt surface layer has a stored temperature modulus relationship, model all asphalt layers as asphalt surface.

Table 5 shows the PEDMOD output for the effective thickness index of the data reduced by WESDEF.

TABLE 5 PEDMOD Output for Effective Thickness Index of Data Reduced by WESDEF

LAYER	MATERIAL	THICKNESS	E-VALUE	LAYER COEFF.
1	AC	10.00	277445	0.80
2	AGBS1	6.00	35620	0.60

EFFECTIVE THICKNESS INDEX AT 77 DEG F. = 11.56

ADJUSTED AC MODULUS @ 77 DEG FOR EFF. THICK. CALC. = 277445
ADJUSTED AC MODULUS @ 90 DEG FOR DESIGN ========== 144235

1 psi = 6.89 kPa
1 inch = 25.4 mm
77°F = 25°C
90°F = 32°C

STRUCTURAL DESIGN OF PAVEMENT

PEDMOD's design component performs structural design for existing and new pavement systems using layered elastic theory. The design component allows computation of asphalt overlays as well as design of new (or reconstructed) asphalt concrete pavement. Each pavement type incorporates either aggregate or cement-stabilized subbase layers.

The design process involves computation of stresses and strains using BISAR (*3*). The computed values are then compared to limiting stresses and strains that are determined based on riding quality (i.e., pavement smoothness) and the need for structural maintenance (i.e., pavement cracking). If either the computed strain or stress from the imposed loading exceeds the limiting values, new computations are made for thicker pavement until computed values are within tolerance. For flexible pavements the limiting strain criteria are indicated by Equations 1 and 2.

PEDMOD will prompt the user for input, including elastic modulus, material type and existing pavement thickness. The program incorporates default values, which can be overridden by the user for:

- Elastic moduli of new pavement materials (e.g., overlay layer of new pavement layers);
- Poisson's ratio;
- Standard 80-kN (18-kip) axle load; and
- Computational points based on selected pavement type.

For asphalt concrete overlay and existing asphalt concrete layers, PEDMOD uses the 32°C (90°F) modulus for asphalt concrete overlay and the modulus of the existing asphalt layer adjusted to 32°C (90°F) stored from NDT data reduction.

At the completion of the design process, PEDMOD will also compute the effective thickness index for asphalt concrete pavement systems for comparison to existing VDOT methods. The asphalt modulus adjusted to 25°C (77°F) is used for the effective thickness index computation. PEDMOD output for asphalt overlay requirement is shown in Table 6, while Table 7 shows the output for new/reconstruction design.

TABLE 6 PEDMOD Output For Asphalt Overlay Requirement/AC Overlay Rehabilitation—AC over AC Pavement

LAYER	MATERIAL	THICKNESS	E-VALUE	LAYER COEFF.
OVL	AC	3.48	576000	1.00
1	AC	10.00	276931	0.80
2	AGBS1	6.00	35620	0.60
3		0.00	30625	0.00

EFFECTIVE THICKNESS INDEX = 15.03

REQUIRED OVERLAY THICKNESS = 3.48 (INS)

1 psi = 6.89 kPa

1 inch = 25.4 mm

TABLE 7 PEDMOD Output New/Reconstruction—AC Pavement CTA Base

LAYER	MATERIAL	THICKNESS	E-VALUE	LAYER COEFF.
1	AC	8.68	576000	1.00
2	CTA1	6.00	600000	1.00
3	AGBS1	6.00	30000	0.60
4		0.00	30625	0.00

EFFECTIVE THICKNESS INDEX = 18.28

1 psi = 6.89 kPa

1 inch = 25.4 mm

LIFE-CYCLE COST ANALYSIS

A life-cycle cost analysis, as applied to VDOT pavement management systems, is also included in PEDMOD. It performs an economic analysis to estimate the total cost of a pavement type over a certain period based on present worth. User inputs include initial cost, necessary maintenance, salvage value, and a discount rate, as shown in Table 8.

SUMMARY REPORT

A copy of a typical report generated by PEDMOD, as illustrated in Table 9, is processed by the Report Module in the main menu. The report summarizes results from the Evaluation and Design Components. NDT reports are generated by printing spreadsheets or graphs and the NDT Data Reduction (WESDEF) output file.

LOADING CONDITIONS

PEDMOD uses the AASHTO standard 80-kN (18-kip) single-axle load as the standard loading condition. Mixed traffic is converted to 80-kN (18-kip) equivalent single-axle load repetitions in the evaluation component. The 80-kN (18-kip) axle load is assumed to be distributed on four dual wheels (two on each side of the axle) with a single wheel load of 20 kN (4,500 lb). For layered elastic computation, the dual wheels are assumed to be spaced at 330 mm (13 in.) on center with 690-kPa (100-psi) tire pressure. Again, the user can override the default wheel loading, tire pressure, and wheel spacing.

CLIMATIC VARIATIONS

The layered elastic design method allows the user to factor climatic effects into the evaluation/design process by adjusting the elastic modulus for a temperature (e.g., asphalt) or moisture (e.g., subgrade) susceptible material.

For asphalt materials, PEDMOD will automatically adjust the elastic modulus backcalculated from NDT field data at the test temperature to the elastic modulus at 25°C and 32°C (77°F and 90°F). The 25°C (77°F) modulus is used for effective thickness computations and the 32°C (90°F) modulus is used for evaluation and rehabilitation design. These values are computed from a default temperature module table taken from the 1986 AASHTO Design Guide (*5*) and are stored by PEDMOD for input to applicable evaluation and design modules. Respective air and asphalt concrete pavement temperatures are recorded during testing. Three holes are drilled into the pavement at a depth of 25 mm (1 in.) from the top, at asphalt concrete base middepth and at 25 mm (1 in.) below the asphalt concrete base, respectively. Pavement temperatures are determined by measuring the temperature of glycerine poured into the hole using a digital thermometer with an accuracy of $\pm 1/2$°C (1°F). The same thermometer is used for measuring air temperature. PEDMOD does not contain automatic adjustments for variations of subgrade or granular base moduli as a function of moisture, since this relationship must be based on a longer-term, field-testing program. However, the user can vary subgrade and base course moduli to model variations in strength from fluctuating moisture content.

BEDROCK CONSIDERATION

The layered elastic computations performed within PEDMOD can incorporate bedrock (e.g., a hard layer) at variable depth. If the user chooses to incorporate the hard layer, PEDMOD will default to hard layer placement at 6-m (20-ft) depth.

PEDMOD also defaults to a hard-layer modulus of 6.9×10^6 kPa (1,000,000 psi) and a Poisson's ratio of 0.5. The user can override these default values and place the layer at any depth should existing information (e.g., soil boring logs) indicate a different placement depth.

TABLE 8 Life-Cycle Cost Analysis (7.3 m/lane-kilometer, 30-Year Life to Reconstruction, March 28, 1995

DISCOUNT RATE: 4%

PROJECT NUMBER SAMPLE

I PAVEMENT TYPE: FLEX
II SHOULDER TYPE: FLEX

YEAR	ACTION	COST
	INITIAL COST INCLUDING SHOULDERS	312,500
1		
2		
3		
4		
5		
6	PATCH (5% BOTH LANES, 40 mm)	1,250
7		
8	MILL & RESURFACE (BOTH LANES, 40 mm)	20,313
9		
10		
11		
12	PATCH (5% BOTH LANES, 40 mm)	1,250
13		
14		
15		
16	MILL & REPL. 15% BOTH LN. (75 mm BASE, 40 mm SURF)	24,688
17		
18		
19		
20	PATCH (5% BOTH LANES, 40 mm)	1,250
21		
22		
23		
24	MILL & REPL. 75 mm TRK LN., + OL BOTH LANES 40 mm	38,875
25		
26		
27		
28	PATCH (5% BOTH LANES, 40 mm)	1,250
29		
30		
	PRESENT WORTH (INITIAL COST + MAINTENANCE)	358,445
	ESTIMATED SALVAGE VALUE AT END OF 30 YEARS	156,250
	TOTAL NET PRESENT WORTH	406,620

SUMMARY

This paper described the implementation of the backcalculation technique and the use of the results in pavement evaluation in Virginia. The development of PEDMOD resulted in a significant reduction of the amount of time required for the data entry process and provided a practical means for analyzing the considerable amount of information for pavement evaluation and for determining cost-effective rehabilitation strategies.

PEDMOD has the capability to perform the following tasks:

1. Determine resilient moduli of pavement layers and subgrade;
2. Compare strength of different pavement segments;
3. Compute pavement expected life;
4. Compute the existing pavement effective thickness index;
5. Establish thickness designs for rehabilitation options and new/reconstructed pavements; and
6. Estimate life-cycle costs.

TABLE 9 PEDMOD Evaluation Summary Report

```
EVALUATOR      :  MOHAMED ELFINO
DISTRICT       :  RICHMOND
ROUTE          :  60
COUNTY         :  HENRICO
MILEPOST       :  FROM 1 TO 2

DATE TESTED    :  03/16/95
```

LAYER	MATERIAL	THICKNESS	E-VALUE	LAYER COEFF.
1	AC	10.00	918692	0.80
2	AGBS1	6.00	35620	0.60

```
EVALUATION SUMMARY
==================
EXPECTED LIFE     :       4.02 YEARS
ALLOW. LOAD REPS  :  1.0050E+07
ALLOW. AXLE LOAD  :
EFF. THICK. INCES:       11.56 INS

REHABILITATION OPTIONS
======================
DESIGN LIFE = 20.00 YEARS

[1] AC OVER AC  PAVEMENT                3.48 INS

[2] AC STAB. BASE RECONSTRUCTION:
        AC                              8.68 INS
        CTA1                            6.00 INS
        AGBS1                           6.00 INS
```

```
1 inch = 25.4 mm
1 psi = 6.89 kPa
```

REFERENCES

1. McQueen, R. D. *Documentation and User's Manual PEDMOD Pavement Management Software.* Oakton, Va., April 1990.
2. Van Caulelaert, F. J., D. R. Alexander, T. D. White, and W. R. Barker. Multilayer Elastic Program for Backcalculating layer Moduli in Pavement Evaluation. In *Nondestructive Testing of Pavements and Backcalculation of Moduli,* ASTM STP 1026, ASTM, Philadelphia, Pa., 1989, pp. 171–188.
3. Koninklijke/Shell Laboratorium. *BISAR Users Manual; Layered System under Normal and Tangential Loads.* Amsterdam, Holland, July 1972.
4. *Research and Development of The Asphalt Institute's Thickness Design Manual (MS-1),* 9th ed. Research Report 82-2. The Asphalt Institute, August 1982.
5. American Association of State Highway and Transportation Officials. *AASHTO Guide for Design of Pavement Structure.* Vol. 2, Washington, D.C., 1986.

Publication of this paper sponsored by Committee on Pavement Monitoring, Evaluation, and Data Storage.

Design Considerations for Distributed, Multimedia-Based Highway Information System

KELVIN C. P. WANG AND ROBERT P. ELLIOTT

Two types of data commonly used in highway management systems are video/film images and tabulated data such as pavement width/type, construction/rehabilitation history, layer thicknesses and types, condition data, accident data, traffic history, and signing/marking inventory. Tabulated data can be stored readily in a database, making general access reasonably feasible. However, access to the video/film images has been limited by technology, and the simultaneous access to both data types from a single medium has not been possible. A multimedia-based Highway Information System (MMHIS) is described in this paper that merges the two data types into a single access system that displays moving video images and the corresponding tabulated site data. The system displays the video image and corresponding data on a conventional desktop computer monitor. The MMHIS is installed on a centralized file server, and any PC or workstation networked with the server has access to the images and data. MMHIS has broad applications in highway engineering and management. A state highway agency with a statewide computer network would have access to the entire database from any office on the network. The latest video images and data would be available to field engineers, maintenance superintendents, design engineers, traffic analysts, and planners. Through the use of overhead projection panels, top management meetings regarding specific sites could include the viewing of those sites without leaving the conference room. This paper discusses the design of a low cost MMHIS and identifies the technology associated with the implementation of such a system.

For many years, highway agencies have used 16-mm film and, more recently, broadcast quality video to capture and view visual information for their traffic engineering and infrastructure management. The Connecticut Department of Transportation was the first highway agency to adopt analog-based laser disc systems for pavement video inventory (*1*). Recently, other states, such as Arizona and Arkansas, started using laser disc or Super-VHS (S-VHS) video for their roadway video inventory. These images are used for pavement management, highway signing and marking improvement, and accident analysis. A potentially significant use of these images is pavement surface distress identification and classification; however, there has been limited success in automating the process of surface distress identification and classification.

Another type of information is the tabulated site data contained in traditional engineering databases. These data sets include information on construction and rehabilitation history, pavement layer information, pavement width/type, average daily traffic, accident history, signing/marking inventory, and others. Engineering information in the databases regarding specific roadway sections can be accessed through microcomputer-based local area network (LAN). These two types of information (roadway images and traditional engineering database) can be of daily benefit to the needs of various divisions in state highway departments. However, the facilities used for the two types of data are traditionally managed through separate groups within the agency. Simultaneous access to both visual information and engineering data is presently not possible. The visual images are analog-based and are located in specific offices. To view specific roadway sections, users must go to offices equipped with special, expensive equipment. Even though the benefits for combining these two information sources is evident to highway agencies, the high cost of implementation and the complications associated with the technology required to implement such a system has prevented it from becoming a reality.

The introduction of high performance, low cost microcomputers has ushered a new information age that is affordable to a large number of users. An important feature of this capability is digital video and audio at the desktop, commonly called "microcomputer-based multimedia." The development of a low cost combination of visual data with traditional highway engineering databases has become a viable option. This paper describes available technologies and design considerations for a multimedia-based highway information System (MMHIS) with digital and networkable capabilities.

Department of Civil Engineering, University of Arkansas, 4190 Bell Engineering, Fayetteville, Ark. 72701.

THE REQUIREMENTS OF A MMHIS

To justify the cost and effort of development, a MMHIS must have a distinct advantage over today's nonnetworkable photolog systems and separate engineering data tabulations. To have the needed advantage the following requirements are identified as being practically achievable based on the capabilities of the latest information technology and the current practices of state highway agencies:

1. A dynamically synchronized combination of tabulated data sets with the appropriate visual images so that the images and corresponding data can be viewed simultaneously,
2. Usability in multiple agency functions, including traffic studies, pavement management, highway design, and other information needs,
3. The ability to incorporate and use to the fullest extent possible existing network, hardware, and software to make use of past investments,
4. The ability to accommodate multiple users simultaneously accessing the same images and databases,
5. The ability to view a highway section through text or graphical query and the ability to capture the video images for incorporation into a word-processing document,
6. Sufficient flexibility that the MMHIS can be integrated into a geographic information system (GIS) such as Intergraph's MGE system,

7. Initial video quality to be at S-VHS level, with scalability of incorporating higher resolution video, such as high definition television (HDTV), and
8. Optional capabilities of the (a) ability to store audio comments embedded either in the video or tabulated data files and (b) incorporation of teleconferencing capabilities.

For traffic safety information management, with a MMHIS, each accident data record can be indexed to video frames of the actual accident scene, possibly including pictures of the vehicles involved. This capability will provide more insight into the causes of accidents and will result in better decisions on geometric, signing, or marking improvements. It can also serve as a tool for the legal and insurance systems.

The digitizing of pavement surface images will lend itself to the development of automated surface distress surveys. Although efforts to develop such capability has met only limited success to date, the development of high resolution MMHIS will greatly expand the opportunities and potential for successful development and implementation.

MMHIS will be quite useful in roadway design that involves improvement of existing roadways. The preliminary examination of geometric features can require many hours (or days) of travel time for field trips. With MMHIS the preliminary examination can be performed in the office either individually on a computer monitor or by a group viewing images projected onto a screen.

REVIEW OF AVAILABLE TECHNOLOGY

It was difficult to put TV quality video in computer networks. In recent years, the technological advancement of low-cost equipment resulted in performances at the advanced workstation level. Now the good quality of capturing and playback of digital video can now be achieved in 486 and Pentium level computers with some hardware assistance. Network technologies were also improved in the last couple of years. The following discussions relate to today's video technologies essential for the implementation of a MMHIS.

Analog or Digital

Until recently, computers and television existed in two separate worlds: digital for computers and analog for television. This difference between digital computer display and the consumer video world reflects the fundamental difference between computer images and television images in the way they are handled and displayed. Information in computer displays is comprised of digital data and is stored as sequences of negative and positive charges that the computer reads or writes as the digital numbers 0 and 1. Images in television-based video (including video-form broadcast, VCR, and laser disc) are stored and manipulated as analog information. Analog information is stored in smooth, continuously variable electronic signals that can have an infinite number of possible values. Although a large amount of analog data can be easily stored in tape or laser disc, they are difficult to manipulate, copy, and distribute without introducing electronic "noise" into the original signal. Therefore, the quality of the video image is degraded during the process. In addition, the access to analog video images is also restricted in a number of areas. For example, it is impossible to let multiple users simultaneously access one laser disc. Because digital video can be reduced to a series of numbers, it can be edited, stored, and played back without ever losing any of the original signal fidelity. Digital video can also be easily integrated with other information on the computer to form new types of communications media that will be hybrids of text, computer graphics, and motion video. The data format of digital video is similar to regular computer files in many aspects, so multiple access to the same digital video files is possible. More importantly, speedy random access is an important property of digital data stored in hard drives or optical discs. Therefore, digital video is necessary when high fidelity, fast, and multiple-user access are required of the MMHIS.

Compression and Decompression

The generation of multimedia data (video and/or audio) is conducted through a process called "capturing" from analog sources, such as tape, laser disc, or camcorder. Then the data can be stored and played back on desktop computers. One full color digital image with a NTSC TV resolution (640 × 480) requires approximately 0.92 megabyte of data storage. A full motion video has about 30 frames in 1 second. As a result, about 27 megabytes of storage space are needed for just 1 second of uncompressed motion color video. In addition, the input and output bandwidth of modern microcomputers (disc, bus, and video subsystems) are not capable of processing dozens of megabytes of a huge data stream per second. Therefore, data compression is needed to reduce data storage requirement on the one hand and to improve data flow rate on the other.

With custom chips and compression algorithms, a capture card residing in the computer bus takes in video frames, compresses them, and passes the compressed data onto the computer's storage. The amount of compression ranges from as little as 2:1 to as much as 200:1, depending on what algorithm is used and what level of quality is required. Most image compression algorithms are "lossy," meaning information is lost during the compression of the data. The stored digital data (video and/or audio) can be played back through decompression to give a visually faithful representation of the original image. The same process applies to audio decompression. This entire process is called CODEC for compression and decomposition, sometimes referred to as encoding and decoding. The general rule is: the more compression you use, the poorer the quality of the played back image is. However, quality of compressed video data also depends on the CODEC algorithm and whether hardware-assisted CODEC is used. The following is a brief introduction of the popular formats.

Motion Joint Photographic Experts Group

The Joint Photographic Experts Group (JPEG), an industry standard-setting committee, first developed this compression algorithm for still images, but the standard has been widely adopted for video sequences because the JPEG compression chips are relatively inexpensive. The motion JPEG is based on the original JPEG algorithms and allows easy random access to any frame in a digitized sequence. JPEG compression is conducted exclusively on redundant data in individual frames, and many other CODEC algorithms use interframe compression, resulting in a higher compression ratio. JPEG compression is fairly fast. Hardware-based JPEG CODEC can capture full-screen, full-rate video in real time. The image degrades noticeably if the compression exceeds 20:1. When high compression ratio is not required, this CODEC algorithm is very effective in preserving the details and fidelity of single video frame, which is very important in applications in medical analysis and military targeting.

Motion Picture Experts Group

Unlike JPEG, which only condenses information within each frame, the standard developed by the Motion Picture Experts Group (MPEG) compresses information between frames, such as background information that does not change. This allows video digitization and playback at compression ratios as high as 160:1 while still retaining fairly good quality. Because of its high compression ratio, MPEG is a desirable delivery format for applications that require the digital video stream to be transferred over narrow bandwidth systems such as CD-ROM, video networks, and video conferencing. The forthcoming HDTV is based on a new MPEG CODEC, called MPEG-2 because of its high compression ratio and high quality of motion video. However, because of the asymmetric nature of MPEG, the required high computing power makes it difficult to conduct the compression (encoding) process. The decompression (decoding) of MPEG is relatively easy to implement.

Indeo

Developed by Intel for its i750 chip (used on the ActionMedia II capture board), Indeo-based video can now be played back via software as well as with Intel hardware. Indeo combines both lossless and lossy algorithms. The compressed information with the lossless algorithm can be decompressed to its originality with 100% fidelity. Indeo produces good image quality but fairly low compression ratios (about 10:1). Indeo has been licensed for Macintosh, Windows, and OS/2. Based on prototyping work conducted by the authors, when the compression is conducted in a 486 or Pentium computer, the quality of the playback video based on the i750 chip is not even close to the S-VHS quality that is a requirement for described MMHIS. However, if the compression of the video data is carried out in a super computer through a highly specialized repetitive process, the quality of playback in a 486 computer is very good.

Microsoft Video 1 and IBM Ultimotion

Both Microsoft Video 1 and IBM Ultimotion are software-only compression schemes. Video 1 was developed by Media Vision under the name Motive and was licensed by Microsoft in its Video for Windows. The current maximum video size (160 × 120) and quality provided in Microsoft Video for Windows are not adequate for use in a MMHIS.

From video capturing to play back, the CODEC in Ultimotion included in 32-bit IBM OS/2 is conducted in the computer's central processing unit (CPU). Therefore, the quality of video is compromised, and the cost of obtaining full motion video is kept to a minimum. Currently Ultimotion is only available in the OS/2 environment. Unless an extremely powerful CPU is used, software-only CODEC will not provide the full motion frame rate at or over the S-VHS resolution required for a MMHIS.

Digital Video in a Network

Putting digital video on a network is a complex task; the difficulty is in determining how to keep multimedia data from straining every computer and network component to the utmost. The factors of storage capacity, processor power, network data rate, and networking software determine the availability and quality of the video on the desktop. Any one of these factors can become the bottleneck to the video flow, as shown in Figure 1. Even with compression, VHS-quality digital motion video requires about 2 M bit/sec (Mbps) of bandwidth. Advanced digital video, such as HDTV, could use over 30 Mbps bandwidth after compression (*2*). Common networks based on Token Ring or Ethernet have the shared data bandwidth of 16 Mbps and 10M bps, respectively. In addition, the two types of networks are optimized for carrying packet data and do a poor job of carrying full-motion video. It is clear that to allow multiple access to the video files (more than 10), the throughput of the traditional networks need to be drastically improved. Furthermore, it is required that video streams be delivered in a particular order with very small latency. Otherwise, frame drop and unsynchronization would occur. Therefore, the challenge is to design a proper network that provides the highest data bandwidth and at the same time takes advantages of the existing network capabilities.

It is possible to use Ethernet or Token Ring to carry a limited number of simultaneous streams at S-VHS quality (e.g., less than five users) by using specially designed management software ensur-

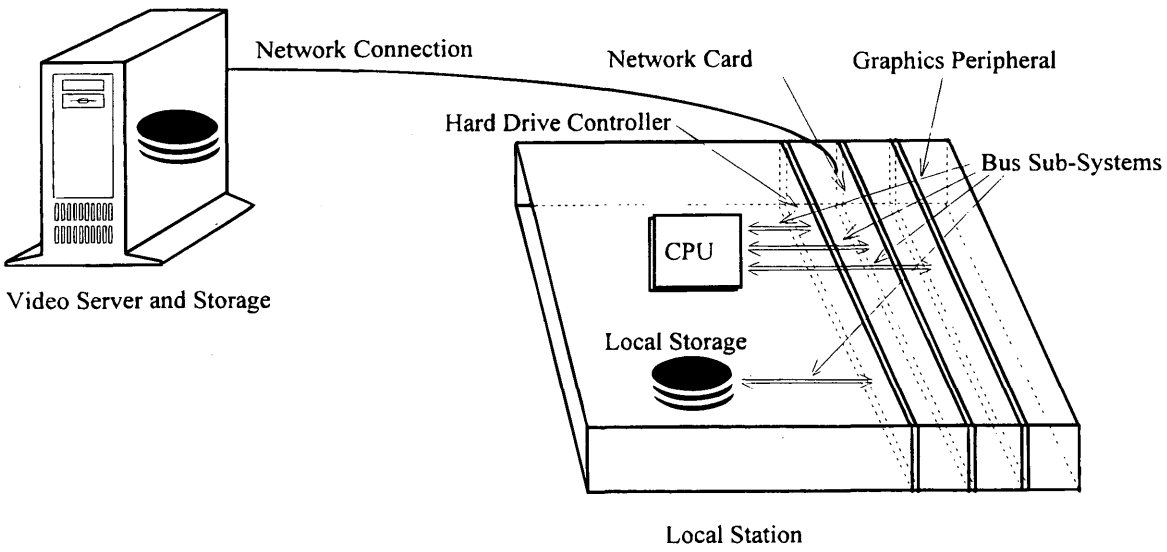

FIGURE 1 Bottlenecks of video data flow in the video server and station. (All identified items are potential bottlenecks).

ing free flow of video/audio data. However, for carrying higher fidelity video/audio for a larger number of users, new and more expensive technologies need to be used, such as asynchronous transfer mode (ATM) and the fiber distributed data interface (FDDI). ATM is a short-packet protocol based on individual connections, and FDDI can be used in a 100-Mbps, shared medium LAN.

ATM

ATM is an extremely fast, high bandwidth, packet-switching technology. ATM technology was invented by the telephone industry. Its connection approach is similar to telephone switches; each telephone has full data bandwidth to the called telephone when connected. This approach is best suited for video and audio transmission (*2*). ATM breaks all traffic (voice, video, or data) into equally sized 53-byte short packets, known as cells. Each cell has a 5-byte header. Therefore, the user data in each cell amounts to 48 bytes or 90% of the total data. In return for the 10% overhead, ATM brings two benefits. First, its short, fixed-length cell makes ATM better than frame relay and existing LAN protocols, which all use variable length packets, for carrying real time data and multimedia applications. Second, ATM's short packet format enables the cells to be formed and routed almost entirely in hardware. This hardware capability is likely to allow far faster network speeds than are possible with today's multiprotocol routers, which rely on software to handle the bulk of the switching task. More importantly, ATM's speed is scalable up to 622 gigabits/sec (*3*), which is adequate for any type of application in the foreseeable future. The resulting bandwidth is available from each station to a server or another station, which poses a big advantage over the shared bandwidth technology in Token Ring and Ethernet.

Integrated Service Digital Network (ISDN) is the digital successor to the analog-based telephone communication technology. It is widely used in video conferencing systems for both video and voice transmission, such as the recently announced ProShare system from Intel. However, ISDN operates at the speed of 64 K bit/sec/channel, which is not suitable for carrying high traffic loads between LAN. ATM is derived from ISDN technologies, so it is sometimes called broadband ISDN.

FDDI

FDDI is based on the same token-passing technique as Token Ring. But it is a more sophisticated implementation, with timing devices enabling data to be transmitted at the higher speed of 100 Mbps, which is 10 times greater than that of Ethernet. Today's FDDI no longer requires fiber optical cable at the desktop. Recent advances in data transmission technology enable the full speed of FDDI to be sustained over standard twisted pair copper cabling over short distances up to 100 m. For many existing applications, FDDI is used as a backbone network, connecting different LANs together within a building or a site, such as a university campus. Individual computers are not connected through FDDI mainly because of cost considerations.

The main advantages of FDDI over Token Ring and Ethernet are performance and reliability. FDDI supports multiple tokens, meaning that many different packets of data can be transmitted over the LAN simultaneously. In addition, FDDI can be implemented over a pair of rings, which has certain fault-tolerant features in case faults occur. The fact that FDDI can run on optical fiber ensures the immunity from electrical interference. The main advantages of FDDI over ATM is its lower price and proven interoperability between products. However, FDDI's price advantage over ATM is disappearing as ATM standards are being set, and the prices of its devices are falling fast. In addition, FDDI has the similar disadvantages of using shared medium as Token Ring and Ethernet do. Recently, 100-Mbps Fast Ethernet has been proposed based on the existing Ethernet technology. How successful the Fast Ethernet will be remains to be seen.

The Video Server and Data Storage

When traditional data are traveling in the network, the data stream is not continuous and steady; rather it is sent in a batch mode resulting in inconsistent delays between batches. This type of data is also called short and bursty data. A dedicated video server can help eliminate the compromises that ordinary servers make between controlling short, bursty data and optimizing large streams of data. The video server along with a proper network protocol for video bypasses the democratic contention scheme and acts as a real time system that ensures reliable data flow. To efficiently manage the multiple simultaneous video streams, multiple processors can be used in the video server. For example, the database maker Oracle uses a massive, parallel n-Cube super computer in its video demand implementation, which is capable of managing thousands of simultaneous consumers. In a MMHIS, simultaneous users would be limited because of its engineering nature, so a low-cost symmetrical computer with a few Pentium processors would provide adequate power to drive 10 to 50 users at the same time.

Storage is another important issue in the video server design. For a MMHIS, a minimum of a few dozens of gigabytes of storage is needed for a highway network of a few thousand miles. A Redundant Array of Inexpensive Discs (RAID) system can be used to ensure the availability of data at all times. A common technique in RAID is stripping, meaning splitting data into multiple drives. The resulting effective sustained data rate can be drastically improved.

All of the above technologies were designed to handle traditional data access, in which short, random, burst transfers that leave gaps in the data stream are common. These gaps last up to 800 milliseconds, which are used to perform drive calibration and error correction tasks. The burst transfer pattern is similar to the traditional data transmission in a network. In a MMHIS scenario, multiple users may access video frames of highway sections in the state highway system. Therefore, a new type of storage device is needed to provide multiple simultaneous data streams and at the same time keep latency as small as possible. Recently, Micropolis Corporation and Pinnacle Micro, Inc., introduced storage products that are specifically designed for applications requiring multiple video stream delivery. The Micropolis AV magnetic hard drives use a proprietary AV management system, providing 30 milliseconds of worst case data access with an average latency of 5.6 milliseconds and a minimum sustained data rate of 3.0 megabytes/sec (MBps). The Pinnacle product is an 5.2-gigabyte optical disc system called ORRAY, which has four removal bays containing four 1.3-gigabyte magneto-optical discs. ORRAY uses the multi-head and multi-platter approach of traditional hard drives. However, its multi-channel architecture allows four-channel reading and writing of data simultaneously to four optical platters. Another important feature of the ORRAY drive is that it has virtually unlimited storage capacity because each optical drive is removable. The sustained data rate is

from 5.0M Bps to 8.0 MBps, which excels at the best performing Winchester hard drive on the market. The technology in ORRAY allows all active surfaces to be read or written independently and simultaneously without requiring complex spindle synchronization or rotational position locking as required in magnetic drives. This feature is especially helpful in the multiple access environment in a MMHIS. As computer storage technologies evolve rapidly, the sustained data rate of AV ready storage is increasing at a very fast space. For example, Seagate just introduced a high capacity drive with data rate of 8 MBps.

THE DEVELOPMENT OF THE MMHIS

The Civil Engineering Department at the University of Arkansas has a project supported by the Mack-Blackwell Transportation Center (a US DOT-sponsored research center) and Intergraph Corporation to develop a distributed MMHIS. This project targeted at improving access to state highway agencies' information in their transportation management systems. Most of the efforts will be devoted to network design and software development because standard hardware equipment will be used. Based on the discussions in the previous sections, the following sections represent the design elements, the appropriate technologies required for the development of MMHIS, and the development plan.

MMHIS Design Elements

The elements of the hardware system include the following subsystems:

1. Video recording and digitizing,
2. Microcomputer requirement: sub-systems such as I/O, microprocessor, or storage,
3. The video displaying system (frames, resolution, and number of colors),
4. LAN and wide area network,
5. Video and database servers,

The software elements include:

1. Operating systems for both the desktop and server,
2. CODEC algorithm (software only or hardware assisted),
3. Network management software for video/audio data stream,
4. Indexing and displaying engineering data and video frames,
5. Modules for integrating MMHIS in an Intergraph MGE environment,
6. Relational database management software.

Client Computers, Server Storage, and ATM

Based on current practices of highway agencies and fast growing capabilities of Intel x86 processor and related I/O sub-systems, the hardware platforms for both the video server and clients are Pentium or higher level computers. Capabilities of managing multiple video data streams are critical in a MMHIS, so the video server needs to be symmetrically based with a minimum of two high powered processors so that the management of data streams can be distributed among processors. The bus system for both server and clients will be based on the new peripheral component interconnect (PCI) standard. The existing version of PCI has a peak I/O bandwidth of 132 MBps. This bandwidth is more than adequate to deliver highest quality video if the graphics subsystem can take advantage of the PCI throughput. Future generations of PCI standard are proposed at the data rate of 264 MBps to 528 MBps, which is likely to be implemented in the next 2 years. The video database will reside in the server, so the storage capability of the server should be large enough to store the video frames. It is assumed that the taping speed is 55 mph and 1 megabyte of compressed video data per second. For a state interstate network with 4,000 lane-miles, it is estimated that the storage needs will exceed 260 gigabytes with full motion (30 frames/sec) and full color at NTSC quality.

ATM devices, including switches and adapter cards, were much more expensive than the rivals, such as Token Ring, Ethernet, and even FDDI. In the summer of 1994, ATM hardware prices dropped to price levels that are competitive to its rivals. Recently IBM announced a $396, ISA-based ATM adapter card with a speed of 25 Mbps (*4*). In the beginning of 1995 PCI-based ATM cards with a speed of 155 Mbps already fell below $900. This lower pricing trend will encourage the wide spread adoption of ATM implementations in LAN connecting Pentium-based computers. Industry groups are setting up standards for the interoperability of ATM equipment from various vendors, most of which will be finalized in 1995. In this MMHIS, ATM will be used in combination with existing networking equipment to increase the overall capabilities of the network's data bandwidth.

Video Data Management in Networks

Current network operating systems usually do not have the capability to coordinate video data flow sufficiently to ensure video quality on the client's desktops. The existing network management software emphasizes data integrity through error control protocols. Flow control and timeliness of delivery are critical for high quality video/audio data but are secondary in the current network software. Therefore, managing and transmitting digital video/audio data poses two major challenges to the network operating system: dealing with large file sizes and meeting the time-dependent needs of video data stream. In a multimedia application, it is required that large block digital video/audio data be transferred simultaneously and continuously to ensure the high degree of consistency in picture frame and synchronization with audio or other data. It is very difficult to manage random, bursty data along with streaming data in the same LAN. This is because of the democratic scheme in using the CPU power in which bits are bits, regardless of the type of represented information, resulting in the same priority for all applications. The data transmission slows down and speeds up along with the data traffic volume in the network. The resulting phenomenon is either the untimely arrival of the requested data at the desktop or a reduced number of frames and degradation of image quality.

It is imperative to ensure that video/audio data streams flow at consistent latency in the network and that there are no traffic clogs for video/audio data. One way to deal with the bottleneck in the network is to throw away all the software and hardware that cause the traffic jam and replace them with new multimedia capable software and hardware. For example, the existing 10-Mbps Ethernet LAN can be replaced with a ATM system at the expense of losing all investment in Ethernet and purchasing a new system. Another solution is to initially improve the limiting hardware and software so that they can handle more data on the one hand and pro-

vide a separate network management protocol for video/audio data on the other. When the cost to install ATM becomes low enough, the old facilities can be replaced with the new equipment.

Turbocharged Star Structure for Video Data

Modern network bus/ring structure is based on star topology, including the newer Ethernet and all token ring networks, shown in Figure 2*a*. However, the shared nature of bus or ring networks makes it difficult to guarantee the dedicated bandwidth required for smooth and reliable video/audio delivery due to the 10-Mbps or 16-Mbps bandwidth, even though such a network can be functional in delivering video with limited capacity and quality. One solution is to turbocharge the Ethernet hub to dedicate 10 Mbps for each desktop. The connection from the hub to the server is connected via FDDI or ATM as shown in Figure 2*b*, providing more than 100 Mbps of bandwidth. The bandwidth may be adequate in this design. This network design is also called "switched Ethernet." However, there is still no guarantee to ensure the timely delivery of digital/audio data in the network in which every application competes with each other on the same level ground to obtain bandwidth.

Network Protocol for Video

Protocols are software layers in the network, which ensure that data arrive without errors and that traffic flows are regulated properly. For video/audio data, a special video protocol is necessary to make sure that there is a highly reliable connection for an uninterrupted stream of data. The flow of regular data can be conducted through the normal protocols. With this parallel protocol approach, video/audio data will have priority over the other data flows. Normal data flows yield right of way to video/audio data. Development of new network protocols for video capable of handling thousands of simultaneous video data streams is a major challenge for the much publicized alliances among large computer companies, telecommunication services, and entertainment consortia.

Microsoft is developing a continuous-media software solution for video in a network. This Windows NT-based network management software for video streams, nicknamed Tiger, purports to enable Intel Pentium chips to control as many as 16 video streams with MPEG-2 quality, plus VCR features like pause and reverse. The challenge in developing the Tiger system lies in managing large numbers of data streams leaving the server. The major advantage of Tiger over other systems being developed is that Tiger fully uses the

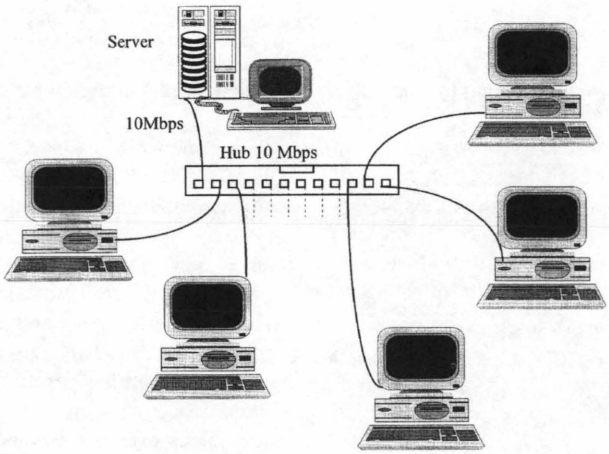

Star topology (shared network) (a)

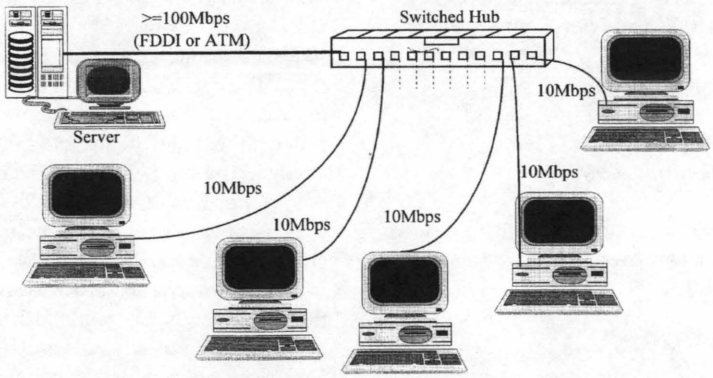

Turbocharged (Switched) star network (b)

FIGURE 2 Two configurations of the star topology. (*a*) Star topology (shared network); (*b*) turbocharged (switched) star network.

power of Pentium-based symmetrical computers, whereas most others take the approach of using proprietary super computer level hardware systems, such as Oracle's venture. In addition, the technologies in Tiger are scalable with the growth of hardware capabilities, meaning that when more powerful processors become available after the current Pentium, Tiger will be able to deliver much more simultaneous video streams and at a higher level quality. Another company, Startlight Networks, has released network management software, StarWorks, for video and audio that takes advantage of the turbocharged start structure shown in Figure 2*b*. It is claimed that the system can deliver 25 to 50 simultaneous data streams. Most existing products are targeted at the consumer and training markets, so the video quality is expected to be below the requirement of the MMHIS.

Software Issues for MMHIS

For the software environment, the 32-bit Microsoft NT operating system and Tiger or StarWorks video management software will be used as the underlying operating environment for the network. Oracle Relational Database Manager will be used in the development. Intergraph's solution to the Geographical Information System, MGE, will be used as the visual environment for data query of MMHIS.

An important feature of the MMHIS is the dynamic display of a superimposed data table with the video frames. The data table includes any type of information relating to the shown highway section's history, condition, accident records, and even environmental data. The techniques to dynamically link regular database records with video frames are unknown at this time. An efficient linking algorithm will be developed in this project so that computer CPU's resources will not be drained (both server and client) when multiple users access the facility. Figure 3 shows the expected capability of MMHIS to display data along with a video frame in a GIS shell.

Development Plan

The implementation of the MMHIS includes two stages. The first 2-year stage will use the current Ethernet networking devices with the S-VHS level video quality. ATM will be tested at the later half of the first stage. The second 2-year stage will focus on the delivery of higher quality video at the desktop through an ATM network. The development will utilize Intergraph's GIS solutions (MGE) to incorporate the MMHIS as a seamless module within MGE.

Data Flow

The data collection for this MMHIS can be conducted in a customized vehicle as shown in Figure 4. Currently, most vehicles use either Super-VHS (Hi-8 mm) or Laser Disk-based storage system, both of which provide NTSC Y/C analog signal connections. Some systems may use the Asian standard PAL-based signal system because of its slightly higher resolution. The tapes or disks can then be sent to the compression system for encoding. The encoding system most likely will be based on the high compression standard MPEG. A selection is needed to be made between two MPEG standards: MPEG-1 and MPEG-2. MPEG-1's source image format (SIF) is 352 × 240 with 30 frames/sec (FPS) in NTSC and 352 × 288 with 25 FPS in PAL. The image quality is important for engineering analysis, so the higher data rate specification of MPEG-2 is needed in this system. MPEG-2 itself includes a set of standards for various resolutions. In the latter half of 1994, IBM, C-Cube, Toshiba, and possibly others introduced cost-effective MPEG-2 encoding chips for main profile at the main level, representing the SIF of 720 × 480 at 30 FPS in NTSC. The data rate for MPEG-2 at this resolution is in the range of 6 to 10 Mbps, and the MPEG-1's data rate is from 1 to 3 Mbps.

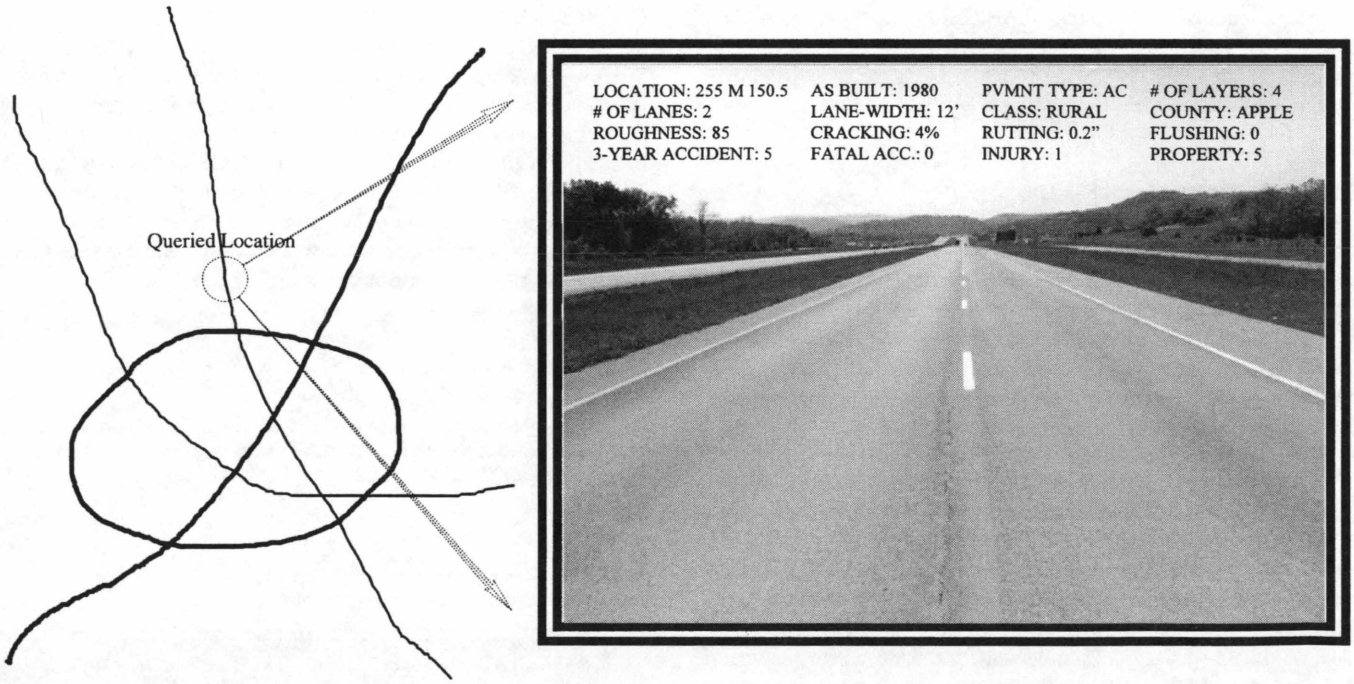

FIGURE 3 An example of the MMHIS in a GIS shell.

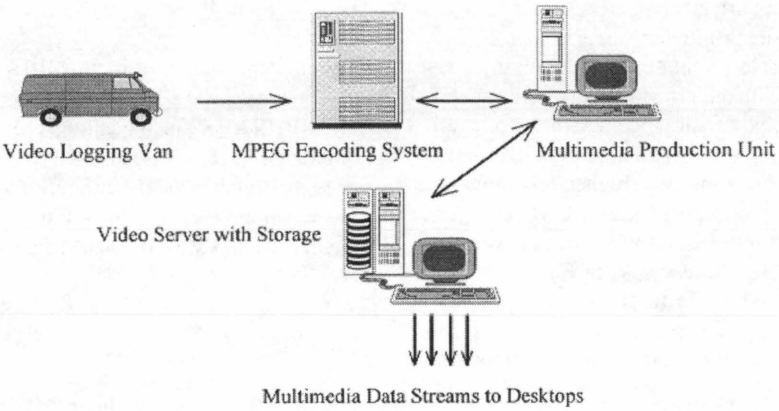

FIGURE 4 Video data flow in the MMHIS for a state highway department.

Figure 4 also illustrates the multimedia data flow within a state highway department. ATM connections are used to link the MPEG-2 encoding system, the production unit, the video server, and desktop computers in various divisions. It is expected that there will be less than 20 simultaneous users accessing the video server for multimedia files. This translates to a maximum total data rate of 160 Mbps at the single stream rate of 8 Mbps for MPEG-2 specification. Therefore, the possible data bottleneck in the ATM-based network is the delivery speed of the hard drives in the video server storage. However, by using techniques of RAID, hard drive stripping and symmetrical processing in the video server, the sustained data delivery rate of 20 MBps (equivalent to 160 Mbps) may be achieved for the network.

Eventually, HDTV will be used in this MMHIS in which effective signing and marking inventory and pavement surface distress survey are needed. The expected data rate for HDTV at the resolution of 1,920 × 1152 (high profile at main level) is 30 to 50 Mbps after MPEG-2 compression, which falls within the current bandwidth of 155 Mbps speed of ATM. In this MMHIS, all video data are off-line information. In the next few years, a traffic monitoring component can be built into this MMHIS so that real time traffic flows on major arterial highways can be observed with desktop computers.

Stage One: Ethernet and S-VHS

About 10 Pentium stations with PCI bus will be used in the development of the MMHIS. The stations will use MPEG-2 as the primary CODEC algorithm, and related hardware CODEC devices will be installed. At this stage, the digital video frames will be linked with regular highway engineering data bases so that engineering data can be shown in a superimposed box dynamically with the moving picture.

The current Ethernet network will be experimented at first. Either Microsoft Tiger software or StarWorks is to be installed at this stage. After an 18-month period, one ATM switch and PCI-based ATM adapter cards connecting the desktop computer to the server will be installed, initially providing a minimum 155-Mbps data rate station to station. When the first phase study is completed, the system will be tested by the Arkansas Highway and Transportation Department for testing and implementation. The video quality at that time will be at S-VHS level.

Stage Two: HDTV and MGE

The second phase targets an ATM-based network and second-generation PCI bus. Over 20 Pentium- and P6-based stations will be used at this stage. Software only CODEC will be tested in the P6 systems because a processor more than twice as fast as today's Pentium may well be able to conduct CODEC in the CPU without any hardware assistance. Using direct digital video technology in the image-capturing process will be an area of study at this stage. In the latter half of the second stage, full digital HDTV technologies will be tested with four times more resolution than the images from the highest possible resolution in the NTSC implementation. In addition, it is expected that tests will be conducted at this phase to automate pavement surface distress survey by using the high resolution images from digital BetaCam or HDTV cameras with proper image-processing algorithms.

CONCLUSION

The expected capabilities of this MMHIS are based on the technologies in the middle 1990s. The equipment and software used for the implementation are based on open technologies that are commercially available from a number of competing vendors. Therefore, the MMHIS will be nonproprietary, resulting in the realization of a low-cost integration of open software and hardware. MMHIS will provide a highway agency with a powerful tool in its management of the highway infrastructure.

REFERENCES

1. Hanley, R. C. and D. A. Larsen. The Connecticut Photolog Laser Videodisc Based Pavement Rating System. *Journal of Transportation Engineering*, Vol. 118, No. 2, 1992.
2. Hurwicz, M. Broadband Decisions. DATAMATION, April 1, 1993.
3. Ubois, J. Preparing for the Multimedia Mix. *Network World*, Vol. 10, No. 17, 1993.
4. Musich, P. IBM Pitches Low Prices on ATM. *PC Week*, July 4, 1994.

Publication of this report sponsored by Committee on Pavement Monitoring, Evaluation, and Data Storage.

Instrumentation and Evaluation of Prestressed Pavement Section in Pennsylvania

PAUL A. OKAMOTO AND SHIRAZ D. TAYABJI

During 1988 and 1989, a 3.2-km (2-mi) section of a prestressed pavement was constructed in Blair County, Pennsylvania as part of a new roadway along U.S. 220. In conjunction with the construction, the Pennsylvania Department of Transportation sponsored a study to instrument the prestressed pavement. Instrumentation was installed to monitor concrete strains, slab horizontal and vertical movements, and response of the pavement truck loading. This paper provides the details of the pavement instrumentation program and a summary of the data collected.

Most problems associated with conventional concrete pavements occur at joints and cracks. The most commonly observed distress in conventional concrete pavements are cracking, faulting, pumping, spalling, and joint sealant failures. In addition, continuously reinforced pavements may develop punchouts. These distress items in conventional concrete pavements contribute to reduced pavement serviceability, need for frequent maintenance, and traffic delays.

The use of prestressed (post-tensioned) concrete pavements has been suggested for many years to obtain extended service life and reduced maintenance. Conventional concrete pavements are designed on the basis of concrete's relatively low modulus of rupture (flexural tensile strength) without effectively utilizing the natural advantages of its high compressive strength. In prestressed pavements, precompression in the concrete because of prestressing allows for increased allowable stresses in the tensile and flexural state. This permits elimination of intermediate cracking because of both concrete volume changes and traffic loading, resulting in a decrease in the required number of transverse joints. Transverse joints in prestressed pavement may be spaced at 122 to 183 m.

Prestressed concrete pavements were first built over 40 years ago. There have been five major prestressed highway concrete pavements built in the United States, which have sufficient age to demonstrate the potential for improved serviceability and performance. A major study during 1985 sponsored by FHWA was conducted between 1976 and 1980 to develop design and construction procedures for prestressed concrete pavements (*1–3*). Work related to the Texas prestressed pavement project also included development of a thickness design procedure for prestress pavement overlays (*4–6*). The five U.S. projects are as follows:

- Virginia: Dulles International Airport Access Roadway, 1971;
- Pennsylvania: Near Harrisburg, 1973;
- Mississippi: U.S. 84, Brookhaven, 1975;
- Arizona: Superstition Freeway near Tempe, 1977; and
- Texas: I-35, Waco, 1985.

P. A. Okamoto, Construction Technology Laboratories, Inc., 5240 Old Orchard Road, Skokie, Ill. 60077. S. D. Tayabji, Transportation Technologies USA, Inc., 9030 Red Branch Road, Suite 230, Columbia, Md. 21045.

During 1989, the Pennsylvania Department of Transportation (PennDOT) sponsored a study to instrument and evaluate the behavior of a prestressed pavement section built along a section of U.S. 220 near Altoona in Blair County, Pennsylvania. The instrumentation and monitoring plan developed was designed to provide information on slab horizontal movements, concrete strains (stresses), and response of the prestressed pavement under truck loading. Details of the instrumentation plan and monitoring of the Pennsylvania prestress pavement are provided in this paper. More comprehensive details of the study are given in the work of Okamoto et al. (*7*).

U.S. 220 PRESTRESSED PAVEMENT

The 3.2-km section of prestressed pavement was constructed during Fall and Winter of 1988 along a section of U.S. 220 in Blair County, Pennsylvania. The prestressed pavement was in the northbound lanes of the four-lane divided highway. The 26,260 m^2 of prestressed pavement is composed of 60 slabs 7.32 m wide and 178 mm thick. Active joints are spaced at 122 m. Slabs between the 122-m joints consist of 120.8 m of main slab and 1.2 m of gap slab. Tied concrete shoulders (using tie bolts) were incorporated with the traffic lanes. The outside tied concrete shoulder is 177.8 mm thick and 3.1 m wide. The inside tied concrete shoulder is 178 mm thick and 1.2 m wide. Shoulders are jointed plain concrete pavement with joints spaced at 6.1 m. Expansion joints were used at the 122-m spacing to match the expansion joints of the prestressed pavement. The cross-section of the prestressed pavement consisted of the following (from top down):

- 178-mm thick prestressed pavement;
- 2 layers of 0.15-mm (6-mil) polyethylene sheets;
- 127-mm thick lean concrete base course;
- 76-mm thick open-graded subbase;
- 76-mm thick Type 2A subbase; and
- Natural compacted subgrade.

Minimum compressive strength for Class AA concrete for the prestressed pavement was specified to be 20.7 MPa at 7 days and 25.8 MPa at 28 days. The following are the prestressing details for the U.S. 220 project:

- Plastic-encased seven-wire strand, grade 1860 MPa;
- Strand diameter: 15.2 mm;
- Strand spacing: 457 mm;
- Number of tendons: 15;
- Ultimate strength of strand: 261 kN;

- Stressing load (80 percent of ultimate): 209 kN; and
- Specified tendon placement: 13 mm below mid-depth.

The prestressed pavement was designed using the procedures given in the work of Nussbaum et al. (*1*) and Tayabji et al. (*2*). The minimum effective mid-slab prestress was computed to be about 400 kPa. Slab end movements were computed using the procedures given in the work of Nussbaum et al. (*1*) and Tayabji et al. (*2*). Total maximum slab end movement at a joint was computed to be 89 mm based on full slab length or 61 mm based on partial slab movement. The calculations based on full slab length are considered to be conservative, as the actual measured joint movements are typically less than those computed because only a smaller portion of the slab is involved in the movement.

Construction Details

Paving for the traffic lanes was performed in 7 days between November 11 and 18, 1988. Air temperatures during the paving period ranged from −1°C to 21°C and averaged approximately 4°C. Concrete temperatures after initial heat of hydration averaged approximately 7°C. Gap slabs were placed and stress transferred in January 1989. Tied jointed concrete shoulders were placed during July 1989.

Construction Specifications

This section presents a brief outline of applicable construction specifications that were unique to the prestressed pavement.

- Friction-reducing membrane: two layers of 0.15-mm (6 mil) thick polyethylene sheets.
- Temporary jacking bridge: the temporary bridge proposed by the contractor consisted of a 51-mm diameter nut internally threaded to accommodate threading of a 400-kN monostrand anchor-wedge system. The 51-mm diameter nut bears on a 13-mm thick plate. The temporary jacking face was used at the north end of the nominal 120.8-m long main slabs. A 1.2-m long gap was used to accommodate prestressing operations.
- Prestressing operations: prestressing operations were conducted as follows:

  1st Step—107 kN @ concrete strength of 6.9 MPa;
  2nd Step—variable; and
  3rd Step—323 kN

  Strands were tensioned from one slab end and then the other at about the same time. Elongation of each tendon was measured and compared to theoretical frictionless elongation.

- Gap slab construction: gap slabs were to be constructed approximately 30 days after main slab placement. Because of late fall paving in November 1988, the gap slabs were not placed until January 1989. The gap slabs were prestressed by transferring the prestress from the temporary jacking face of the main slabs to the active joint side face of the gap slabs. A section of the gap slab is indicated in Figure 1.
- Compression seals: specified seals were required to accommodate 44-mm movement at active joints. This design movement was established based on experience at the existing prestressed pavement near Harrisburg, Pennsylvania. The compression seal was 102 mm wide, 64 mm in height, and required a groove depth of 79 mm.
- Dowel caps: stainless steel dowel bars 38 mm in diameter by 457 mm long, spaced at 457 mm, were used at active joints. Dowel caps were used at one dowel end.
- Shoulders: tied concrete shoulders were constructed after gap slab construction. Because of late fall paving, the shoulders were not

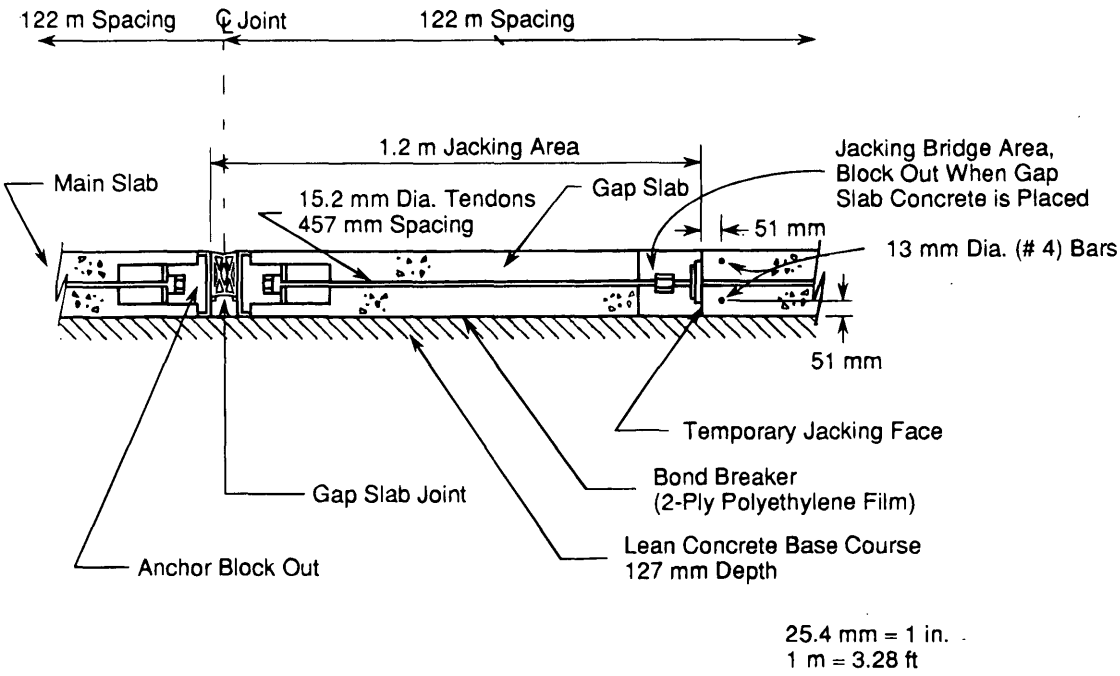

FIGURE 1 Gap slab section.

placed until July 1989. The shoulders were placed over the 127-mm thick lean concrete base used under the mainline pavement. Two applications of white pigmented wax-based curing compound were used over the lean concrete base to reduce slab-to-base friction.

INSTRUMENTATION PLAN FOR THE U.S. 220 PRESTRESSED PAVEMENT

Short-Term Monitoring

The objective of the short-term monitoring plan was to obtain information related to slab movements and concrete strains and stresses during the early age (over a period of several days) of the pavement. Pavement monitoring was initiated soon after concrete placement and was continued for up to 15 days. Shoulders and gap slabs were not yet constructed during the short-term monitoring period. Instrumented Slab 1 cast on November 14, 1988 was the 10th two-lane slab paved. Instrumented Slab 2 cast on November 17, 1988 was the 22nd slab of 30 slabs (two-slab pair) paved. Gap slabs were placed approximately 50 days after construction.

Long-Term Monitoring

The objective of the long-term monitoring plan was to obtain information related to slab movements and concrete strains after concrete shoulder placement. Long-term monitoring of the installed instrumentation and condition survey was conducted as follows:

1. During April 1989 (early spring time), the initial post-construction cracking survey was performed (before shoulder placement).
2. At the time of the August 1989 load testing, measurement of joint widths and slab length changes, monitoring of installed instrumentation (concrete strains, temperature), and second post-construction cracking survey (after shoulder placement) were performed.
3. During March 1990 (late winter), measurement of joint widths and slab length changes and third post-construction cracking survey were performed.

Tied concrete shoulder construction was performed in July 1989, before load testing. Load testing was conducted after the construction of concrete shoulders during the first week of August 1989. Load testing was conducted over a period of 2 days. The falling weight deflectometer (FWD) testing was done in September 1989.

Load Testing

The objective of pavement load testing was to determine the response (strain and deflection) of the prestressed pavement to actual single-axle and tandem-axle truck loadings. In addition, a FWD was used to characterize the deflection response of all 30 outside lane slabs.

Instrumentation Layout

Two inside lane slabs were monitored both during the short- and long-term visits. Joint widths at all 31 joints were measured during the long-term monitoring phase of the study. The two slabs monitored were selected from the third and sixth day of paving. Similar to the prestressed slabs, the second instrumented slab had two layers of polyethylene placed under the jointed concrete shoulders. The instrumentation was placed at two sites (Sites 1 and 2) at each of five stations (Stations A, B, C, D, and E), as indicated in Figure 2. At Sites 1 and 2, the embedded sensors (strain gauges and thermocouples) were installed by boxing out concrete at these locations, removing the boxed-out concrete, installing the sensors mounted on "chairs," and carefully replacing the concrete in the box-out area around the sensors. Sensors were prewired and positioned under the boxes before paving. Wiring for the instrumentation was run through a polyvinyl chloride conduit buried 102 mm into the granular subbase. The conduit was prepositioned before lean concrete construction. The lean concrete base was later cored to provide access to the conduit. A discussion of the specific instrumentation used in the U.S. 220 project is given in the work of Okamoto et al. (*7*).

Load Testing Details

Full-scale load testing of the prestressed pavement was conducted soon after the concrete shoulders were constructed and before the pavement was opened to traffic. Load testing was conducted at the two instrumented slabs. At each slab, instrumentation was installed to determine mid-slab edge strain (outside lane), mid-slab deflection, joint deflection, and joint load transfer. Load tests were also conducted on an adjacent new 279-mm thick jointed plain concrete pavement (referred to as Slab 3). This pavement was placed over a 102-mm open-graded base and 127-mm granular subbase, and has transverse-skewed doweled joints placed at 6.1 m. Strain and deflection data were recorded for 8,080-kg single-axle and 17,750-kg tandem-axle truck loadings. Data were recorded for axle placements along the outside lane edge and a distance of 457 mm inward from the lane edge. Trucks were operated at creep speed to measure load-induced deflection and strain. Load testing was carried out several times during the day, starting early in the morning, to determine the effect of temperature variations on slab deflections and concrete strains because of loading.

In conjunction with the full-scale load testing, FWD testing was conducted along all 30 outside lane slabs. Testing for each slab was conducted at joints and interior stations along the outside lane.

Materials Testing

Data on concrete tests performed by others were obtained for analysis of early age strength gain (post-tensioning operations). Compressive strength testing was specified by PennDOT. Concrete cylinder strengths at early age were tested for initial and final post-tensioning considerations. Modulus of elasticity and compressive strength tests were also performed on cylinders fabricated during concrete placement. Testing was conducted to establish a project-specific relationship to predict modulus of elasticity from compressive strength data.

SUMMARY OF SHORT-TERM MEASUREMENT DATA

Ambient and Concrete Temperatures

Ambient air and concrete temperatures were recorded every hour for the first 17 days for instrumented Slab 1 and 14 days for instru-

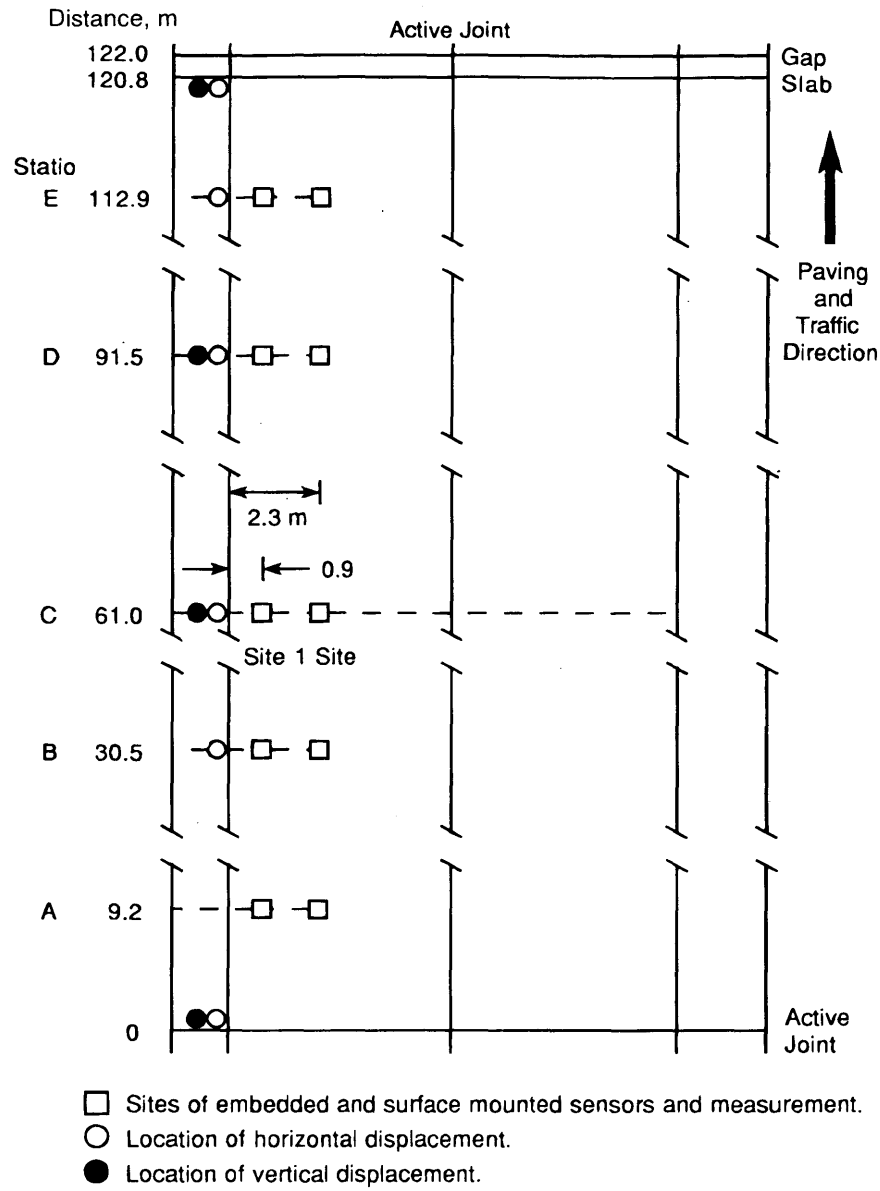

FIGURE 2 Instrumentation layout at a slab.

mented Slab 2. Air temperatures at the site during this phase of testing typically ranged from −1°C to 10°C. Typically, slab temperatures decreased from 21°C to 4°C within 5 days. The use of straw insulation sandwiched between two layers of white polypropylene retained the heat of hydration. The typical daily range in concrete temperatures was 3°C. No significant temperature fluctuation was observed, even when the insulating layers were removed, because of relatively cool and constant ambient temperatures and minimal solar radiation effects.

Concrete temperature 152 mm from the surface was slightly higher than the temperature at 13 mm from early evening to about mid-day (12:00 noon). The temperature differential between the 13-mm and 152-mm depths was minimal over the entire monitoring period. Typically, for both instrumented slabs, the differential temperature was less than 1°C during the short-term monitoring period.

Concrete Strain

The concrete strain was monitored with embedment, sister (strain gauges bonded to deformed bars), and Carlson gauges positioned at slab mid-depth. Embedment gauges were also positioned at 38- and 140-mm depths to provide data on strain variation with depth. Surface-mounted strain gauge data were also used to monitor concrete strain changes. Initially, it was planned to mount the gauges on the surface approximately 24 to 36 h after concrete placement, after the concrete had attained sufficient strength. Because of delays in starting construction, the concrete was placed in much colder than anticipated weather. The relatively slower concrete strength gain and retention of moisture by polypropylene and straw insulation prevented gauges from being adequately bonded to the surface until after about 60 h. Strain changes were similar in trend to near-surface embedment gauges.

The measured strains include effects of temperature, subbase friction, prestress, concrete creep, and drying shrinkage. Concrete creep and drying shrinkage effects increase strain (compression-positive sign convention) as the slab shortens. Since average daily concrete temperatures remained uniform between the second and third prestress levels, the general strain increase is attributed to shrinkage and creep.

Prestress Stages

For both Slabs 1 and 2, the strains dropped significantly (loss in prestress) after the first prestress stage at 1.7 and 1.4 days, respectively. This drop was fully recovered with the second prestress stage approximately 24 h later. The loss can be attributed to concrete contraction caused by shrinkage and temperature. The concrete temperature record during the first day for both slabs indicated a downward trend as the slab heat of hydration dissipated. During the first 36 h for Slab 2, the measured concrete temperatures approached 21°C. By the second stage of prestress, concrete temperatures (average of four depths) dropped to approximately 16°C. The effects of first-stage prestressing (post-tensioning) are clearly indicated to offset the tensile subbase restraint stresses built up as the slab cooled after the peak heat of hydration. Without the critical first stage of prestress at about 36 to 48 h, the tensile restraint stresses could have exceeded the concrete tensile strength.

Also, the subbase restraint had an effect on effective prestress. At slab mid-span (Station C), the prestress is significantly lower than near the ends at Stations D and B. The largest prestress was near the slab end where frictional subbase restraint was lowest.

Larger decreases in strain (drop in prestress) between the first and second prestress stages were measured at Station C for Slab 2. Decreases in sister gauge readings at Slab 2 Stations C and D after first-stage stressing possibly indicate that the gauges were not properly monitoring strain at 24 h. The change in strain at other stress levels indicated consistent increases. It appears that the gauges had not quite stabilized at 24 h for Slab 2.

Stresses were computed from strains and the modulus of elasticity estimated from compressive strength. Concrete stresses and strains generally increased more (compression) with each prestress level at the ends than near mid-span. At the final prestress stage, the stress near the slab ends for the three gauge types ranged from 1.0 to 1.5 MPa higher than that at mid-span for Slab 1. For Slab 2, the stresses at the ends ranged from 0.4 to 2.2 MPa higher than at mid-span. Generally for Slab 1, both sister and embedment gauges indicated the final prestress levels were somewhat symmetrical around mid-span. For Slab 2 gauges, the final prestress was not as symmetrical. Final prestress at Slab 1 mid-span ranged from 0.6 to 0.7 MPa and averaged 0.7 MPa for the three gauge types.

The embedment gauge strain was monitored at depths of 38, 89, and 140 mm from the slab surface. The average stress difference for the first two prestress stages between top and bottom gauges was 124 and 41 kPa for Slabs 1 and 2, respectively. For prestress Level 3, the change in strain was generally higher at the top than at the bottom of the slab. The average third level prestress gradient was 227 and 138 kPa higher compressive stress at the top than at the bottom for Slabs 1 and 2, respectively. Final prestress gradient ranged from 427 kPa lower to 338 kPa higher compressive stress near slab bottom than the top. The overall average for both slabs at all stations (compressive stress) was about 21 kPa higher at slab top than at bottom.

Daily Strain Variations

Strains measured at mid-depth with Carlson gauges are indicated in Figure 3 for Slab 2. There is a decrease in compressive strain from early morning to mid-day as the slabs expand because of an increase in air temperature. As the slab temperature drops near mid-day, the compression strains increase. The apparent strain because of creep and drying shrinkage shortening of the slab are observed by the slowly rising general trend in strain.

Horizontal Slab Movement

Horizontal slab movement was monitored using dial gauges mounted on reference rods embedded 0.6 m into the subgrade. Monitoring was performed for both slabs three times a day (at approximately 8:00, 12:00, and 16:00) for about the first 2 weeks after concrete placement. Horizontal movements were monitored to evaluate the effects of post-tensioning, temperature variations, and initial concrete shrinkage. Movements were monitored at slab ends, mid-slab, and quarter points along the slab length.

The slab temperatures and gradient with depth did not vary because of the relatively cold air temperatures, low solar radiation, and use of straw insulation at earlier ages. Very small displacement magnitudes were measured throughout the day. Longitudinal end movements for Slab 1 at 17 days and Slab 2 at 14 days averaged 14 mm and 15 mm. Movements at 31 m from transverse joints averaged 8 mm.

Vertical Slab Movement

Vertical slab movements were monitored simultaneously with longitudinal displacement. Gauges were mounted on reference rods positioned 0.6 m into the subgrade. Curling because of temperature variations and prestressing was monitored at mid-slab and at both slab end corners. Similar to longitudinal displacement data, curling effects because of slab thermal gradients were negligible throughout the first day. Very small changes in curl were measured at the mid-span edge and corners as the slab temperature increased.

Curl, relative to the day of placement, was significantly higher at 4 days for Slab 1 at both the edges and corners. Similar increases were noted at 2 days for Slab 2. For both slabs, the curl magnitude within 1 or 2 days after casting was higher at the corners than at the mid-slab edges. The measured curl was about 1 mm at slab corners after the first few days. Typical of most days during the short-term monitoring period, temperature gradients ranged from 0.2°C/in. (temperature at bottom greater than top) to zero. This was partly because of the cool water-like temperatures and the straw cover used over the new pavement.

Tendon Elongations

Tendon elongation for all slabs was measured for each level of stressing. For the 120-m main slab prestressing, the total theoretical tendon elongation after final post-tensioning was 907 mm. Data provided by PennDOT indicated that measured elongations were generally less than the calculated elongations. Differences are mainly attributable to plastic casing friction and tendon wobble. Measured tendon elongations ranged from about 740 to 910 mm.

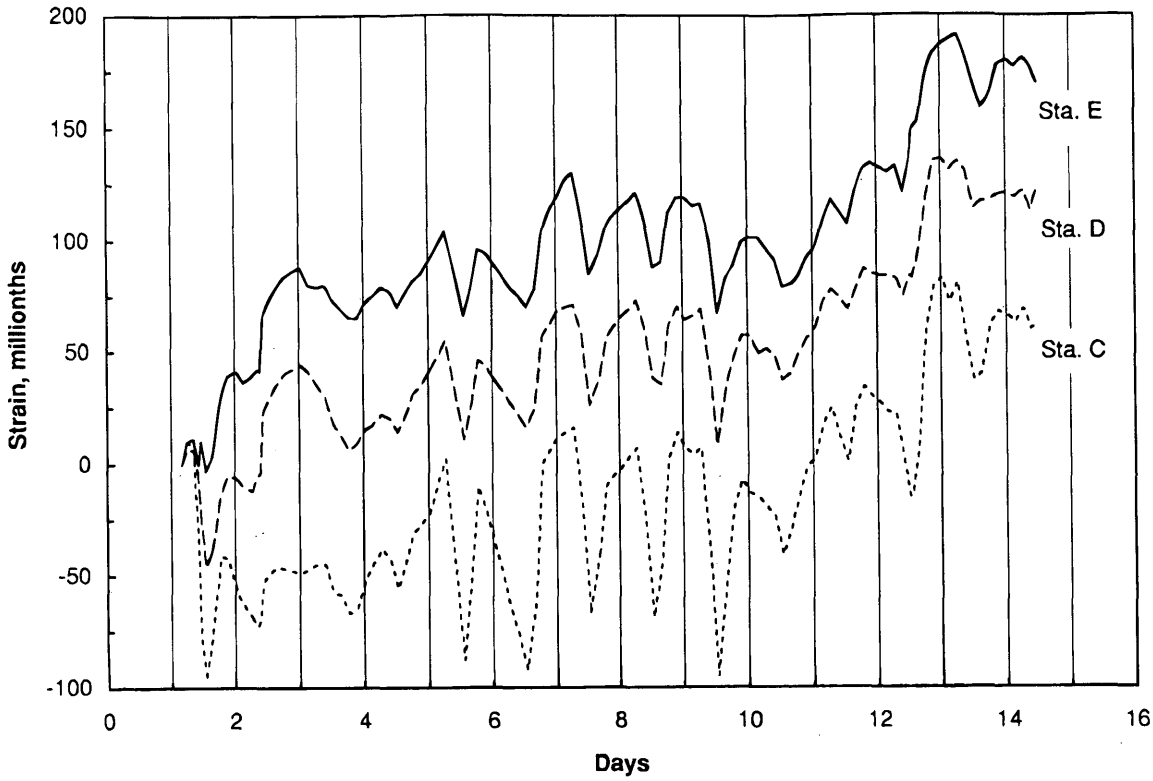

FIGURE 3 Slab 2 Carlson gauge strains.

SUMMARY OF LONG-TERM MEASUREMENT DATA

The objective of long-term monitoring was to obtain information related to slab movements and concrete strains and stresses after a period of several months. The monitoring of strains was conducted during the first week in August 1989 in conjunction with load testing.

Concrete Strain

Analysis of the sister and embedment gauge strain data relative to the initial short-term monitoring resulted in inconsistent trends and magnitudes. Concrete strain was monitored with the embedment, sister, and Carlson gauges. The embedment and sister gauges used in the short-term monitoring possibly drifted over the extended period of time. Since the sister and embedment gauge data could not be directly related back to the initial readings, the data was referenced to the summer visit initial readings.

The Carlson gauges used were initially selected during the project planning since they are considered very reliable over a long period of time. Because of the relatively high gauge cost, the number of gauges was limited to three per slab. The Carlson gauges, as expected, provided consistent strain data relative to the initial short-term monitoring approximately 9 months earlier. The Carlson gauge data reported is relative to the 17-h baseline used in the analysis of short-term strain monitoring. No strain data adjustments were made in Carlson gauge data to account for early and long-term creep and drying shrinkage effects.

Surface-mounted strain gauge data was also collected for Slab 2. Changes in strain with temperature were significantly larger compared to other gauges. Larger changes were attributed to effects of temperature on the gauge instead of changes in true concrete strain. Since the gauge data could not be reliably compensated for temperature, and the trends in strain were similar to embedment gauges at 38 mm below the surface, strain gauge data from surface-mounted gauges are not discussed in the analysis of long-term data.

Relative Strain Response

The slab response to thermal changes appears to be symmetrical. Changes in strain because of temperature at Stations A (9.2 m) and E (112.9 m) follow the same trend and magnitude change.

For Slab 1, embedment gauges at depths of 38, 89, and 140 mm were monitored at all five stations to evaluate the effects of temperature gradients on prestress distributions with depth. The gauges at depths of 38 mm generally indicated a larger strain-change magnitude than the gauges at depths of 89 mm. The gauge at mid-depth also consistently had a larger relative strain change than the gauges at 140 mm. This corresponds to the relatively larger temperature ranges recorded during peak daylight hours near the surface.

Absolute Strain Response

Carlson gauge data measured over a period of 24 h are relative to the initial short-term monitoring period (baseline 17-h age). No adjustments for early and long-term drying shrinkage or creep were made on the data. Because of long- and short-term creep and drying shrinkage effects, the slab shortening caused an increase in compressive strain. With slab shortening there is a loss in effective prestress.

Ranges in daily strain measured using Carlson gauges for both slabs was 92 to 144 $\times 10^{-6}$ mm/mm. No significant change in range was measured between the stations for Slab 2. For Slab 1, the range in strain was significantly higher at Station C than at Stations A and B. Measured strain magnitudes for Slab 1 ranged from 175 to 354 $\times 10^{-6}$ mm/mm at the three stations (relative to hour 17). For Slab 2, strain magnitudes ranged from 274 to 555 $\times 10^{-6}$ mm/mm at the three stations.

Joint Width

Joint widths were measured at each of the 30 transverse joints and at the two terminal joints using a measuring scale. Measurements were conducted at several different times of the day to evaluate opening and closing rates and magnitudes. Readings were taken 610 mm from the slab edges. Initially, both inside and outside lane joint measurements were taken. After several time periods no significant differences in joint width for the inside and outside lane movement were recorded.

Joint widths were measured August 3 and 4, 1989 and March 7 and 8, 1990. Air temperatures during the summer monitoring period ranged from 23°C to 33°C. Air temperature at the winter visit ranged from −8°C to 13°C. Daily transverse joint width changes on average were about 8 and 13 mm during the summer and winter visits, respectively. Larger changes were measured in the winter because of larger air temperature ranges. Overall average width for transverse joints was 44 and 73 mm for summer and winter monitoring, respectively.

Vertical Slab Movement

Vertical curl changes were measured with dial gauges mounted on reference rods positioned 1.5 m into the subgrade. Relative changes in curl were monitored at the slab corner, mid-span, and at other interior stations for both instrumented slabs. In addition to the prestressed slab curl, vertical movement was also recorded at a jointed concrete slab adjacent to the project section. Curl was measured in conjunction with full-scale load testing. Curl was measured for the outside (truck) lane.

No significant differences in magnitude or trend were measured at different stations of the prestressed slabs. Curl was similar at the corner, mid-slab, and intermediate stations for the prestressed slabs. Maximum curl deflection relative to initial readings was 0.5 and 0.7 mm for the 178-mm thick prestressed Slabs 1 and 2, respectively. Minimum curl (down) occurred at 12:30 p.m. and 1:00 p.m. for Slabs 1 and 2, respectively. Maximum relative curl for Slab 3, the 279-mm thick plain-jointed slab, was 0.5 mm.

LOAD TESTING DATA SUMMARY

Full-scale load testing was performed on the prestressed slabs during August 1989. Surface edge strain and deflection data for the two prestressed slabs and the one plain slab were measured for an 8,080-kg single-axle dual wheel and 17,750-kg tandem-axle dual wheel truck loading. Data under moving loads were recorded for wheel placement along the outside edges of the driving lane and at a distance of 457 mm inward from the edge. Trucks were operated at creep speed of 3.2 to 4.8 km per hour. FWD testing along all 30 outside lane slabs was conducted in September 1989.

Load Truck Response

A summary of measured load-induced edge strains (in millionths) is given below for mid-slab locations:

	Slab 1	*Slab 2*	*Slab 3*
Single-axle loading—morning			
edge loading	33	27	10
load at 457 mm from edge	14	8	2
Single-axle loading—afternoon			
edge loading	18	14	7
load at 457 mm from edge	8	9	3
Tandem-axle loading—morning			
edge loading	31	32	8
load at 457 mm from edge	22	—	3
Tandem axle loading—afternoon			
edge loading	10	21	7
load at 457 mm from edge	6	9	5

Average edge strains decreased significantly as the load shifted from edge to 457 mm from the edge. Load-induced strain in the prestressed slabs decreased during the afternoon as slabs curled down with temperature. Load-induced strain on the 279-mm thick plain concrete slab was less sensitive to curling effects. Thinner slabs have greater temperature gradients and therefore greater curl deformation than thicker slabs.

A summary of measured load-induced edge deflections (in mm) is given below for mid-slab locations:

	Slab 2	*Slab 3*
Tandem-axle loading along edge—morning	0.38	0.13
Tandem-axle loading along edge—afternoon	0.15	—

Measured deflections were sensitive to stationing for the prestressed slabs. Significantly higher deflections were measured at mid-span in the prestressed slabs than at stations away from mid-slab and at the joints. Differences in deflections with stationing were significant only for the earliest set of readings. For the last two sets of deflection data for each slab, when slabs had the least upward curl, there was no significant difference in deflection with stationing.

FWD Test Results

A Dynatest 8002 FWD was used to evaluate deflection load transfer efficiency and estimate modulus of subgrade reaction. Two types of testing were conducted. Joint testing was performed to calculate joint efficiency at each joint in the center of the outside (truck) lane. Basin deflection testing was done to calculate modulus of subgrade reaction.

The effective modulus of subgrade reaction was backcalculated for each slab at 61.0 m and 91.5 m. Load deflection transfer efficiency is the unloaded divided by loaded slab deflection (percent). A summary of joint efficiency and modulus of subgrade reaction data is given below:

	Subgrade Support, MPa/m	*Joint Effciency, percent*
Minimum	43	59
Maximum	103	94
Average	77	77
Standard deviation	14	9

CONDITION SURVEY DATA

The first condition survey of the 60 prestressed slabs was made in April 1989. Gap slabs were placed by the April 1989 visit and prestress transferred from the main slab to the gap slabs. Shoulders had not yet been placed. The second condition survey was performed approximately 2 weeks after tied shoulder construction during the long-term monitoring and load testing in August 1989. The third cracking survey was performed in March 1990 during the winter site visit to measure joint movements.

Tied concrete shoulders were added to the prestressed slabs in July 1989. The full-depth concrete shoulders were jointed plain concrete with 6.1-m joint spacing. Construction traffic was allowed on the prestressed slabs. Several hairline transverse cracks in the prestressed slabs were noted during the August 1989 condition survey. Cracking generally was within 6.1 m of the mid-span of prestressed slabs. Cracks were observed in the 5th through 11th and 15th through 18th two-lane slab sections. Two other slab sections, the 1st and 28th slabs, also had transverse cracking. All slabs with multiple cracks were from the third paving day. Of the five pairs of slabs cast on the third paving day, two had one crack, one had two cracks, and two had three cracks.

A follow-up survey in March of 1990 (second winter) indicated a significant amount of additional cracking. For the 30 pairs of prestressed slabs, 132 cracks were observed. Cracks were noted in all but 7 of the 30 pairs cast. Cracks were generally within the mid 61 m of the 122-m long prestressed slab. Eighteen pairs had five or fewer cracks. Four and five pairs of prestressed slabs had 7 and 9 cracks, respectively. The other three pairs of prestressed slabs had 11, 13, and 15 cracks at the time of the March 1990 survey. Cracks were noted in slabs cast on all paving dates with the exception of two slabs cast on the last paving day. Minor spalling was observed along several cracks in the prestressed slabs.

Similar to the prestressed slabs, the second instrumented slab had two layers of polyethylene placed under the jointed concrete shoulders. At the time of the March 1990 survey, the first instrumented slab (slab section 10 from the third paving day) had seven transverse hairline cracks. Instrumented Slab 2 (slab section 22 from the sixth paving day) did not have any cracks at the time of the March 1990 condition survey. Results of the August 1989 (first summer) and March 1990 (second winter) cracking survey are indicated in Figure 4.

The excessive number of cracks within slab sections 4 through 10 and 13 through 16 indicates that prestressing of the slabs was not effective. Cracking can be attributed to both construction problems and design deficiencies. Other problems associated with the tied concrete shoulder were the effects of differences in joint movements. Numerous shoulder slabs (outside lane) at the time of the March 1990 condition survey exhibited joint spalling and corner breaks. The prestressed slab expands and contracts over its full length. The jointed shoulder slabs only move over their 6.1-m lengths. The differential movement problem was clearly observed at prestressed slab active joints. The prestressed slab differential movement resulted in an observable offset in joint positions. At the time of the August 1989 survey, the prestressed slab joints were up to 25 mm away from the adjacent shoulder joint. The offset also

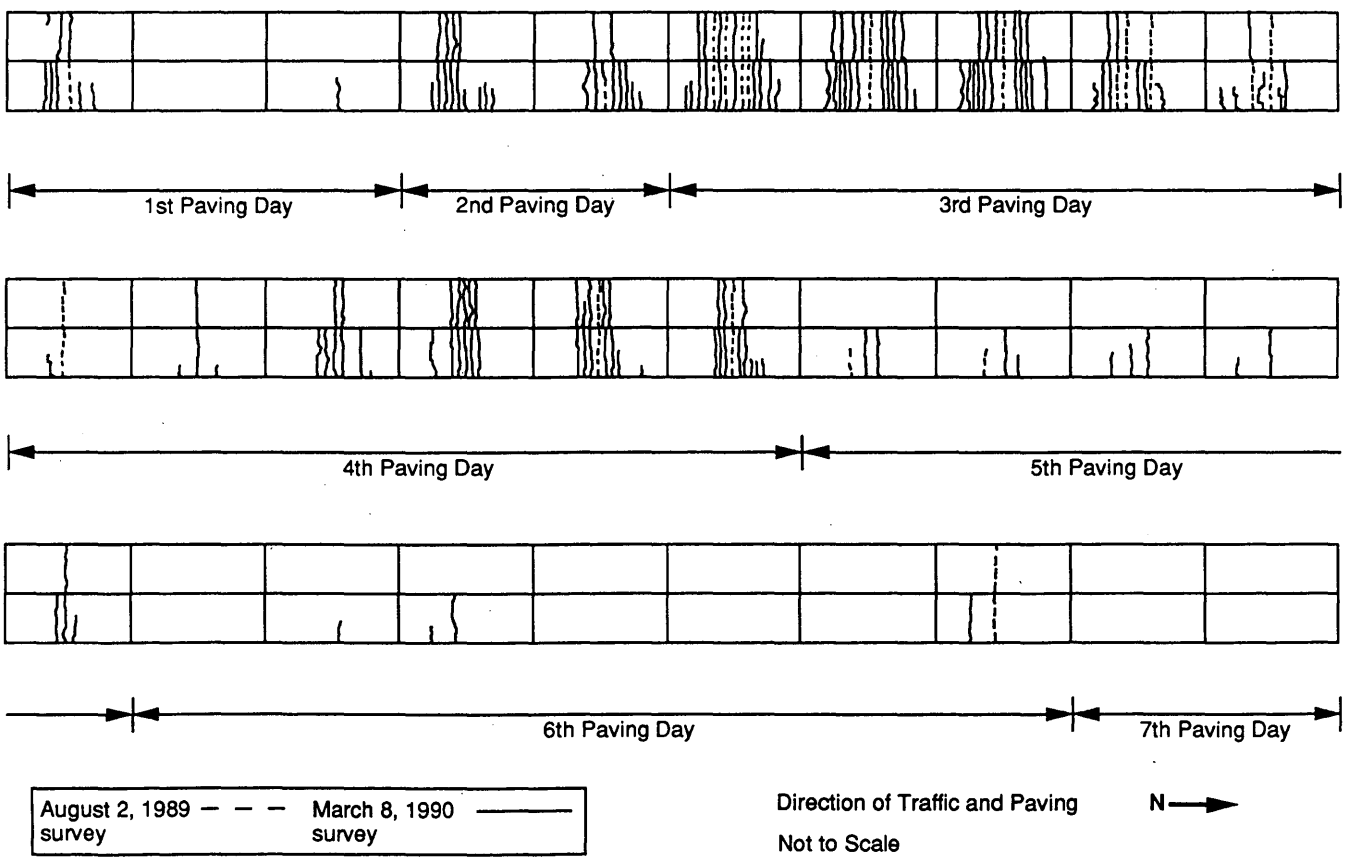

FIGURE 4 Transverse-cracking condition survey.

caused very large shear deformations in the joint sealant at the shoulder joint.

SUMMARY

Long-term monitoring data indicate that at 8 months, concrete creep and shrinkage were about 70 kPa higher than anticipated, assuming no steel relaxation losses. Effective calculated mid-slab prestress using design data for the prestress pavement and increased concrete shrinkage of 200×10^{-6} mm/mm was 393 kPa (permanent). The effective measured mid-slab prestress after 8 months was 517 and 1392 kPa for the two instrumented slabs. A condition survey was performed soon after tied jointed concrete shoulders were placed. Several small transverse hairline cracks near mid-spans were noted in some slabs. A follow-up survey 8 months later indicated a significant increase in transverse cracking. Most of the cracking can be attributed to some effective prestress loss during transfer of prestress and to use of the jointed plain concrete shoulders. As of early 1995, the prestressed pavement section was providing a very good ride, even over sections exhibiting a large amount of cracking. No significant amount of additional cracking had taken place in most of the slabs.

This project has provided verification that prestressed concrete pavements are viable pavement alternatives. The thinner prestressed pavements are promising candidates for unbonded concrete overlays for projects in which grade constraints may not allow thicker conventional jointed concrete pavements.

ACKNOWLEDGMENTS

This investigation was sponsored by the Office of Research and Special Studies of the Pennsylvania Department of Transportation. Special thanks go to Wade Gramling, Steven Davis, Jim Merrill, Ed Stoltz, William Replogle, Randall Knepp, and Gary Marks of the Pennsylvania Department of Transportation for their valuable assistance during the study.

REFERENCES

1. Nussbaum, P. J., S. D. Tayabji, and A. T. Ciolko. *Prestressed Pavement Joint Designs.* Report FHWA/RD-82/090. FHWA, U.S. Department of Transportation, June 1983.
2. Tayabji, S. D., B. E. Colley, and P.J. Nussbaum. *Prestressed Pavement Thickness Design.* Report FHWA/RD-82/091. FHWA, U.S. Department of Transportation, June 1983.
3. Nussbaum, P. J., B. F. Friberg, A. T. Ciolko, and S. D. Tayabji. *Prestressed Pavement Construction Manual.* Report by Construction Technology Laboratories for the FHWA, U.S. Department of Transportation, June 1981.
4. Diaz, A. M., N. H. Burns, and B. F. McCullough. *Behavior of Long Prestressed Slabs and Design Methodology.* Report FHWA/TX-87/71. FHWA, U.S. Department of Transportation, Sept. 1986.
5. Maffei, J. R., N. H. Burns, and B. F. McCullough. *Instrumentation and Behavior of Prestressed Concrete Pavements.* Research Report 401-4. Center for Transportation Research, University of Texas, Austin, Tex., Nov. 1986.
6. Mendoza Diaz, A., et al. *Design of the Texas Prestressed Concrete Pavement Overlays in Cooke and McLennan Counties and Construction of the McLennan County Project.* Research Report 555/556-1. Center for Transportation Research, University of Texas, Austin, Tex.
7. Okamoto, P. A., S. D. Tayabji, and E. J. Barenberg. *Instrumentation and Evaluation of a Prestressed Pavement, U.S. 220, Blair County, Pennsylvania.* Research Report 87-19. Office of Research and Special Studies, Pennsylvania Department of Transportation, Harrisburg, Pa., April 1991.

Publication of this report sponsored by Committee on Pavement Monitoring, Evaluation, and Data Storage.

Automated Distress REcording System (ADRES)

JEROME F. DALEIDEN AND BRIAN M. KILLINGSWORTH

As Pavement Management Systems become the primary tool by which agencies allocate the funds for pavement rehabilitation, the accuracy of data collected for these systems becomes paramount. Distress data play a significant role in such pavement evaluations and there are many different methods available for collecting this data, one of these being manual distress surveys. However, manual (visual) distress surveys have their limitations. Inaccuracies that arise in the manual accumulation and summarization of the distress data can limit or impair its use significantly. In this study the latest "electronic clipboard" technology was employed to create a computerized system that will store and summarize distress data automatically. Software was developed so that as a distress and its associated location are identified and drawn "electronically," pertinent information about the distress is stored in a data base that is used to automatically summarize the results. Using this system greatly reduces the potential for errors that occur when distress surveyors process and relay information from one set of forms to another. The system has been developed so that a surveyor can conduct a distress survey on a computer without the need for a keyboard. The pen computer technology takes the concept of "user-friendly" technology to another level. Not only can this system be adapted to any distress survey procedure, but this technology appears to have significant potential for an almost unlimited array of comparable applications.

Pavement Management Systems (PMS) continue to grow in popularity as a means of justifying or allocating the distribution of limited resources for maintaining an agency's pavement network. These systems, however, can only be as accurate as the data that are collected for them. Similarly, studies on the performance of pavements, such as the Long Term Pavement Performance Studies (LTPP) initiated by the Strategic Highway Research Program (SHRP) and currently continuing under the FHWA, will be restricted by the quality of the data collected for each test section under observation.

Distress data play a significant role in such pavement evaluations. Automated photographic equipment can be utilized to collect parts of this distress data. However, use of such equipment can be cost-prohibitive, and, as found in the SHRP and FHWA LTPP program, can have limited reliability for those distresses in which depth perception or fine resolution is required (*1*). Hairline cracking, fault measurements, lane-to-shoulder drop-off, and similar distresses are currently still presenting problems for this type of equipment.

Manual distress surveys serve as an alternative to the collection of this data, but they have their limitations as well. Distress identification manuals, like SHRP's "Distress Identification Manual for Long Term Pavement Performance (LTPP) Studies" and other similar documents (*2–4*) provide a uniform basis for collection of this type of distress data. Although such manuals normally provide sufficient descriptions of the distresses themselves and their associated severity levels and instructions on how to measure each distress, inaccuracies arise in the processing of this data as they are transferred from the field to the distress maps, to the summary sheets, and then to an electronic storage medium (i.e., a data base). To minimize these inaccuracies, considerable work time is expended in quality assurance exercises, which include reviewing the data at various phases of its processing to catch and eliminate as many of the errors as possible.

With the creation of the Automated Distress REcording System (ADRES) for the storage and summarization of this information, considerable hours of quality assurance time can now be saved, and the potential for inaccuracies in the distress data can be reduced considerably. Not only is the collection process expedited, but all summarization is done automatically.

Brent Rauhut Engineering Inc., 8240 Mopac, Suite No. 220, Austin, Tex. 78759.

RESEARCH WORK PERFORMED

In general, the work performed under this Phase 1 research was the development of an operating prototype of the computer-based pavement distress identification system. Included in the development of this prototype was the programming of all associated software and the procurement and development of all the hardware necessary to complete a working system. This includes hardware that provides the system with the position of the distresses within the test section so that operator entry of this data may be bypassed as well.

With the ADRES, the distress surveyor has a decreased amount of data to process and transcribe from one set of forms to another. Therefore, the number of potential errors will be reduced and, ultimately, survey production will be increased. The reduction of errors and increases in productivity will enhance the validity of the data and their use in predicting pavement performance. Ultimately, such improvements will optimize the use of the available resources for managing our nation's infrastructure.

Work on this project was divided into three tasks: (a) hardware procurement and configuration; (b) software development; and (c) testing and validation.

Hardware Procurement and Configuration

Evaluations of available hardware were conducted to identify the most suitable and cost-efficient system available for the proposed field application. The "electronic clipboard," or pen computer technology, was selected to allow input into the system so that a keyboard would not be exposed to the elements in the field. Dust, mist, and other types of contaminants are of particular concern when conducting field work on the side of a highway. Using the pen interface should also prove particularly advantageous in that distress surveyors need not touch a keyboard at all. This aspect will enhance the

user-friendliness of the system and inevitably lead to much more accurate surveys.

Operators interface with the system through a "touch screen" by pointing the magnetic pen at the desired screen symbols (buttons) to initiate the survey activities required. This technology is fairly similar to the "mouse" technology currently employed by most personal computer (PC) users (both in the expense of the hardware and the costs associated with software development), but it eliminates the awkwardness of utilizing a mouse in the field and the problems associated with track balls (inverted mouses for portable PCs) when exposed to the elements. This pen technology was developed specifically for gathering field data and is now commonly used for bridge inspection, survey work, and other similar field applications.

After choosing the pen computer technology as the means of gathering the data, a search was begun to find the most field-worthy and economical system. Power management, durability, and screen visibility in direct sunlight were evaluated to establish field worthiness.

The pen system selected was a GRiD 486 notebook Convertible. This system has a keyboard that was used in conjunction with the pen interface to facilitate the development of the ADRES software; however, the keyboard is not required to operate the ADRES software. The GRiD system comes with a 4-h battery, automatic standby for improved power management, and a feature to allow batteries to be switched in the middle of an operation without losing any data. This feature was particularly appealing due to the fact that with the addition of a spare battery the system could be run for a full 8 h without down time or data loss. Also, the system has a backlit screen for ease of use under direct sunlight, and was sold for less than the other pen systems available at the time. At the time the GRiD system was purchased, there were several other hardware manufacturers that were in the process of developing pen-based notebook computers. The available pen-based machines varied, but the ADRES software should run on any hardware system with the proper operating system present. The ADRES may even be run without the benefit of a pen-based system by utilizing the mouse of a standard computer; however, this defeats many of the previously noted advantages of the pen system.

Initial efforts were also made to explore the feasibility of developing hardware and software that would obtain the x and y coordinates of distresses contained within the limits of the test section lane and provide the locations to the ADRES software during runtime. Two feasible alternatives were identified. The first was to mount a distance-measuring instrument (DMI) in a light collapsible frame on wheels, much like a golfclub cart (for portability). Two wires connected to the electronic clipboard would lead to "electronic hubs" on the DMI frame, one to measure distance longitudinally (x) and one to measure distance transversely (y). The second system utilized the DMI concept as before for the x coordinate and a laser system to locate the y coordinate from a fixed height.

Software Development

Before generating any computer code, a user's manual was prepared to ensure that the generated software followed a logical progression and was easy to use. The user's manual then became both the design document and the function test document.

Once the hardware was acquired and configured, and the first draft of the user's manual was completed, development of the software began. The primary challenge of this particular project was developing the software to be as user-friendly as possible, which will facilitate its acceptance by field technicians and minimize the potential for error.

The software was written to provide data entry through two basic screens. The first is the main screen (see Figure 1), which serves three primary purposes. In this screen, the user is asked to provide header information for labeling and storing the distress data to be collected, such as section identification and date, as well as information regarding the conditions under which the survey was conducted.

Once all header information has been entered, the surveyor can initiate the survey by tapping the appropriate button for the type of pavement surface to be surveyed. These buttons store all header information and take the surveyor to the surveyor's screen to initiate the distress mapping and recording. The surveyor's screen will be discussed in greater detail in the following paragraphs.

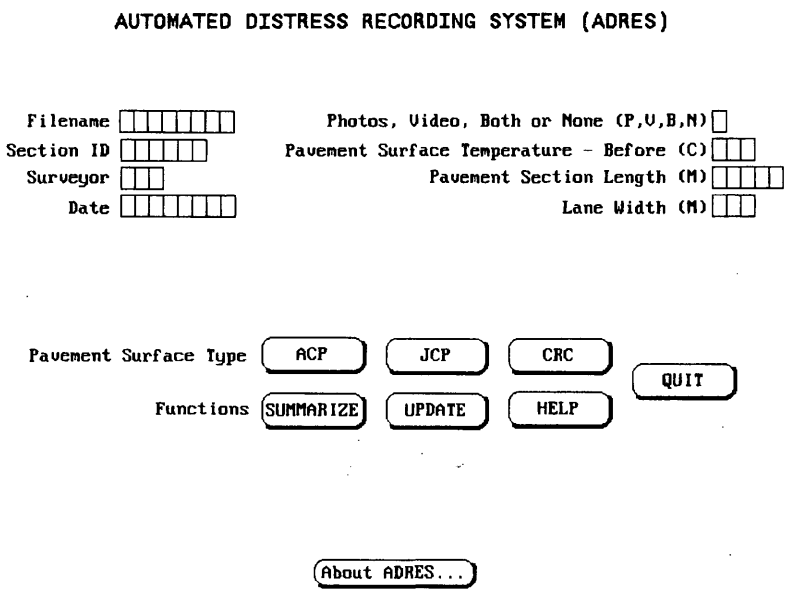

FIGURE 1 Main screen.

The final set of buttons on the main screen provides support functions such as summarizing and printing the maps generated or the summary quantities calculated, bringing up help screens, and exiting the system.

With the electronic clipboard, the header data can be written on the screen with the magnetic pen (which will convert the data written into ASCII format, which is then stored in a data file), or a visual image of a keypad can be brought up on the screen with the operator touching the pen to the "screen keypad" for the keystrokes desired.

After the header information has been entered, selecting one of the pavement type buttons on the main screen will bring up the second screen, which is the surveyor's screen. The top half of this screen provides a scaled grid comparable to that provided for distress mapping as part of the SHRP LTPP Guidelines for distress surveying. The bottom half of the screen has buttons for specifying the type of distress noted and auxiliary functions as necessary. An example of this type of screen for asphalt concrete surface pavements with some associated subscreens is shown in Figure 2. Only those distress types applicable to the chosen pavement surface type will be shown on the surveyor's screen. More than 100 support screens have been generated, which will be used as needed while the operator conducts the survey. As an example, on entry into the jointed concrete pavement or continuously reinforced concrete surveyors screens, support screens come up asking for the number of longitudinal joints sealed and the presence of joint sealant for transverse joints in jointed concrete pavements.

When a distress is noted on the pavement being surveyed, the surveyor simply notes the type of distress by touching the appropriate distress category button. This opens up another screen for the surveyor to note additional details regarding the distress (see Figure 3).

When the details for the distress being recorded have been entered, and the surveyor touches the "OK" button with the pen, a dialogue box will open (see Figure 4) requesting the current x and y position. At this point the surveyor may accept the current coordinates or input new ones by editing the fields. No editing of the coordinates will be required if the surveyor utilizes the total system (cart and computer) and locates the cart at the proper locations along the boundaries of the distress. With the establishment of the preferred coordinates, the surveyor can then touch the "OK" button and the surveyor's screen will reappear. Once a given distress has been initiated, the surveyor just touches the pen to the map as necessary to outline either the perimeter of an areal distress or the path of a linear distress.

After the first point of a given distress is positioned, the surveyor may either continue mapping the distress initiated or begin another distress. To continue with the mapping of the current distress, the surveyor must touch the map with the pen. This brings up the location screen again. Three options are then available to proceed. By selecting the "draw" button on the location screen, the system will incorporate the coordinates of the last point that the surveyor touched on the map in the distress being diagrammed. As a second option, the surveyor may use the coordinates provided by the positioning system and just touch the "OK" button (assuming the location cart is being utilized). As a third and final option the surveyor may change the coordinates by inputting his or her own. This option is particularly helpful if a distress is noted to exist throughout the length of the section, but the surveyor has not yet reached the end of the section.

If an attempt is made to begin diagramming the distress before a type has been specified, the surveyor will be redirected to the distress type buttons so that the distress may be defined first.

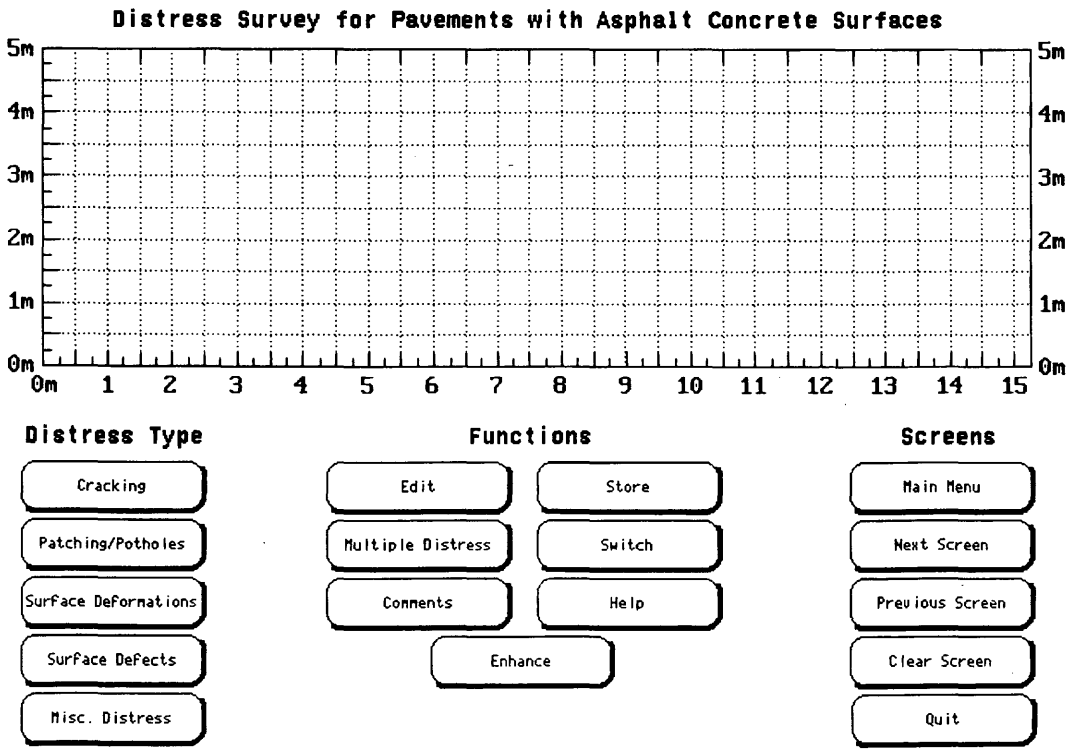

FIGURE 2 Example surveyors screen for 15.24 m of asphalt concrete pavement.

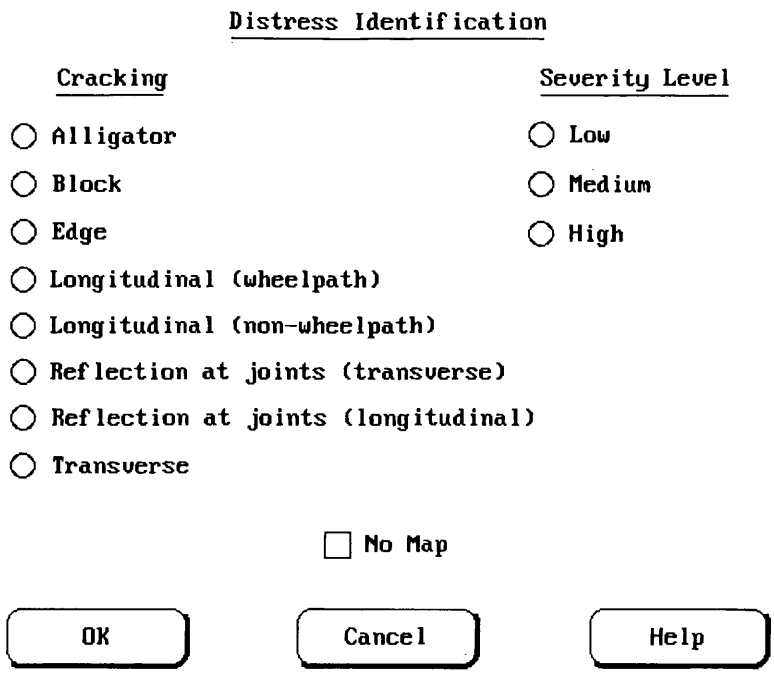

FIGURE 3 Distress identification screen for cracking in asphalt concrete pavements.

The distress types and their associated subtypes are shown in Tables 1 to 3.

If the surveyor does not wish to include a distress on the map (to avoid clutter), he or she can select the "no-map" button when specifying the other features of the distress in question (severity, type, etc).

Selection of several of the distresses (rutting, faulting in jointed concrete, lane-to-shoulder drop-off, and lane-to-shoulder separation) brings up support screens for the entry of the actual values measured. No mapping is performed or necessary for these distresses. The surveyor can collect and enter all or portions of these measurements at any point during the survey process. Some surveyors prefer to collect this data after all other mapping is completed, whereas other surveyors collect this data as they progress through the site. Any of these surveying styles may be accommodated by the ADRES.

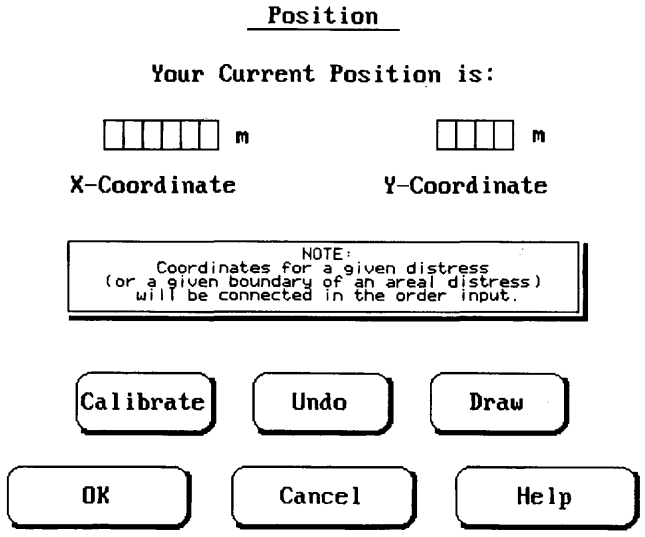

FIGURE 4 Distress location screen.

The function buttons provided on the surveyor's screen were programmed to provide the surveyor with flexibility and to improve efficiency in collecting the distress data. Included in the function buttons are features that allow for entry of more than one distress at a time, editing of errant points, entry of comments into the data base, storing of distress entries completed, and enhancement of the map to provide additional notes or markings on the map as necessary.

Buttons are also provided so that users may return to the main menu, proceed to the next screen for the next 15.24 m of a test section, return to the previous screen, clear the screen should they wish to start over, or quit. There are currently a total of 10 surveyor's screens for each pavement type (to accommodate a section of 15.24 m in length). The surveyor simply progresses through each of the screens as one would progress through the section to conduct the survey. The flexibility is provided by the system to backup or skip screens should the need arise while conducting the survey.

ADRES will continue seeking coordinates for a given distress until that distress is stored or another distress is initiated with the multiple distress button.

When the survey is completed, the surveyor can print out the results of the survey conducted, start another survey, or exit the system altogether. When a print request is initiated through the "Summarize" button on this main menu, a dialog box is provided to collect additional details regarding what information is to be printed (see Figure 5). Options include writing the distress quantities to a file in a format compatible with the LTPP Information Management System, or printing paper copies of the maps, summaries, or both. The software will calculate the quantities of each distress and summarize them in the same format as currently prescribed for SHRP-LTPP. Automated summarizing is conducted with the use of an external Fortran program that is run by the ADRES system when

TABLE 1 Asphalt Concrete-Surfaced Pavement Distress Types

DISTRESS TYPE	UNIT OF MEASURE	DEFINED SEVERITY LEVELS?
Cracking		
1. Fatigue Cracking	Square Meters	Yes
2. Block Cracking	Square Meters	Yes
3. Edge Cracking	Meters	Yes
4a. Wheel Path Longitudinal Cracking	Meters	Yes
4b. Non-Wheel Path Longitudinal Cracking	Meters	Yes
5. Reflection Cracking at Joints		
Transverse Reflection Cracking	Number, Meters	Yes
Longitudinal Reflection Cracking	Meters	Yes
6. Transverse Cracking	Number, Meters	Yes
Patching and Potholes		
7. Patch/Patch Deterioration	Number, Square Meters	Yes
8. Potholes	Number, Square Meters	Yes
Surface Deformation		
9. Rutting	Millimeters	No
10. Shoving	Number, Square Meters	No
Surface Defects		
11. Bleeding	Square Meters	Yes
12. Polished Aggregate	Square Meters	No
13. Raveling	Square Meters	Yes
Miscellaneous Distresses		
14. Lane-to-Shoulder Dropoff	Millimeters	No
15. Water Bleeding and Pumping	Number, Meters	No

the summarizing option is chosen. This program reads the data bases generated throughout the survey process and calculates the lineal or areal quantities for each distress type by utilizing the coordinates stored for each distress. Lineal quantities are simply calculated using the Pythagorean theorem, and areal quantities are calculated by using a numerical approximation procedure called the trapezoidal rule. Error associated with this procedure is quite small because of some internal error-reducing techniques utilized by the program developers.

Testing and Validation

Continued testing and refinement of the system were conducted throughout the programming phase. Every effort was made to ensure that this prototype was as complete and bugfree as possible. The prototype system was taken out in the field and used by persons other than the developers to conduct distress surveys and seek "bugs" in the system. Any flaws identified were corrected.

RESULTS OBTAINED

An operational, computer-based, pavement distress identification prototype system has been created. As noted above, although there are only two primary types of screens required for data entry, more than 100 screens were developed to support or facilitate the systems operation and make it easier to use.

With the exception of the "Help" buttons and the positioning system, all other aspects of this prototype are fully operational. Completion of the "Help" buttons requires development of the appropriate text support screens to be displayed at the appropriate points in the system. The only reason this has not yet been accomplished is that it is anticipated that the text provided in the help screens may be dictated by the types of problems users encounter as they implement the system to some extent. Full testing and validation is not yet completed and hence further development of these "Help" screens is still pending. Initially, however, these support screens will contain portions of the user's manual or the LTPP DIM.

The positioning system has been tested and proofed and the software to support its operation is incorporated into the working prototype, although the actual hardware has not yet been field tested in conjunction with the prototype software. The system has been constructed so that it can function independently of the positioning hardware, or simply stated, the surveyor can specify the appropriate coordinates when the system asks for them. However, it is still anticipated that the system can and will function more efficiently in conjunction with the positioning hardware.

A second phase of this project is planned and is currently awaiting funding. Included in Phase 2 are enhancements to the system to

TABLE 2 Jointed Concrete-Surfaced Pavement Distress Types

DISTRESS TYPE	UNIT OF MEASURE	DEFINED SEVERITY LEVELS?
Cracking		
1. Corner Breaks	Number	Yes
2. Durability Cracking ("D" Cracking)	Number of Slabs, Square Meters	Yes
3. Longitudinal Cracking	Meters	Yes
4. Transverse Cracking	Number, Meters	Yes
Joint Deficiencies		
5a. Transverse Joint Seal Damage	Number	Yes
5b. Longitudinal Joint Seal Damage	Number, Meters	No
6. Spalling of Longitudinal Joints	Meters	Yes
7. Spalling of Transverse Joints	Number, Meters	Yes
Surface Defects		
8a. Map Cracking	Number, Square Meters	No
8b. Scaling	Number, Square Meters	No
9. Polished Aggregate	Square Meters	No
10. Popouts	Number/Square Meter	No
Miscellaneous Distress		
11. Blowups	Number	No
12. Faulting of Transverse Joints and Cracks	Millimeters	No
13. Lane-to-Shoulder Dropoff	Millimeters	No
14. Lane-to-Shoulder Separation	Millimeters	No
15. Patch/Patch Deterioration	Number, Square Meters	Yes
16. Water Bleeding and Pumping	Number, Meters	No

TABLE 3 Continuously Reinforced Concrete-Surfaced Pavement Distress Types

DISTRESS TYPE	UNIT OF MEASURE	DEFINED SEVERITY LEVELS?
Cracking		
1. Durability Cracking ("D" Cracking)	Number, Square Meters	Yes
2. Longitudinal Cracking	Meters	Yes
3. Transverse Cracking	Number, Meters	Yes
Surface Defects		
4a. Map Cracking	Number, Square Meters	No
4b. Scaling	Number, Square Meters	No
5. Polished Aggregate	Square Meters	No
6. Popouts	Number/Square Meters	No
Miscellaneous Distress		
7. Blowups	Number	No
8. Transverse Construction Joint Deterioration	Number	Yes
9. Lane-to-Shoulder Dropoff	Millimeters	No
10. Lane-to-Shoulder Separation	Millimeters	No
11. Patch/Patch Deterioration	Number, Square Meters	Yes
12. Punchouts	Number	Yes
13. Spalling of Longitudinal Joints	Meters	Yes
14. Water Bleeding and Pumping	Number, Meters	No
15. Longitudinal Joint Seal Damage	Number, Meters	No

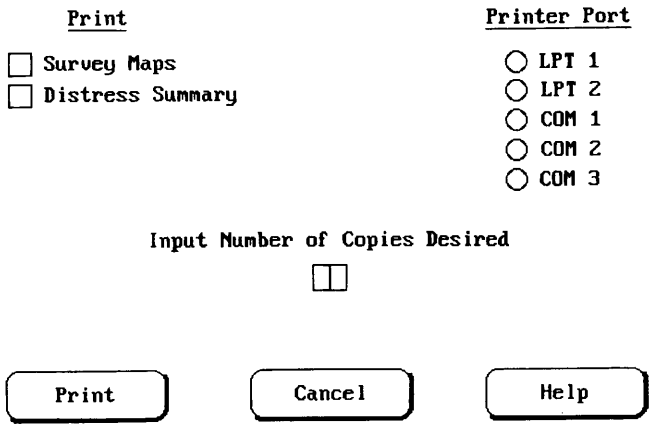

FIGURE 5 Printing screen.

complete the "Help" features, upgrade the graphical capabilities for even greater system efficiency, refine the hardware, and conduct a full scale beta test of the revised software and hardware.

CONCLUSIONS

A working prototype of the ADRS has been developed to collect and summarize pavement distress data. This particular system was developed to be consistent with the LTPP format. However, it is anticipated that with some software modifications, the prototype system would be readily adaptable to whatever format might be of interest. Typically, fewer distress types are monitored for pavement management systems implemented by cities, counties, and state highway agencies. However, such modifications would not be difficult to accomplish.

Similarly, the software on this particular prototype is set up to summarize the data in the LTPP format. Most agencies have their own unique format for summarizing distress data (typically providing a composite index value for comparison with other test sections). Modifications of this type would ultimately need to be made in the software to suitably adapt the prototype system for use by other agencies, but again such modifications would not be difficult.

The majority of this research effort is directly adaptable to any other agency (federal, state, or local) that may wish to use it. The primary thrust of this work is in the application of the pen computer hardware to field applications such as pavement distress surveying. Most of the software development was focused on maximizing the use of this "electronic clipboard" technology and the "*x* and *y* positioning" capabilities. Both of these features should be directly applicable to any agency currently involved in manual collection of field data or data in which positioning is involved.

Phase 2 research is currently underway to refine this existing system and conduct extensive beta testing.

REFERENCES

1. Daleiden, J. F., and A. L. Simpson. Evaluation of SHRP LTPP Distress Data Collection Procedures. Presented at 1994 Annual Transportation Research Board Meeting, Washington, D.C., 1994.
2. *Distress Identification Manual for the Long-Term Pavement Performance Studies.* Strategic Highway Research Program, SHRP-LTPP/FR-90-001, TRB, National Research Council, Washington, D.C., 1990.
3. "Pavement Condition Index Field Manual," APWA, July 1984.
4. Smith, R. E., S. M. Herrin, and M. I. Darter. *Highway Pavement Distress Identification Manual.* FHWA, National Cooperative Highway Research Project 1-19, U.S. Department of Transportation, March 1979.

Publication of this report sponsored by Committee on Pavement Monitoring, Evaluation, and Data Storage.

Three-Dimensional Finite Element Model for Analysis of Concrete Pavement Support

CHEN-MING KUO, KATHLEEN T. HALL, AND MICHAEL I. DARTER

A three-dimensional (3-D) finite element model for concrete pavements called 3DPAVE was developed to analyze the many complex and interacting factors that influence the support provided to a concrete pavement, including foundation support (subgrade k value); base thickness, stiffness, and interface bond and friction; slab curling and warping due to temperature and moisture gradients; dowel and aggregate interlock load transfer action at joints; and improved support with a widened lane, widened base, or tied concrete shoulder. The ABAQUS general-purpose finite element software was used to develop a powerful and versatile 3-D model for analysis of concrete pavements. The 3DPAVE model easily overcomes many of the inherent limitations of two-dimensional (2-D) finite element models that reduce the accuracy of the results obtained from 2-D models. The 3-D model was validated by comparison with deflections and strains measured under traffic loadings and temperature variations at the AASHO Road Test, the Arlington Road Test, and the Portland Cement Association's slab experiments. In every comparison with measured field data, 3DPAVE's calculated responses were found to be in good agreement with the measured responses and significantly closer to the measured responses than those calculated by 2-D programs. The development and validation of the 3DPAVE model are described.

Many pavement researchers have resorted to three-dimensional (3-D) finite element models as the best method of solving complicated structural analysis problems. Two-dimensional (2-D) finite element models have inherent limitations related to plate theory assumptions; thus, many interesting problems cannot be realistically modeled by 2-D finite element programs. Thanks to the development of finite element techniques and computer capabilities and speeds, well-developed versatile 3-D finite element packages are capable of modeling numerous complex mechanisms in engineering problems within tolerable computer run times. A realistic simulated pavement system may then be built in a computer model instead of in the field.

In the 1990s, the general-purpose 3-D finite element package ABAQUS gained popularity in simulating pavement problems concerning nonlinear subgrades, dynamic loading (*1*), and falling weight deflectometer tests (*2*). This paper presents a brief overview of ABAQUS, a summary of the sensitivity study of feasible element types in ABAQUS, a description of the development of a 3-D concrete pavement model with ABAQUS, and a variety of analyses conducted to validate the 3-D concrete pavement model (3DPAVE) by comparison with measured field data from the AASHO Road Test and other experiments.

OVERVIEW OF ABAQUS

ABAQUS has been used widely for stress/strain, fatigue, flow, and thermal analysis in many fields, such as structures, geotechnical engineering, hydrosystems, and materials. It is available in most research computer systems. Because it was not developed specifically for pavements, preparation of an input file requires understanding of the organization of ABAQUS and the conventions of finite element model building. The ABAQUS components used in 3DPAVE are ABAQUS/Standard, a general-purpose finite element program, and ABAQUS/Post, an interactive postprocessing program. A summary of the ABAQUS model input options, element library, materials library, analysis procedures, and postprocessing capabilities is provided elsewhere (*3*).

Department of Civil Engineering, University of Illinois at Urbana-Champaign, 205 N. Mathews, Ave., Urbana, Ill. 61801.

FEASIBILITY STUDY OF ELEMENT TYPES

An appropriate element is essential to a good pavement model. It must be capable of simulating pavement behavior realistically and efficiently. Furthermore, ABAQUS provides a wide variety of elements potentially suitable for plate-type problems. A study of element performance is necessary to choose the most appropriate element to build a 3-D model for concrete pavement analysis.

The accuracy of finite element analysis is sensitive to mesh fineness. The mesh must be sufficiently fine, especially in the vicinity of the load, to achieve an acceptable level of accuracy. Different types of elements may require different degrees of mesh fineness to achieve the same accuracy.

2-D Elements

In the first stage of this development process, a 2-D model was developed in ABAQUS and compared with ILLI-SLAB and Westergaard's solutions, which are both based on plate theory. ABAQUS provides a wide variety of shell elements suitable for shell and plate problems. The 2-D element used in ILLI-SLAB and also in the popular general-purpose finite element code FINITE is a four-node rectangular element called RPB12. The rectangular shell elements in ABAQUS provide additional degrees of freedom for consideration of transverse shear, a capability generally considered unnecessary for thin plate modeling. A thin plate is defined as one with a length-to-thickness ratio greater than about 20. (Note that what in the structural analysis literature is called a "thin plate" is often called in the pavement literature a "medium-thick plate" but the definition is the same). Transverse shear may become a significant factor when the loaded area is small or when the slab does not satisfy the thin plate definition.

The maximum stress computed with ABAQUS using an eight-node rectangular element (S8R5) was found to agree well with that of ILLI-SLAB regardless of mesh fineness. This element is not, however, as efficient as ILLI-SLAB's element because it has almost three

times as many nodes as the RPB12 element. However, in some cases in which pavement slabs are too thick to be modeled appropriately as thin plates, S8R5 will yield better results than ILLI-SLAB.

The ABAQUS four-node rectangular (S4R5) element did not agree well with the ILLI-SLAB result when a coarse mesh was used but converged to the ILLI-SLAB result with increasing mesh fineness. ABAQUS also provides a linear triangular element (STR135) that has properties similar to the RPB12 element and is efficient in modeling thin plates. The triangular element produces stress results close to those of ILLI-SLAB even with a coarse mesh. However, a triangular element is not as convenient as a rectangular element for modeling rectangular pavement slabs.

3-D Elements

The objectives of this portion of the feasibility study were to select the most appropriate element for a 3-D pavement model and to identify the mesh fineness and other criteria for achieving acceptable accuracy. The 3-D solution should agree with the 2-D solution for slabs that satisfy the thin plate definition. The 3-D solution should also agree with Westergaard's equations, within the range of load sizes for which Westergaard's equations are applicable, for slabs that satisfy the thin plate definition.

Three sets of analyses were conducted in the 3-D element feasibility study. A slab resting on a Winkler foundation was run and compared with Westergaard's interior and edge loading equations. Another set of comparisons dealt with a simply supported rectangular slab with a large distributed load. The results were compared with an analytical solution to investigate the mesh effect. It should be pointed out that both analytical solutions only serve as benchmarks, instead of exact solutions, because these equations are all based on plate theory, which ignores slab compressibility and shear deformation.

Several candidate brick elements were considered. The first one selected was C3D8, which is a linear interpolation element with a node at each corner of a brick. The support is modeled with the FOUNDATION option that requires as input a spring coefficient (e.g., k value). After several runs with various mesh designs, it was concluded that the C3D8 linear element does not compare well with Westergaard's solution. Even when a single pavement layer was meshed up to four layers of bricks elements with aspect ratio 1:1:1, the results did not show significant improvement. Therefore, the C3D8 element was ruled out in later comparisons.

The next category of brick elements considered was quadratic elements, which have a node at each corner and also a node at the midpoint of each edge. According to the *ABAQUS Example Problems Manual* (*4*)," quadratic elements perform well even with a coarse mesh. There are many types of quadratic elements provided in the ABAQUS element library. According to finite element theory (*5–7*), some 3-D elements may lock when the major deformation mode is bending, which usually happens in transversely loaded plate problems. Reduced integration elements should be used to remedy this problem. Thus, only two quadratic elements, C3D20 and C3D20R (the latter with reduced integration), were considered further.

C3D20R converged to Westergaard's analytical solution for stress better than the C3D20 element did in a finer mesh. The two elements gave almost the same deflections for various meshes. The calculated vertical compressibility of the concrete slab in these examples was about 5×10^{-5} in. (1.3×10^{-3} mm), or $\epsilon_{zz} = 0.01$, which is less than 0.7 percent of deflection. This justifies one of the hypotheses for thin plate theory that transverse compressibility (ϵ_{zz}) of the plate is negligible in some cases.

However, the vertical shear stresses are significant compared with the maximum stresses, about 15 percent of the maximum tensile stresses. This shows that the assumption of neglecting transverse shear in thin plate theory is not appropriate in some cases. The following observations were made based on the sensitivity analysis results:

- High shear stresses only occur in the vicinity of the loaded area. Most of the plate has no significant transverse stresses. Westergaard mentioned this problem and developed an equation based on special theory to take the shear deformation near a small loaded area into account.
- Load size plays a key role. Although the length-to-thickness ratio of the plate analyzed was 50, which satisfies the thin plate criterion, a small load may still violate plate theory in the vicinity of the loaded area. When the load is distributed over a large area, transverse shear should be negligible as assumed in thin plate theory.

Performance of 3-D Elements Versus 2-D Elements

Another issue in developing a 3-D model is how 3-D results compare with 2-D results. They are not expected to match in all cases because some plate responses are neglected in 2-D model formulation. Agreement of 2-D and 3-D models can only be expected when the plate is sufficiently thin, the load size is sufficiently large, the meshes meet requirements for accuracy, and the problem is restricted to the type for which 2-D models apply.

Interior Loading Case

To compare the 2-D and 3-D elements for various meshes and loading sizes, a series of runs was made using different elements and changing the loading area, while holding the load magnitude, slab size, thickness, modulus, Poisson's ratio, and subgrade k constant. The interior and edge stresses and deflections were computed using Westergaard's equations, ILLI-SLAB and FINITE (2-D models), 2-D elements in ABAQUS (STR13, S4R, and S8R), and the 3-D brick element in ABAQUS (C3D20R).

Westergaard's interior stress equation predicts lower stresses than the finite element results at small load sizes and predicts higher stresses than the finite element results at large load sizes. The latter trend supports the statement that Westergaard's equations apply only when the loaded area is small in comparison with the radius of relative stiffness (*7*). However, the transverse shear effect may become significant when the loaded area approaches a point load. Consequently, Westergaard's interior stress equation agrees with the 3-D model within an intermediate range of load area size. Research on load size effects on 2-D finite element results has shown the same conclusion (*8*).

Interior stress results were similar for nearly all of the 2-D and 3-D element types over a wide range of load sizes. The exception was the ABAQUS 2-D S4R element, which was expected to agree more closely with the 3-D results than the other elements because it takes into account transverse shear.

Interior deflections for all element types converge as the load size increases, but Westergaard's deflection solution diverges from the finite element solutions as the load size increases. In the range of

small load sizes, the finite element deflection results form two groups: one group consists of the ABAQUS element types that consider transverse shear, and the other group consists of the ILLI-SLAB, FINITE, and ABAQUS STR13 element types that ignore transverse shear.

These results indicate that 2-D elements are capable of good agreement with 3-D results for interior stress over a wide range of load sizes, but a discrepancy exists over a wide range of load sizes between the interior deflections computed using 2-D elements and those computed using 3-D elements.

Edge Loading Case

Another set of sensitivity runs was conducted for edge loading, using load sizes from 9 to 36 in. (229 to 914 mm) square, and all of the other parameters the same except for the slab size, which was a constant 10 by 20 ft (3 by 6 m). The edge stresses and deflections were computed using Westergaard's equations, ILLI-SLAB and FINITE (2-D models), 2-D elements in ABAQUS (STR13 and S8R), and the 3-D brick element in ABAQUS (C3D20R).

The edge stress results indicate that Westergaard's edge solution agrees with the 3-D finite element solution until the load size becomes larger than about 20 in. (508 mm) square. The RPB12 element (used in ILLI-SLAB and FINITE) predicts somewhat higher edge stresses than do the shell and solid elements in ABAQUS. This discrepancy narrows as the load size becomes larger. Thus, it might be explained by the transverse shear effect in edge loading being slightly more significant than in the interior loading situation. Further investigation of this is needed. Although STRI3 is a thin shell element like RPB12, the geometry and different formulation (e.g., using 6 degrees of freedom instead of 3 degrees of freedom in RPB12) might explain the gap between the STRI3 and ILLI-SLAB edge stress curves. However, the gap is less than 5 percent even under very concentrated loading.

Westergaard's edge deflection solution diverges dramatically from all of the finite element solutions as the load size increases. The edge deflections computed with ABAQUS using the 2-D S8R element and the 3-D C3D20R element are higher than the edge deflections computed with ILLI-SLAB, FINITE, and the STR13 element over the full range of load sizes examined. The gap narrows with increasing load size.

The edge loading results using the 3-D model agree with the 2-D model results for slabs that could be considered thin plates, that is, having length-to-thickness ratio of 20 or less. However, in analysis of thicker and smaller slabs that did not satisfy the definition of a thin plate, discrepancies between the 3-D and 2-D results became more significant. The edge loading comparison may be summarized as follows:

- The performance of various element types in edge loading is similar to that in interior loading.
- Thin plate elements produce either higher or lower stresses than solid elements. Transverse shear effects might be responsible for these discrepancies.
- Westergaard's edge stress and deflection solutions are best suited for small loads.
- Good agreement between the 3-D and 2-D models is achieved for edge deflection and stress results when the slab is a thin plate (i.e., when the length-to-thickness ratio is more than 20.) Below this limit progressively greater discrepancies exist.

Element Proportions

In finite element analysis, a balance must be achieved between accuracy of results and efficiency of computation. The mesh must be sufficiently fine to yield results with an acceptable level of accuracy. However, computer storage space and CPU time increase with mesh fineness. In 3-D analysis with solid elements, not only the horizontal fineness of the mesh but also its vertical fineness may be important to the accuracy of results. An examination of the sensitivity of solid element size was conducted to assess its significance. Instead of placing a plate on a foundation, a simply supported plate under interior loading is considered, because the responses of a simply supported plate are more sensitive to changes in the analysis parameters than a plate resting on a foundation. The load was applied over a large area to eliminate the effect of transverse shear caused by concentrated loading.

Compared with the exact solution derived by thin plate theory, the maximum stress calculated with the solid element model yielded less than 2 percent discrepancy even with the coarse mesh ($2a/h = 2$). The mesh becomes more plate-like as this ratio increases. Therefore, the model will lose accuracy if it is meshed with a plate-like solid. For highway pavements, the $2a/h$ ratio rarely exceeds 1 under normal truck wheel loads if the model is meshed no larger than the load size. Hence, the mesh fineness will generally be satisfactory from the standpoint of accuracy if the element aspect ratio $2a/h$ is less than 2. For larger loaded areas it may be necessary to divide the loaded area into multiple elements.

Limitations of 2-D Models and Motivation for 3-D Model Development

The previous comparison of 2-D and 3-D element types demonstrates that it is possible, with careful element selection and mesh definition, to achieve good agreement between 2-D and 3-D models, for the limited range of problems that 2-D models are able to solve. The performance comparison is necessarily limited to those types of problems. The motivation for developing 3DPAVE was that many aspects of concrete pavement behavior cannot be realistically modeled in two dimensions. Among the aspects considered important to this study are the following:

- Curling or warping of a slab off a base layer: In 2-D models the slab and base always have the same curvature, and though the layers may be unbonded horizontally, the slab and base can never be any distance apart at any node.
- Direct modeling of nonlinear or unequal temperature, or both, or moisture gradients in the slab and base: A 2-D element is by its nature incapable of modeling a nonlinear gradient within a single pavement layer. The 2-D models such as ILLI-SLAB are also incapable of modeling unequal gradients in the slab and base. Although ILLI-SLAB allows different slab and base gradients as input, the program converts these into a single linear gradient through the full slab and base thickness. Some 2-D methods represent a nonlinear gradient by an equivalent linear gradient or add the stresses due to linear and nonlinear components of the total nonlinear gradient. A direct and more realistic analysis of the effects of nonlinear gradients through the slab or base, or both, requires a 3-D model.
- Widened base, widened lane, and mismatched joints and cracks: In 2-D models the horizontal boundaries of the slab and base must coincide. 3-D modeling permits analysis of more realistic

geometries in which the slab and base have mismatched edges, joints, and cracks.

- Friction coefficients and horizontal and vertical bond strengths: These interface characteristics can be directly and realistically modeled in 3-D. In 2-D models, layer interfaces can only be bonded or unbonded.
- Thicker pavement and base cross sections: Transverse shear stress is significant for thicker cross sections but cannot be considered in analytical solutions (e.g., Westergaard) based on medium-thick plate theory or in most of the available 2-D programs.
- Layer compressibility: 3-D modeling permits direct definition of the compressibility of the slab and base layers. In 2-D plate models all layers above the subgrade are incompressible.

In addition to these capabilities, a 3-D model developed within a powerful and versatile finite element package such as ABAQUS provides the potential to model a wide variety of other pavement behaviors that would be of interest to other research efforts. Some of these are

- Dynamic loading,
- Viscoelastic behavior,
- Temperature-dependent properties,
- No tension in unbound materials,
- Explicit modeling of steel reinforcement (for JRCP and CRCP),
- Variable joint width and variable load transfer in doweled or undoweled joints,
- Stress-dependent response of unbound materials, and
- Concrete behavior beyond the elastic range, including inelastic response, cracking failure, and behavior after cracking.

DEVELOPMENT OF 3DPAVE MODEL

The 3DPAVE model was developed by first developing a 2-D model, to gain experience with the many options and commands of ABAQUS, and then upgrading the 2-D model to a 3-D model. Each step in the development process involved many challenges in model input, element properties, execution problems, results checking, and so forth.

3-D Solid Element (Brick Element)

On the basis of the element study presented earlier, C3D20R was selected as the standard element for this model. However, the C3D20R element had difficulty converging to a solution when contact problems were modeled. Because it is important to be able to model the mechanisms of contact and loss of contact when a slab curls on top of a stiff base, the C3D27R element was used in place of the C3D20R element. C3D27R is a variable node element, similar to C3D20R but with extra nodes on faces that are contact surfaces.

By using the quadratic elements C3D20R and C3D27R it is possible to model a bilinear temperature gradient through the slab, using the nodes at the top, middle, and bottom of the element. More nonlinear temperature distributions may be modeled with multiple layers of C3D27R elements. However, modeling a slab with multiple layers instead of a single layer dramatically increases the computer run time. Thus, unless the stress distribution through the slab depth is a major concern, a single-layer mesh is considered adequate for calculation of curling stresses at the top and bottom of the slab.

Interface Element

To investigate the effects of separation between layers, interface friction, and bonding, the interface should be modeled. ABAQUS provides many interface elements for surface contact problems. The INTER9 element is an interface element that can be used with the C3D27R element. Detailed interface responses (e.g., vertical contact stress or separation, and horizontal stress or slip) may be calculated when this element is used in the model. Further studies of complex behavior under loading, such as crack growth, are also available in the options associated with this element.

The interface element can be either no thickness, which is the case when two layers are in contact, or can have a thickness equal to the distance between two layers of nodes to simulate an initial gap. Analyses involving separation between layers, such as curling or erosion problems, require several iterations to converge to a solution.

Subgrade Modeling

Dense liquid foundations and elastic solid foundations can easily be modeled in ABAQUS. For a dense liquid foundation, a keyword FOUNDATION is available for all solid, shell, and membrane elements to provide spring support under elements. However, introducing interface elements between the slab and subgrade hinders the use of the dense liquid foundation because FOUNDATION is not compatible with interface elements. Hence, when the FOUNDATION option is used, a membrane element should be used below the interface element so that the dense liquid foundation can be modeled under the interface element. The stiffness and thickness of the extra membrane layer is minimal to eliminate its effect on slab stresses. To investigate the error caused by this membrane layer, the results from two models were compared with no curling, one model with brick elements directly resting on the foundation, and another model incorporating the interface and membrane elements between the slab and the foundation. The differences in maximum stresses and deflections were all less than 0.05 percent.

To model the subgrade as an elastic solid foundation, layers of brick elements may be used to a depth at which the foundation deflection is assumed to be negligible. This requires the determination of the depth to which deflection is expected, and it takes much more computer storage space and execution time to complete one run because of the number of elements. An alternative that addresses both of these drawbacks is to use infinite elements, a new feature in ABAQUS.

Bonding and Friction

In ABAQUS version 5.2, new options named DEBONDING and BOND SURFACE have been added for advanced modeling of contact problems. Users may specify debonding criteria or debonding mechanisms as parameters of the keyword DEBONDING. Separation between layers may also be modeled with DEBONDING. Two fatal problems with these new options were found during the model development. Because of these difficulties, alternative methods were developed to consider vertical and horizontal interface stresses together.

Vertical bonding may be specified without vertical separation, or a vertical bond strength may be specified. With the latter option, the layers are allowed to separate when the vertical interface stress exceeds the specified bond strength. If two layers are vertically bonded, the output file will print the vertical stresses at each node. If separation occurs, the vertical interface stress is zero and the gap size will be reported in the output file.

Friction (horizontal bonding) may be modeled using a variety of parameters provided by ABAQUS. One option is full bond, which is equivalent to a friction coefficient approaching infinity. Another option is classical Coulomb friction with an optional limit on the shear stress. Some relative motion (elastic slip) is permitted when the interface is still sticking. Permitting a large amount of relative motion during sticking makes convergence of the solution more rapid, at the expense of local solution accuracy. Permitting only a small amount of relative sliding motion better simulates behavior in which no slip is permitted in the sticking state, but requires more iterations to converge. A variable degree of bonding may be modeled by specifying the ultimate bonding stress that can be carried by the bond in the field. After a load is applied, some region may remain bonded, whereas bond breaks at those nodes whose calculated interfacial shear stresses exceeds the ultimate bond stress.

The situation with no bonding but accounting for friction at the interface may be achieved by specifying a realistic friction coefficient. The last situation is fully unbonded and no friction considered. This case may be modeled by setting the friction coefficient and vertical bond strength to zero.

Dowel Bars and Aggregate Interlock

Dowel bars are modeled in 3DPAVE with beam elements. Unlike the dowel models available in 2-D programs, the use of beam elements in ABAQUS eliminates the need to assign bending stiffness and shear stiffness values to the dowels elements. Instead, only physical properties (i.e., steel elastic modulus, bar diameter, and dowel spacing) are needed. When dowel bars are modeled in 3DPAVE with beam elements, the results agree with those obtained from ILLI-SLAB with a high dowel-concrete interaction factor (high load transfer). An option is available in ABAQUS to allow the dowel bars to slip relative to the slab.

Aggregate interlock is modeled in a straightforward manner by formulating the joints connecting slabs by shear springs. Finding the spring stiffness that represents the load transfer provided by aggregate interlock has been a subject of research (*9*). For the same shear interlock stiffness, ABAQUS and ILLI-SLAB yielded close values of load transfer efficiency and maximum slab stresses.

A schematic illustration of the 3DPAVE model is shown in Figure 1. More detailed information on its development is provided elsewhere (*10*).

VALIDATION OF 3DPAVE

Validation of the new model was the next and most important step of its development. Validation was done by comparison with full-scale field test data.

AASHO Road Test

The comparison between 3DPAVE and AASHO Road Test measurements was made with the data measured on the main loops. The main loop test was set up to measure the edge deflections and strains under moving truck loads. These data are valuable because the measured location was fixed at the midslab edge, whereas Loop 1 measurements were located at various positions and only the maximum strain data reported.

Stress Validation

According to the AASHO Road Test vehicle specifications (*11*), air pressure in the tires was maintained to ensure that the contact pressure was uniform for all test vehicles and axle loads. Thus, in the 3DPAVE model validation runs, contact pressure was held constant and load size was varied with varying axle load magnitudes. Finite element meshes were adjusted to match the tire prints that changed as axle loadings changed. Also, meshes were refined when the plate thickness was less than the smallest element width.

The primary subgrade k value test conducted at the AASHO Road Test was for the elastic k, which was obtained from measurements of the elastic deformation of the subgrade (not including permanent deformation) under a 30-in.-diameter (762-mm) plate after a 15-sec loading. The mean elastic k value for springtime conditions was 86 psi/in. (23 kPa/mm) (*12*). However, it is reasonable to expect that a higher k value is required to match the deflections and stresses measured on the main loops under wheel loads moving at 30 mph (48 km/hr). Simulation of single-axle and tandem-axle loads on the main loops showed that the stresses computed from measured field-

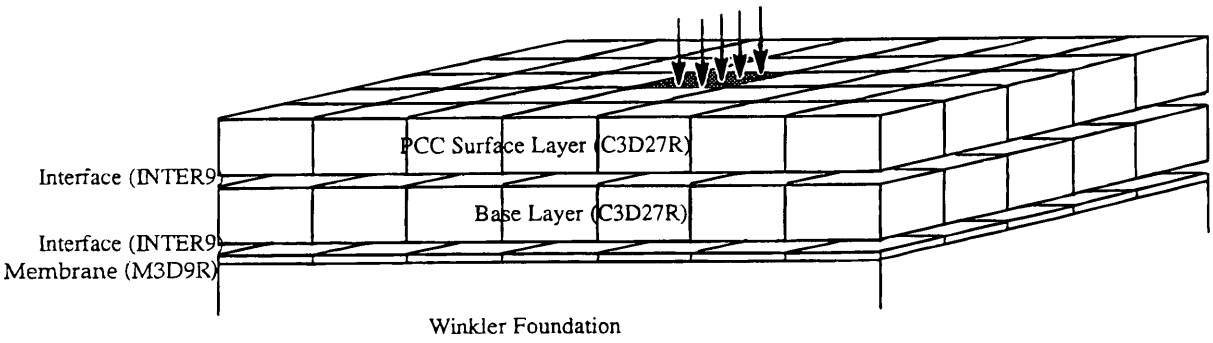

FIGURE 1 3-D single slab model in ABAQUS.

measured strains matched closely with those computed by the 3DPAVE model when the subgrade k value was selected as 170 psi/in. (46 kPa/mm), which is about double the measured plate load k_E. AASHO Road Test stresses calculated from measured strains are compared with stresses computed using 3DPAVE in Figure 2.

k Value Traffic Speed

At the AASHO Road Test, deflections and strains were measured for a range of truck speeds from creep speed to 60 mph (97 km/hr). An equation to compute the reduction factor for deflection and strain measured on the main loops for any speed between 2 and 60 mph (3.2 and 97 km/hr) was provided (*12*). Because the main loop tests were conducted at a speed of 30 mph (48 km/hr), the strains and deflections measured at the speed may be used in the empirical equation (*12*) to estimate the deflections and strains at creep speed. These results were used to develop a relationship for the AASHO Road Test main loop experiment between k value and speed. 3DPAVE was run to analyze the axle loads on the main loop slabs using a range of k values, and the stresses and deflections obtained were used to calculate reductions factors from the creep speed deflections and strains. These reduction factors were used to determine the speed corresponding to each input k value. For example, the estimated k value for creep speed loading is about 75 psi/in. (20 kPa/mm), which is close to the elastic k value of 86 psi/in. (23 kPa/mm) obtained by plate load tests on the subgrade.

Crack Initiation Location at AASHO Road Test

Crack development locations were recorded at the AASHO Road Test. Cracks in thin slab sections [3.5 and 5 in. (89 and 127 mm)] were first observed along the wheelpath, starting at the transverse joint. In thick slabs (6.5 to 12.5 in.), cracks most often developed from the edge at midslab.

To verify crack initiation in thin and thick slabs with 3DPAVE, two pavements with slab thicknesses of 4 and 12 in. (102 and 305 mm) were modeled with loads applied at various positions. Examination of the principal stress contours from 3DPAVE confirms that in thin slabs the highest stress occurs at the bottom of the slabs when the wheel load is at the joint. The critical loading position for thicker

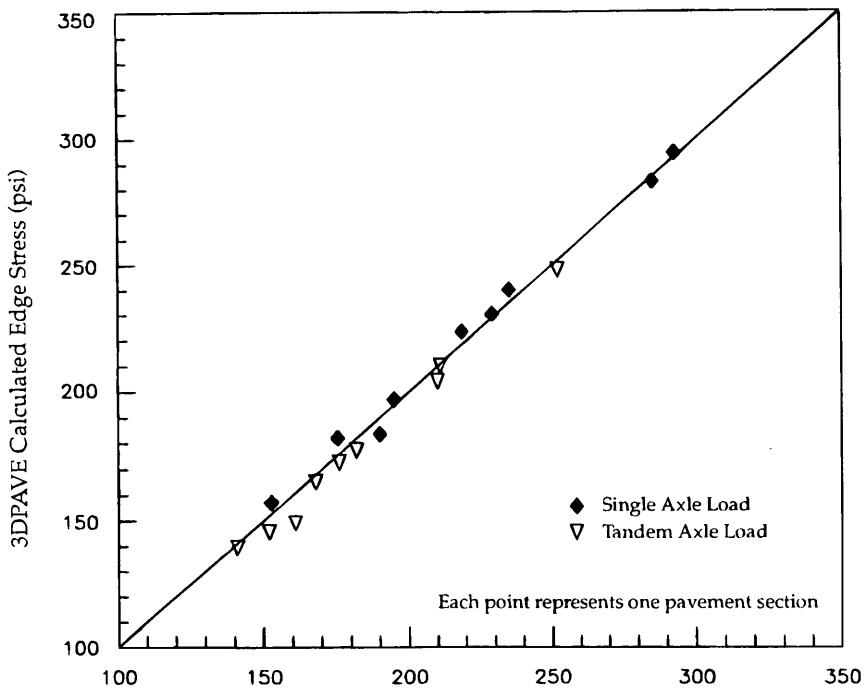

PCC E = 6.25 million psi [43063 MPa]
PCC μ = 0.28
k = 170 psi/in [46 kPa/mm]
Speed = 30 mph [48 km/hr]
Axle load range = 12 to 48 kips [53 to 214 kN]
Slab thickness range = 6.5 to 11 inches [165 to 279 mm]
1 psi = 6.89 kPa
3DPAVE/AASHO stress ratio range is from 0.93 to 1.03
Mean 3DPAVE/AASHO stress ratio is 1.00
R^2 = 0.99
n = 18

FIGURE 2 3DPAVE calculated stresses versus AASHO Road Test stresses from measured strains.

slabs [6.5 in. (165 mm) and greater] is midslab loading. The highest stress is located at the bottom of the slab at the longitudinal edge, which is also where transverse cracks initiated.

PCA Tests on Cement-Treated Bases

The Portland Cement Association conducted tests in the 1950s to investigate the responses of pavements with cement-treated bases (*13*). Many designs were constructed and tested in the laboratory. Among the sections for which data are available, fully bonded sections were analyzed with 3DPAVE because no detailed information was provided in the report for the other sections with various interface treatments.

Comparisons were made for both interior loading and free edge loading conditions. Because edge loading deflections of slabs with bonded bases were only available in "edge with ledge" sections [i.e., the base extended 1 ft (0.3 m) beyond the edge of the slab], a widened base was modeled in 3DPAVE. This is easily accomplished by constructing the two layers with brick elements and then removing a row of brick elements from the edge of the slab layer.

In addition to 3DPAVE, the analysis was also performed with ILLI-SLAB and the Westergaard equations. Figure 3 shows the deflection comparisons for interior loading. For the 3DPAVE and ILLI-SLAB analyses, the k value used for each section was the value measured by the PCA in plate load tests on the subgrade at that location. For the computation using Westergaard's equation, the k value used was the value measured by the PCA in plate load tests on the cement-treated base at that location. 3DPAVE model and ILLI-SLAB predict interior deflections very well for the 5-in. (127 mm) slab sections on 6-in. (152 mm) and 9-in. (229 mm) cement-treated bases. Some scattered results are observed for 7-in. (178 mm) slabs (7B6,7B9). In general, every analysis method predicted fairly well for interior loading conditions.

For edge loading conditions, the 3-D model results match the measured deflections much better than the other conventional analyses, as shown in Figure 4. Again, for the 3DPAVE and ILLI-SLAB analyses, the k value used for each section was the value measured by the PCA in plate load tests on the subgrade at that location. For the computation using Westergaard's equation, the k value used was the value measured by the PCA in plate load tests on the cement-treated base at that location. Significant gaps between both the ILLI-SLAB and Westergaard results and the measured test data and 3DPAVE results illustrate the improved capability of the 3-D model. Because Westergaard's solution and ILLI-SLAB are not capable of considering a widened base, they tend to overpredict deflections. The 3DPAVE successfully reproduced the PCA pavement test results with widened bases.

Arlington Road Test

Data from the Arlington Road Test provide curling stresses computed from measured strains (*14*). These field results were compared with 3DPAVE analysis results as well as results obtained using ILLI-SLAB.

Longitudinal edge stresses in the Arlington Road Test slabs were computed from measured strains during periods of maximum thermal gradients for several days in 1934. For this comparison, a linear temperature distribution was assumed in the 3-D finite element model and no wheel loading was applied. The stresses computed from the measured strains for the 6- and 9-in. (152- and 229-mm) slabs and the computed finite element edge stresses are compared in Figure 5.

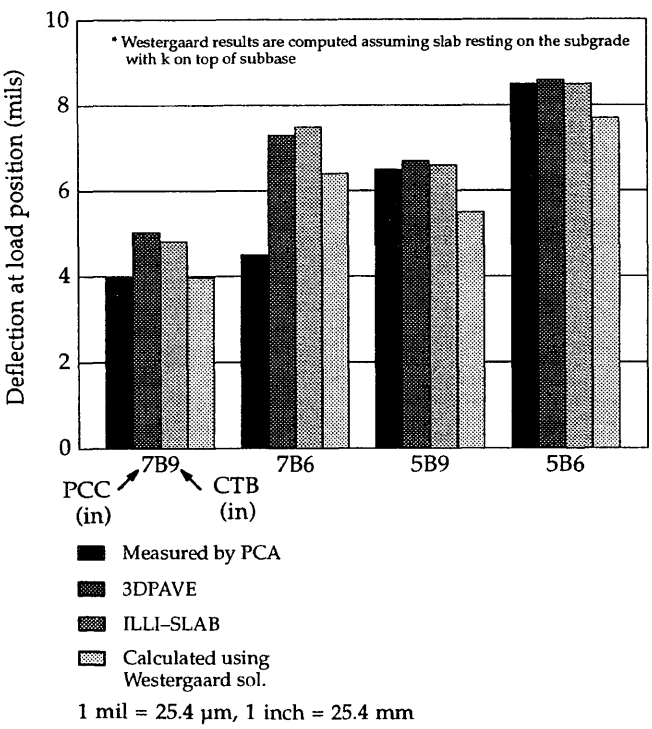

FIGURE 3 PCA data versus computed results for interior loading.

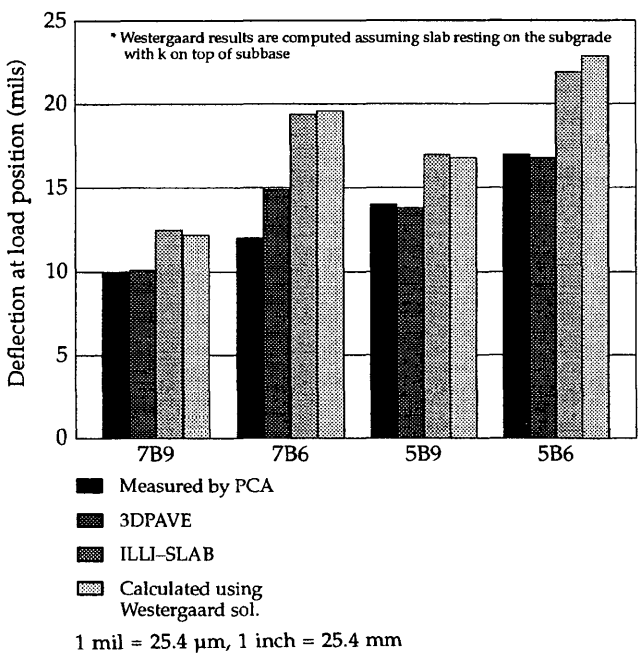

FIGURE 4 PCA data versus computed results for edge loading.

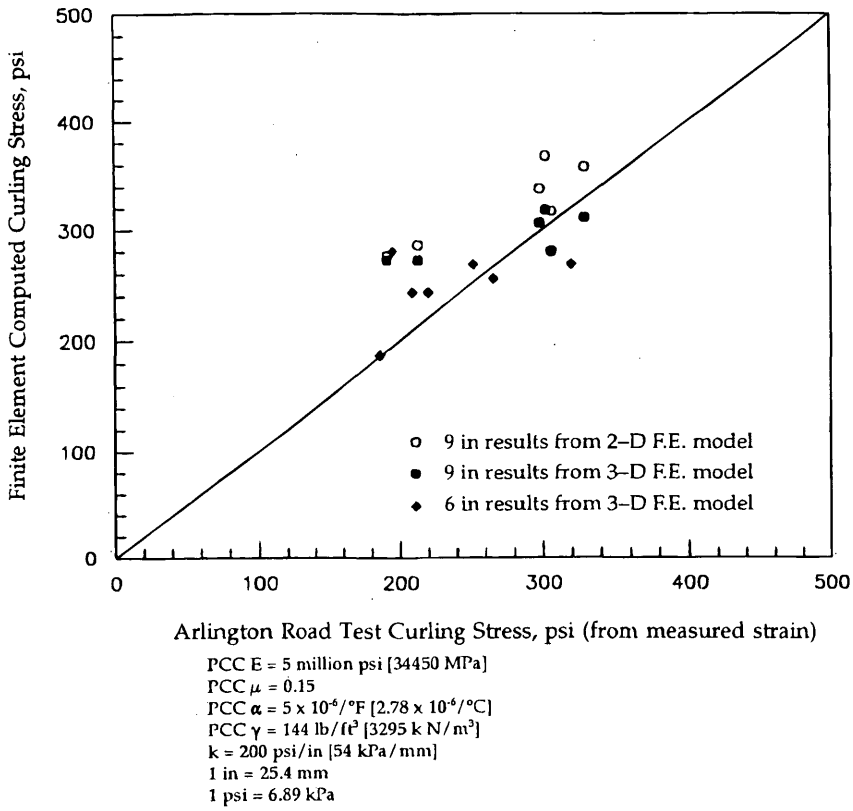

FIGURE 5 Curling stresses in Arlington Road Test slabs, computed from measured strain and from 2-D (ILLI-SLAB) and 3-D (3DPAVE) finite element models.

As noted in research by Darter and Barenberg (*15*), the curling stresses computed by the 2-D finite element program are higher than the stresses computed from measured strains. This is demonstrated in Figure 5 by the 2-D results all being above the equality line. However, the stresses computed using 3DPAVE not only generally agree with the measured stresses but also are distributed on both sides of the line. These results provide additional evidence that the 3DPAVE model has been properly built to handle temperature curling and demonstrates its predictive capability.

CONCLUSIONS

3DPAVE, a 3-D finite element model for concrete pavements was developed to analyze the complex and interacting factors that influence the support provided to a concrete pavement, including the following:

- Foundation support (subgrade *k* value);
- Base thickness, stiffness, and interface bond or friction;
- Slab curling and warping due to temperature and moisture gradients;
- Dowel and aggregate interlock load transfer action at joints; and
- Improved support with a widened lane, widened base, or tied concrete shoulder.

The ABAQUS general-purpose finite element software was used to develop a powerful and versatile 3-D model for analysis of concrete pavements. The 3DPAVE model outperformed the 2-D model and Westergaard's solutions for a variety of problems.

ACKNOWLEDGMENT

The research described was conducted for NCHRP Project 1-30, *Support Under Portland Cement Concrete Pavements*. The research is documented in full elsewhere (*3,16*).

REFERENCES

1. Zaghloul, S. M., and T. D. White. Use of a Three-Dimensional, Dynamic, Nonlinear Analysis to Develop Load Equivalency Factors for Composite Pavements. Presented at the 73rd Annual Meeting of the Transportation Research Board, Washington, D.C., 1994.
2. Mallela, J., and K. P. George. Three-Dimensional Response Model for Rigid Pavements. Presented at the 73rd Annual Meeting of the Transportation Research Board, Washington, D.C., 1994.
3. Darter, M. I., K. T. Hall, and C. M. Kuo. *"Support Under Portland Cement Concrete Pavements."* Appendixes, NCHRP Project 1-30 Final Report: TRB, National Research Council, Washington, D.C., 1995.
4. *ABAQUS Users Manual.* Version 5.2, Hibbitt, Karlsson, and Sorensen, Inc., Pawtucket, R.I. 1993.
5. Cook, R. D., D. S. Malkus, and M. E. Plesha. *Concepts and Applications of Finite Element Analysis,* 3rd Edition, McGraw-Hill, N.Y., 1988.

6. Zienkiewicz, O. C. *The Finite Element Method in Engineering Science,* McGraw-Hill, N.Y., 1971.
7. Timoshenko, S., and S. Woinowsky-Krieger. *Theory of Plates and Shells,* 2nd Edition, McGraw-Hill, N.Y., 1959.
8. Ioannides, A. M. *Analysis of Slab-On-Grade for a Variety of Loading and Support Conditions.* Ph.D. thesis, University of Illinois at Urbana-Champaign, 1984.
9. Ioannides, A. M., and G. T. Korovesis. Aggregate Interlock: A Pure-Shear Load Transfer Mechanism. In *Transportation Research Record 1286,* TRB, National Research Council Washington, D.C., 1990.
10. Kuo, C. M. *Three-Dimensional Finite Element Model for Analysis of Concrete Pavement Support.* Ph.D. thesis, University of Illinois at Urbana-Champaign, 1994.
11. *Special Report 61C: The AASHO Road Test, Report 3, Traffic Operations and Pavement Maintenance.* Appendix A, HRB, National Research Council, Washington, D.C., 1962.
12. *Special Report 61E: The AASHO Road Test, Report 5, Pavement Research.* HRB, National Research Council, Washington D.C., 1962.
13. Childs, L. D. "Tests of Concrete Pavement Slabs on Cement-Treated Subbases. In *Highway Research Record 60,* HRB, National Research Council, Washington, D.C., 1964.
14. Teller, L. W., and E. C. Sutherland. The Structural Design of Concrete Pavements, Part 2—Observed Effects of Variations in Temperature and Moisture on the Size, Shape, and Stress Resistance of Concrete Pavement Slabs. *Public Roads,* Vol. 16, No. 9, 1935.
15. Darter, M. I., and E. J. Barenberg. *Design of Zero-Maintenance Plain Jointed Concrete Pavement.* Report FHWA-RD-77-111, Vol. 1, 1977.
16. Darter, M. I., K. T. Hall, and C. M. Kuo. *NCHRP Report No. 372: Support Under Portland Cement Concrete Pavements.* TRB, National Research Council, Washington, D.C., 1995.

Publication of this paper sponsored by Committee on Rigid Pavement Design.

Improved Methods for Selection of *k* Value for Concrete Pavement Design

KATHLEEN T. HALL, MICHAEL I. DARTER, AND CHEN-MING KUO

The results of research conducted to improve guidelines for *k*-value selection for concrete pavement design are summarized in this paper. The research included a review of the evolution of *k*-value concepts and methods, a review of *k*-value results from several field studies, an examination of the AASHTO Guide's *k*-value methods, and proposed new guidelines for selection of design *k* values by a variety of methods. The *k* value was originally considered a useful and simple parameter for characterizing slab support provided by natural soils of fairly low shear strength. Recognizing that real soils are not true dense liquids, early researchers developed standardized test methods which provided *k* values in good agreement with full-size slab deflections. Later, substantially higher *k* values were attributed to granular and stabilized base layers, based on plate tests on top of bases, although slab tests had shown that such bases did not increase *k* values. Based on the historical review, review of results from several field studies, and a thorough examination of the *k*-value methods introduced in the 1986 AASHTO Guide, it is recommended that *k* values be selected for natural soil materials, and that base layers be considered in concrete pavement design in terms of their effect on the slab response, rather than their supposed effect on *k* value. Improved guidelines were developed for determining *k* value from a variety of methods, including correlations with soil type, soil properties, and other tests; backcalculation methods; and plate-bearing test methods. Guidelines for seasonal adjustment to *k*, and adjustments for embankments and shallow rigid layers were also developed.

In the AASHTO Guide for Design of Pavement Structures, and in all other accepted concrete pavement design procedures, the support a foundation provides a concrete pavement is characterized by a *k* value, which represents a *dense liquid* (elastic springs) foundation. The AASHTO Guide also has a loss of support input which is intended to represent the potential for reduction of support at slab corners over the design life of the pavement. However, the AASHTO Guide's procedures for selecting these inputs do not produce values which are truly representative of the *support* the concrete slab will experience over its design life, and which are truly representative of the effect of support on the performance of the concrete pavement.

Conventional plate-bearing tests were often conducted to determine subgrade *k* values through the 1950s, and even to the 1980s by some agencies. These tests are extremely expensive and time-consuming, and thus are rarely conducted today. Other approaches exist for estimating *k* values for design, including correlation with soil properties and other soil tests, and backcalculation from deflection testing on concrete pavements. The different approaches to selecting *k* values often give different results.

Since the 1960s, *k* values intended to represent plate-bearing test values estimated on top of the base have commonly been used in concrete pavement design. These *top of base* or *composite k* values overestimate the support the slab actually experiences in the field. This is particularly true for stabilized base layers or existing concrete or asphalt pavement structures. The *composite k* concept also does not realistically reflect the effect that a base layer has on stress in a concrete slab due to load, temperature, and moisture influences. A better approach to characterizing concrete pavement support would assign realistic *k* values to natural subgrades and embankments, and account for base effects in slab stressed.

Department of Civil Engineering, University of Illinois at Urbana-Champaign, 205 North Mathews Avenue, Urbana, Ill. 61801.

EVOLUTION OF THE *k* VALUE

A thorough historical review of the *k*-value concepts and methods which have evolved over the last hundred or more years was conducted for this study and yielded valuable insights into the meaning and practical significance of the *k* value. This review is documented in detail in References 1 and 2, and its main findings are briefly summarized below.

Introduction of Dense Liquid Support Model

The concept of a foundation which deflects in proportion to an applied vertical load, without shear transmission to adjacent areas of the foundation, dates back to the nineteenth century. The dense liquid model represents one end of the spectrum of elastic soil response (the other end of the spectrum is the elastic solid model). The elastic response of real soils lies somewhere between these two extremes. Furthermore, the behavior of real soils is not purely elastic, but plastic, and time-dependent as well. The *k* value of saturated cohesive soils may be substantially higher under rapid-loading than under slow-loading, because under slow-loading, primary consolidation occurs gradually as pore water pressures dissipate. In most cases, the deformation of the soil reaches some stable value, but soils may also exhibit secondary (creep) deformation, if the load magnitude exceeds the creep strength of the soil (*3,4*). Consolidation and creep behavior of soils necessitate some standardization of load test methods.

Westergaard's Equations for a Slab on a Dense Liquid

Westergaard presented the first equations for deflection of a concrete slab on a dense liquid foundation, and also introduced the terms *modulus of subgrade reaction* for the spring constant of the subgrade and *radius of relative stiffness* for the stiffness of a concrete slab relative to that of the subgrade (*5*). Westergaard suggested that the subgrade *k* value could be backcalculated from deflections of the slab surface rather than from load tests on the subgrade (*5,6*).

Arlington Road Tests

In the early 1930s, the Bureau of Public Roads conducted extensive field tests to investigate concrete pavement behavior. One of the objectives of these field tests was to verify Westergaard's equations. Among the many valuable findings of the Arlington tests were those concerning measurement of subgrade *k* values, effects of seasonal moisture variation on *k* values, effects of slab-curling on corner *k* values, and effect of subgrade *improvement* on *k* values (*7*). The Arlington researchers did extensive experimentation to develop methods to determine the subgrade *k* value from plate load tests and from full-size slab testing. The *k* values determined from repeated loads on large plates (e.g., at least 30-in [762-mm] diameter) at a deflection at 0.05 in [1.25 mm] yielded *k* values which agreed well with those backcalculated from deflections induced by loads on top of concrete slabs.

Corps of Engineers Field Studies

In the 1940s, the U.S. Army Corps of Engineers conducted load tests on subgrades and concrete slabs at Wright Field in Ohio and several other airfields. One of the objectives of the Wright Field slab tests was to develop a standard test method for determining subgrade *k* values (*8*). The *k* values obtained at a deflection of 0.05 in [1.25 mm] using a 30-in. [762 mm] diameter plate consistently yielded subgrade *k* values in close agreement with volumetric *k* values obtained from test on concrete slabs (calculated by dividing the load by the volume of the deflection basin) (*8,9,10*). "The only exception to this pattern is the high *k* value obtained on moderate base course thicknesses which generally must be adjusted downward to match full-size slab performance" (*8*). The Corps of Engineers' test method for *k* became the basis for the ASTM and AASHTO standard test methods developed later.

Correlation of *k* Value and CBR and Soil Classification

In 1942, Corps of Engineers researchers published perhaps the first chart correlating *k* value to California Bearing Ratio (CBR) and the Unified and Public Roads (now AASHTO) soil classification groups (*10*). This chart became the basis for correlation charts and tables later published in concrete pavement design manuals by the U.S. Army and the Portland Cement Association.

Effect of Base Layers on *k*

In the 1940s, numerous reports appeared in the literature concerning plate load tests on subgrades and on base layers. These studies contributed to a trend to quantifying *k* value increases as a function of base thickness and base material. The Corps of Engineers also apparently changed its position on the effect of base layers on *k* value, but apparently did not attempt to validate its design curves for "base *k* value" with deflection tests on concrete pavements (*11*).

ASTM Plate-Bearing Test Methods

The first American Society for Testing and Materials (ASTM) test methods for plate-bearing tests on soils were published in 1952: D 1195, Repetitive Static Plate Load Test, and D 1196, Nonrepetitive Static Plate Load Test. These were based on the Corps of Engineers test methods and have changed very little since they were originally published. Neither of the ASTM test methods gives any guidance on calculation of the subgrade *k* value from the test results, unlike the Corps of Engineers test method, and the AASHTO test methods T221 and T222, which were not standardized until the 1960s.

AASHO Road Test

Plate load, California Bearing Ratio (CBR), moisture content, and density tests were made on the subbase and the embankment at the AASHO Road Test. At the time of the Road Test, AASHO did not have standard test methods for plate-bearing tests, and the test procedure used did not conform to the then-current ASTM or Corps of Engineers standards. The procedure used was similar to that used at the Arlington Road Test, and involved cycling loading and unloading at three load levels using a 30-in. [762-mm] diameter plate. An average elastic *k* value was determined by dividing each of the individual loads by the elastic deformations they produced and a gross *k* value was determined for each load level by dividing the load by the total deformation produced, including permanent deformation. The elastic *k* values averaged 77 percent greater than the corresponding gross *k* values (*12*).

A *k* value of 60 psi/in. [16 kPa/mm] was used to represent AASHO Road Test conditions in the development of the AASHO rigid pavement design equation (*13*). This is the mean springtime gross *k* value from tests on top of the subbase. It is almost as conservative a value as could possibly have been picked to represent the Road Test conditions. The only more conservative value would have been the slightly lower springtime gross *k* value of 49 psi/in. [13 kPa/mm] on top of the subgrade. Why the subbase gross *k* was selected rather than the subgrade *k* is not documented.

The Corps of Engineers conducted load tests on top of the existing slabs at the AASHO Road Test site in 1962 and calculated volumetric *k* values between 25 and 92 psi/in. [7 and 26 kPa/mm] from the slab deflection basins (*14,15*). Loop 1 of the AASHO Road Test was tested using a Falling Weight Deflectometer for this study in May 1992. Care was taken in the analysis to account for the effects of temperature, load transfer, slab size, and concrete compressibility. The mean backcalculated dynamic *k* of 148 psi/in. [40 kPa/mm], when divided by 2, yields an estimated static *k* of 74 psi/in. [20 kPa/mm], which is within the range obtained from plate load tests on the subgrade and also within the range obtained by the Corps of Engineers from static tests on top of the slabs.

Portland Cement Association

In the 1960s, the Portland Cement Association (PCA) conducted plate tests on subgrade soils, untreated gravel and crushed stone bases, cement-treated subbases, and soil-cement pavements. The tests on the granular bases yielded slightly higher *k* values than the subgrade *k* values, but the tests on the cement-treated bases yielded considerably higher *k* values. Tests on concrete slabs constructed on the cement-treated bases showed decreases in maximum edge and interior deflections with increasing base thickness (*16*). The PCA used these results to develop curves for top-of-base *k* values for granular and cement-treated bases, which were incorporated in PCA's concrete pavement design procedures.

In this study, the slab deflection data reported by PCA were used to backcalculate k values, and the values obtained were much more similar to those reported for the subgrade plate tests than to those reported for the plate tests on the cement-treated base.

1972 AASHO Interim Guide

The 1972 Interim Guide (*17*) recommended the use of the subgrade gross k value, and provided a nomograph to determine a composite k value on top of a subbase. The 1972 Guide also suggested that an adjustment to the k value might be warranted to reflect loss of support. Both the subbase adjustment and the loss of support adjustment are inconsistent with the derivation of the AASHTO rigid pavement model, which was already calibrated to the subbase k value of the Road Test, and was also calibrated to the performance (including the effect of substantial pumping and loss of support) of the AASHO Road Test's granular-base concrete pavement sections.

Correlation of k to Soil Type and Degree of Saturation

The 1977 Zero-Maintenance study proposed that the k value in various seasons could be estimated from its AASHTO classification and the degree of saturation in the upper 5 ft [1.5 m] of soil (*18*). The curves developed for k value were obtained using correlations between resilient modulus, static elastic modulus, and degree of saturation which were developed from an extensive field and laboratory study of Illinois soils (*19*).

Backcalculation Methods

In the last 15 years, several methods were developed for efficient estimation of k values from deflection test data. These methods used finite element programs or Westergaard's equations to determine the subgrade k value as a function of the deflection basin measured by a Falling Weight Deflectometer or similar device. Nomographs and equations for backcalculation of concrete elastic moduli and foundation k values and concrete E values for concrete or composite pavements were incorporated in the overlay design procedures in Part III of the 1993 AASHTO Guide (*20*).

The dynamic k values obtained from FWD data are typically about twice as high as the static k values which would be expected for the same soils in standard plate bearing tests. The rule of thumb gives reasonable results, as numerous field studies reviewed for this research have shown. It is very difficult to provide a more sophisticated method for converting dynamic k values to static k values, due to the complexities of modelling dynamic soil behavior and the sparsity of side-by-side comparisons of dynamic and static soil response. Nonetheless, it may be true, and future research may show, that the relationship between dynamic and static k varies in a predictable way as a function of soil properties, loading characteristics, or other factors.

AASHTO GUIDE k VALUE METHODS

The 1986 version of the AASHTO Guide (*21*) contained five modifications to the k value guidelines of the 1972 Interim Guide:

1. An equation was provided for k value for an unprotected subgrade;
2. A revised nomograph for composite (top-of-base) k was provided;
3. An adjustment for depth to a rigid foundation was introduced;
4. A seasonal adjustment procedure for k was provided; and
5. A loss-of-support procedure was provided.

k Equation for Unprotected Subgrade

A simple linear relationship described as a "theoretical relationship between k values from a plate bearing test and elastic modulus of the roadbed soil" was presented in the 1986 AASHTO Guide:

$$k = \frac{M_R}{19.4} \tag{1}$$

Part II of the AASHTO Guide makes no distinction between the laboratory-measured resilient modulus of a soil sample (M_R) and the in situ elastic modulus of a subgrade soil mass (E). The relationship between k and resilient modulus given in the Guide's Appendix HH was derived using an elastic layer computer program to model a circular load on an elastic half-space. Because an elastic layer program cannot model rigid plate loading, k was not computed as pressure divided by deflection, but rather as load divided by deflection volume. These two definitions for k are equivalent only when the total deflected volume is equal to the plate deflection times the contact area. However, in the derivation of Equation 1, the k corresponding to each input E was computed by dividing the plate load by only the portion of the deflected volume within the radius of the load plate.

In a real plate load test on a natural subgrade material, the shear stress at the edge of a flexible load plate is equal to the applied pressure. The shear stress at the edge of a rigid load plate is considerably higher. If this shear stress exceeds the shear strength of the soil, the plate will punch down into the soil and relatively little deflection will occur outside the load plate. To the extent that this happens, the real soil's response approaches that of an ideal Winkler foundation. However, an elastic layer program is not capable of reproducing the type of discontinuous deflected shape of the subgrade surface which would really occur in plate tests on most natural soils of relatively low shear strength.

If an elastic layer program is used to model a concrete slab on subgrades with the set of E values used to derive Equation 1, the k values which may be backcalculated from the slab deflections are substantially less than those indicated by Equation 1. A real example of this is the AASHO Road Test soil itself: the laboratory resilient modulus of the Road Test soil was about 3000 psi [20.7 MPa] for springtime moisture conditions. Dividing 3000 by 19.4 yields a k value of about 155 psi/in. [42 kPa/mm], nearly twice as high as the springtime elastic subgrade k value, 86 psi/in. [23 kPa/mm].

Composite k Nomograph for Base and Subgrade

The 1986 AASHTO Guide presented a nomograph for determining a composite k as a function of subgrade resilient modulus and the thickness and elastic modulus of a base layer. The development of this nomograph was documented in the Guide's Appendix LL. Again, the subgrade's laboratory resilient modulus was presumed equal to the in situ elastic modulus. The nomograph was developed by simulating plate load tests with an elastic layer program. A k

value was calculated as the plate pressure divided by the maximum deflection under the plate. One anomaly of the AASHTO composite k nomograph is that, although it yields very high k values for base layers, in some cases these k values are lower than the k values that would be assigned to the subgrade if the base were not present. Furthermore, elastic layer analyses conducted in this study showed that the Guide's composite k nomograph yielded substantially higher k values than those backcalculated from slab deflections.

Adjustment to k for Shallow Rigid Foundation

The 1986 Guide introduced a nomograph for adjustment to the composite k value when a rigid foundation was present at a depth within 10 ft [3 m]. The basis for the AASHTO Guide's nomograph is not documented, although it is presumed to have been developed using elastic layer simulation in a manner similar to the development of the composite k nomograph.

Seasonal Adjustment Procedure for k

The 1986 Guide provided a method for determining a design k value which represents the range of k values expected in various seasons, weighted with respect to the relative damage done to the pavement in those seasons. The relative damage is calculated using the AASHTO rigid pavement design equation. This damage-weighted seasonal adjustment is reasonable in concept, although the nomograph provided suggests that relative damage is sensitive to slab thickness, and close examination of the nomograph and equations reveals that slab thickness has little or no effect. Another inconsistency of the seasonal adjustment procedure is that the design equation itself is not calibrated to a seasonal average k for the AASHO Road Test site, but rather the springtime k value. This inconsistency, by the way, is present in the flexible pavement design procedure as well, where the impact on required pavement thickness is much more dramatic.

Loss of Support Adjustment to k

The nomograph introduced in the 1986 Guide for reducing the k value for potential loss of support due to base erodibility produces dramatic reductions in k values for erodible bases. Little or no adjustment is applied when the base is a relatively inerodible stabilized material. This loss of support adjustment is a major inconsistency in the AASHTO design procedure, because the rigid pavement design equation is based on the performance of AASHO Road Test pavements which had granular bases and experienced substantial loss of support. The loss of support adjustment is also inconsistent with the k value of 60 psi/in. [16 kPa/mm] embedded in the rigid pavement design equation. According to the loss of support nomograph, the granular base at the AASHO Road Test site would be assigned a loss of support factor from 1.0 to 3.0, which would reduce the k value to between 6 and 22 psi/in. [1.6 and 6 kPa/mm].

IMPROVED METHODS FOR DETERMINING k VALUE

The elastic k value on top of the subgrade or prepared embankment is the recommended design input. Only the elastic component of deformation is considered representative of the response of the subgrade to traffic loads on the pavement. Three categories of methods were compiled in this study for estimating the elastic k value of the subgrade for a pavement design project: correlation methods, backcalculation methods, and plate-testing methods.

Correlation Methods

Guidelines were developed for selecting an appropriate k value based on soil classification, moisture level, density, California Bearing Ratio (CBR), Hveem Stabilometer data (R-value), or Dynamic Cone Penetrometer (DCP) data. These correlation methods are anticipated to be routinely used for design. k values obtained from correlation methods may need adjustment for embankment above the subgrade or a shallow rigid layer beneath the subgrade.

k Value Correlations for Cohesionless Soils (A-1 and A-3)

A cohesionless material may be characterized by its shear modulus, which is fairly insensitive to moisture variation and is predominantly a function of void ratio and overall stress state (which in turn are functions of dry density and depth). Recommended k value ranges for A-1 and A-3 soils are given in Table 1.

k Value Correlations for A-2 Soils

Soils in the A-2 class are all granular materials falling between A-1 and A-3. Although it is difficult to predict the behavior of such a wide variety of materials, the available data indicates that in terms of bearing capacity, A-2 materials behave similarly to cohesionless materials of comparable density. Recommended k value ranges for A-1 and A-3 soils are given in Table 1.

k Value Correlations for Cohesive Soils (A-4 through A-7)

Some characteristics of the various classes of cohesive soils are summarized in Table 1. The bearing capacity of these cohesive soils is strongly influenced by their degree of saturation, which is a function of moisture content, dry density, and specific gravity. Recommended k values for each cohesive soil type as a function of degree of saturation are shown in Figure 1. Each line represents the midrange of reasonable values for k. For any given soil type and degree of saturation, the range of reasonable values is about + 40 psi/in. [11 kPa/mm]. So, for example, an A-6 soil might be expected to exhibit k values between about 180 and 260 psi/in. [49 and 70 kPa/mm] at 50 percent saturation, and k values between about 5 and 85 psi/in. [1 and 23 kPa/mm] at 100 percent saturation. Note that two different types of materials can be classified as A-4. The line labeled A-4 in Figure 1 is representative of predominantly silty materials (at most 25 percent retained on the #200 sieve) with densities between about 90 and 105 lb/ft^3 [14300 and 16700 N/m^3] and CBRs between about 4 and 8. Mixtures of silt, sand, and gravel (up to 64 percent retained on the #200 sieve) can also be classified as A-4, but have densities between about 100 and 125 lb/ft^3 [15900 and 19900 N/m^3] and CBRs between about 5 and 15. The line labeled A-7-6 is more representative of this latter group.

TABLE 1 Recommended *k* Value Ranges for Various Soil Types

AASHTO Class	Description	Unified Class	Dry Density (lb/ft^3)	CBR (percent)	k value (psi/in)
Coarse-Grained Soils:					
A-1-a, well graded	gravel	GW, GP	125 - 140	60 - 80	300 - 450
A-1-a, poorly graded			120 - 130	35 - 60	300 - 400
A-1-b	coarse sand	SW	110 - 130	20 - 40	200 - 400
A-3	fine sand	SP	105 - 120	15 - 25	150 - 300
A-2 Soils (Granular Materials with High Fines):					
A-2-4, gravelly	silty gravel	GM	130 - 145	40 - 80	300 - 500
A-2-5, gravelly	silty sandy gravel				
A-2-4, sandy	silty sand	SM	120 - 135	20 - 40	300 - 400
A-2-5, sandy	silty gravelly sand				
A-2-6, gravelly	clayey gravel	GC	120 - 140	20 - 40	200 - 450
A-2-7, gravelly	clayey sandy gravel				
A-2-6, sandy	clayey sand	SC	105 - 130	10 - 20	150 - 350
A-2-7, sandy	clayey gravelly sand				
Fine-Grained Soils:					
A-4	silt	ML, OL	90 - 105	4 - 8	5 - 165 *
	silt/sand/ gravel mixture		100 - 125	5 - 15	40 - 220 *
A-5	poorly graded silt	MH	80 - 100	4 - 8	5 - 190 *
A-6	plastic clay	CL	100 - 125	5 - 15	5 - 255 *
A-7-5	moderately plastic elastic clay	CL, OL	90 - 125	4 - 15	5 - 215 *
A-7-6	highly plastic elastic clay	CH, OH	80 - 110	3 - 5	40 - 220 *

* k value of fine-grained soils is dependent on degree of saturation. See Figure 1.
1 lb/ft^3 = 159 N/m^3, 1 psi/in = 0.27 kPa/mm

Correlation of k Value to Other Tests

Correlations were also developed in this study to estimate *k* value from California Bearing Ratio (CBR), R-value, and Dynamic Cone Penetrometer (DCP) penetration rate and are presented in Reference 2.

Backcalculation Methods

Backcalculation methods are suitable for determining *k* value for design of overlays of existing pavements, or for design of reconstructed pavements on existing alignments, or for design of similar pavements in the same general location on the same type of subgrade. An agency may also use backcalculation methods to develop correlations between nondestructive deflection testing results, and subgrade types and properties. Cut-and-fill sections are likely to yield different *k* values. No embankment or rigid layer adjustment is required for backcalculated *k* values if these characteristics are similar for the pavement being tested and the pavement being designed, but backcalculated dynamic *k* values need to be reduced by a factor of approximately two to estimate a static elastic *k* value for use in design.

AREA Methods

Equations and nomographs for backcalculation of concrete elastic moduli and subgrade *k* values for concrete and composite pavements are provided in Part III of the 1993 AASHTO Guide. This

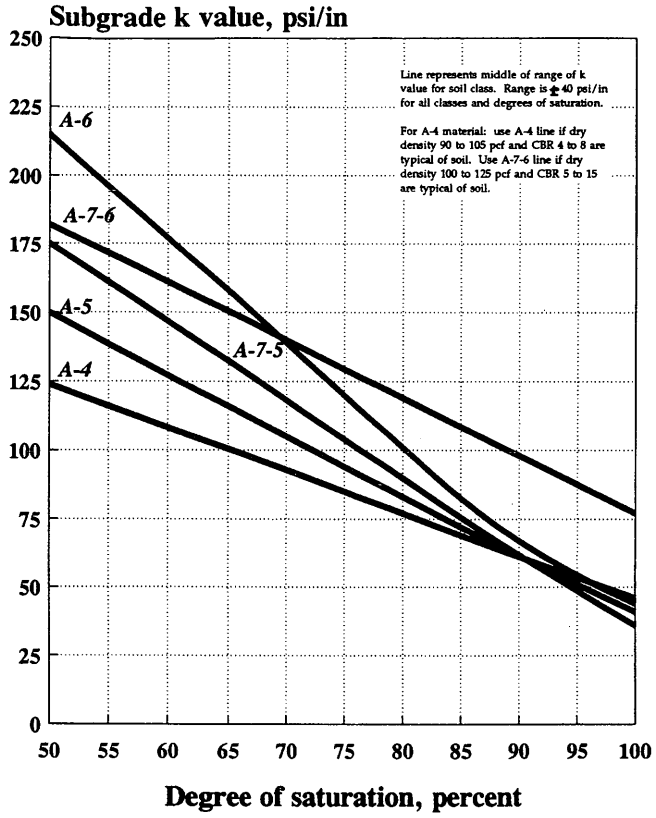

FIGURE 1 *k* Value versus degree of saturation for cohesive soil classes.

solution method is based on deflection of an infinite slab, and produces a dynamic elastic k value, which should be reduced by a factor of two to estimate a static elastic k value for design. This procedure is also based on a four-sensor definition of the deflection basin. For the SHRP sensor positions of 0,8,12, 18,24,36, and 60 inches [0, 203,305,457,601,914, and 1524 mm] from the load center, AREA is calculated from the following equation:

$$\text{AREA}_{\text{SHRP}} = \frac{4\,d_0 + 6\,d_8 + 5\,d_{12} + 6d_{18} + 9\,d_{24} + 18\,d_{36} + 12\,d_{60}}{d_0} \quad (2)$$

The radius of relative stiffness is calculated from the following equation:

$$\ell = \left[\frac{\ln\left(\frac{60 - \text{AREA}_{\text{SHRP}}}{289.708}\right)}{-0.698}\right]^{2.566} \quad (3)$$

$\text{AREA}_{\text{SHRP}}$ values between 35 and 50 correspond to typical l values of 25 to 55 for concrete highway pavements. (The corresponding range of AREA values according to the four-sensor definition would be 27 to 33). In theory the two AREA definitions should yield the same ℓ, but in practice the two may give different ℓ values, primarily because $\text{AREA}_{\text{SHRP}}$ includes a deflection at a much greater distance from the load.

The subgrade k value and concrete E value may be calculated from Westergaard's deflection equation and definition of radius of relative stiffness, or may be calculated from any of the sensor deflections, using the following equations:

$$k = \frac{P\,d_r^*}{d_r\,\ell^2} \quad (4)$$

$$E = \frac{12\,(1 - \mu^2)\,P\,\ell^2\,d_r^*}{d_r\,h^3} \quad (5)$$

where

P = load magnitude
d_r = measured deflection at radial distance r
h = slab thickness
μ = slab Poisson's ratio
D = slab bending stiffness:

$$D = \frac{E\,h^3}{12\,(1 - \mu^2)} \quad (6)$$

d_r^* = nondimensional deflection coefficient for radial distance r:

$$d_r^* = ae^{[-be(-c\ell)]}. \quad (7)$$

The values for the $a,b,$ and c constants in this equation are given in Table 2. Note that k and E values computed from two or more sensor deflections should not be considered independent estimates, because they are all derived from a common ℓ value which was determined from the AREA computed from all of the deflections. Note also that these equations were developed for the FWD load plate radius of 5.9 inches [150 mm], although they are not very sensitive to load size. Similar equations for the large FWD load plate have also been developed.

Solution for Any Arbitrary Sensor Arrangement

The backcalculation methods based on any given sensor arrangement are limited in application to data collected with that sensor arrangement. It is also possible to solve for l from any two deflections at any two radial distances greater than 0, because for a given load plate size, the nondimensional deflection coefficient is a function of a single parameter, the radial distance normalized to the radius of relative stiffness, as shown in Figure 2. The following equation was obtained for this curve:

$$d^* = 0.12497e^{-0.46308\left(\frac{r}{\ell}\right)^{1.55212}} \quad (8)$$

Any two deflections d_x and d_y measured at radial distances x and y (both greater than 0 and x greater than y) may be used to solve for ℓ:

$$\ell = \sqrt[1.55212]{\frac{-0.46308\,(x^{1.55212} - y^{1.55212})}{\ln\left(\frac{d_x}{d_y}\right)}} \quad (9)$$

Edge and Corner Solutions and Slab Size Effects

As Crovetti (22) has shown, Westergaard's equations for maximum edge, interior, and corner deflection may be represented as quadratic

TABLE 2 Regression Coefficients for d Versus ℓ Relationships

Radial distance (in)	a	b	c
0	0.12450	0.14707	0.07565
8	0.12323	0.46911	0.07209
12	0.12188	0.79432	0.07074
18	0.11933	1.38363	0.06909
24	0.11634	2.06115	0.06775
36	0.10960	3.62187	0.06568
60	0.09521	7.41241	0.06255

$R^2 \geq$ 99.7 percent (predicted versus actual values) for all models.
$\sigma_Y \leq 0.01$ for all models.
1 in = 25.4 mm

equations of the following form (note that $a,b,$ and c are quadratic equation constants and a_r is the load radius):

$$\frac{d_0 D}{P\ell^2} = x_1 + x_2\left(\frac{a_r}{\ell}\right) + x_3\left(\frac{a_r}{\ell}\right)^2 \quad (10)$$

The equations for interior, edge, and corner loading become (*22*):

$$\textit{Interior: } \frac{d_0 D}{P\,\ell^2} = 0.1253 - 0.008\left(\frac{a_r}{\ell}\right) - 0.028\left(\frac{a_r}{\ell}\right)^2 \quad (11)$$

$$\textit{Edge: } \frac{d_0 D}{P\ell^2} = 0.4311 - 0.707\left(\frac{a_r}{\ell}\right) - 0.2899\left(\frac{a_r}{\ell}\right)^2 \quad (12)$$

$$\textit{Corner: } \frac{d_0 D}{P\ell^2} = 1.148 - 1.50\left(\frac{a_r}{\ell}\right) - 0.6565\left(\frac{a_r}{\ell}\right)^2 \quad (13)$$

Each of these equations can be rearranged to isolate ℓ on the right side and solve for ℓ as a root of the quadratic equation:

$$\ell = \frac{b - \sqrt{b^2 - 4\,a\,c}}{2\,a} \quad (14)$$

where, for example, for the interior deflection equation:

$a = 0.1253$
$b = -0.008a_r$
$c = -0.028\,a_r^2 - (d_0\,D/P)$

This approach to determining ℓ permits backcalculation of edge and corner k values if the concrete E is assumed or is backcalculated from interior deflection basins (e.g., by the AREA method). Again, adjustment may be required for slab size.

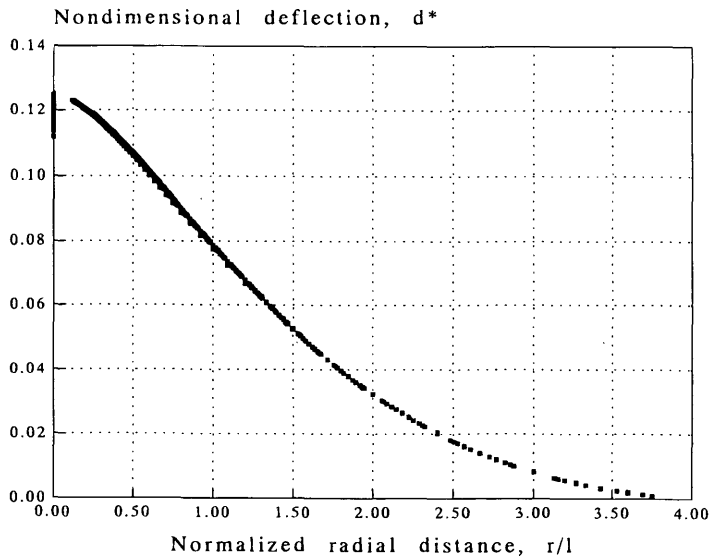

FIGURE 2 Nondimensional deflection coefficient versus normalized radial distance.

Seasonal Variation in Backcalculated k Values

The *k* value determined from backcalculation represents the *k* value for the season in which the deflection testing was conducted. An agency may wish to conduct deflection testing on selected projects in different seasons of the year to assess the seasonal variation in backcalculated *k* values for different types of subgrades.

Plate-Bearing Test Methods

The most direct method of determining *k* is by repetitive or nonrepetitive static plate-loading tests (AASHTO T 221 or T 222, ASTM D 1195 or D 1196) on a prepared section of the subgrade or embankment. Because these tests are costly and time-consuming, it is not anticipated that they will be conducted routinely. AASHTO T 221 and T 222 specify that if the pavement is to be built on an embankment, the plate-bearing tests should be conducted on a test embankment.

In the repetitive test, the elastic *k* value is determined from the ratio of load to elastic deformation (the recoverable portion of the total deformation measured). In the nonrepetitive test, the load-deformation ratio at a deformation of 0.05 in [1.25 mm] is considered to represent the elastic *k* value, according to the research by the Corps of Engineers. Note also that a 30-in. [762-mm] diameter plate should be used to determine the elastic static *k* value for use in design. Smaller-diameter plates will yield much higher *k* values which are inconsistent with slab behavior under load.

Assignment of *k* Values to Seasons

A season is defined as a period of time within a year which can be characterized by some set of climatic parameters. Among the factors which should be considered in selecting seasonal *k* values are the seasonal movement of the water table, seasonal precipitation levels, winter frost depths, number of freeze-thaw cycles, and the extent to which the subgrade will be protected from frost by embankment material. A *frozen k* may not be appropriate for winter, even in a cold climate, if the frost will not remain in a substantial thickness of the subgrade throughout the winter. If it is anticipated that a substantial depth (e.g., a few feet) of the subgrade will be frozen, a *k* value of 500 psi/in. [135 kPa/mm] would be a reasonable *frozen k*.

The seasonal variation in degree of saturation is difficult to predict, but in locations where a water table is constantly present at a depth of less than about 10 ft [3 m], it is reasonable to expect that fine-grained subgrades will remain at least 70 and 90 percent saturated, and may be completely saturated for substantial periods in the spring. The highest position of the water table, but not its annual variation, can be determined from county soil reports.

A seasonally adjusted *effective k* value may be obtained by combining the seasonal *k* values. The *effective k* value is essentially a weighted average based on some performance measure such as fatigue damage. The *effective k* value results in the same performance over the entire year that is caused by the seasonally varying *k* value. Determination of a seasonally adjusted *effective k* value within the context of any specific design procedure must be done using the performance model intrinsic to that procedure. In this study, an improved seasonal adjustment procedure was developed for the AASHTO Guide, using a proposed revised performance model calibrated to the seasonally adjusted *k* value of the AASHTO Road Test site, as described in Reference 1.

Adjustment to *k* for Fill Thickness and Rigid Layer

The nomograph shown in Figure 3 was developed for adjustment of the seasonally adjusted effective subgrade *k* value if (a) fill material will be placed above the natural subgrade, and/or (b) a rigid layer (e.g., bedrock or hard clay) is present at a depth of 10 ft [3 m] or less beneath the existing subgrade surface. Note that the rigid layer

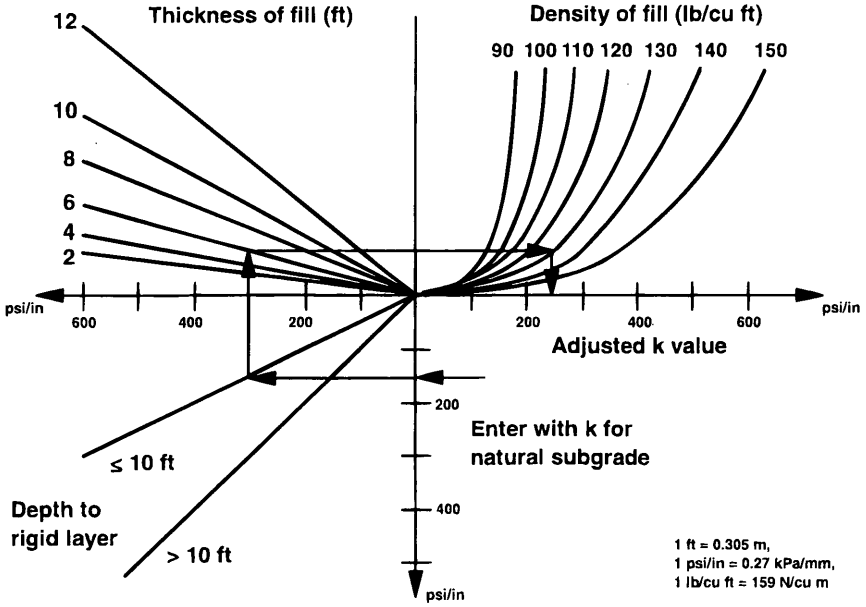

FIGURE 3. Adjustment to *k* for fill and/or rigid layer.

adjustment should only be applied if the subgrade k was determined on the basis of soil type or similar correlations. If the k value was determined from nondestructive deflection testing or from plate-bearing tests, the effect of a rigid layer is already represented in the k value obtained.

CONCLUSIONS AND RECOMMENDATIONS

This paper presents the results of research conducted to develop improved guidelines for k value selection for concrete pavement design. The research included a review of the evolution of k value concepts and methods, a review of k value results from several field studies, an examination of the AASHTO Guide's k value methods, and proposed new guidelines for selection of design k values by a variety of methods. These include correlations with soil type, soil properties, and other tests; deflection testing and backcalculation methods; and plate-bearing test methods. Guidelines for seasonal adjustment to k and adjustments for embankments and shallow, rigid layers were also developed.

ACKNOWLEDGMENT

The research described in this paper was conducted for NCHRP Project 1-30, "Support Under Portland Cement Concrete Pavements." The research is documented in full in References 1 and 2.

REFERENCES

1. Darter, M. I., K. T. Hall, and C.M. Kuo. Support Under Portland Cement Concrete Pavements, *NCHRP Report 372.* TRB, National Research Council, Washington, D.C., 1995.
2. Darter, M. I., K. T. Hall, and C. M. Kuo. Support Under Portland Cement Concrete Pavements, *Appendices to NCHRP Project 1-30 Final Report.* TRB, National Research Council, Washington, D.C., 1995.
3. Selvadurai, A. P. S. Elastic Analysis of Soil-Foundation Interaction. *Developments in Geotechnical Engineering.* Vol. 17, Elsevier Scientific Publishing Company, The Netherlands, 1979.
4. Peck, R. B., W. E. Hanson, and T. H. Thornburn. *Foundation Engineering,* 2nd ed. John Wiley and Sons, New York, 1974.
5. Westergaard, H. M. Computation of Stresses in Concrete Roads. *Proceedings.* HRB, National Research Council, Washington, D.C., 1925. Also published as Stresses in Concrete Pavements Computed by Theoretical Analysis. *Public Roads.* Vol. 7, No. 2, 1926.
6. Westergaard, H. M. Theory of Stresses in Road Slabs, *Proceedings, Fourth Annual Meeting of the Highway Research Board.* HRB, National Research Council, Washington, D.C., 1925.
7. Teller, L. W., and E. C. Sutherland. The Structural Design of Concrete Pavements, Part 5, An Experimental Study of the Westergaard Analysis of Stress Conditions in Concrete Pavements of Uniform Thickness. *Public Roads.* Vol. 23, No. 8, 1943.
8. Sale, J. P. Rigid Pavement Design for Airfields. *Proceedings, First International Conference on Concrete Pavement Design,* Purdue University, West Lafayette, Indiana, 1977.
9. Phillippe, R. R. Field Bearing Tests Applied to Pavement Design. *Symposium on Load Tests of Bearing Capacity of Soils,* American Society for Testing and Materials, Special Technical Publication No. 79, 1947.
10. Middelbrooks, T. A., and G. E. Bertram. Soil Tests for Design of Runway Pavements. *Proceedings,* HRB, National Research Council, Washington, D.C., 1942.
11. Ahlvin, R. G. Origin of Developments for Structural Design of Pavements. *Technical Report GL-91-26,* U.S. Army Corps of Engineers, Waterways Experiment Station, Vicksburg, Mississippi, 1991.
12. Highway Research Board. The AASHO Road Test, Report 5, Pavement Research, *Special Report 61E,* 1962.
13. Langsner, G., T. S. Huff, and W. J. Liddle. Use of Road Test Findings by AASHO Design Committee, from The AASHO Road Test, Proceedings of a Conference Held May 16–18, 1962, St. Louis, Mo. *HRB Special Report No. 73,* National Research Council, Washington, D.C., 1962.
14. U.S. Army Corps of Engineers. Results of Modulus of Subgrade Reaction Determination at the AASHO Road Test Site by Means of Pavement Volumetric Displacement Test. Ohio River Division Laboratories, April 1962.
15. Vesic, A. S., and S. K. Saxena. Analysis of Structural Behavior of AASHO Road Test Rigid Pavements, *NCHRP Report No. 97,* HRB, National Research Council, Washington, D.C., 1970.
16. Childs, L. D. Cement-Treated Subbases for Concrete Pavements. *Record No. 189,* HRB, National Research Council, Washington, D.C., 1967.
17. American Association of State Highway Officials. *Interim Guide for Design of Pavement Structures.* Washington, D.C., 1972.
18. Darter, M. I. Design of Zero-Maintenance Plain Jointed Concrete Pavement, Volume 1—Development of Design Procedures. *Report No. FHWA-RD-77-111* University of Illinois at Urbana-Champaign, 1977.
19. Thompson, M. R., and Q. L. Robnett. Resilient Properties of Subgrade Soils. *Illinois Cooperative Highway Research Program, Report No. UILU-ENG-76-2009,* University of Illinois and Illinois Department of Transportation, 1976.
20. American Association of State Highway and Transportation Officials, *Guide for Design of Pavement Structures,* Washington, D.C., 1993.
21. American Association of State Highway and Transportation Officials, *Guide for Design of Pavement Structures,* Washington, D.C., 1986.
22. Crovetti, J. A. Evaluation of Jointed Concrete Pavement Systems Incorporating Open-Graded Subbases. Ph.D. thesis. University of Illinois at Urbana-Champaign, 1994.

Publication of this paper sponsored by Committee on Rigid Pavement Design.